



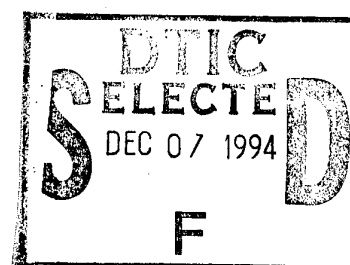
AGARD-LS-197

AGARD-LS-197

AGARD

ADVISORY GROUP FOR AEROSPACE RESEARCH & DEVELOPMENT

7 RUE ANCELLE, 92200 NEUILLY-SUR-SEINE, FRANCE



AGARD LECTURE SERIES 197

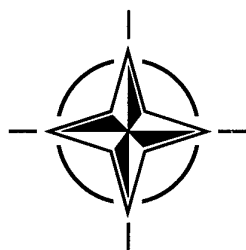
Flight in an Adverse Environment

Le Vol en Environnement Hostile

This publication was prepared at the request of the Flight Vehicle Integration Panel and under the sponsorship of the Consultant and Exchange Programme of AGARD and will be presented on 7-8 November 1994 in Braunschweig, Germany, 10-11 November 1994 in Lisbon, Portugal, and 15-16 November 1994 in Atlantic City, USA.

This document has been approved
for public release and sale; its
distribution is unlimited.

19941129 117



NORTH ATLANTIC TREATY ORGANIZATION

Published November 1994

Distribution and Availability on Back Cover

AGARD

ADVISORY GROUP FOR AEROSPACE RESEARCH & DEVELOPMENT

7 RUE ANCELLE, 92200 NEUILLY-SUR-SEINE, FRANCE

AGARD LECTURE SERIES 197

Flight in an Adverse Environment

Le Vol en Environnement Hostile

This publication was prepared at the request of the Flight Vehicle Integration Panel and under the sponsorship of the Consultant and Exchange Programme of AGARD and will be presented on 7-8 November 1994 in Braunschweig, Germany, 10-11 November 1994 in Lisbon, Portugal, and 15-16 November 1994 in Atlantic City, USA.

Accession For	
NTIS	<input checked="" type="checkbox"/>
CRA&I	<input checked="" type="checkbox"/>
DTIC	<input type="checkbox"/>
TAB	<input type="checkbox"/>
Unannounced	<input type="checkbox"/>
Justification	
By	
Distribution/	
Availability Codes	
Dist	Avail and/or Special
A-1	



North Atlantic Treaty Organization
Organisation du traité de l'Atlantique Nord

DTIC QUALITY INSPECTED 5

The Mission of AGARD

According to its Charter, the mission of AGARD is to bring together the leading personalities of the NATO nations in the fields of science and technology relating to aerospace for the following purposes:

- Recommending effective ways for the member nations to use their research and development capabilities for the common benefit of the NATO community;
- Providing scientific and technical advice and assistance to the Military Committee in the field of aerospace research and development (with particular regard to its military application);
- Continuously stimulating advances in the aerospace sciences relevant to strengthening the common defence posture;
- Improving the co-operation among member nations in aerospace research and development;
- Exchange of scientific and technical information;
- Providing assistance to member nations for the purpose of increasing their scientific and technical potential;
- Rendering scientific and technical assistance, as requested, to other NATO bodies and to member nations in connection with research and development problems in the aerospace field.

The highest authority within AGARD is the National Delegates Board consisting of officially appointed senior representatives from each member nation. The mission of AGARD is carried out through the Panels which are composed of experts appointed by the National Delegates, the Consultant and Exchange Programme and the Aerospace Applications Studies Programme. The results of AGARD work are reported to the member nations and the NATO Authorities through the AGARD series of publications of which this is one.

Participation in AGARD activities is by invitation only and is normally limited to citizens of the NATO nations.

The content of this publication has been reproduced
directly from material supplied by AGARD or the authors.

Published November 1994

Copyright © AGARD 1994
All Rights Reserved

ISBN 92-836-1006-7



*Printed by Canada Communication Group
45 Sacré-Cœur Blvd., Hull (Québec), Canada K1A 0S7*

Abstract

The environment in which an airplane must operate is a major cause of aircraft accidents. This lecture series focuses on specific aspects of the environment, both natural and man-made, which are the major contributors to these accidents as follows:

- wake turbulence and the generation of trailing vortex systems;
- the results of an extensive flight test program concerning winter storms off the east coast of Canada including effect on aircraft operations. The Canadian Atlantic Storms Program (CASP) includes effects of airframe icing, strong winds, turbulence, wind shear, precipitation, reduced visibility, reduced ceilings and electrification;
- electromagnetic effects including electrical discharge properties, in-flight test programs, in-flight lightning models and lightning simulation techniques;
- response of an aircraft to wind shear and methods of detection and quantifying this natural hazard;
- heavy rain effects on aircraft systems performances in the light of full-scale and model tests with analysis of the results on aerodynamic performance and operations;
- measurements of atmospheric turbulence, treatment of aircraft response to random turbulence and discrete gusts.

This Lecture Series, sponsored by the Flight Vehicle Integration Panel of AGARD, has been implemented by the Consultant and Exchange Programme.

Abrégé

L'environnement dans lequel un aéronef doit évoluer est l'une des principales causes des accidents d'avion. Ce cycle de conférences se focalise sur les aspects spécifiques de l'environnement, tant naturels qu'artificiels, qui jouent un rôle majeur dans ces accidents, à savoir :

- la turbulence du sillage y compris la génération du vortex de bord de fuite;
- les résultats d'un vaste programme d'essais en vol concernant les orages hivernaux au large de la côte Est du Canada, y compris l'impact sur les opérations aériennes. Le programme canadien sur les orages de l'atlantique (CASP) porte sur les effets du givrage du fuselage, les vents forts, la turbulence, les modèles du foudroiement en vol, et les techniques de simulation de la foudre;
- la réponse d'un aéronef au cisaillement du vent et les méthodes de détection et de quantification de ce risque naturel;
- les effets des fortes pluies sur les performances des systèmes de bord, au vu des essais effectués en vraie grandeur et sur modèles, ainsi que l'analyse de l'impact des résultats sur les performances aérodynamiques et les opérations;
- les contrôles de la turbulence atmosphérique, la gestion de la réponse de l'aéronef à la turbulence, y compris des modèles technogéniques aléatoire et aux rafales discrètes.

Ce cycle de conférences est présenté dans le cadre du programme des consultants et des échanges, sous l'égide du Panel de Conception Intégrée des Véhicules Aérospatiaux de l'AGARD.

List of Authors/Speakers

Lecture Series Director: Dr. Barnes W. McCORMICK
Boeing Professor Emeritus of Aerospace Engineering
The Pennsylvania State University
Dept. of Aerospace Engineering
233 Hammond Building
University Park, PA 16802
USA

Authors/Speakers

Mr. J. Ian MacPHERSON
Flight Research Laboratory
Institute for Aerospace Research
National Research Council
Montreal Road
Ottawa, ONT K1A 0R6
CANADA

Mr. John J. REINMANN
Chief
Icing & Cryogenic Technology Branch
NASA Lewis Research Center
Cleveland
Ohio 44135
USA

Mr. R. Earl DUNHAM, Jr.
Assistant Division Chief
NASA Langley Research Center
Mail Stop 156A
Hampton, VA 23665-5225
USA

Mr. Jean Louis BOULAY
Dept. of Physics
ONERA/OP, BP 72
29 Avenue de la Div. Leclerc
92322 Châtillon Cedex
FRANCE

Mr. Alan A. WOODFIELD
Aviation Research Consultant
9 Colworth Road
Sharnbrook
Bedford MK44 1ET
UK

Dr. Manfred SWOLINSKY
Senior Research Engineer
Inst. of Flight Guidance & Control
University of Braunschweig
Hans-Sommer-Str.66
38106 Braunschweig
GERMANY

Contents

	Page
Abstract/Abrégé	iii
List of Authors/Speakers	iv
Introduction and Overview by Dr. Barnes W. McCORMICK	I
Wake Turbulence: Generation Decay and Hazard by Dr. Barnes W. McCORMICK	1
Winter Storms Research in Canada by Mr. J. Ian MacPHERSON and George A. ISAAC	2
ESD and Lightning Interactions on Aircraft by Mr. Jean Louis BOULAY	3
Icing: Accretion, Detection, Protection by Mr. John J. REINMANN	4
Wind Shear and its effects on Aircraft by Mr. Alan A. WOODFIELD	5
Heavy Rain Effects by Mr. R. Earl DUNHAM, Jr.	6
Turbulence: Engineering Models, Aircraft Response by Dr. Manfred SWOLINSKY	7

Introduction to FLIGHT IN AN ADVERSE ENVIRONMENT

Barnes W. McCormick, Boeing Professor Emeritus
The Pennsylvania State University, 233 Hammond Building
University Park, PA 16802, USA

The environment in which an airplane must operate, whether natural or artificial, is a major cause of aircraft accidents. This lecture series focuses on specific aspects of the environment, both natural and man-made, which are the major contributors to these accidents.

The series begins with a presentation on wake turbulence which treats the generation and decay of trailing vortex systems. The hazard to smaller aircraft encountering a wake from a larger aircraft is considered followed by recommendations for avoidance and alleviation of the hazard.

Next, as a lead-in to the remainder of the material which follows, a lecture is presented which presents the results of an extensive flight test program concerning winter storms off of the east coast of Canada and their effect on aircraft operations. The Canadian Atlantic Storms Program (CASP) includes the effects of airframe icing, strong winds, turbulence, wind shear, precipitation, reduced visibility, reduced ceilings and electrification.

The next presentation is one specific to electromagnetic effects including electrical discharge properties, in-flight test programs, in-flight lightning models, and lightning simulation techniques.

The many aspects of icing is the topic of the next lecture. It includes information on the physics of icing, the hazard to aircraft and ice protection systems including de-icing and anti-icing.

Wind shear is the next hazard of the flight environment to be covered in some detail. This specific topic will be defined and its

cause explained. The response of an aircraft to wind shear is discussed together with methods of detecting and quantifying this natural hazard. Some guiding principles for the pilot operating under conditions where wind shear may be present are also presented.

Next, heavy rain effects are covered including the general effects of heavy rain on aircraft systems and performance, the physical characteristics of heavy rain and the frequency of occurrence. Full-scale and model tests conducted in heavy rain are described and an analysis given of the results on aerodynamic performance and operations.

The series concludes with a presentation on the effects of gusts and turbulence on an aircraft. The principal topics include a description of random turbulence and discrete gusts, the measurement of atmospheric turbulence, and aircraft response to turbulence. The presentation will include engineering models and examples of aircraft response to random turbulence and discrete gusts.

A true perspective of the role which the environment plays in aircraft safety can be had by simply examining recent articles in aviation publications. In the newspaper, USA TODAY, on February 16, 1994 a headline read "New distances urged for landing behind 757s". The article stated that "The National Transportation Safety Board (US) said the present 3- or 4-mile rules are not enough to keep planes out of the turbulent wake of 757s, which may have played a role in two crashes that killed 13 people since December 1992." More detail on the 757 problem was covered in the February 21, 1994 issue of Aviation Week magazine under the title "NTSB Urges

Changes in Separation Rules. More on this issue will be presented in the lecture on wake turbulence.

Several of the lectures in this series consider hazards resulting from turbulence and wind shear as caused by high winds and storm systems. Accidents due to these environmental factors continue to occur with some regularity. In the January 1994 issue of AOPA Pilot magazine, an article appeared entitled "High-Wind Warnings". The question was asked in the article "What causes most weather-related general aviation accidents?" and the answer given, according to a recent compilation of NTSB statistics, was that 42% involved adverse winds. The article then covers the characteristics of warm and cold fronts, surface winds and low-level jet streams. The article concludes with an interesting observation. "Another set of NTSB statistics singles out "lousy" pilot attitude as perhaps the root cause of the majority of all weather-related accidents. There was no record of any type of weather briefing prior to 55 percent of the accident flights. Poor judgement, not high winds seems to be the biggest problem."

Recently, a China Eastern MD-11 was reported (Aviation Week, April 12, 1994) to have encountered enroute turbulence. Approximately 160 passengers were injured, one fatally. Two weeks later, the same magazine reported the crash of a Japan DC-9 while trying to land at Hanamaki Airport in high crosswinds.

The crash of United Airlines 585, a Boeing 737 on March 3, 1991 has been well-publicized by the aviation press. The airplane was on a final approach with everything apparently going alright when it suddenly rolled and yawed to the right until it was inverted with the nose nearly straight down. The cause of the uncontrolled motion has not been definitely determined but there is the possibility that the airplane encountered a wind rotor, or horizontal vortex, formed by high surface winds over mountain ridges close and to the right of the airplane's track. An article on the wind rotor phenomena appeared in the December 14/21, 1992 issue of

Aviation Week where accidents of a USAF B-52, a BOAC Boeing 707, a BAC 111 and a Fairchild F27B were all suspected to have resulted from wind rotor encounters.

On September 14, 1993 a Lufthansa A320-200 crashed during a landing at Warsaw, Poland. Wind shear, aircraft touchdown speed and a wet runway all apparently contributed to this accident.

A joint NASA/FAA study to develop more reliable wind shear detection instrumentation was covered in articles which appeared in Aviation Week in late 1992 and October 18, 1993. This environmental hazard is associated with strong winds and downdrafts which occur in the vicinity of thunderstorms. Current sensors installed on commercial transports are reactive and detect wind shear only after the aircraft has begun to encounter it. However, a modified Doppler weather radar system installed on NASA's Boeing 737 is predictive and was reported to detect consistently wind shear 20-40 seconds before an encounter.

Another environmental hazard of extreme importance is icing. Two alleged icing accidents have been the subject of TV movies. These were the Continental DC-9 crash on takeoff at the Denver airport during a freezing rain and the Air Florida crash into the Potomac River while departing from the Washington National Airport during a snow storm. The deicing problem is currently receiving a lot of attention, particularly from a regulatory standpoint. The FAA has recently passed a ruling which essentially places final responsibility for most commuter-type aircraft on the pilot for determining that an aircraft's wing and all control surfaces are clean of any ice, snow or frost. An FAA-approved, pre-takeoff contamination check must be performed within 5 minutes of takeoff or alternative, suitable sensors can be installed on the wing and control surfaces.

In view of the continuing accidents which are happening as a result of environmental factors, it is felt that this lecture series is very timely and should be of benefit to those persons concerned with these factors.

WAKE TURBULENCE

Barnes W. McCormick, Boeing Professor Emeritus
The Pennsylvania State University, 233 Hammond Building
University Park, PA 16802, USA

SUMMARY

Wake turbulence is a misnomer. Turbulence implies a random process whereas the term "wake turbulence" refers to the hazard posed to smaller airplanes by the ordered, rotational flow in the trailing vortex systems behind larger airplanes. This lecture begins by examining the relationship of aircraft size, geometry and operating conditions to the strength of an aircraft's trailing vortex system. Next, the velocity field initially induced close behind the generating airplane by its trailing vortex system is defined. This is followed by a discussion of the various ways in which a vortex system can dissipate and the many factors which affect the dissipation. In particular, the effects of atmospheric turbulence, ground proximity and vortex bursting on the ensuing behavior of the vortex system are considered. The paper continues with a study of the dynamics of an aircraft encountering the wake of a larger airplane. The degree to which an aircraft is threatened by a given vortex system of known characteristics is analyzed and the hazard posed by a given vortex system to a following aircraft quantified. Finally, the paper concludes with recommendations on possible ways to alleviate the safety and operational problems associated with wake turbulence.

LIST OF SYMBOLS

a	$dC_l / d\alpha$
a	vortex core radius
A	Aspect ratio
b	wing span
c	section chord
\bar{c}	mean wing chord, S/b

C_L	wing lift coefficient
l	rolling moment
r	radial distance
R	radius for $\Gamma(R)$
S	wing planform area
v(a)	V_θ at core radius
$v_i(a)$	initial value of v(a)
V	true airspeed
V_θ	tangential velocity
W	airplane gross weight
y	lateral distance along wing
α	angle of attack
Γ	circulation at any radius
Γ_0	midspan bound circulation, total vortex strength
$\Gamma(R)$	circulation averaged over radius from 0 to R
ρ	air mass density
ν	kinematic viscosity

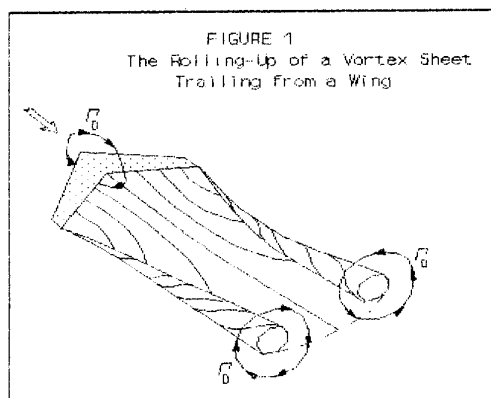
Subscripts

G	airplane generating vortex
F	following airplane encountering vortex

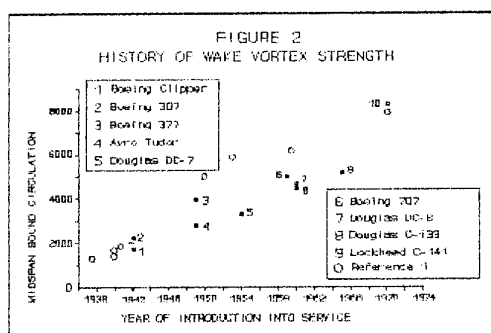
INTRODUCTION

Wake turbulence is the name given to the disturbance of a smaller aircraft which encounters the vortex system generated by a larger aircraft. It is really a misnomer since turbulence implies a random, or stochastic process. Wake turbulence is not random but is the result of the ordered flow caused by a trailing vortex system.

A vortex sheet trails from any finite lifting surface and rolls up asymptotically into a pair of trailing vortices. This well-known process is pictured in Figure 1. As shown in the figure, the ultimate circulatory strength of each trailing vortex will equal the midspan value of the wing's bound circulation, Γ_0 .



The circulatory strengths of trailing vortex systems have increased continuously over the years as shown in Figure 2. This increase in vortex strength coupled with the increase in commercial and general aviation traffic produced a rapid increase in accidents caused by wake turbulence beginning in the middle 60's. The introduction of heavy jet transports in the early 70's further aggravated the problem. During the 80's, the problem lessened because of better separation standards and increased knowledge of wake turbulence by pilots and air traffic controllers.



The principal hazard associated with wake turbulence occurs when a smaller airplane is aligned with the axis of a vortex trailing from a larger airplane. A rolling moment is produced on the smaller airplane which can exceed its maximum aileron control. For example, the rolling moment produced on a small single-engine airplane can be over twice its control power if it encounters the wake of a B-727 at five miles or less.

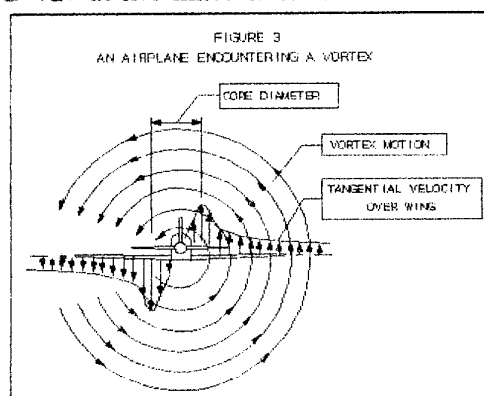


Figure 3 illustrates an airplane, looking forward, aligned with the axis of a vortex. The circular flow about the vortex, depicted by the concentric, circular streamlines, gives rise to an upward velocity on the right wing and a downward velocity on the left wing. Thus the angles-of-attack along the right wing are increased while those along the left wing are decreased by a corresponding amount. The ensuing increased lift on the right wing and decreased lift on the left wing results in a counter-clockwise rolling moment on the airplane. The situation depicted corresponds to an airplane encountering the vortex shed from the right wing of an airplane ahead.

Also illustrated in Figure 3 is the typical variation of the tangential velocity associated with a vortex. Near the center of the vortex, the velocity increases linearly with the radius. As the radius increases, the rate of increase begins to drop. At some radius, known as the core radius, the tangential velocity reaches a maximum. Outside of the core, the velocity decreases more or less inversely with the

radius.

One of the first accidents in the US attributed to wake turbulence occurred in 1965 at Hartz Field in Atlanta, GA. A Beech Bonanza was cleared for an intersection takeoff and lifted off at the same point as a DC-7 which departed shortly before. The Bonanza climbed to 50 feet above the runway and then suddenly rolled inverted and crashed as it encountered one of the vortices generated by the DC-7.

The moments on the following airplane caused by wake turbulence do not have to exceed the aileron control to present a hazard. On an approach close to the ground, the perturbing moments can cause rapid changes in attitude to which the pilot cannot react in time before striking the ground or an obstacle. Several years ago a DC-9 crashed into a hanger while practicing touch-and-go landings after encountering the wake of a DC-10. This encounter at altitude would have resulted in an appreciable rolling of the DC-9 but would not have been catastrophic.

In the last 30 years, extensive analyses, laboratory and flight tests have been performed to define the flow field associated with trailing vortex systems including the motion of the vortices in and out of ground-effect. Also, studies have been undertaken relating to the behavior of an airplane encountering a given vortex system.

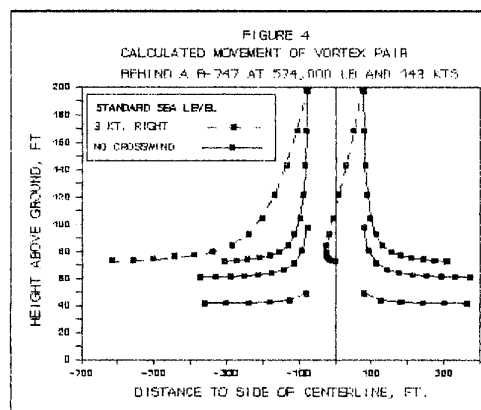
INITIAL BEHAVIOR OF A VORTEX SYSTEM

After the vortex sheet shed from a wing rolls up into a pair of vortices, the pair will descend toward the ground. Initially, this self-induced motion can be calculated fairly accurately using potential flow methods. After some time as the vortex diffuses or interacts with the ground's boundary layer, potential flow is not applicable. To illustrate vortex movement, Figure 4 has been prepared using the Biot-Savart Law and assuming the flow to be two-dimensional. In this case, each vortex induces a tangential velocity

which propels the other one. This velocity, V_θ , varies directly with the vortex strength and inversely with the radial distance from the vortex center.

$$V_\theta = \frac{\Gamma_0}{2\pi r} \quad (1)$$

Included in the calculation are two image vortices of equal and opposite strength placed below the ground. The movement of each vortex is determined by numerically integrating the velocity induced at each vortex by the other and by the image vortices. The image vortices are necessary to assure that the velocity induced normal to the ground vanishes.



Observe that with no wind, the vortices, when generated at altitude descend vertically and then spread laterally outward at a height above the ground which is approximately three-quarters of the wing semi-span. When generated close to the ground, the vortices move laterally outward. Any crosswind velocity is superimposed on the induced motion. In this case, for a three knot crosswind from the right, the vortex pair generated at 200 feet above the ground descend to the left. As they approach the ground, the induced velocity at the left vortex adds to the wind and that vortex moves

rapidly away from the centerline. However, the induced velocity at the right vortex opposes the crosswind close to the ground resulting in this vortex remaining stationary over the centerline. Obviously this is a hazardous situation for following, smaller aircraft during landing operations.

As the trailing vortex sheet rolls up into the pair of vortices, the vorticity, produced in the wing's boundary layer, rolls up with the sheet to form the rotational flow in the each vortex. By imposing the condition that the first and second moment of the elemental circulation remain constant during the rollup, Reference 1 determines a tangential velocity distribution in close agreement with large-scale experimental measurements such as those reported in Reference 2. Reference 3 argues that the velocity field around the vortex is dictated by turbulent diffusion of the circulation which leads to a prediction that the circulation will vary linearly with the logarithm of the radius. The logarithmic model also fits well the data of Reference 2 and was used by Reference 4 as the basis of analysis. The models of References 1 and 3 both become invalid very near the center of the vortex.

The semi-empirical approach of Reference 4 offers a practical basis for predicting the initial velocity of the rolled-up vortex sheet before any significant decay occurs. The prediction is based on the analysis of model and full-scale data taken under very stable atmospheric conditions. Flight testing was done with a Piper Cherokee and a Cessna O-1 (or L-19) with far-field measurements being made at distances up to 1300 chord lengths downstream, or approximately 1500 m. In addition to the far-field measurements, vorticity contours were mapped at several distances less than one chord length behind the trailing edge. The full-scale tests corresponded to Reynolds numbers of approximately 3×10^6 while the model tests were done at approximately 3×10^5 . From this study, the following conclusions were reached concerning the tangential velocity field for the rolled-up vortex sheet.

a. The circulation at the core radius is equal to 16% of the total strength of the vortex for full-scale Reynolds numbers. The model tests produced a number closer to the 71.6% predicted by Lamb's solution of the Navier-Stokes equations. (Reference 5) Thus, for full-scale Reynolds numbers,

$$\Gamma(a) = 0.16\Gamma_0 \quad (2)$$

b. Just downstream of the wing, the initial maximum tangential velocity at the core radius, as a fraction of the freestream velocity, increases linearly with the wing lift coefficient and is given approximately by

$$\frac{v_t(a)}{V} = 0.63C_L \quad (3)$$

c. As a fraction of the initial maximum tangential velocity, the maximum tangential velocity decays downstream as a function of the ratio of the downstream distance to the mean chord. This empirical function is given by

$$\frac{v}{v_i} = \frac{1}{\sqrt{1 + 0.0065 \frac{z}{c}}} \quad (4)$$

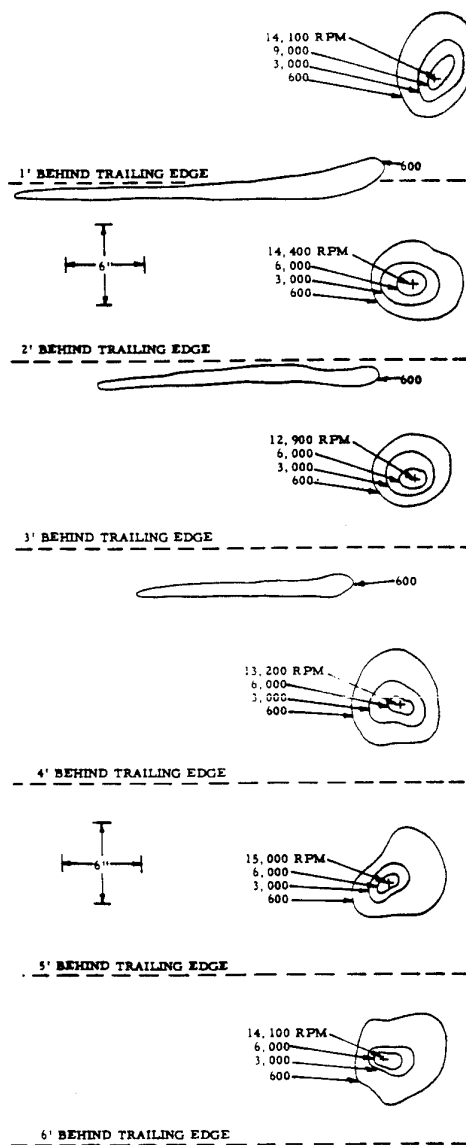
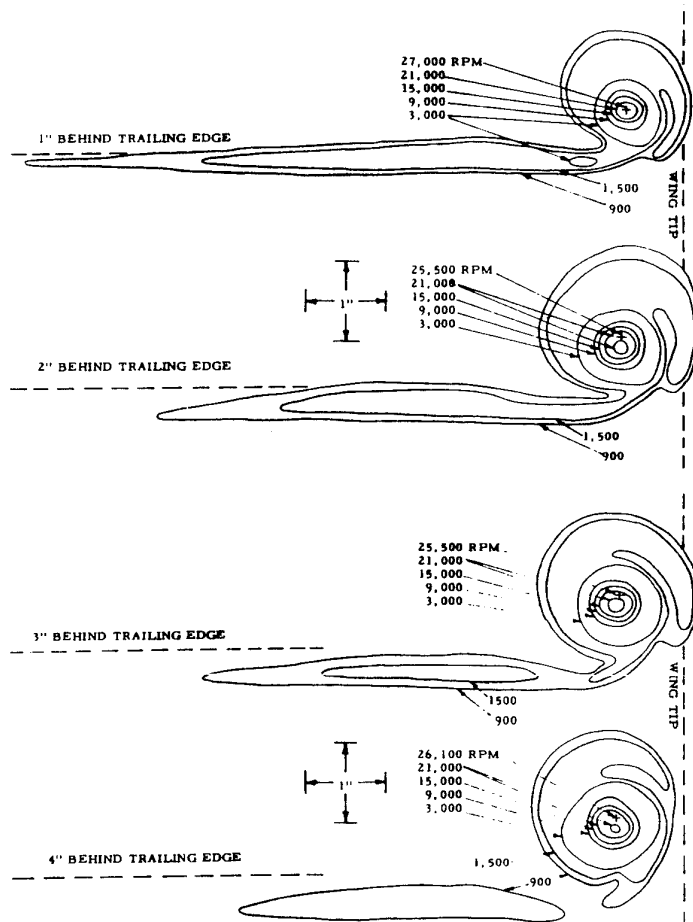
As the rolled-up vortex decays, the circulation at the core radius remains constant. This is in agreement with Lamb's solution even though the flow in the vortex is probably not laminar.

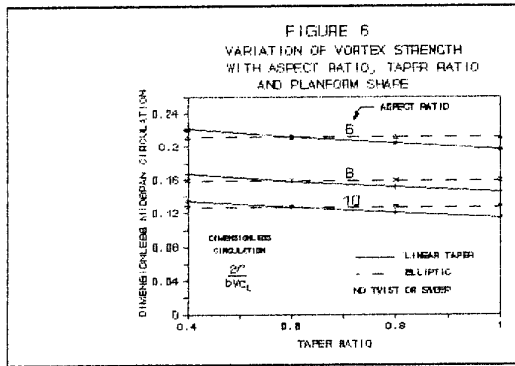
The vorticity contour measurements of Reference 4 show that the vortex sheet behind a wing rolls up rapidly. Figure 5, taken from the reference, shows that within less than one mean chord length (4.83 ft), the vortex sheet has nearly disappeared with all of the measurable vorticity being contained within a circular region approximately 15 cm in diameter.

FIGURE 5
VORTICITY CONTOUR MEASUREMENTS
BEHIND L-19 WING

MODEL DATA
ANGLE OF ATTACK = 12 DEGS
V = 75 MPH

FULL-SCALE
V = 65 KT





The midspan bound circulation, calculated from a lifting-surface model, is presented in Figure 6 for linearly tapered and elliptic planform shapes with no twist or sweep. Observe that Γ_0 , for a given wing lift coefficient, does not vary significantly with taper ratio for linearly-tapered wings. Also note that, for the same aspect ratio, the predicted values of Γ_0 for linearly-tapered wings do not differ significantly from those predicted for the elliptic wing.

Thus Γ_0 , for a given aspect ratio, can be closely estimated from

$$\Gamma_0 = \frac{4}{\pi \rho V b} W \quad (5)$$

The core radius and maximum tangential velocity at the core radius can be estimated from the above knowing the wing lift, geometry and downstream distance. The radial variation of the tangential velocity is then determined from the logarithmic variation derived in Reference 3.

$$\frac{v(r)}{v(a)} = \frac{1 + \ln\left(\frac{r}{a}\right)}{\frac{r}{a}} \quad (6)$$

The full-scale detailed measurements of a trailing vortex system presented in Reference 4 are believed to be the first of such

measurements and showed that the theoretical predictions of Reference 6, made prior to the time of Reference 4, were in serious error. Core diameters predicted on the basis of Reference 6 are too large by a factor of approximately 30.

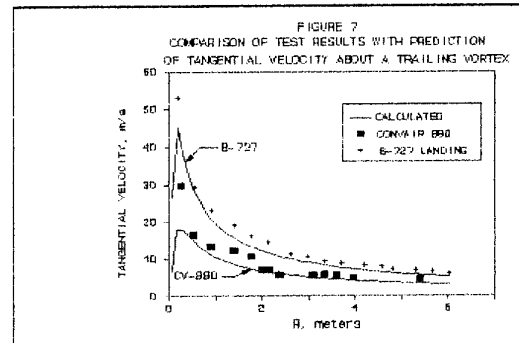


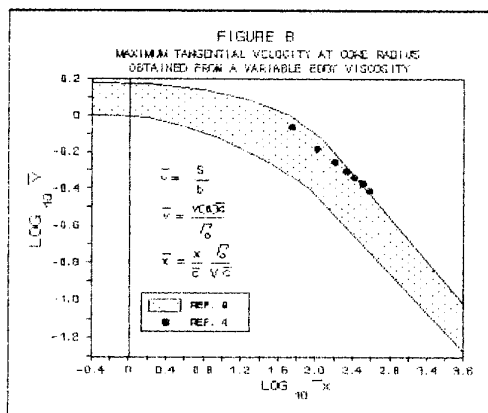
Figure 7, using data from Reference 2, shows fairly good agreement between the predictions of the tangential velocity based on the above relationships and the experimental data obtained by the FAA using a tower instrumented with an array of 3-component hot-film anemometers. Reference 7 states that predictions of rolling accelerations on airplanes encountering wake turbulence agreed well with predictions based on using the velocity field obtained from Equations 1 through 4. However, the decay at large separation distances found by Reference 7 was greater than that predicted by Equation 3. This may be because of the stable, early morning atmosphere in which the data of Reference 4 was obtained. In general, the agreement shown in Figure 7, is found for most of the data obtained by the FAA in their extensive tower fly-by tests. However, it should be noted that this data applies to relatively short separation distances.

FAR-FIELD VORTEX CHARACTERISTICS

In 1954, Reference 9 identified a characteristic Reynolds number for a vortex, Γ_0 / v . The reference also noted that the vortex geometry was probably dependent upon the wing's boundary layer and therefore a

characteristic length for the core was probably the geometric mean chord of the wing. This characteristic Reynolds number and length formed the basis for the analysis presented in Reference 8 undertaken eight years after Reference 4. In the interim, many other investigators had obtained full-scale and model data over a wide range of Reynolds numbers.

Using a variable eddy viscosity, Reference 8 was able to correlate the experimental data available on the structure and decay of vortices. The principal results of that study are presented in Figure 8 together with some points calculated on the basis of Reference 4.



The band shown in Figure 8 encompasses a voluminous amount of data. Although the width of the band is not too great as shown, it represents a factor of 1.5 to 2.0 in the maximum tangential velocity from the upper bound to the lower bound. Therefore, in examining the wake turbulence hazard, one is advised to analyze both band limits.

Reference 8 found that the ratio of the circulation at the core radius to the total circulation agreed with Lamb's solution at the low Reynolds numbers. At the higher Reynolds the ratio was again found to be constant but with a value of only 0.4. This is higher than the value of 0.16 found by Reference 4. Since Reference 8 is based on a considerable amount of data using sophisticated instrumentation developed after

the time of Reference 4, it is felt that the number of 0.4 is probably more accurate. Also, the number is further justified by the analysis found in the reference.

An example will now be given on the use of Figure 8 to predict the velocity field downstream of a airplane. Consider the prediction of the wake five nautical miles behind a Boeing 747 in the approach configuration. A gross weight of 574,000 lb (260,360 kg) is assumed and an approach speed of 143 kts. The planform area of the 747 is 511 m^2 with a span is 59.6 m and a mean geometric chord of 8.57 m. At standard sea level conditions, these numbers result in a wing lift coefficient of 1.49 neglecting trim lift on the horizontal tail. The quantity \bar{x} is defined as

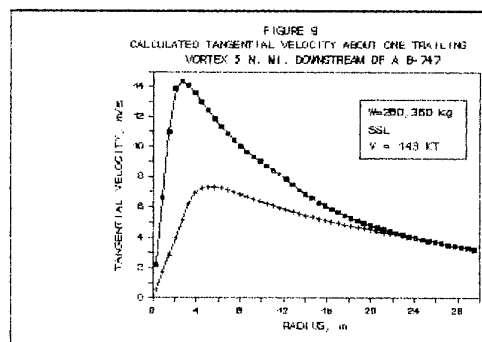
$$\bar{x} = \frac{x \Gamma_0}{c \bar{V} c}$$

and for this example will equal 1025. The log of this (to the base 10) will be 3.01 which, from Figure 8, gives the limits on \bar{v} of

$$0.107 \leq \bar{v} \leq 0.209$$

where

$$\bar{v} = \frac{v(a)c}{\Gamma_0}$$



From Equation 1, $\Gamma_0 = 600.8 m^2/s$. At vortex

Reynolds numbers above 10^5 , the circulation at the core radius is equal to 40% of the total circulation. Thus, since $\Gamma(a)=240\text{m}^2/\text{s}$, it follows that the core radius lies between 2.62 and 5.1 meters.

The graph of Figure 9 was prepared using the above numbers. This graph assumes a solid body rotation of the flow out to the radius where the logarithmic solution of Reference 3 is matched in magnitude and gradient. The uncertainty in the velocity field shown by this figure is certainly not desirable but probably realistic in view of the uncertainties resulting from atmospheric turbulence and the spread of the experimental measurements shown in Figure 8.

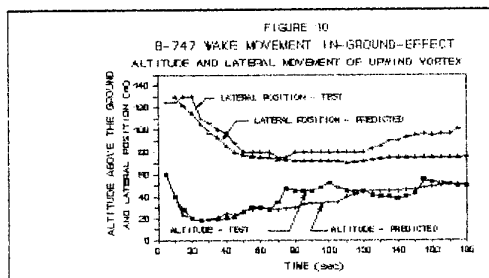
After rolling up, the pair of trailing vortices will gradually diffuse as they begin to move downward. This motion can be viewed as a downward velocity induced on each vortex by the other. When generated at a high altitude, measurements have shown that the pair will generally not move downward more than approximately 300 m. Generated at lower altitudes, the vortices will spread apart as they approach the ground. Typically the speed at which a vortex moves along its path is of the order of 2 or 3 m/sec. Any wind is superimposed on this induced motion. Thus, near the ground where a vortex is moving laterally outward, a crosswind of the right magnitude can cancel the induced lateral velocity causing the vortex to remain in proximity to a runway. Also, in a parallel runway situation, the downwind vortex can move rapidly to another runway before decaying significantly.

In addition to turbulent diffusion, the velocity field of a vortex can change rapidly for other reasons. At altitude, an instability exists whereby the vortex filaments progressively assume a sinuous shape eventually breaking and linking with each other to form a series of loops, somewhat like vortex rings. This may cause the wake turbulence hazard to lessen but, even after linking, significant vortex segments are observed which are probably dangerous to a smaller airplane. This linking

of a pair of vortices has become known as the Crow instability after the author of Reference 10 who first obtained an analytical solution of this unusual behavior. Whether or not this instability will occur is highly dependent upon the ambient turbulence level.

Another phenomenon which can rapidly alter the velocity field about a vortex is the instability known as vortex bursting or vortex breakdown. Viewed in the steady sense, vortex bursting is a standing wave at a point along the vortex where the flow suddenly transits from one energy state to a lower one while conserving mass and momentum across the wave. It is a 3-D analogy to the 2-D hydraulic jump. This instability in the flow apparently occurs at high swirl angles. Ahead of the burst point one would describe the vortex as "tightly wound" with a small core radius and a high tangential velocity. After bursting, the core radius will expand considerably with a corresponding decrease in the tangential velocity. However, the total circulation, or angular momentum, is conserved along each streamline across the bursting. Thus, bursting does not necessarily ensure a significant decrease in the rolling moment which would be experienced by an airplane encountering the vortex.

Earlier, in Figure 4, it was shown that a pair of vortices will descend toward the ground and then separate laterally just above the ground. Pilots were advised for many years to avoid wake turbulence by maintaining a flight path above the larger airplane ahead since "vortices always descend." However, recent measurements and calculations have shown that this is not always the case near the ground as the vortex interacts with the earth's boundary. Figure 10, based on Reference 11, presents a comparison of test data with predictions from an elaborate CFD code (Computational Fluid Dynamics) which models the fluid mechanics of the situation. Observe that, in this case, the wake from a B-747 settles to within 20 m (66 ft) of the ground and then rises to a height of approximately 55 m (180 ft.). This is 31 m (103 ft.) higher than one would ever expect according to Figure 4.



THE HAZARD IMPOSED ON A FOLLOWING AIRCRAFT BY WAKE TURBULENCE

The major hazard from wake turbulence is the rolling moment which can be produced on an airplane which encounters it. As stated earlier, the worst scenario, with regard to rolling moment, is the case where an airplane's axis is coincident with the axis of one of the pair of trailing vortices.

Considering the effect of only one vortex and using a simple strip analysis, the rolling moment caused by the above can be written as

$$l = \rho V^2 \int_0^{b/2} ac \frac{\Gamma(r)}{2\pi r} r dr \quad (7)$$

If the chord, c , and the slope of the section lift coefficient curve, a , are taken to be constant, and if $\Gamma(R)$ is defined by

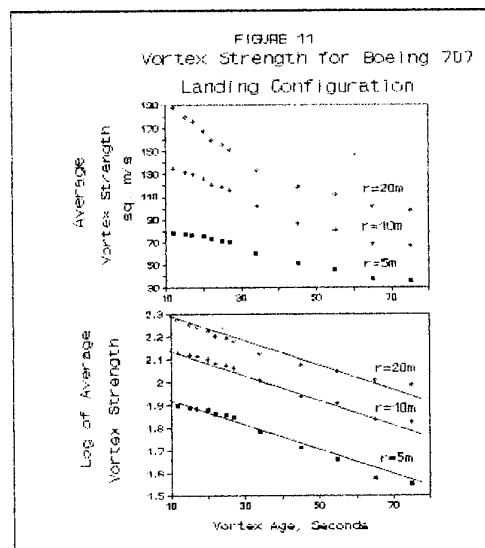
$$\bar{\Gamma}(R) = \frac{1}{R} \int_0^R \Gamma(r) dr$$

the above can be written as

$$l = \frac{\rho V^2 a}{\pi A} \bar{\Gamma} \left(\frac{b}{2} \right) \quad (8)$$

$\bar{\Gamma}(R)$ is called the average circulation and can be seen to be a measure of the rolling

moment which would be imposed on an airplane having a semi-span of R .



Reference 12 presents velocity measurements behind a Boeing 747 at various distances and with different flap settings. The measurements were taken relatively close to the ground using a non-intrusive, laser doppler velocimeter (LDV). The upper graph in Figure 11 is taken from the reference and presents the average circulation as a function of time for 4 different averaging radii. These data are for a B-747 at a speed of 74.15 m/s, a mean chord of 8.3 m, and $\Gamma_0 = 620 \text{ m}^2/\text{s}$. As

shown in the lower graph, when $\Gamma(R)$ versus time is plotted on a log scale, the data tend to collapse to straight lines, all having the same slope. One cannot use this data and Equation (6) directly to estimate the maximum rolling moment because the simple strip analysis neglects tip losses. A rolling moment calculated by neglecting tip losses is significantly greater than the value obtained from lifting surface methods. Even so, the relative trend of the data presented in this form provides comparative information on the induced rolling moments. For example, a DC-9 has a semi-span of 13.6 m. Thus, behind a B-767, Figure 11 shows that the rolling moment on a DC-9 would decrease by a factor of 2 when the vortex age increases

TABLE 1 US Separation Standards

Leading Airplane	Following Airplane		
	Heavy	Large	Light
heavy	4 (7.4)	5 (9.3)	6 (11.1)
large	3 (5.6)	3 (5.6)	4 (7.4)
light	3 (5.6)	3 (5.6)	3 (5.6)

from 10 seconds to 80 seconds. This corresponds to separation distances of 0.4 and 3.2 n.mi. respectively.

The wake geometries presented in Reference 8 do not agree well with the predictions of Reference 4. The results of Reference 4 predict a much smaller core diameter and a higher swirl velocity at the core than shown by the data of Reference 8. The velocities reported by Brashears et al were obtained using a non-intrusive laser doppler velocimeter (LDV). The B-747 was the test aircraft for this work and the results of predictions based on Equations 4,5 and 6 for this airplane differ significantly from the data presented in the reference.

Consider again Figure 11, based on Figure 8 of the reference. The calculated value of Γ_0

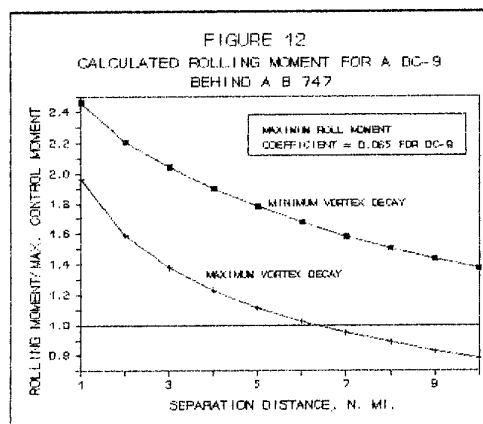
for this example is reported to be $620 \text{ m}^2/\text{sec}$. The velocity for this test is reported in the original reference as being approximately 144 kts. Thus for an age of 9.8 secs., the vortex was measured at a distance of 727 m behind the wing of the B-747. This is equivalent to 85 mean chord lengths. The lift coefficient of the airplane is quoted as equal to 1.41. Thus, from Equation 5, $v_i = 66.8 \text{ m/sec}$. From Equation 6, this velocity is reduced to a value of 53.5 m/sec. This is considerably higher than the value of 13 m/sec shown in Figure 8. According to Equation 4, the circulation at the core should equal $99.2 \text{ m}^2/\text{sec}$. Thus the core radius is predicted to equal 0.295 m which is appreciably less than 4 m given in Reference 8.

US standards define heavy, large and light

airplanes according to the following weights.

Heavy: $W > 300,000 \text{ lb}$ (136,000 kgf)
 Large: $12,500 < W < 300,000 \text{ lb}$
 light: $W < 12,500 \text{ lb}$ (5670 kgf)

The corresponding prescribed US separation distances in nautical miles (km) are shown in Table 1.



Consider Figure 12 which presents the calculated rolling moment on a DC-9 at various distances behind a B-747 in the landing configuration. For these calculations, a vortex lattice model was used for the wing and Reference 8 (Figure 8) to define the velocity field about the vortex. According to this figure, the rolling moment calculated using the upper decay curve on Figure 8 will exceed the maximum aileron control at distances well in excess of 10 n. mi. For the lower decay curve of Figure 8, it is predicted that the rolling moment will exceed the aileron control for distances less than 6 n. mi.

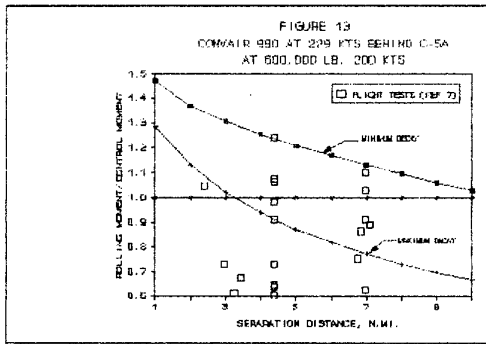


Figure 13 offers further substantiation of the methods presented here for calculating the rolling moments due to wake turbulence. In this figure, the calculated and measured rolling moments experienced by a Convair 990 in the wake of a C-5A are presented as a function of separation distance. The measured data were obtained from the roll accelerations resulting from a wake encounter. There is a considerable amount of scatter in the data which reflects the fact that most encounters are not centered on the trailing vortex axis and therefore do not represent the worse case. It should be noted that the calculated results using the minimum decay rates given by Figure 8 appear to define the upper bound of the test data. Based on an extrapolation of this curve, it appears that the rolling moment induced on a Convair 880 by a C-5A could exceed the aileron control of the 990 up to separation distances in excess of 10 n.mi.

An alternate approach to the estimation of rolling moments can be found in Reference 15. The semi-empirical approach taken there is based on the following. Assume that the velocity field around the vortex is that given by a point vortex in two-dimensional flow.

$$v_{\theta} = \frac{\Gamma}{2\pi r} \quad (9)$$

If a wing is centered on this vortex, a section of the wing a distance of y from the centerline will experience an increase in the angle of attack given by

$$\Delta\alpha = \frac{\Gamma}{2\pi yV} \quad (10)$$

A decrease in α of the same amount will occur at the corresponding section on the other side of the wing. Thus, using a simple strip analysis, the rolling moment on the wing is obtained by integrating the moment of the differential lift over the span.

$$l = \frac{1}{2} \rho V^2 \int_{-b/2}^{b/2} a \frac{\Gamma}{2\pi yV} cy dy \quad (11)$$

or,

$$l = \frac{\rho Va\Gamma}{4} \pi \int_{-b/2}^{b/2} c dy$$

The integral is simply equal to the wing planform area so that the rolling moment coefficient becomes

$$\begin{aligned} C_l &= \frac{l}{\frac{1}{2} \rho V^2 S b} \\ &= \frac{a}{2\pi} \frac{\Gamma}{Vb} \end{aligned} \quad (12)$$

Substituting Equation (5) for Γ results in

$$C_l = \frac{2a}{\pi^2} \frac{W_G}{\rho V_G b_G V_F b_F} \quad (13)$$

In general, using other forms for V_{θ} , the equation is obtained except for a slightly different constant on the right side. Thus, Reference (15) concluded that

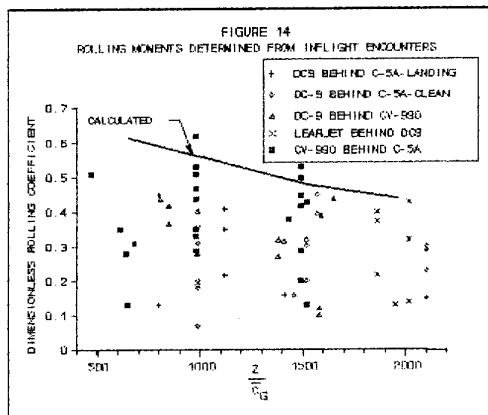
$$C_l \propto \frac{W_G}{\rho V_G b_G V_F b_F} \quad (14)$$

where a sub G refers to the airplane generating the vortex and a sub F refers to

the following airplane.

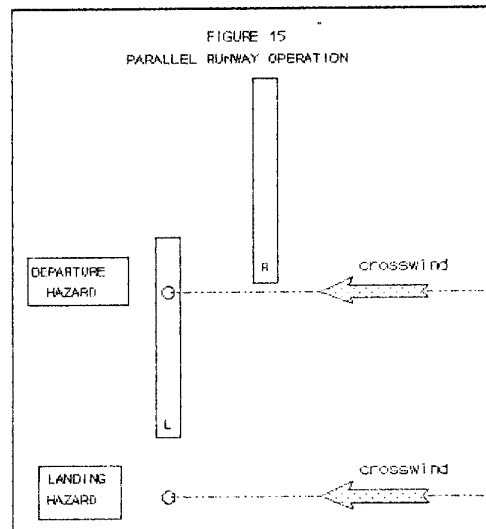
Reference 7 presents measured rolling accelerations on various airplanes as they intersect the vortices trailing from various larger airplanes ahead. Knowing the mass moment of inertia for a following airplane, one can solve for the rolling moment, and hence, the rolling moment coefficient produced by the encounter.

In this way, Reference 15 produced the results which are presented in Figure 14. This is, of course, simply a plot of the constant of proportionality in Equation 14 as a function of the downstream distance as a fraction of the geometric mean chord of the airplane generating the vortex. There is considerable scatter in the data which is undoubtedly the result of not hitting the center of the vortex on every encounter. This conclusion is substantiated by calculations done on the basis of Figure 8. As shown in the figure, these calculations provide a least upper bound to the data.



Parallel runway operations can be hazardous under certain wind conditions as illustrated in Figure 15. Two parallel, displaced, north-south runways are shown with the wind coming from the east. If an airplane lands on the right runway, its wake may be blown over to the left runway where a departing airplane can encounter it. In the other instance, a right crosswind can carry the wake of a landing airplane over to the left runway where

a landing airplane may encounter it. There are, of course, other situations, depending upon the runway orientation and wind direction, which can also be hazardous.



Avoidance of Wake turbulence

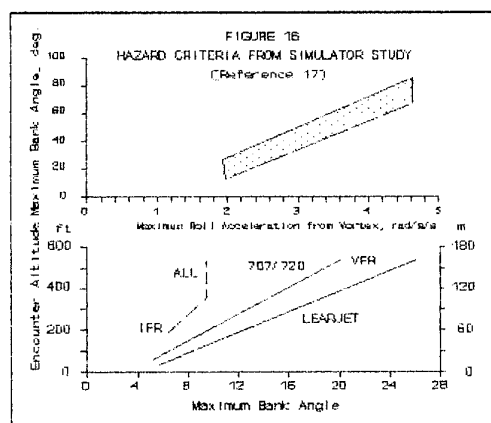
The principal way of avoiding wake turbulence is to allow sufficient time for a wake to dissipate before taking off or landing behind a larger airplane. The wait will allow the vortex both to dissipate and be blown away by prevailing winds. Of course, if there is a light crosswind with little ambient turbulence, one of the vortices may persist in the vicinity of the runway for a long time as indicated by some of the preceding figures.

A fairly sure way to avoid wake turbulence is to stay well above the flight path of the airplane ahead. In almost all cases, the pair of vortices will descend after being generated. There are two exceptions to this behavior. The first is close to the ground which has already been discussed. The second case involves a strong inversion layer. There are some data and calculations which indicate that a pair of vortices descending down on an inversion layer will behave in a manner similar to that when approaching the ground.

Although vortex rebound is a factor of

concern, the pilot of a light plane landing behind a heavy one should still be able to stay well above any wake turbulence. The runway ahead is two or three times longer than the light plane will need. Thus a steeper approach with a touchdown near the runway center will keep the light plane well clear of any wake turbulence, rebound notwithstanding.

Reference 17 presents the results of a moving-base simulator study of the wake turbulence hazard. Two classes of airplanes were considered; the light, general aviation airplane represented by the Learjet, and the large four-jet transport represented by the Boeing 707/720. The results are, of course, subjective since several pilots were used in the study and were asked to define whether or not a given vortex encounter was hazardous. The reader is referred to this interesting study for more detailed results. Figure 16 is presented here as representative of the type of results which were obtained.



The upper graph in this figure presents a band covering the maximum bank angles experienced by the pilots as a function of the maximum roll acceleration produced on the airplane by a given vortex. The lower graph presents boundaries defining whether or not the encounter is hazardous as a function of the maximum bank angle and altitude. The encounter was judged by the pilots to be hazardous if the bank angle exceeded those defined by the lines on this graph. As can be seen, and not unexpectedly, a given encounter

is judged to be more hazardous the lower the altitude and under IFR conditions as compared to VFR operation.

Given a particular combination of a leading aircraft and a following aircraft, one could use the methods presented earlier to calculate the maximum roll acceleration which would be produced on the following aircraft. Using Figure 16, a determination could then be made as to whether or not the wake encounter is hazardous. This is an alternative to the "hazard factor" presented in Reference 16.

Conclusions

Wake turbulence is a hazard to a smaller airplane operating behind a larger one but it can be avoided. The accident rate due to wake turbulence has improved considerably because of increased knowledge on the part of both air traffic controllers and pilots. However, based on the material presented herein, the US standard separation distances for small or large airplanes behind heavy ones and small airplanes behind large ones are marginal even considering that decay rates are probably higher than the minimum rates shown in Figure 8. This conclusion is augmented by a statement found in Reference 16 which defines a "hazard factor" as a fraction of the aileron control for which a wake encounter can be hazardous. At low altitudes, the rolling moment may be less than the aileron control but still be hazardous as noted previously.

The fact that more accidents do not occur for small airplanes behind larger ones is attributable to several factors. Calculations such as these represent the worst possible situation. The effect of the ground, crosswinds, atmospheric turbulence, vortex bursting and the Crow instability lessen the hazard which is predicted on the basis of Figure 8. Also, small traffic frequently uses a different runway from the heavy traffic and the approach angle, except for IFR operations, tends to be higher for a smaller airplane keeping the smaller airplane above

the flight path of the larger one. An operational change which would further lessen the hazard of wake turbulence would be to provide displaced runway thresholds and steeper glideslopes for any airplane operating behind a much larger one.

It is also felt that the weight classes are not divided finely enough. For example, an airplane weighing 13,000 lb. behind one weighing 200,000 lb. is as hazardous as an average "large" behind a "heavy". For the former, the present separation distance is only 3 n. mi. while for the latter case, the distance is 5 n. mi. even though the former situation is probably as hazardous, or more so, than the latter. If a new set of classes were defined, say at increments of 2000 lbs at the lower weights up to increments of 50,000 lbs. at the higher weights, the separation distances could be prescribed more efficiently possibly allowing for a higher landing and takeoff traffic density than that allowed by current practice.

Postscript

Since this paper was prepared some events have occurred which support the conclusions reached above. The headline for Reference 18 reads:

NTSB URGES CHANGES IN SEPARATION RULES

Safety board says 'large aircraft' category covers too great a weight range.

It cites recent accidents involving small- and medium-weight aircraft trailing the Boeing 757. This jet transport with a typical operating weight of approximately 250,000 lb. falls at the upper end of the "large" weight class. The NTSB has recommended that the separation distances shown in Table 1 be increased behind a 757 to 5 n. mi. for medium-weight jet transports such as the 737, DC-9 or MD-80; to 5 n. mi. for business aircraft such as the Learjet, and to 6 n. mi. for small, piston-powered aircraft. This essentially moves the 757 up to the "heavy" class for aircraft following it but keeps the 757 in the "large" class when following a "heavy"

aircraft. This appears to your author to be a quick and unsatisfactory, "fix" to the basic problem of too large of a weight range for the existing classes. A better solution, as recommended in the above conclusions, might be to define more weight classes.

References

1. Donaldson, Coleman duP., "A Brief Review of the Aircraft Trailing Vortex Problem", A.R.A.P. Report No. 155, presented at the National Aerospace Electronics Conference, Dayton, Ohio, May 17-19, 1971
2. Garodz, L. J., Lawrence, D. M., Miller, N. J., "Measurement of the Trailing Vortex Systems of Large Transport Aircraft using Tower Fly-By and Flow Visualization", FAA Report FAA-RD-75-127, January 1976
3. Hoffman, E. R. and Joubert, P. N., "Turbulent Line Vortices", J. of Fluid Mechanics, 16,3, July 1963
4. McCormick, B. W., Tangler, J. L., and Sherrieb, H. E., "Structure of Trailing Vortices", J. of Aircraft, 5,3, May-June 1969, pp. 260-267
5. Lamb, H., Hydrodynamics, Cambridge University Press, London, New York, 1932
6. Spreiter, J. R. and Sacks, A. H., "The Rolling Up of the Trailing Vortex Sheet and Its Effect on the Downwash Behind Wings", J. of Aero. Sci., Vol 18, No. 21, 1951
7. Andrews, W. H., Robinson, G. H., and Larson, R. R., "Exploratory Flight Investigation of aircraft Response to the Wing Vortex Wake Generated by Jet Transport Aircraft", NASA TN D-6655, 1972
8. Iversen, J. D., "Correlation of Turbulent Trailing Vortex Decay Data", AIAA J. Aircraft, Vol 13, No. 5, May 1976

9. McCormick, B. W., "A Study of the Minimum Pressure in a Trailing Vortex System", PhD Dissertation, The Pennsylvania State University, June 1954
10. Crow, S. D., "Stability Theory for a Pair of Trailing Vortices", AIAA J., 8, (1970, 2172-2179)
11. Robins, R. and Delisi, D., "The Potential Hazard of Aircraft Wake Vortices in Ground Effect and Crosswind", AIAA Paper 89-3400, AIAA Atmospheric Flight Mechanics Conference, August 14-16, 1989, Boston, MA
12. Brashears, M. R., Zalay, A. D., Hallock, J. N., and Burnham, D. C., "Laser Doppler Flight Test Measurements of B-747 Wake Vortex Characteristics", Proceedings of the Aircraft Wake Vortices Conference, March 15-17, 1977, Cambridge, MA
13. McCormick, B. W., "Aircraft Wakes: A Survey of the Problem", presented at FAA Symposium on Turbulence, March 22-24, 1971
14. Robinson, G. H. and Larson, R. R., "A Flight Evaluation of Methods for Predicting Vortex Wake Effects", NASA TN D-6904, November 1972
15. McCormick, B. W., "An Assessment of the Effect of a Trailing Vortex System on a Following Aircraft," Air Force Flight Dynamics Laboratory, Workshop on Wake Turbulence, Wright-Patterson AFB, OH, June 4-5, 1974
16. Burnham, D. C. and Hallock, J. N., "Chicago Monostatic Acoustic Vortex Sensing System, Volume IV: Wake Vortex Tests", DOT/FAA/RD-79-103, IV, July 1982
17. Sammonds, Robert J. and Stinnett, Jr., Glen W., "Criteria Relating Wake Vortex Encounter Hazard to Aircraft Response", AIAA J. of Aircraft, 8, 10, October 1977.
18. Philips, Edward H., "NTSB Urges Changes in Separation Rules", Aviation Week Magazine, February 21, 1994, p. 39

WINTER STORMS RESEARCH IN CANADA

Flight in an Adverse Environment

J. Ian MacPherson
Flight Research Laboratory
Institute for Aerospace Research
National Research Council,
Ottawa, Ontario, Canada

George A. Isaac
Cloud Physics Research Division
Atmospheric Environment Service
Environment Canada
Downsview, Ontario, Canada

1. SUMMARY

Canada has undertaken long-term research programs to study winter storms in coastal regions, with the objectives of improving their forecast and understanding their embedded mesoscale features, rapid intensification, and microphysical conditions associated with aircraft icing. In cooperation with the Atmospheric Environment Service of Environment Canada (AES), the National Research Council (NRC) Twin Otter and Convair 580 aircraft have been instrumented to measure the motion and thermal structure of the atmosphere and the microphysics of cloud and precipitation. The aircraft have been flown in two Atlantic Storms projects in conditions that pilots usually attempt to avoid. Examples of the hazardous conditions encountered in these research flights will be presented in this paper, along with supporting air motion and microphysics data recorded aboard the aircraft. Incidents of airframe icing, turbulence, strong winds and wind shear will serve as an introduction to the more detailed treatment of these subjects by subsequent lecturers in this series. Other related subjects to be covered include research on reduced visibility and on-ground icing of aircraft. Information will be presented on recent developments in instrumentation for the early recognition and warning of hazardous flight conditions. The paper will conclude with a look to the future for coping with winter storms in Canada, including planned research field programs.

2. INTRODUCTION

Winter storms in Canada commonly cause great hardship. In many of these storms, winds are strong, precipitation is heavy, and precipitation types can vary among rain, snow and freezing rain/drizzle. These characteristics are especially evident in the Canadian East Coast region where the effects of the storms are felt both on the land and at sea. Aviation, both commercial and military, are significantly affected by these powerful maritime storms. Flight delays and de-icing operations not only inconvenience passengers, but also drive up the operational costs to the airlines. Aircrews of the Canadian military's Aurora maritime patrol aircraft and the Search and Rescue aircraft are often required to operate in the hazardous flying conditions associated with these large storms.

Although forecasts have improved in the last decade, the track, movement and often rapid intensification of these storms are not adequately handled by existing weather prediction models. Canada has undertaken a long term program, the Canadian Atlantic Storms Program (CASP), to study winter storms in the Atlantic Region (Ref. 1). To date, two comprehensive field programs have been conducted to study storm behaviour, embedded mesoscale features and complementary oceanographic phenomena. CASP-I was based near Halifax, Nova Scotia, from January 15 to March 15, 1986; CASP-II was operated from St. John's, Newfoundland, for the same 2-month period in 1992. Figure 1 shows the operational areas for the two projects and the composite tracks for the 16 storms that occurred during CASP-I.

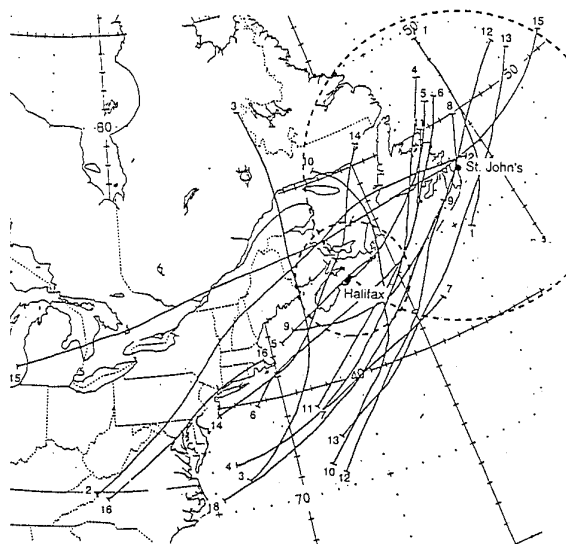


Fig. 1: Tracks of the low pressure centres for the storms studied in CASP-I. Circles denote the operational ranges of the Twin Otter from Halifax/Shearwater in CASP-I and the Convair 580 from St. John's in CASP-II.

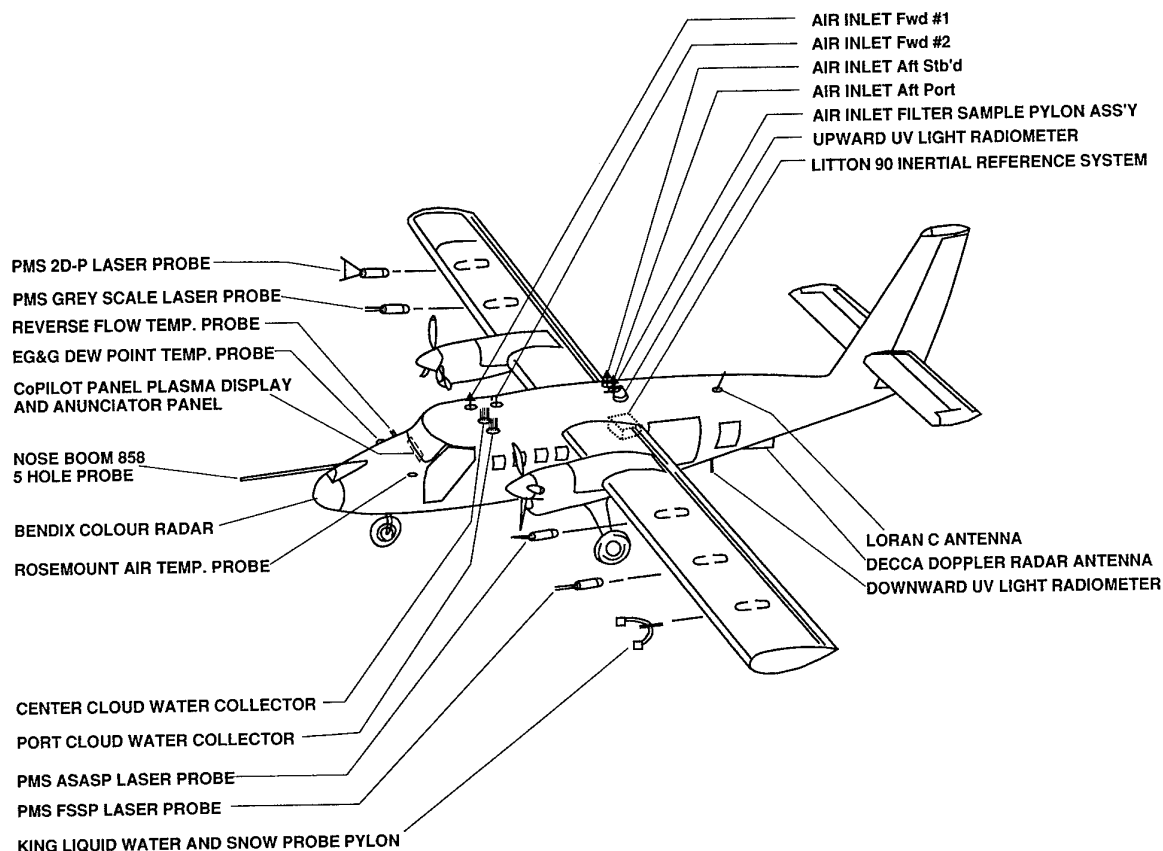


Fig. 2: NRC Twin Otter Atmospheric Research Aircraft as instrumented to measure atmospheric motion and cloud physics parameters.

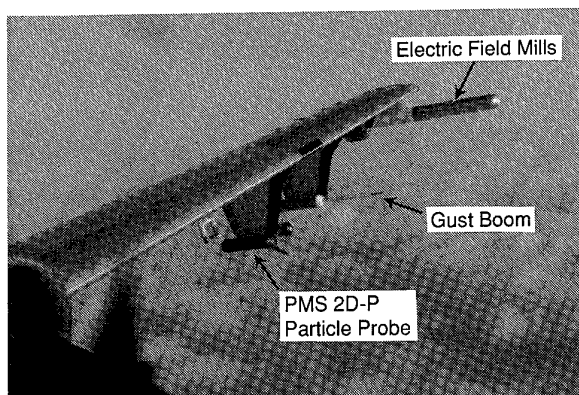
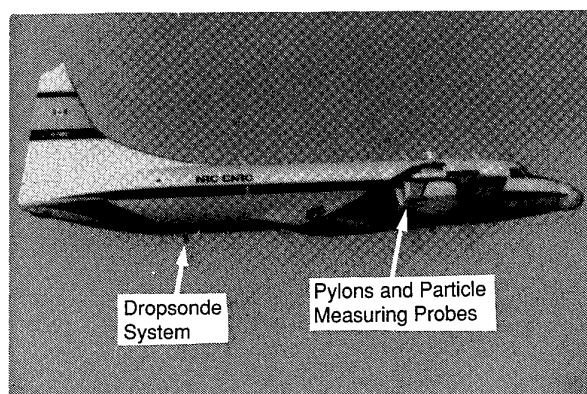


Fig. 3: NRC Convair 580 as instrumented for CASP-II.

The NRC Twin Otter atmospheric research aircraft (Fig. 2, Ref. 2), fully instrumented for air motion and cloud physics measurements, flew 31 missions in CASP-I, operating from Canadian Forces Base Shearwater near Halifax, Nova Scotia. Its recorded measurements form an important component of a comprehensive dataset from a variety of coordinated sensing systems focused on these storms (Ref. 1). These included a second aircraft (Canada Centre for Remote Sensing DC-3), satellites, three weather radars, meteorological towers, oceanographic buoys, ships, radiometers and an enhanced radiosonde network. For CASP-II, aircraft range and alternate airfield considerations

dictated the use of a larger aircraft, the NRC Convair 580 (Fig. 3), also instrumented to measure winds and turbulence (Ref. 3) and the size and concentration of cloud and precipitation particles (Ref. 4). The aircraft was also fitted with an NCAR¹-developed dropsonde system to monitor the two-dimensional kinematic and thermodynamic fields across the storms. A total of 16 storms were studied in almost 200 hours of research flying in CASP-II. Approximately one-third of the flight hours were devoted to in-flight icing research.

1. National Center for Atmospheric Research, Boulder, Colorado

In normal aircraft operations, pilots attempt to avoid the very conditions that were the subject of this research program. Great care had to be taken in the planning and operation of the research flights to ensure safety, while at the same time collecting important data on atmospheric motion and precipitation within the storms. This paper outlines measures taken to improve the de-icing capabilities of the NRC Twin Otter, and presents example results for icing encounters during the CASP flights. Illustrations of other storm-related hazards experienced during these flights are given, including high winds, crosswind landings, wind shear and turbulence. These examples of 'flight in an adverse environment' will serve as an introduction to the more-detailed treatment of these subjects in the lectures that follow.

3. AIRCRAFT RANGE, VISIBILITY, AND ALTERNATE AIRPORTS

The very first flight hazard to be considered in aircraft operations in CASP was the prospect of reduced ceiling and visibility, resulting in possible diversion to an alternate airfield. For operation of the Twin Otter in major east-coast storms, a significant limitation is the range of the aircraft in IFR conditions. The Twin Otter has a fuel capacity of 2450 lb. However, with the scientific instrumentation required for CASP, a crew of four and survival gear, only 2200 lb of fuel could be carried at takeoff for the majority of the project flights. In normal cruise, the aircraft burns about 600 lb/hour and has a maximum true airspeed of only 140 knots. Clearly, the operational range is small relative to the scale of Atlantic storms, so particular care had to be given to go/no-go decisions and the selection of a safe alternate airfield.

For IFR flight, a sufficient fuel reserve must be carried to allow for diversion to the alternate and 45 minutes of holding. When this reserve is subtracted from the 2200 lb takeoff fuel, the result is the amount available for project operations from takeoff to initial approach at the project base (CFB Shearwater). Figure 4 depicts the available flight endurance for project use as a function of the alternate airfield. For example, if a project flight time of 3 hours was required, then this could be done only when Halifax International was an available alternate. On the other hand, if Moncton was the only alternate above limits, then an approach to the base at Shearwater would have to be made after about two hours of IFR flight, to allow enough fuel to divert to Moncton. Two hours of data collection was considered a minimum to meet scientific objectives, with a preference for 2-1/2. The figure shows that this imposes a serious restriction on the available alternates. Furthermore, given the size of the storms, it often happened that several of these potential alternates were below limits simultaneously.

Although these restrictions caused some flight delays, and cancellation in two or three cases, the Twin Otter did accomplish 31 project flights in ten storms during CASP-I. The careful flight planning and weather forecasting contributed to the fact that on none of these flights was a diversion to an alternate airport required.

Similar considerations were applied early in the planning stages for CASP-II, to be operated from St. John's, Newfoundland. St. John's has a treacherous climate, and the highest frequency of freezing precipitation in Canada (about 160 hours annually). Only three other fully IFR airports are available on the island of Newfoundland (Fig. 5): Gander, at a range of 110 n. miles from St. John's,

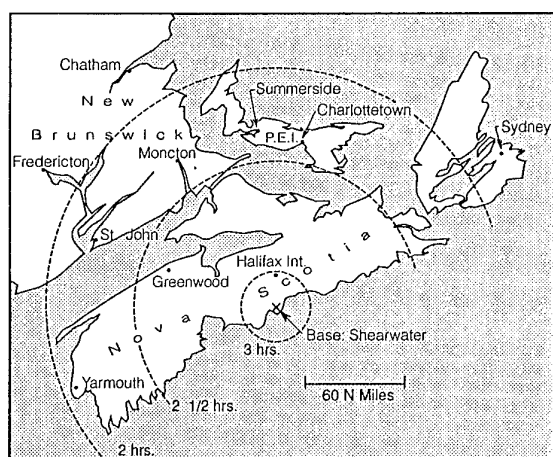


Fig. 4: The CASP-I operational area showing the locations of the project base at CFB Shearwater and potential IFR alternates for the Twin Otter. Maximum available project flight time is dependent on the alternate selected.

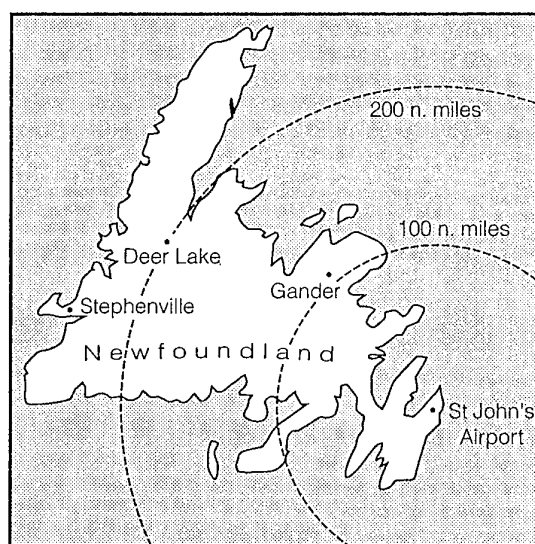


Fig. 5: Newfoundland showing locations of CASP-II project base at St. John's Airport, and three IFR alternate airports.

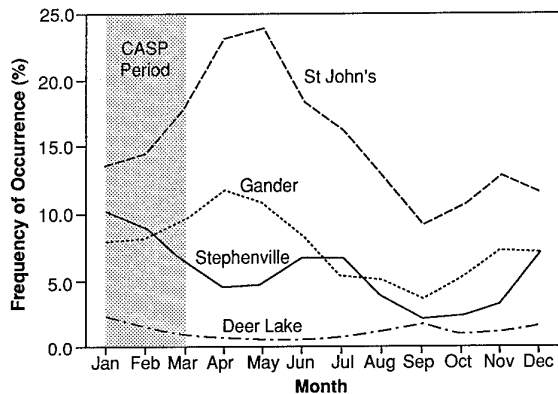


Fig. 6: Month to month variation of the frequency of occurrence of either ceiling height or visibility falling below their respective critical values for the four IFR airports of Newfoundland [From Ref. 5, Stuart].

Deer Lake (200 n. miles) and Stephenville (230 n. miles). Clearly, only Gander is a possible alternate for the Twin Otter.

Aviation interests were well aware of the problems caused by adverse weather conditions at Newfoundland airports, but detailed climatologies of these limiting conditions were quite limited. Consequently, in support of CASP-II, the AES contracted a private firm to develop software to provide frequency distributions of ceiling height and visibility in both graphical and tabular formats for a variety of stratifications, including wind direction, month, and time of day (Ref. 5). Figure 6 depicts the monthly frequency of limiting conditions (ceiling below 200 feet or visibility less than 0.5 mile²) based on the climatological records of hourly data from the four IFR airports of Newfoundland. At St. John's, the possibility of a diversion occurs about 15 percent of the time during the planned January-March CASP-II period. Of probably more importance, however, is another output from the new software package, the *joint* probability of an alternate airport being below limits at the same time as the destination. Figure 7 illustrates that when St. John's is below limits, there is a 35 percent probability that the nearest alternate, Gander, is also below limits during the CASP-II period. The airports at the west end of the island are much less likely to be down, but these airports are beyond a practical diversion range for the Twin Otter. This analysis was one of the primary considerations in the decision to use the NRC Convair 580 as the research aircraft in CASP-II. In the subsequent operation of the Convair 580 at St. John's from January 15 to March 15, 1992, only one diversion (to Deer Lake) was required in 44 project flights.

2. Because of surrounding topography and runway orientation, limitations at Stephenville were: ceiling < 416 feet or visibility < 1 mile

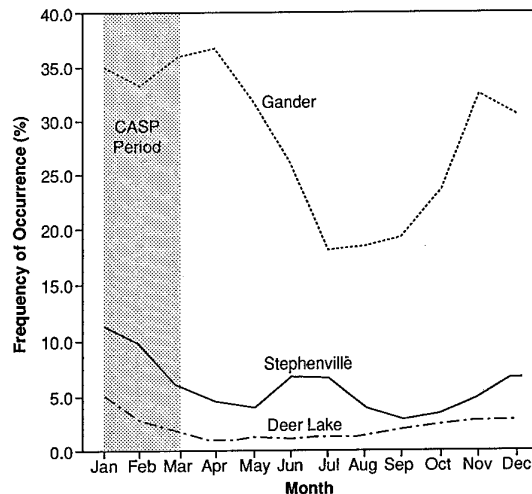


Fig. 7: Joint probability that alternate airports on Newfoundland are below limits when St. John's Airport is below limits [From Ref. 5, Stuart].

Accidents in which aircraft are operated under Visual Flight Rules (VFR) into adverse weather conditions occur regularly, and claim a disproportionately high number of fatalities each year. Canadian statistics for 1976-85 show that this type of accident accounted for only 6 % of the total, but resulted in 26 % of the fatalities during the ten-year period (Ref. 6). About 80% of these accidents occurred during the enroute phase of the flight, and 51 % of the Canadian VFR-into-IMC (Instrument Meteorological Conditions) accidents occurred in mountainous terrain. Of the 33 helicopter accidents in this category, 27 occurred when pilots encountered white-out conditions in which they were not able to visually maintain adequate reference to the ground. At the NRC Flight Research Laboratory, research is under way on advanced cockpit displays to improve the pilot's situational awareness in conditions of reduced visibility.

4. IN-FLIGHT ICING

4.1 Icing Protection for the Aircraft

The NRC Flight Research Laboratory and the NASA³ Lewis Research Center both operate Twin Otter aircraft in atmospheric research roles. The NASA aircraft is used primarily in airframe icing research. To record cloud droplet sizes and concentrations, it carries laser-based particle spectrometers similar to those operated by NRC/AES mounted on identical under-wing pylons (Fig. 2). NASA developed the capability to selectively de-ice airframe components to determine their contribution to the total drag increase due to icing. Aircraft performance losses in terms of lift and drag coefficient changes were

3. U. S. National Aeronautics and Space Administration

obtained by flying in icing conditions for up to an hour, then exiting cloud to do steady level speed-versus-power measurements, while progressively de-icing selected airframe components. Engine inlet and propeller icing were excluded from this study, as their de-icing systems must be run continuously during icing conditions.

Data reported in References 7 to 9 show aircraft lift coefficient decrements from 7 to 17 percent in the NASA studies. Aircraft drag coefficients at normal operating speeds increased from 30 to 75 percent over un-iced baseline measurements. Figure 8 shows results from a flight in mixed rime/glaze icing, where the aircraft drag coefficient C_D increased about 33%, and a flight in glazed icing, in which C_D was up by nearly 50%. The shape of aircraft ice accretion is the principal factor influencing performance. Glaze ice is produced at the warmer temperatures nearer 0 deg C, so freezing is slower and the resulting surface rougher. In the cases shown, the glaze ice case produced the greater drag increase although the exposure time was lower and cloud water concentration was only half that of the mixed-icing case. The temperature was -5.0 deg C, however, 4.5 deg C warmer than during the mixed rime/glaze icing case.

Figure 8 illustrates significant differences in the proportion of the drag due to icing of the different airframe components. This had important implications in plans to operate the NRC Twin Otter in CASP where glaze icing was anticipated. On the standard Twin Otter, only the wing and horizontal tail have de-icing boots. In the glaze icing case shown, operating the standard boots will only shed ice responsible for 40 percent of the additional drag; 60 percent of the drag is due to ice on the remainder of the aircraft! A standard Twin Otter similarly iced would have, at best, a very limited capability of climbing should an engine be lost. Figure 8 shows that if the vertical tail, wing struts and wheel struts are also de-iced, then nearly 3/4 of the drag due to ice can be shed in the glaze ice case, with an even higher proportion removed in rime icing. De-icing of the vertical tail also improves its performance in engine-out, asymmetrical flight.

NASA arranged our contact with the suppliers of their custom-built de-icing boots (B. F. Goodrich, Akron, Ohio), and a similar system was produced and installed on the NRC aircraft prior to CASP-I. Total cost was less than \$5000 U.S. and the weight penalty was only 33 lb. It should be mentioned that FAA or Transport Canada type-approvals were not sought for these installations. NASA and NRC operate their aircraft in a restricted category and are responsible for the safety of their own modifications.

4.2 Twin Otter in CASP-I

During the CASP-I experiment, the Twin Otter encountered significant icing on three flights. On each occasion, the full de-icing system was used including the newly-installed boots on the struts and the vertical tail, and fully satisfactory results were obtained from a safe-flight point of view. There appeared to be notable differences in the adherence of the ice, however, which was considered interesting from a meteorological perspective. Since the aircraft was fully instrumented to measure droplet spectra and cloud water concentrations, a further analysis of these events was undertaken.

Table 1 summarizes the cloud characteristics during the three icing encounters. For each case, the three minute period in which the liquid water content (LWC) was highest was selected for comparison. The liquid water content was measured using a PMS⁴ King probe, which operates on the principle that the rate of cooling of a heated wire is proportional to the amount of water impacting upon the wire. The concentration of droplets and precipitation particles in the size ranges from 2 to 30 μm and from 200 to 6400 μm were measured using PMS FSSP (Forward Scattering Spectrometer Probe) and 2D-P probes respectively. The maximum one-second FSSP droplet concentrations and King LWC are also listed, as well as the droplet mean volume diameter (MVD) as determined from the FSSP data.

4. Particle Measuring Systems, Boulder, Colorado

Date Time GMT	Alt. k ft	Temp C	LWC g m ⁻³	Max LWC g m ⁻³	FSSP cm ⁻³	Max FSSP cm ⁻³	MVD μm	2D-P m ⁻³	% FAA Max LWC
Feb 18 1753-1756	7.1	-5.2	0.47	0.56	139	195	16.3	344	60
Mar 2 1614-1617	13.7	-11.7	0.04	0.31	21	42	19.5	380	10
Mar 2 2005-2008	8.0	-9.0	0.42	0.79	52	90	22.9	710	90

TABLE 1: Microphysical Conditions During Twin Otter Icing Events In CASP-I

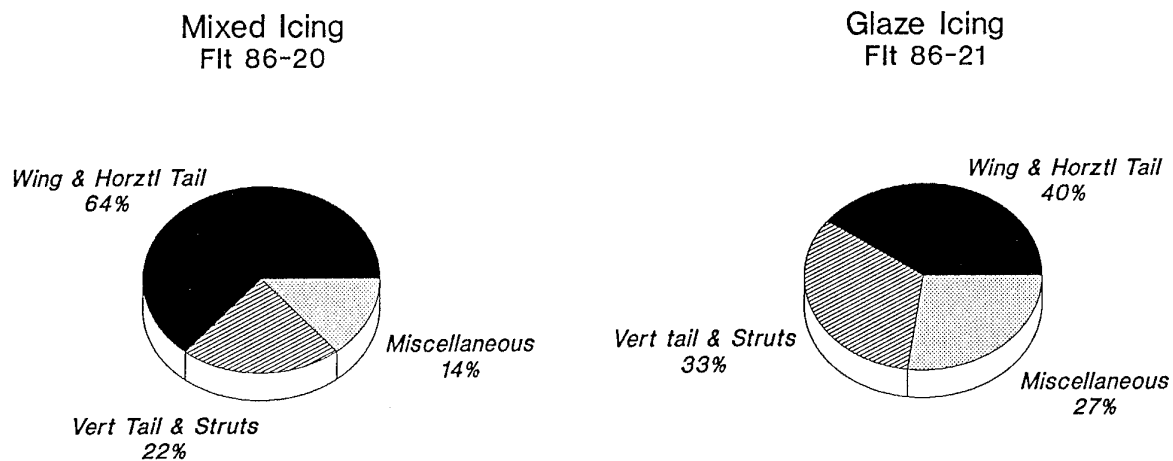
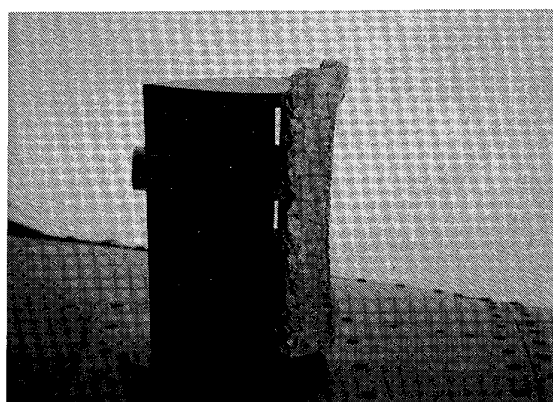


Fig. 8: Proportion of drag increase due to icing on different airframe components for a case of mixed icing and glaze icing. Data were measured on a Twin Otter by NASA (Ref. 7 to 9).

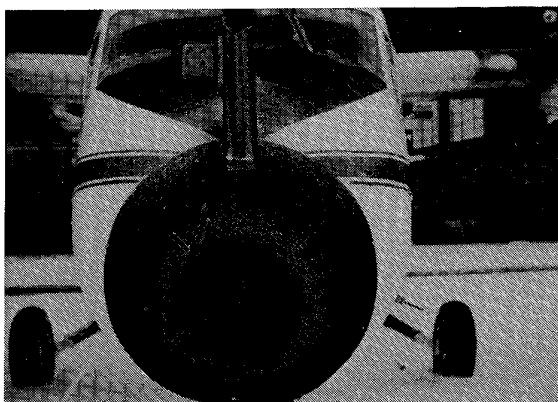


(a)

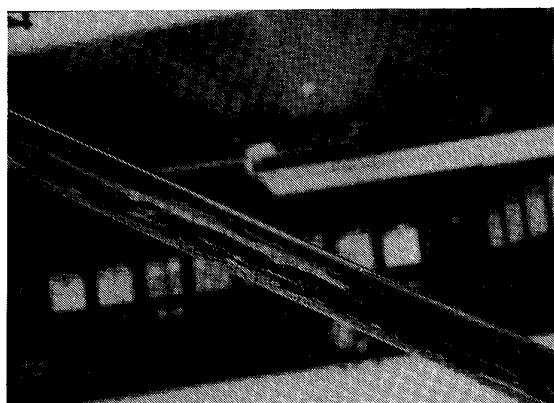


(b)

Fig. 9: Icing case on February 18, 1986, showing: (a) reverse-flow temperature probe and (b) deicing boots on horizontal tail, wing strut and landing gear strut.



(a)



(b)

Fig. 10: Icing case for first flight on March 2, 1986, showing rough ice (a) on aircraft nose and (b) adhering to the wing strut deicing boot after landing.

Figures 9 and 10 illustrate the major differences in the ice properties between the flights on February 18 and March 2, 1986. On February 18, about 2 cm of a rough glaze ice built up on the aircraft, as shown by the reverse flow temperature probe in Fig. 9a. On this occasion, activation of the pneumatic de-icing boots removed all of the ice on the boots (Fig 9b). On both flights on March 2, however, much of the ice remained tenaciously attached to the de-icing boots even after landing, as shown by the photograph of the wing strut in Figure 10b. The crew reported ice forming in streaks on the cockpit side windows, indicating slow freezing that leads to glaze icing.

The most severe of the icing encounter occurred on the second flight of March 2. Figure 11 shows analog traces of liquid water content, static pressure, temperature, true airspeed and angle of attack for this event. The aircraft was flying at 8000 ft msl on an easterly heading into the rear of the same storm sampled on the earlier flight. An indicated airspeed (IAS) just above 122 knots (143 knots true airspeed) was being maintained in conditions of light snow. A sudden onset of icing occurred at 1957:10, and the airspeed started to fall and the angle of attack increased. The slowing of the aircraft as a result of that initial burst of cloud liquid water is fairly typical of the Twin Otter in icing. Five minutes later, at 2002:10, the pilot commented on the voice-tape that the IAS was down to 112 knots and that the de-icing system had not yet been activated. Only 40 seconds later, the cloud started to

thicken and the pilot announced "107 knots" and de-icing was commenced. By 2003:30 GMT, the liquid water content reached 0.1 g m^{-3} and was increasing rapidly to a peak above 0.6 g m^{-3} (Figure 11). Comments were made on the tape that the ice had considerable tensile strength and was adhering to the struts. There was little improvement in airspeed, and at 2007:30 the IAS had decreased further to 104 knots despite application of maximum continuous power. At 2009 a descent and turn was commenced as the pilot felt it was necessary to exit the storm.

It is interesting to note that on this second flight on March 2, when the most severe conditions were encountered, the temperature at the flight level was -9°C , that is, colder than the February 18 case when the temperature was near -5°C . However, the mean volume diameter (MVD, Table 1) of the cloud droplets was considerably higher on March 2. The NASA results (References 7 to 9) suggest that the glaze icing would be worse at the warmer temperatures where the water would flow and freeze more slowly. However, in this case, the problem was mainly the inability of the boots to shed all of the ice at the colder temperatures. The larger droplet sizes and the presence of snow in significant concentrations (2D-P data, Table 1) may have led to the 'stickiness' of the ice on the boots.

The icing conditions encountered in these three cases were compared with the FAA design envelopes for stratiform cloud icing conditions (Ref. 10). The design envelopes consider the mean effective droplet diameter, the air temperature and the horizontal extent of the icing cloud. Using the microphysical conditions as outlined in Table 1, the liquid water content on February 18 reached 60 percent of the maximum proposed by the FAA, while for the first flight on March 2, it was only 10 percent of the maximum. However, in correspondence with the pilot's comments and actions, the second flight on March 2 was the most severe, reaching 90 percent of the FAA design envelope maximum liquid water content.

4.3 Convair 580 in CASP-II

In CASP-II, the Convair 580 performed flights over the Atlantic Ocean within an 800-km range of the operational base at St. John's. The Convair 580 has an anti-icing system that uses engine bleed air to heat the leading edges of the wings and tail. The aircraft was fully equipped with cloud physics instrumentation including: two King probe liquid water content meters, an FSSP probe for measuring droplet sizes from 3 to $95 \mu\text{m}$, a Rosemount icing detector, and several Particle Measuring Systems 2-D laser probes for measuring the size, concentration and shapes of water droplets and ice crystals (Ref. 4). The project was ideally suited for maritime aircraft icing research, which led to the involvement of the Boeing Commercial Airplane Group and Airbus Industrie of France. Boeing and Airbus were interested in characterizing the maritime Atlantic icing environment to help substantiate aircraft requirements for cross-oceanic flights by twin-engined passenger aircraft (Ref. 11).

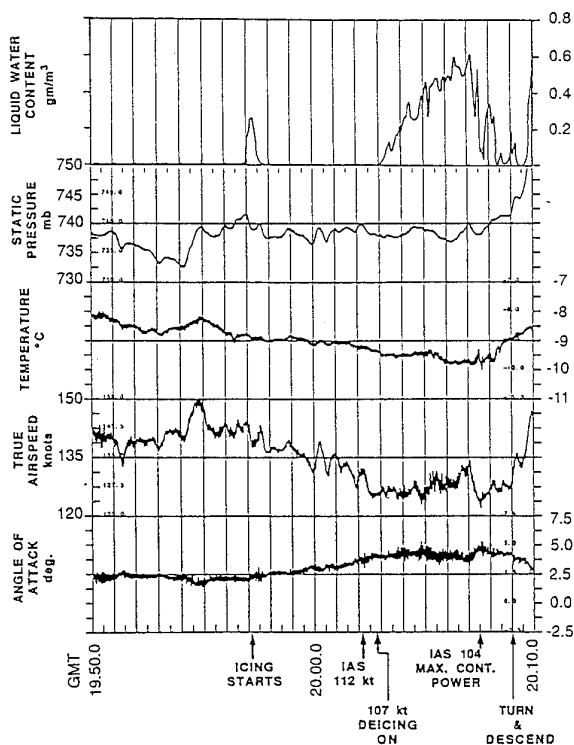


Fig. 11: Data recorded on Twin Otter during icing encounter on second flight on March 2, 1986.

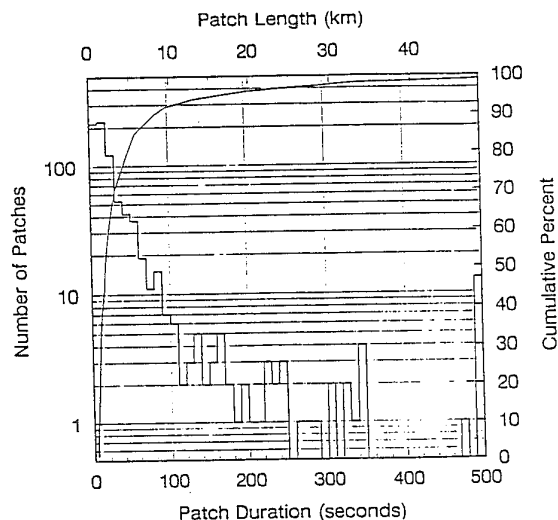


Fig. 12: Histogram of SLWC patch durations encountered by Convair 580 in CASP-II. All patches with durations longer than 500 sec are included in the last bin [Reproduced from Ref. 4, Cober *et al.*].

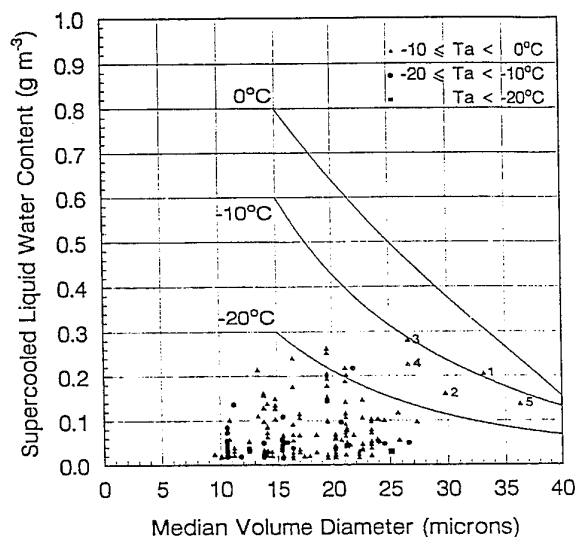


Fig. 13: Comparison of 300-second SLWC averages to the maximum continuous icing envelopes of FAR 25-C [Reproduced from Ref. 4, Cober *et al.*].

The Convair 580 encountered approximately 1500 km of icing conditions in 190 hours of research flight in CASP-II. Data from each flight were analyzed in one-second intervals (approximately 100 m of flight path). An interval was considered to have supercooled liquid water content (SLWC) if the static temperature was less than 0.0 deg C and the SLWC $> 0.025 \text{ g m}^{-3}$. An icing 'patch' was defined as having SLWC $> 0.025 \text{ g m}^{-3}$ for > 5 seconds ($\sim 0.5 \text{ km}$). Figure 12 shows a histogram of the 801 SLWC patches measured by the Convair 580 in CASP-II. Icing patches had an average length of 4.3 km, with average droplet concentrations of 130 cm^{-3} , liquid water contents of 0.13 g m^{-3} , and droplet mean volume diameter

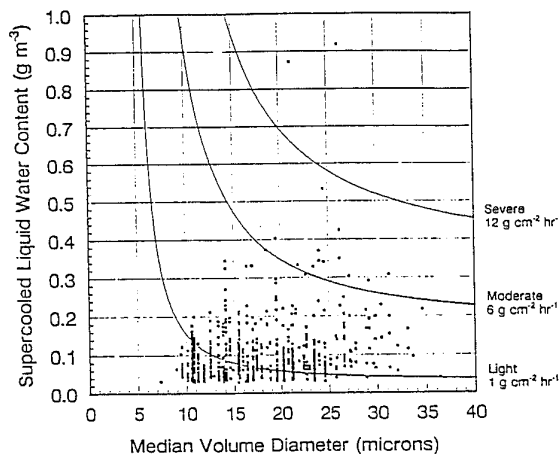


Fig. 14: Comparison of the potential accumulation rates of SLWC patches to the icing intensity envelopes of Newton in Reference 12 [Reproduced from Ref. 4, Cober *et al.*].

of $18 \mu\text{m}$. In general, the icing intensity was classified as light, although moderate to severe icing was observed in several patches.

The U.S. Federal Aviation Regulation Part 25 Appendix C (FAR 25-C) icing envelopes detail the probable maximum icing conditions expected in winter storms. The envelopes were defined in the late 1940s and were based on data obtained from approximately 1000 icing measurements across the United States. For certification for flight into icing conditions, aircraft must demonstrate the ability to fly in an environment characterized by the maximum envelopes. Although the envelopes have been criticised for various limitations (References 12 and 13), they are widely used as a measure of the most severe icing conditions.

The Convair 1-second data were averaged into 300-second intervals, which corresponded to flight legs of approximately 16 n. miles. This allowed direct comparison with the FAR 25-C icing envelopes for maximum continuous icing (which are based on flight for 17.6 n. miles). Figure 13 shows a comparison between the 182 intervals in which SLWC exceeded 0.015 g m^{-3} and the FAR 25-C envelopes. Most of the data points fell well short of the maximum envelopes, although the -10 deg C envelope was exceeded on one occasion by icing at -9.5 deg C (point 1 on Fig. 13). The five heaviest icing cases are numbered. Points 1 and 2 occurred consecutively during flight at 13000 feet through a cold frontal region, while Points 3 and 4 occurred during flight at 2500 feet through a low-level stratus cloud. The results of Figure 13 are quite similar to those shown in Ref. 14 for icing events recorded on the Twin Otter over Nova Scotia during CASP-I.

An alternative set of icing envelopes was proposed by Newton in Reference 12, in which the icing intensity is defined in terms of the rate of accumulation in $\text{g cm}^{-2} \text{ hr}^{-1}$

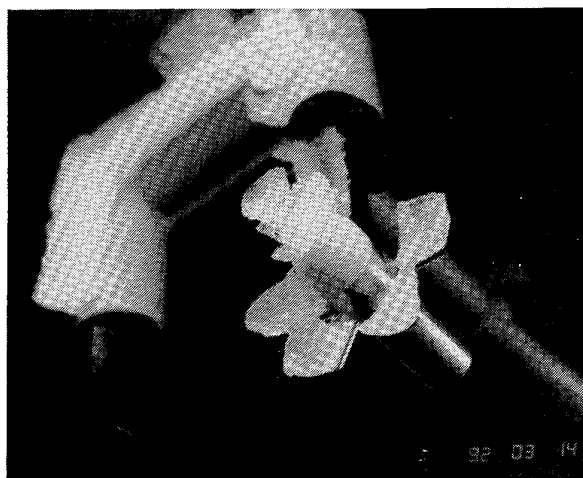


Fig. 15: Ice on Convair 580 five-arm reverse-flow temperature probe after freezing drizzle encounter on March 14, 1992. Second un-iced probe in background is Rosemount heated total temperature probe.

on a 7.6-cm (3-inch) cylinder. These envelopes have a more physical basis than those in FAR 25-C and can be used to describe a wider range of icing conditions. Figure 14 shows the Convair SLWC data and mean volume diameter, averaged over each icing patch, plotted against the Newton envelopes, which represent potential accumulation rates of 1, 6 and 12 g cm² hr⁻¹ (corresponding to light, moderate and severe icing). In general, the icing encountered corresponded to light icing, although there were a number of patches with moderate and two cases with severe icing rates. Note that a severe patch lasting 60 seconds would likely be rated as a light icing patch when averaged into a 5-minute period when no other icing was encountered. This explains the tendency for the icing data in Figure 14 to appear heavier than in Figure 13. The Convair 580 experienced no difficulties in any of the icing conditions shown in Figures 13 and 14.

During four of the CASP-II flights, the Convair 580 encountered regions of supercooled drizzle with droplets sized between 0.1 and 1.0 mm, as detected by the PMS 2D probes (Ref. 4). On two of these occasions, a rapid accumulation of ice on the pilot's windshield necessitated aborting the flight path and exiting the icing region. These cases are not included in the data above, for the response of the King LWC probe to droplets larger than 50 μ m is unknown, and the FSSP only measured droplets to a maximum diameter of 47 μ m. Consequently, SLWC and mean volume diameters could not be accurately determined. These encounters represented the most severe cases of icing in CASP-II.

One of the freezing drizzle cases was encountered on the flight of March 14, 1992, which penetrated a trough line associated with a small scale wave and a redeveloping low pressure region. Figure 15 shows an example of the ice accretion and Figure 16 shows analog traces from some of the instruments during this icing event. At 13:28 GMT

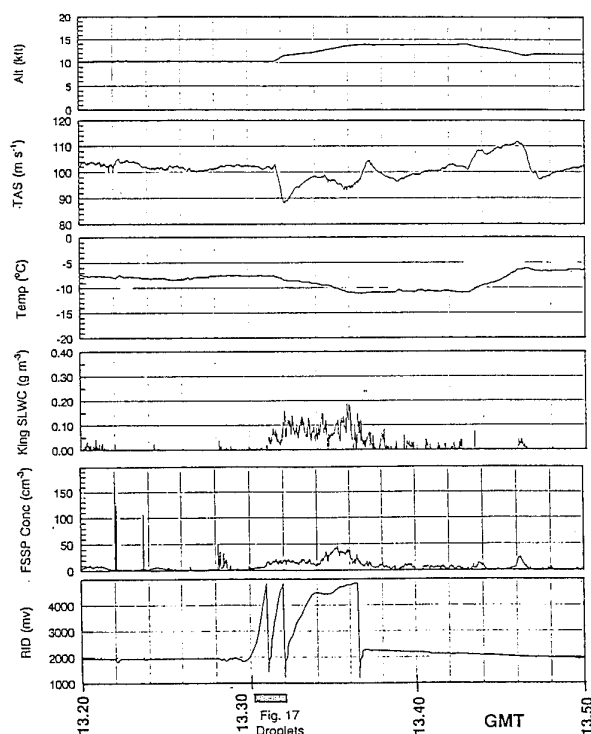


Fig. 16: Data recorded during the March 14, 1992, freezing drizzle case. The bottom trace shows the voltage signal for the Rosemount Ice Detector (RID), which indicates ice accretion between 13:30 and 13:36 GMT. Bar on x-axis indicates time when drizzle droplets shown in Fig. 17 were recorded.

the aircraft entered a region of freezing drizzle at -8 deg C and 10000 ft, a relatively high altitude for drizzle. Because of a rapid accumulation of ice on the windshield, the pilot initiated a climb and exited the drizzle region at 12500 ft and -10 deg C. This region was topped with supercooled cloud extending from 11800 to 13600 ft. The King-measured SLWC did not exceed 0.2 g m⁻³, although only a partial response from drizzle-sized drops could be expected. The voltage signal from the Rosemount Ice Detector (which cycles back to near zero when the probe is de-iced) shows most of the ice accumulation occurred between 13:30 and 13:36 GMT. Figure 17 shows 2D images of the drizzle droplets measured by a 2DC Grey particle spectrometer, indicating droplets with diameters from 100 to 500 μ m. A videotaped icing cylinder mounted on one of the wing pylons recorded an accretion of 1.1 cm of ice between 13:29 and 13:34 GMT. The corresponding potential accumulation was 10.5 g cm⁻² hr⁻¹, implying that under Newton's envelopes, the icing intensity was between moderate and severe. Between 13:29 and 13:31 GMT the King probe failed to measure SLWC above 0.05 g m⁻³, indicating that the SLWC was mainly in droplets larger than 50 μ m. Freezing drizzle is considered to represent a significant hazard because the droplets can run back on the wings before freezing and cause a significant degradation of the airfoil performance (Ref. 13).

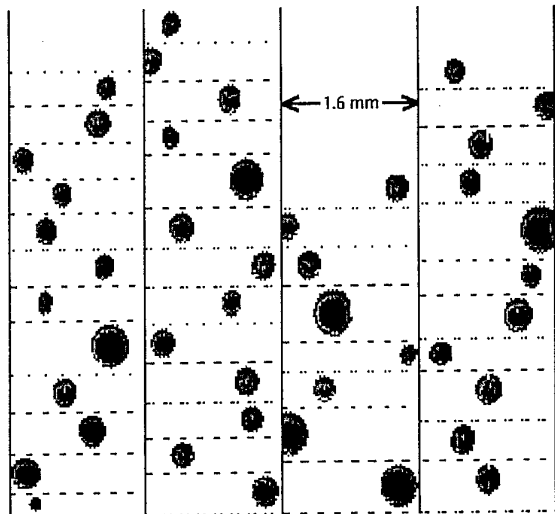


Fig. 17: Images of freezing drizzle drops recorded by PMS 2DC Grey probe between 13:30 and 13:31 GMT on March 14, 1992. The largest drops shown have a diameter of approximately $420 \mu\text{m}$ [Reproduced from Ref. 4, Cober *et al.*].

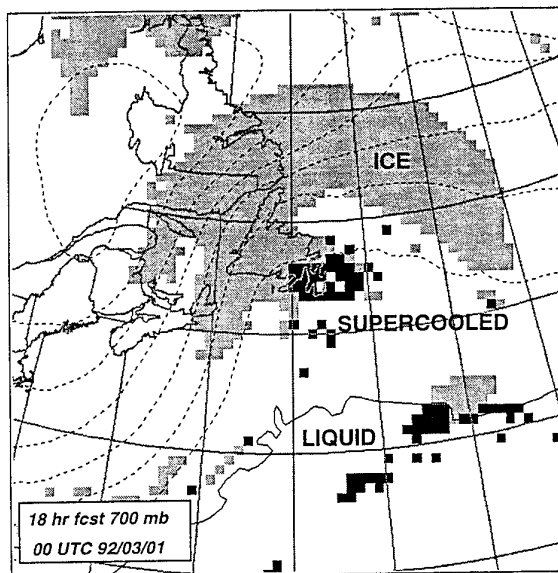
The CASP II data have already had commercial benefits. A Canadian commercial operator (Kelowna Flightcraft) has used the data in the certification process of the stretched Convair 5800 for flight in icing conditions. In addition, Boeing has used the data to obtain FAA approval to eliminate a 5% fuel penalty as a requirement for Extended Range Operation with Two-Engine Airplanes (ETOPS) for the Boeing Model 777 airplane.

4.4 Icing Forecasts

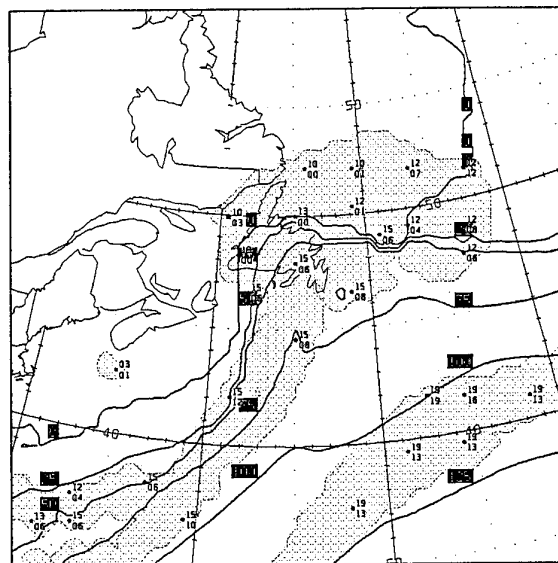
Accurate forecasting of regions of potential icing is crucial for flight planning and poses a challenge for the meteorologist. Currently, Canadian operational meteorological forecasting models do not account for the prediction of regions of supercooled water in the atmosphere. Icing forecasts are constructed on simple indicators such as temperature, dew point depression and vertical motion fields, and typically tend to be overestimated (Ref. 15). This causes a tendency for pilots to ignore the forecasts, and does little for Search and Rescue pilots who need to know the conditions they might encounter. CASP-II provided the opportunity to evaluate new forecasting schemes, since, in probing the storms, the instrumented aircraft collected data which could be compared directly with icing predictions by the computer models.

For this study, the Canadian operational regional finite-element (RFE) model was modified with improved parameterization of cloud liquid water and ice. Reference 16 provides details of the model as well as several case studies comparing model results with Convair CASP-II data. To provide an example of an application of this modified model, Fig. 18a shows a constant pressure (700 mb) map of predicted cloud phase superimposed with air

temperature generated from an 18-hour mesoscale forecast. The map shows the distribution of cloud ice, cloud water and supercooled water in 50-km grid elements. The extent of the SLWC is localized to well-defined regions near the -5 deg C isotherm. This is very different from the current operational icing forecast algorithm (Fig. 18b), where



(a)



(b)

Fig. 18: Icing forecast maps. (a) Output from new model for 700 mb level, showing cloud phase and air temperature from an 18-hour forecast. The black squares depict forecast supercooled water. (b) Output from current operational forecast; shading delineates regions of rime icing [Reproduced from Ref. 16, Tremblay *et al.*].

aircraft icing is predicted over most of the cloud shield. The procedure underlying the production of this forecast simply locates points where the model vertical velocity is upward and the dew point depression is < 2 deg C. It is not based on a sufficient knowledge of cloud physics and therefore does not have the potential to accurately track regions of SLWC. Thus it creates a tendency for pilots to ignore the icing forecast. The new model, when it is fully tested and implemented operationally, should improve the icing forecasts and generate more confidence in their guidance with the aviation community.

5. PRECIPITATION AND ON-GROUND ICING

In many of the CASP flights heavy snowfall presented the obvious problem of reduced visibility and flight delays because conditions were below IFR limits. Although unavoidable, this was sometimes frustrating because these meteorological conditions were of scientific interest to the program and airborne measurements of the cloud and precipitation were highly desirable. Various strategies were employed to achieve as many flights in snow as possible. Sometimes the aircraft was flown upstream to meet the precipitation, complete the sampling and land prior to the airport going below limits. On other occasions the aircraft was launched as soon as possible after the snowfall diminished, and then flown into the rear quarters of the retreating storm. The latter case usually meant a takeoff in light snow. Caution had to be exercised because towing the warm aircraft out of the hangar into snow and below freezing conditions would cause ice and sticky snow to adhere to the wings as the aircraft cooled down. Opening the hangar doors for 30 minutes to cool the aircraft prior to towing usually did not alleviate the problem. In most cases the aircraft had to be de-iced with a spray of warm de-icing fluid.

This hazard was amply demonstrated by an incident during CASP-I that involved the second aircraft used in the experiment, a DC-3. A night-time flight was to be made in a snowstorm traversing the area from the southwest. The Twin Otter was unable to fly because of a lack of an available alternate within range, but the DC-3, with its 6-hour endurance, could use Quebec City as an IFR alternate. As it was snowing at the airport, the wings and tail of the DC-3 were de-iced using standard techniques and a glycol-water solution. On the subsequent takeoff attempt the aircraft would not lift off, due to a heavy snow build-up on the port wing in an area not visible from the cabin or the cockpit. The takeoff was successfully aborted and the flight cancelled, but the danger of the situation was well recognized. A subsequent investigation of the incident found that the mixture of de-icing fluid used in this case had been inadvertently diluted with too much water.

In recent years there have been two fatal takeoff accidents of commercial jet aircraft during conditions of east-coast winter storms. The crash of a Fokker-28 at LaGuardia Airport in New York (which occurred in the week follow-

ing the completion of CASP-II) was attributed to a stall after takeoff due to ice contamination of the aircraft wings (Ref. 17). The surface temperature was just below the freezing point, but there was a significant snowfall rate in the 35 minutes that elapsed between de-icing of the aircraft and the attempted takeoff. The investigation raised issues as to the holdover time of de-icing fluids. On January 13, 1982, an Air Florida 737 crashed after takeoff in snow from Washington National Airport, 50 minutes after airframe de-icing; snow/ice contamination was again a major factor in the accident (Ref. 18). In Canada, a similar accident occurred to another Fokker-28 during a snowstorm in Dryden, Ontario, on March 10, 1989. In this case the aircraft was not de-iced prior to the takeoff attempt. According to wind tunnel studies by the aircraft manufacturer, a wing upper surface roughness consisting of particles only 1-2 mm diameter, at a density of about one particle per square centimetre, can cause lift losses on the F-28 wing of about 33 percent in free air, and about 22 percent in ground effect (Ref. 17). It is clear from these experiences that the on-ground icing of aircraft is at least as serious a safety hazard as in-flight icing.

Canadian winter conditions are particularly harsh. Aircraft often have ice on their wings and control surfaces which must be removed before take-off. Care must also be taken to ensure that additional ice does not form while the aircraft is preparing to take off. Ground de-icing and anti-icing is performed using fluids at all major centres across the country. To illustrate the importance of ground de-icing for our country, Canada has the only *independent* laboratory in the world (at Université du Québec à Chicoutimi, Ref. 19) currently performing de/anti-icing fluid holdover evaluations; all other facilities are run by chemical companies. Table 2 presents holdover times in snow and freezing precipitation for Type-I fluids (de-icing) and Type-II fluids (anti-icing, for aircraft with rotation speeds > 85 knots), excerpted from Reference 20. The

Temp deg C	TYPE I		TYPE II	
	Snow	Freezing rain	Snow	Freezing rain
0 to -7	6 - 15	1 - 3	20 - 45	8 - 20
-7 to -14	6 - 15	n/a	20 - 45	n/a

Holdover times in minutes

Table 2: Pilot guideline for approximate holdover times for SAE Type-I and Type-II fluids, excerpted from Tables 1 and 2 of Reference 20. Figures for Type-II fluid applied neat, unmixed with water, thus the figures represent maximum protection times; Type-I mixture with freezing point at least 10 deg C below ambient temperature. 'Freezing rain' is interpreted by the authors to include freezing drizzle.

holdover times of Type-I fluids are very short, particularly in freezing precipitation. Type-I fluids were used to de-ice the aircraft in the LaGuardia and Washington accidents mentioned above. Currently in Canada, the use of Type-I fluids still predominates; Type-II fluids are not yet available at most Canadian airports, including St. John's. This places severe restrictions on aircraft operations in winter storms.

One of the surprising results of CASP-II is that a significant proportion of the freezing precipitation events in the St. John's area results from a condensation-coalescence process (the so-called 'warm rain process'), previously thought to be rare at these latitudes, particularly in winter (Ref. 21). It is commonly accepted that freezing precipitation forms from *frozen* precipitation falling through an above-zero C warm layer, and back into an below-freezing zone near the surface (as in trace 'a' in Figure 19). The frozen precipitation melts, and then either supercools in the lower level or freezes on a cold surface on contact. It is also generally accepted that the formation of ice crystals in winter clouds is usually an efficient process, but that development of large supercooled water drops by the condensation-coalescence process (i.e., condensation on supercooled cloud droplets, and coalescence of these droplets into precipitation-sized drops) is inefficient by comparison. The nucleation of ice crystals and their rapid growth and multiplication in supercooled cloud will usually inhibit this process. For this reason, it was a surprise to find that on two of the four freezing drizzle cases encountered by the Convair 580 in CASP-II, there was no above-freezing zone at *any* level in the atmosphere (i.e., as in trace 'b' in Figure 19).

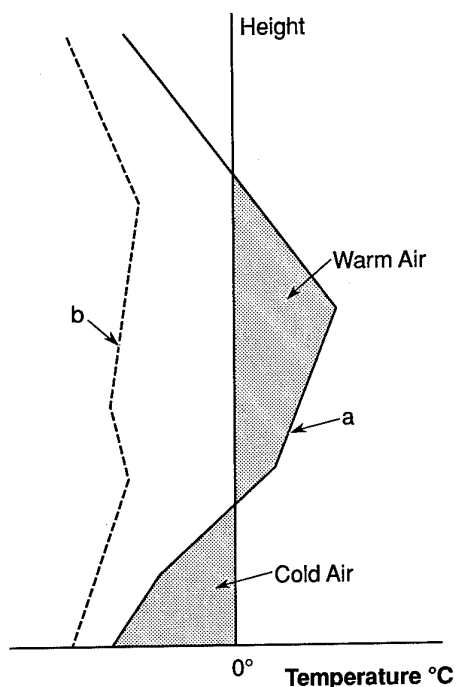


Fig. 19: Atmospheric temperature profiles for formation of freezing precipitation.

This led to additional investigations. Twenty years of surface and upper air records were examined for several sites (only St. John's data will be discussed here). For each freezing rain and freezing drizzle episode, the upper air data from the St. John's radiosonde were examined to determine the maximum air temperature in the air aloft, and this was plotted versus the surface temperature in Figure 20. Each plotted point represents a reported freezing precipitation event (x for drizzle, square for rain) at the radiosonde release time (00 or 12 GMT). The plotted line represents a maximum upper air temperature equal to the surface temperature; if the warmest upper air temperature is at the surface, the points will fall on this line.

The figure can be broken into three zones. Points lying along the 1:1 line are cases where the warmest air is at the surface; the layer of cloud forming the precipitation is even colder than the surface temperature. These are condensation-coalescence cases, and are almost all episodes of freezing drizzle rather than freezing rain. In zone A, there is a layer aloft that is warmer than the surface temperature, but it is still below 0 deg C. Again, in these cases the freezing precipitation must have formed by condensation-coalescence. In zone B, there is a layer aloft warmer than 0 deg C. In these cases the freezing precipitation observed at the surface resulted from snow melting on its passage through a melting layer, i.e., the 'conventional' process.

Other observations can be made from Figure 20. First, of the 312 observations of freezing rain or drizzle at 00 or 12 GMT, 67 % were for drizzle and 33 % were rain. Freezing drizzle is seen to occur at colder temperatures than freezing rain; the coldest surface temperature during a freezing rain event was -4.4 deg C. Approximately 60 % of the freezing drizzle cases were from clouds with no above-zero temperatures (cold clouds), compared with only 13 % of the freezing rain cases. Therefore, cold clouds produce freezing drizzle more often than freezing rain, consistent with the condensation-coalescence process, which must first go through a drizzle stage, and may develop into rain if conditions are suitable. In contrast, there are equal numbers of freezing rain and freezing drizzle events when temperatures aloft are higher than 0 deg C, consistent with a different process. In summary, approximately 45 % of the freezing precipitation cases arise from cold clouds, examples of the growth of supercooled drops by the condensation-coalescence process.

On 12 December, 1985, a chartered DC-8-63 took off from Gander Airport in Newfoundland, and crashed seconds later, killing all 256 on board, including 248 members of the 101st U.S. Army Airborne Division. After a lengthy and troubled accident investigation by the Canadian Aviation Safety Board, a report was issued which stated that the aircraft stalled after takeoff due to

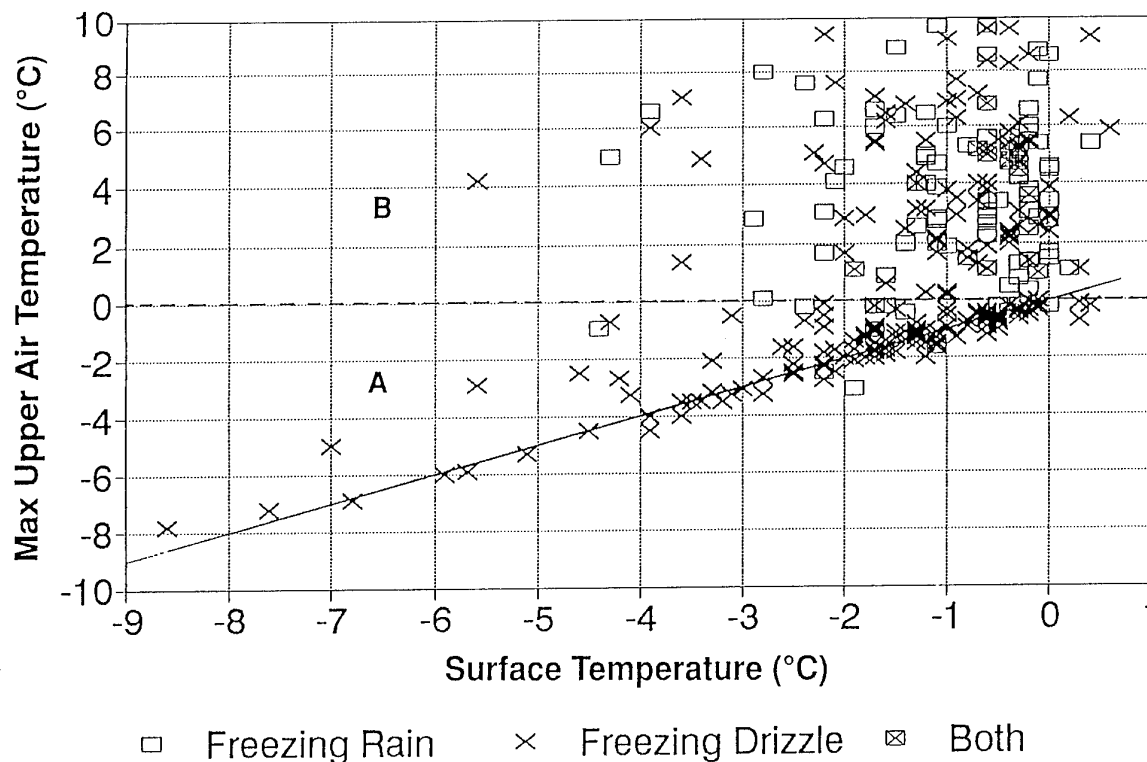


Fig. 20: Comparison of surface and maximum upper air temperatures for all freezing precipitation cases at St. Johns, 1971-1992 [Reproduced from Ref. 21, Strapp *et al*].

increased drag and reduced lift caused by ice contamination of the wing (Ref. 22). There were several dissenting members of the Board, and the ice theory was later revoked due to a lack of evidence.

Of particular interest here was the record of light freezing drizzle in the surface observations at the Gander Airport for the three consecutive hours before the disaster, but not in the observations 15 and 30 minutes before, and 15 minutes after the accident. Pilots of aircraft landing just after the accident reported very light drizzle. The DC-8 crashed shortly after takeoff, and never reached the cloud base 700 feet above ground; any ice encountered would have to have been from freezing drizzle below cloud base, either during the takeoff or on the refuelling stop (the aircraft was not de-iced prior to taxi). Given the allegations of icing being a potential factor in the accident, it is now interesting to examine the case in light of 'warm-rain' analysis presented above. There were no upper air observations right at Gander, but observations from St. John's and Stephenville two hours after the accident reveals that both soundings had no temperatures above 0 deg C. In-cloud temperatures covered the range -6 deg C to -10 deg C at St. John's and -10 deg C to -12 deg C at Stephenville (Ref. 21). Therefore, it is probable that the freezing drizzle observed at Gander near the time of the accident was produced from cold cloud through the condensation-coalescence process.

6. STRONG WINDS AND TURBULENCE

The strongest winds ever measured by the NRC Twin Otter were experienced during the CASP-I experiment. This occurred on January 28, 1986, when a strong jet stream from the south-southwest was blowing up the entire east coast of North America (Ref. 23). At 1800 GMT, a 975 mb low was situated just north of the Gulf of St. Lawrence, with a cold front trailing down across Nova Scotia. This explosively deepening storm has been further described in Reference 24.

The effect of these winds on a slow speed aircraft such as the Twin Otter is dramatically illustrated by the flight track in Figure 21. The mission was flown to the north-east (downwind) of Halifax and included a climb to 14000 ft, level flight to the turn point, then a descent to 9000 ft for most of the return leg. At 1720 GMT another climb was made to 14000 ft, followed by a descent sounding to the Shearwater Airport. The outbound leg took 26 minutes (including the climb to 14000), while the return portion took 98! The spacing of the 5-minute markers on the ground track demonstrate the wind's effect on groundspeed. Over the period marked 'A' on Fig. 21, average groundspeed at 14000 ft was 229 knots and winds averaged 178 deg at 111 knots. The peak 4-sec average wind was 132 knots. On the portion of the return leg marked 'B', average groundspeed at 9000 ft was 61 knots and the winds were measured as 190 deg at 94 knots.

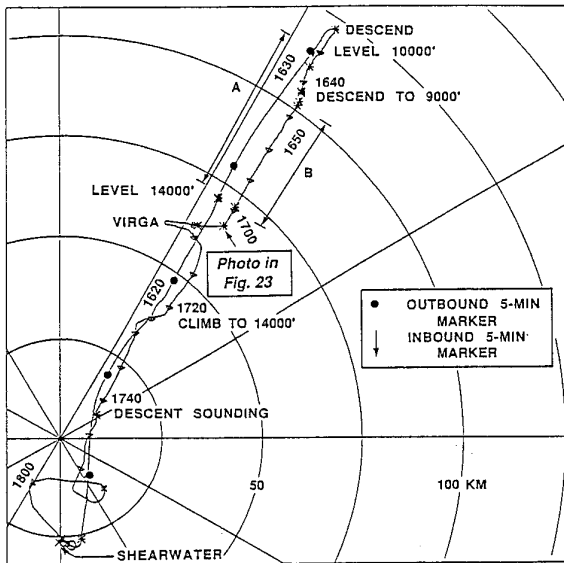


Fig. 21: Ground track for January 28, 1986, flight in high winds.

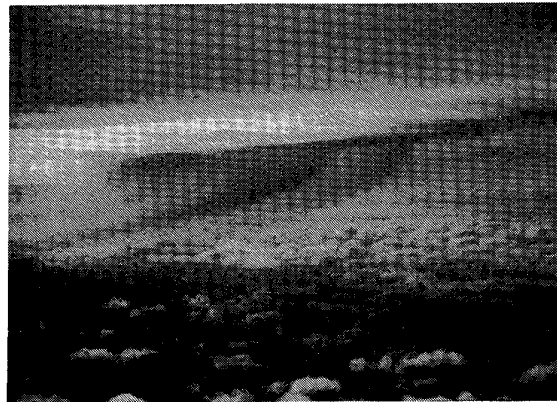


Fig. 23: Wind shear manifested by photograph of virga taken at 9000 ft at 1702 GMT on January 28, 1986. View looks crosswind to the west from the position marked on the flight track in Figure 21.

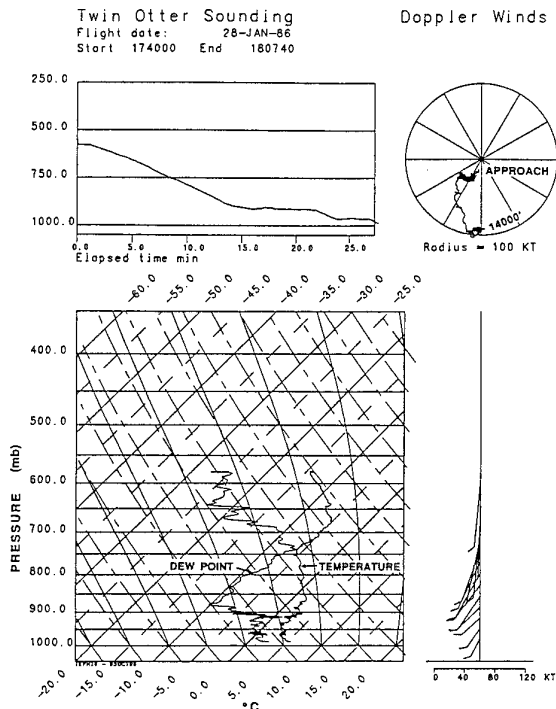


Fig. 22: Atmospheric profile recorded by Twin Otter during descent from 14000 feet and approach on January 28, 1986.

Figure 22 shows atmospheric profile data measured by the Twin Otter during the descent sounding from 14000 ft. The plotted wind vectors and the hodograph show winds at the top of the sounding were southerly near 100 knots, but southwest and considerably weaker (30 knots) below 3000 ft. Temperature and dew point show an inversion above a saturated layer at 740 mb with a stable, isothermal layer from about 740 to 670 mb (7400-10200 ft). About half of the wind shear occurred in this layer, the remainder in another stable layer near 870 mb. The upper shear layer is clearly illustrated by the virga shown in Figure 23. This photo was taken at 9000 ft looking west from the position indicated on the flight track plot (Fig. 21). This crosswind view shows precipitation from the faster moving upper air falling into the slower air below the flight level. The high winds encountered were oriented along the nearby surface cold front which was a relatively common occurrence during CASP-I (References 25 and 26).

CASP-II also had its memorable high-wind event, associated with a deepening low that became known by project personnel as 'the hurricane of the north'. After passing Newfoundland, this storm stalled over the Labrador Sea, which is common for intense east-coast storms. The satellite photo shown in Figure 24 was taken on March 2, 1992, near the time of the second Convair 580 flight that probed this storm. The interesting portion of this flight was a descent to near the sea surface in the 'eye' of the storm. The storm exhibited many of the characteristics of a hurricane, including embedded convection in the cloud wall structure and an air temperature (-2.5 deg C at 300 m altitude) very much warmer than outside the eye. Two intersecting 40-60 km

low-altitude (1000 ft) runs were made in the eye of the storm to measure the winds, turbulence and the vertical transport of heat and water vapour. Figure 25 shows the wind vectors computed from the Convair 580 data, as well as the locations of the minimum pressures measured on each of these passes, which coincide with the minimum wind speeds. The wind vectors clearly demonstrate the counter-clockwise flow near the centre of the low. On Run 1, it appears that the aircraft passed just west of the centre of the storm, measuring a minimum wind speed of 6.1 m s^{-1} ; at the east end of Run 2, the aircraft was very close to the centre of the storm, with a wind of only 2.1 m s^{-1} . The final vector shown depicts a wind from the southeast, suggesting that the aircraft flew through the centre of the low. At this point a climb was initiated, so no additional data were recorded at the 1000 ft altitude. The recorded wind data showed that the centre of this storm was relatively smooth, with an RMS vertical gust velocity of about 0.5 m s^{-1} .

The recorded data from these two passes were used to compute the minimum surface pressure at the centre of this storm. It was concluded that the sea-level pressure was 937 mb (27.67 inches of Hg), within a confidence interval of $\pm 1 \text{ mb}$. It is possible that this was a record low pressure measured in Canada or over Canadian waters.

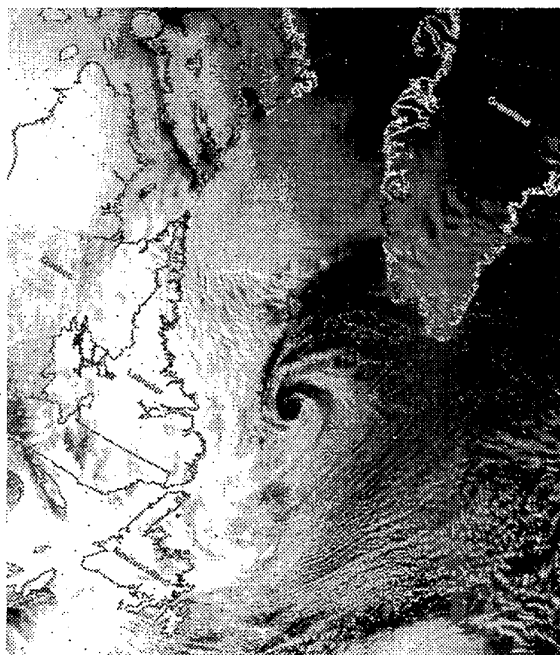


Fig. 24: Satellite photograph of storm over Labrador Sea taken at 17:11 GMT on March 2, 1992, eight minutes after aircraft completed runs shown below.

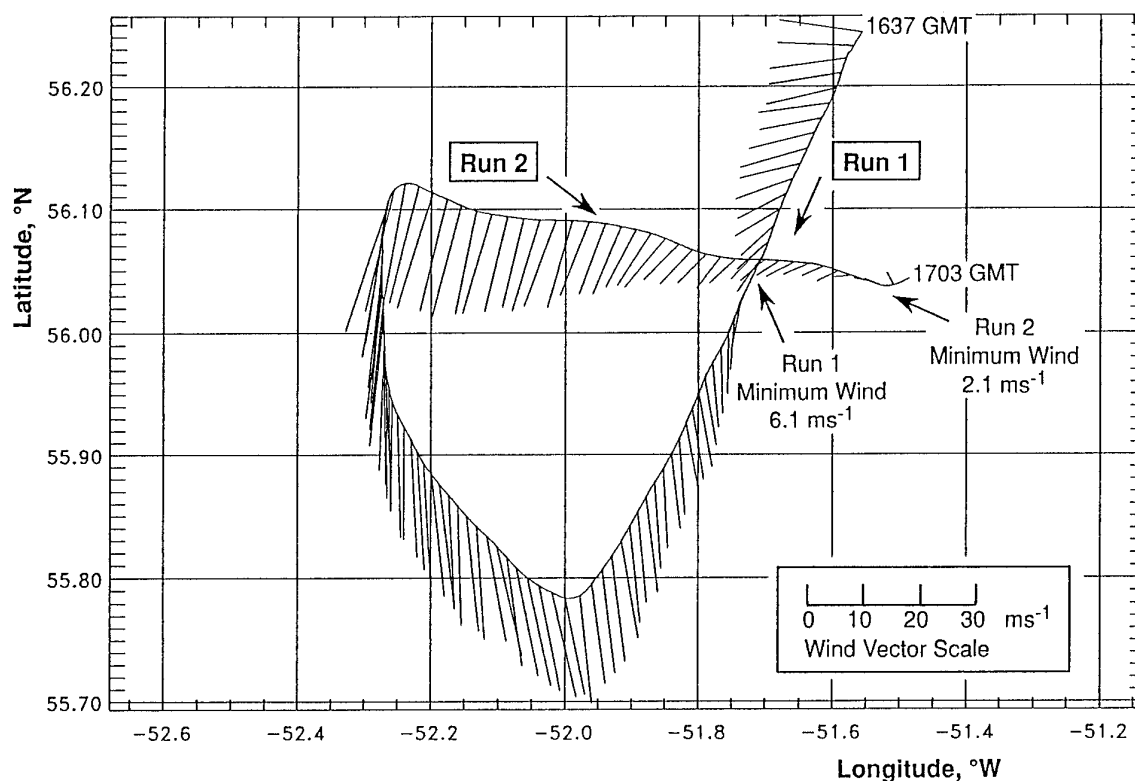


Fig. 25: Convair 580 flight track for runs at 1000 ft altitude in the clear 'eye' of the storm shown in Figure 24. Measured wind vectors are shown at a 15-second interval.

	Run 1	Run 2
Length of run , km	178	220
Altitude, m (ft)	158 (518)	153 (502)
Mean Wind: direction, deg true	255	253
speed, m s ⁻¹	27.0	28.3
(knots)	(52.5)	(55.0)
RMS wind components, m s ⁻¹ ,		
north	2.30	2.07
east	2.08	2.28
vertical	1.48	1.47
Peak vertical gusts, m s ⁻¹ , up	6.7	6.8
down	4.1	3.8
Peak vert. acceleration, G, up	0.31	0.27
down	0.29	0.28

Table 3: Summary of wind and turbulence data from low-altitude runs southeast of Newfoundland on March 1, 1992.

Another objective of CASP-II was to measure the exchange of heat and energy between the atmosphere and the ocean, and in particular, to examine the differences in these processes between open and ice-covered ocean (Ref. 27). This required flights at altitudes of 150-500 ft on long transects across the interface between the pack ice and open ocean. One such flight was flown on March 1 in the southeast quadrant of the intense storm described above. Winds averaged 55 knots and it was quite turbulent, more so over the open water than over the ice. Table 3 summarizes the wind and turbulence data recorded on two long runs on reciprocal headings along the same track. For these over-ocean runs the vertical transport of heat and momentum was surprisingly large (approximately 300 Watts m⁻² and -1.6 N m⁻² respectively).

These were unforgettable flights for us. It must be remembered, however, that over-ocean flights at these altitudes and often in these conditions are within the routine operational requirements of aircrew flying Canada's long-range patrol aircraft, fisheries survey aircraft, and Search and Rescue helicopters and fixed wing aircraft.

7. WIND SHEAR, TURBULENCE AND CROSSWIND LANDINGS

During CASP-I, there were two Twin Otter landings that were made quite difficult by crosswinds and wind shear. The first of these occurred on the January 28 flight with

the high winds discussed above. Figure 22 showed the wind profile during the descent sounding right down to the landing. This plot indicates that winds on approach were SSW at about 30 knots. The tower called the winds as 220/250 deg true at 15 to 20 knots one minute before landing on the runway which had a true heading of 265 deg (true headings are quoted here to correspond with the plots from the flight-recorded data). Perhaps due to the effects of hangars, the actual winds encountered in the landing had a considerably more southerly (crosswind) component than reported by the tower. The Twin Otter has a low wing loading (approximately 24 psf) and a very large vertical tail, which can be troublesome when landing in crosswinds in excess of 15 knots. The approach was made, therefore, with a reduced flap setting (15 deg) and a target touchdown speed of about 90 knots. After touchdown, the pilot had difficulty maintaining runway heading as the aircraft attempted to weathercock into wind. Consequently, he decelerated cautiously to maintain rudder effectiveness, and a landing ground roll almost twice the normal distance resulted. Heavy braking of the starboard mainwheel required to assist in directional control produced considerable tread wear on that tire.

Data recorded during this approach and landing are shown as analog traces in Figure 26. The bottom two traces show the headwind and crosswind components of the total wind vector. Note that the aircraft instrumentation is also capable of measuring winds during the rollout on the ground. The centreline of the heading trace represents the runway heading (265 deg true). During the approach, the wind direction averaged about 200 deg, but with a gradual shearing to a more southerly direction. The magnitude of the headwind decreased during the approach, but the crosswind remained strong, fluctuating about a 15-knot mean during the last 40 seconds before touchdown. It was quite turbulent with gusts of about 10 knots.

The heading trace on Figure 26 shows that during the approach, the aircraft was pointing to the left of the runway centreline to compensate for the wind, with correction to the runway heading at touchdown (Point 'B' on the plot). Shortly after touchdown, there was a significant increase in the crosswind to about 20 knots. The aircraft heading then began to veer to the left, reaching a heading nearly 9 deg left of the runway heading at 'A' about 11 seconds after touchdown. Recovery was then effected. Note that the time of this recovery coincides with a change in wind direction, and a resultant decrease in the crosswind component at Point 'A' on Figure 26.

The second case study involves the approach after a snow sampling flight on February 22, 1986. During this storm (Ref. 23), snowfall accumulations in some parts of Nova Scotia exceeded 75 cm, breaking 100 year records. Near the time of landing, there was a low pressure centre of 993 mb southwest of Nova Scotia. There were also some interesting precipitation patterns occurring around that time. Halifax International Airport received 30 cm of snow, while 25 km away, only a few centimetres of snow

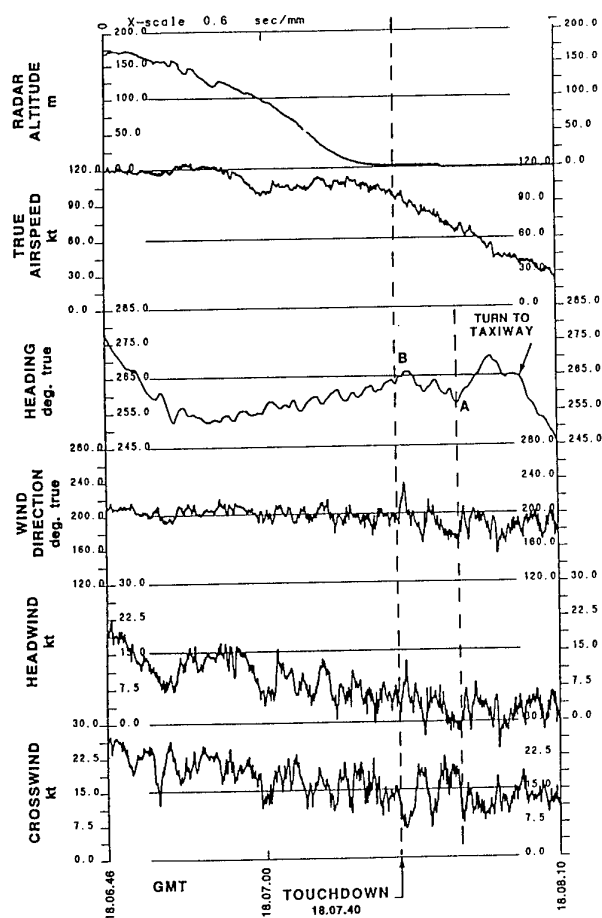


Fig. 26: Data recorded on Twin Otter crosswind landing on January 28, 1986.

fell at Shearwater before the precipitation changed to freezing rain for one hour followed by 40 mm of rain. The region of rain was over the water while the snow region was over land. There were strong directional wind shears and accelerations linked to the coastline (Ref. 24).

Figure 27 shows analog plots for this case for the same parameters (and at the same scales) as those given for the previous case in Figure 26. Runway 11 (true heading of 085 deg) was in use. Winds down to a height of about 100 m on the approach averaged 020 deg at about 27 knots. At this point, the aircraft began to encounter a directional wind shear as the wind shifted to a more northerly heading. It also became very turbulent, with gusts in excess of 15 knots for the remainder of the approach. The wind shear is further demonstrated by the bottom two traces in Figure 27, where the headwind component died off, but the mean crosswind component remained above 16 knots until the aircraft height was down to 40 m, and then decreased to about 8 knots by 5 seconds prior to touchdown. At this point ('B' in the figure), the radar altimeter height was about 5 m and the wind was an almost pure crosswind from about 340 deg true. The

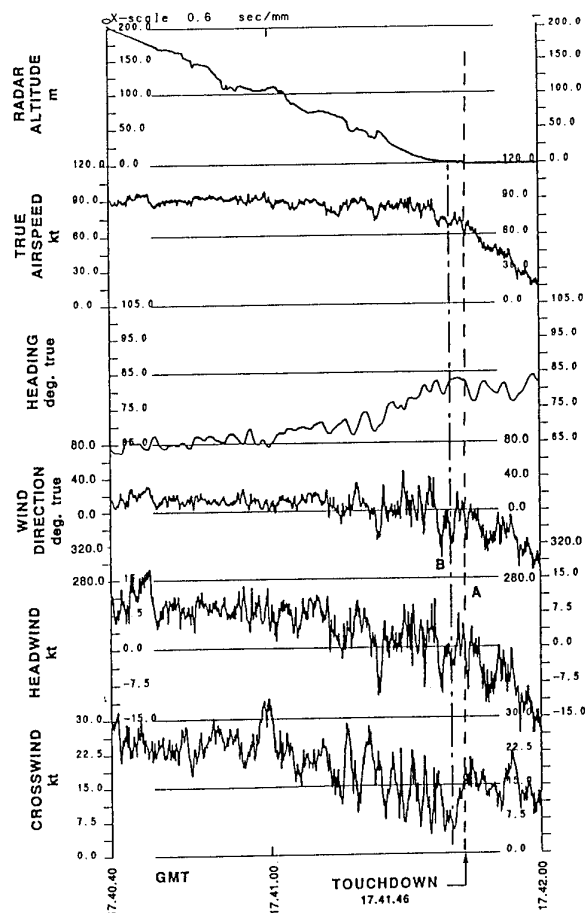


Fig. 27: Data recorded during crosswind landing on February 22, 1986.

measured wind is then seen to increase, with the crosswind component exceeding 15 knots during the touchdown and subsequent ground roll. After touchdown (at 'A'), the wind sheared further to the northwest, giving a tailwind component in addition to the substantial crosswind. Some difficulty was experienced maintaining runway heading, but the ground roll was less than half that in the case above. As can be seen in the true airspeed plot, touchdown in this case was made at near 60 knots, indicating that the normal landing flap configuration was used.

Again in this case, the winds reported by the tower were significantly different from those experienced by the pilot and recorded by the aircraft wind-measuring system. The last tower report on the voice tape quoted winds from 030 deg true at 15 knots. When the aircraft was at about 5 m altitude, the aircraft-measured wind direction was actually about 350 deg. The approach end of Runway 11 was, however, downwind of a hill and was displaced at least a half mile from the tower that measured the airfield winds. Wind shear and local topographical effects can account for the differences experienced during both these cases.

St. John's Airport is located on a rocky peninsula near the eastern-most tip of North America. The approaches to both ends of Runway 11/29 overfly rugged cliffs at the coastline of the ocean; the airport is less than 6 km from the coast, but is 137 m above sea level. Turbulence on this approach appears to be the norm, rather than the exception.

One of the principal turbulence encounters in CASP-II occurred in the early stages of a nighttime approach on February 1, 1992. St. John's was under the influence of a strong low lying just east of Nova Scotia. In the hours prior to the landing, 10 to 15 cm of snow and ice pellets had fallen in the area, under a strong and persistent northeast flow. Runway 11 was active. The Convair 580

arrived from the east, overflying the airport in a downwind leg. Winds at about 2000 ft above ground were 35 m s^{-1} (nearly 70 knots). During the procedure turn about 11 km from the threshold of Runway 11, while still at about 2000 ft altitude, the aircraft encountered moderate turbulence. Peak measured vertical gusts reached $+6.1$ and -5.3 m s^{-1} , which resulted in vertical acceleration excursions of $+0.48 \text{ G}$ up and -0.63 G down (Figure 28a). Figure 28b illustrates the power spectra for the horizontal and vertical components of the wind (RMS = 3.13 and 1.28 m s^{-1} , respectively) for the 4.5 minutes of data shown in Figure 28a. The slopes of the spectra approximate the $-5/3$ slope of the von Karman spectra, depicted by the straight line segments. The vertical gust spectrum exhibits a flattening at the lower frequencies,

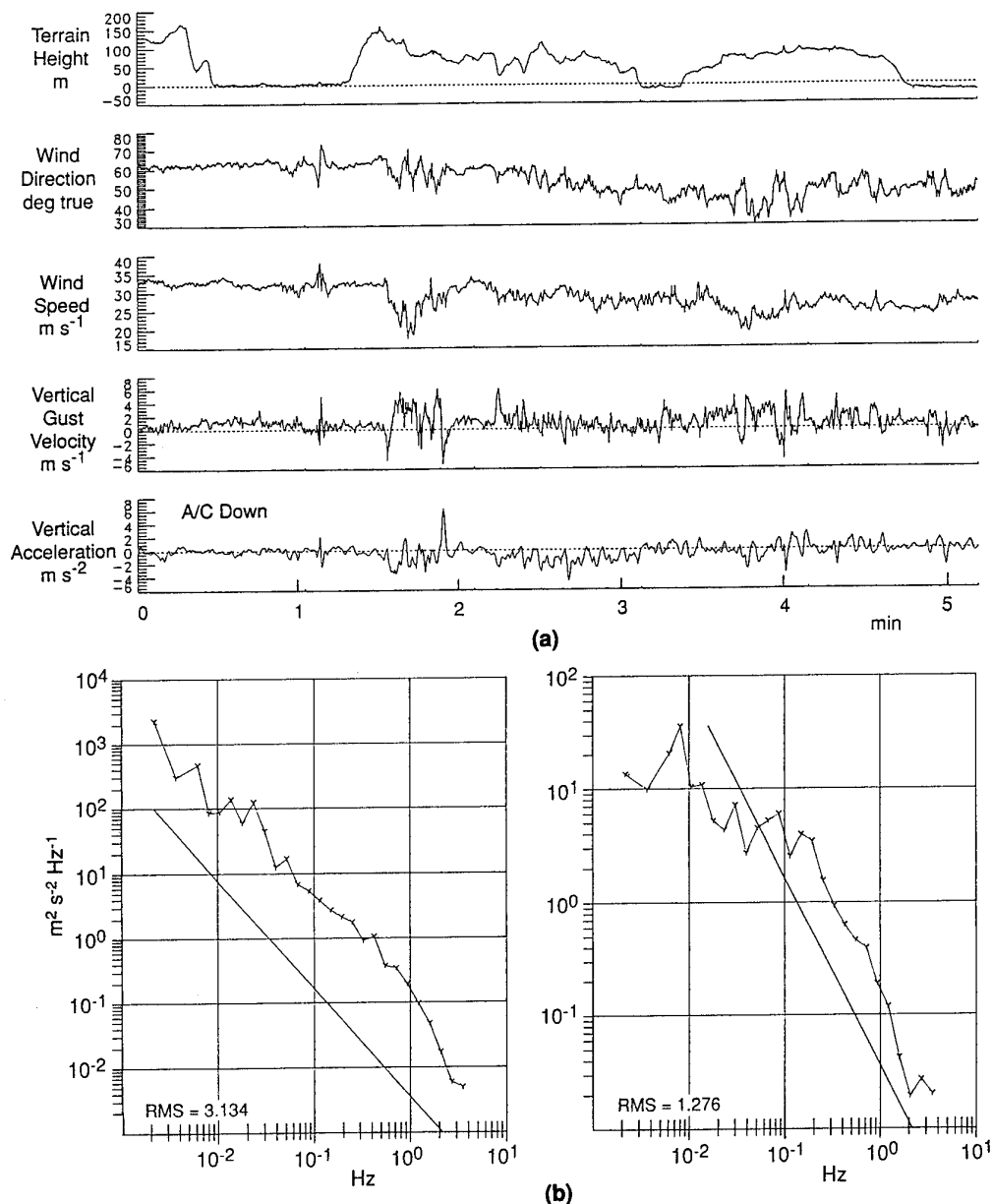


Fig. 28: Turbulence recorded by Convair 580 on Approach to St. John's, February 1, 1992.
(a) Analog traces (b) Power spectra for horizontal (left) and vertical (right) components of wind.

i.e., left of the 'knee' at 0.1 Hz, a result of the dampening of the long wavelength turbulent motion of the atmosphere due to proximity to the ground.

The top trace in Fig. 28a shows terrain height, and reveals that this turbulence event was orographically produced over a rugged island (Bell Island in Conception Bay), which has cliffs rising to about 150 m (500 ft) above the water. Turbulence for the remainder of the approach tended to be light, despite the strong winds which decreased to about 10 m s^{-1} at touch down.

8. ELECTRIFICATION

To investigate the possibility of high electric fields in Atlantic storms and study the processes leading to their formation, electric field measurements were made in CASP-II in a joint study with New Mexico Tech. Three electric field mills were mounted in the pods at each wing tip of the Convair 580 (Fig. 3) and their recorded signals were processed to derive a three-dimensional representation of the electric field within the storm clouds. Significant electric fields were measured on only one flight in CASP-II, but no lightning was experienced.

At St. John's, lightning is reported in the regular hourly observations less than once per winter (December-March) on average. The same could be said for Toronto and Montreal-Dorval for the three-month period December to February. Lightning does not appear to be a problem in eastern Canadian winter storms. However, off-shore over the Gulf Stream, more lightning could be encountered and satellite photographs tend to show more convection in this area.

9. NEW TECHNOLOGIES AND THE FUTURE

9.1 Hardware

New sophisticated pieces of hardware are rapidly being developed to assist the aviation industry to avoid and better handle severe weather. It would be impossible to mention all the hardware, so only a few examples will be given in this section. The prime example is the development and deployment of the Terminal Doppler Weather Radar (TDWR) and the enhanced Low Level Wind Shear Alert System (LLWAS) in the United States, which will help detect and warn pilots of hazardous wind shear events (Ref. 28). Microwave radiometers can possibly detect regions of supercooled liquid water that might lead to hazardous in-flight icing, and these have been evaluated in Canadian east coast storms (Ref. 29). New satellite sensors, such as the DMSP-SSM/I (Defence Meteorological Satellite Program - Special Sensor Microwave/Imager), might also lead to better detection of these supercooled cloud regions, although further evaluations of the techniques are required (Ref. 30). Sensors placed within aircraft wings can employ electric field measurements to detect the presence of ice or de-icing

fluid (Refs. 31 and 32) on the wing surface; one such system is currently being evaluated on an Air Atlantic BAe-146. New light-weight de-icing 'fabrics and materials' are being developed to help remove ice on aircraft structures (Ref. 33).

The use of advanced technology in the cockpit is becoming increasingly important as pilots are required to carry out mission-oriented tasks in addition to those required for flying and navigation. Advances in the technologies of the cockpit may provide significant reductions in pilot workload as well as increased pilot situational awareness in degraded visibility. In recognition of this concept, the Flight Research Laboratory of NRC has a number of new and ongoing research projects on cockpit technology issues, including helmet-mounted displays, advanced 'head down' displays, and speech recognition in the cockpit environment. These systems can be tested in a real flight environment on the NRC Airborne Simulator (Bell 205) or Advanced Systems Research Aircraft (Bell 412).

9.2 Weather Forecasting

There are several projects now being conducted in Canada and the U.S. with the purpose of developing better forecasts of winter storm conditions. The U.S. Winter and Icing Storms Project (WISP) has concentrated on weather in the lee of the Rockies (Ref. 34). The Canadian studies, as discussed in this paper, are concentrating on east coast winter storms. However, in September and October, 1994, the NRC and AES will once again cooperate in a major field project, this time on Canada's Arctic Coast in the Beaufort and Arctic Storms Experiment (BASE). The NRC Convair 580 will participate in this experiment, instrumented similarly to its configuration in CASP-II. This data set will provide interesting comparisons to the east coast observations.

A significant finding from CASP-II was the high incidence of freezing drizzle resulting from the condensation-coalescence process (Ref. 21). At an aircraft icing workshop in Ottawa in 1993, pilots of helicopters and fixed wing aircraft commented that freezing drizzle was very common along Canada's east coast, and that it was difficult to avoid. Consequently, a field project will be funded by Canada's Search and Rescue Secretariat which will focus on the microphysics of freezing drizzle formation, with the ultimate objective of reducing the danger to aircraft through either better forecasts or avoidance based on a better physical understanding. This project is planned for March 1995, with the instrumented Convair 580 operating again from Newfoundland.

The work reported earlier in this paper, to better define in-flight icing conditions, is being implemented into Canadian operational weather forecasting models. However, further improvements are required to better forecast the occurrence of freezing precipitation, and the field project mentioned above will help provide and verify some new forecast algorithms.

The Dryden Commission Implementation Project (DCIP) of Transport Canada was set up following the crash of the Fokker-28 during a snowstorm in Dryden, Ontario in March, 1989. DCIP is funding many studies on aircraft icing, including a study to provide better weather information to pilots, who are responsible for ensuring that their aircraft are properly de-iced before take-off. This study will combine new ground-based and remote sensing devices with the latest weather information, and an improved short term forecast of weather conditions. Pilots will then be able to determine whether to de-ice or anti-ice their aircraft with the proper fluid. If an anti-ice fluid is used, then some estimate will be provided of the effective hold-over time of that fluid for the conditions prior to take-off. An operational test of a prototype nowcasting system is scheduled to be conducted during the winter of 94/95.

Techniques are now being developed to put sensors onboard commercial aircraft which can automatically transmit data directly to meteorological data banks, to be used in initializing numerical weather forecasting models (eg., Commercial Aircraft Sensing Humidity, CASH, Ref. 35). This should significantly increase the accuracy of weather forecasts. However, reports from aircraft pilots also provide invaluable assistance to meteorologists preparing their next forecast, or to researchers trying to develop new forecasting techniques. Unfortunately, few pilot reports are made, and those which are made seldom are transferred to meteorologists and researchers. This was a problem during CASP-II. Although many aircraft were operating in the area during the research project, and efforts were made with commercial operators and Transport Canada to get pilot reports of icing, very few were received. Hopefully, ways can be found to overcome this problem.

10. CONCLUDING REMARKS

With the exception of vortex wakes and lightning, research flights in the Canadian Atlantic Storms Program exposed the NRC Twin Otter and Convair aircraft and their crews to most of the adverse environmental conditions that are the subject of this lecture series. By providing detailed case studies of incidents of in-flight and ground icing, high winds, turbulence and wind shear, we have attempted to give a balanced presentation of both the aeronautical hazards and the meteorological conditions associated with flight in Canadian winter storms. We hope that these provide an effective introduction to the lectures to follow.

11. ACKNOWLEDGEMENTS

The CASP field projects were supported by the Federal Panel on Energy Research and Development (PERD), the Atmospheric Environment Service of Environment Canada and the National Research Council of Canada. The aircraft icing research in CASP-II was funded by the National Search and Rescue Secretariat, the Canadian Department of National Defence, the Boeing Commercial Airplane Group and Airbus Industrie.

The authors would also like to thank Stewart Cober, Walter Strapp and Andre Tremblay of the AES and Myron Oleskiw of NRC for their significant contributions to this paper.

12. REFERENCES

1. Stewart, R.E., Shaw R.W., and Isaac, G.A., "Canadian Atlantic Storms Program: The Meteorological Field Project", Bulletin of the American Meteorological Society, Vol. 68, No. 4, April 1987, pp. 338-345.
2. MacPherson, J.I., "Wind and Flux Calculations on the NAE Twin Otter", Laboratory Technical Report LTR-FR-109, National Research Council Canada, Ottawa, January, 1990, 38 pages.
3. MacPherson, J.I., "Use of a Wing-mounted Airflow Pod for Airborne Wind and Flux Measurement", Proceedings of the Eighth Symposium on Meteorological Observations and Instrumentation, Anaheim, January 1993, pp. 169-174.
4. Cober, S.G., Isaac, G.A., and Strapp, J.W., "Aircraft Icing Measurements in East Coast Winter Storms", Accepted for publication in the Journal of Applied Meteorology.
5. Stuart, R.A., "A Climatology of Low Ceiling Height and Visibility Conditions in Newfoundland", Weather Research House, Downsview, Ontario, March, 1992, 48 pages.
6. Transportation Safety Board of Canada, "Report of a Safety Study on VFR Flight into Adverse Weather", Report No. 90-SP002, Ottawa, Nov. 13, 1990.
7. Mikkelsen, K.L., McKnight, R.C., and Ranaudo, R.J., "Icing Flight Research: Aerodynamic Effects of Ice and Ice Shape Documentation with Stereo Photography", NASA TM-86906 and AIAA-85-0468, January 1985.
8. Ranaudo, R.J., Mikkelsen, K.L., McKnight, R.C., Ide, R.F., and Reehorst, A.L., "The Measurement of Aircraft Performance and Stability and Control After Flight Through Natural Icing Conditions", NASA TM-87265 and AIAA-86-9758, April 1986.

9. Ranaudo, R.J., Mikkelsen, K.L., McKnight, R.C., and Perkins, P.J., "Performance Degradation of a Typical Twin Engine Commuter Type Aircraft in Measured Natural Icing Conditions", NASA TM-83564 and AIAA-84-0179, January 1984.
10. Federal Aviation Agency, "Airworthiness Standards: Transport Category Airplanes", FAA Part 25, Section 25.1419 and Appendix C, 1980.
11. Patnoe, M.W., Tank, W.G., Isaac, G.A., Cober, S.G., and Strapp, J.W., "Airplane Icing Research at the Boeing Company: Participation in the Canadian Atlantic Storms Program", Proceedings of the Fifth International Conference on Aviation Weather Systems, 1993, American Meteorological Society, Boston, pp. 432-434.
12. Newton, D.W., "An Integrated Approach to the Problem of Aircraft Icing", *Journal of Aircraft*, 15, 1978, pp. 374-380.
13. Sand, W.R., Cooper, W.A., Politovich, M.K., and Veal, D.L., "Icing Conditions Encountered by a Research Aircraft", *Journal of Climate and Applied Meteorology*, 23, 1984, pp. 1427-1440.
14. Isaac, G.A., "Microphysical Characteristics of Canadian Atlantic Storms", *Atmospheric Research*, 26, 1991, pp. 339-360.
15. Cober S.G., Isaac, G.A., and Tremblay, A., "Verification of the CMC Aviation Forecasts with In-Situ Aircraft Measurements", draft manuscript.
16. Tremblay, A., Glazer, A., Szyrmer, W., Isaac, G.A., and Zawadzki, I., "On the Forecasting of Supercooled Clouds", Submitted to *Monthly Weather Review*.
17. National Transportation Safety Board, "Aircraft Accident Report: Takeoff Stall in Icing Conditions, USAIR Flight 405, Fokker F-28, N485US, LaGuardia Airport, Flushing, New York, March 22, 1992", NTSB AAR-93/02, Feb. 17, 1993.
18. National Transportation Safety Board, "Aircraft Accident Report: Air Florida Inc. Boeing 737-222, N62AF, Collision with 14th Street Bridge, Near Washington National Airport, Washington, D.C., January 13, 1982", NTSB AAR-82-8, August 10, 1982.
19. Louchez, P.R., Laforte, J.L., Bouchard, G., and Farzaneh, M., "Facility for Evaluation of Aircraft Ground De/Anti-icing Products", Transcriptions of the SAE Aircraft Ground Deicing Conference, Salt Lake City, Utah, June 15-17, 1993, pp. 61-69.
20. Society of Automotive Engineers, "SAE ARP 4737", (draft).
21. Strapp J.W., Stuart, R.A., and Isaac, G.A., "On the Development of Freezing Precipitation in Newfoundland", Proceedings of the Rotary-Wing Aircraft In-flight Icing/De-icing Workshop, Ottawa, June 1993, National Research Council of Canada and Dept. of National Defence.
22. Canadian Aviation Safety Board, "Aviation Occurrence Report: Arrow Air Inc. Douglas DC-8-63 N950JW, Gander International Airport, Newfoundland, 12 December 1985", Report No. 85-H50902.
23. Strapp, J.W., Power, J., and MacDonald, K., "CASP Field Summary", Atmospheric Environment Service Internal Report.
24. Stewart, R.E. and Donaldson, N.R., "On the Nature of Rapidly Deepening Canadian East Coast Storms", *Atmosphere-Ocean*, Vol. 27, pp. 87-107.
25. Stewart, R.E., Lin, C.A., and Macpherson, S.M., "The Structure of a Winter Storm Producing Heavy Precipitation over Nova Scotia", *Monthly Weather Review*, Vol. 118, 1990, pp. 411-426.
26. Stewart, R.E. and Macpherson, S.M., "Winter Storm Structure and Melting-induced Circulations", *Atmosphere-Ocean*, Vol. 27, pp. 5-23.
27. Smith, P.C., Tang, C.L., MacPherson, J.I., and McKenna, R.F., "Investigating the Marginal Ice Zone on the Newfoundland Shelf", *EOS Transactions, American Geophysical Union*, Vol. 75, Number 6, Feb. 8, 1994. pp. 57, 60-62.
28. Federal Aviation Agency, "FAA Aviation Weather Development Program: Integrated Terminal Weather System (ITWS)", FAA ARD-80, 2 August 1993.
29. Blaskovic, M., Sheppard, B.E., Rogers, R.R., and Box, T.C., "Radiometric Observations during the Canadian Atlantic Storms Program", *Journal of Atmospheric and Oceanic Technology*, Vol. 6, No. 1, Feb. 1989, 109-120.
30. Curry, J.A. and Liu, G., "Assessment of Aircraft Icing Potential Using Satellite Data", *J. Appl. Met.*, 31, 1992, pp. 605-621.
31. Inkpen, S., Brobeck, C., and Nolan, C., "Development of a Sensor for the Detection of Aircraft Wing Contaminants", Paper AIAA 92-0300 of the Proceedings of the 30th Aerospace Sciences Meeting, American Inst. of Aeronautics and Astronautics, Reno, January, 1992.
32. Oleskiw, M.M., "Laboratory Evaluation of a Sensor for the Detection of Aircraft Wing Contaminants", Paper AIAA 92-0301 of the Proceedings of the 30th Aerospace Sciences Meeting, American Inst. of Aeronautics and Astronautics, Reno, January, 1992.
33. Technology Dynamics Group Inc., "Further Investigations into the Capabilities of a Conductive Fiber Heater for Use in Electro-Thermal Aircraft Ice Protection Systems", Document E91-014, 13 April, 1992.
34. Rasmussen, R., Polotovich, M., Marwitz, J., Sand, W., McGinley, J., Smart, J., Pielke, R., Rutledge, S., Wesley, D., Stossmeister, G., Bernstein, B., Elmore, K., Powell, N., Westwater, E., Stankov, B., and Burrows, D., "Winter Icing and Storms Project (WISP)", *Bulletin of the American Meteorological Society*, Vol. 73, No. 7, pp. 951-974.
35. Fleming, R.J. and Hills, A.J., "Humidity Profiles via Commercial Aircraft", Proceedings of the Eighth Symposium on Meteorological Observations and Instrumentation, American Meteorological Society, Anaheim, January 1993, pp. J125-J129.

ESD AND LIGHTNING INTERACTIONS ON AIRCRAFT

by J.L. Boulay

Office National d'Etudes et de Recherches Aéronautiques
BP 72, 92322 CHÂTILLON CEDEX, FRANCE

Summary

Under certain adverse conditions, particularly inside or in the vicinity of clouds, aircraft may be affected by two different electric phenomena: electrostatic discharges and lightning discharges.

When electrostatic charges accumulate on an aircraft structure, electric discharges occur. These discharges generate RF interference that severely impairs the operation of onboard radio navigation and communication equipment. Sometimes energetic discharges have direct effects on structural components like radomes, windshields and canopies.

Lightning discharges may have a very powerful and dangerous effects on an aircraft in flight. The electromagnetic coupling of any repetitive current pulses through the airframe can upset or deteriorate airborne equipment; and under certain circumstances, lightning flashes may also cause serious direct damage to structural components.

1. Introduction

When an aircraft flies nearby or through clouds, it is usually affected by external phenomena associated with the dynamic, the temperature distribution, or the microphysical structure of the surrounding environment. Some of these external phenomena are relatively common, such as turbulence, icing and moderate rain. Others are less frequent but more dangerous, such as wind shear, heavy rain, hail impacts. These phenomena are presented in the different lectures given during the present program.

Two other phenomena involving electrical or electromagnetic processes may also have consequences on aircraft: the electrostatic discharges (ESD) and the lightning discharges. The former are relatively frequent in a cloud environment, but they are not really dangerous except under some very specific conditions. The latter are not so common but are more severe and may sometimes lead to catastrophic accidents.

The origins of these electromagnetic phenomena are included in the simultaneous presence of cloud particles (droplets or ice crystals) and opposing wind velocities.

It is known that, in order for a charging mechanism to exist, different types of particles must

come into contact. Two such mechanisms are then possible: the aircraft impacts the particles at flight speed, creating charges of one polarity on the structure and leaving charges of the other polarity in the cloud. Those on the aircraft increase the aircraft potential with respect to its surroundings; and if this potential is sufficiently high, ESD may occur. In the second situation, we have an updraft-downdraft structure locally within the cloud. Particles of different types collide, creating charges of one polarity on a given type of particle and of the opposite polarity on the other type. As the wind acts differently on the two types of particles, the positive and negative charges become separated. This separation increases the local electric field. If this field reaches a critical value, a natural lightning discharge can be triggered. Propagating over very long distances, the lightning discharge may interact with an aircraft flying in the vicinity.

ESD discharges on aircraft essentially disturb radio communication and radio navigation equipment. Under certain conditions, strong ESD discharges may occur on dielectric frontal surfaces of the airframe, such as radomes, windshields and antenna covers, leading to more severe effects and sometimes to the destruction of the equipment. The aircraft's ESD protection is relatively simple in principle: static dischargers or antistatic treatments on nonconductive surfaces considerably reduces ESD interference. But applying these protection systems is more delicate in practice. New optimized methods and new controlling equipment have been developed in this domain over recent years and their applications are now just starting.

Lightning discharges, depending on their current amplitude, are generally considered as more severe than ESD. The discharge current passing through much of the airframe gives rise to strong electromagnetic fields which can penetrate the airframe skin by diffusion or by aperture coupling. The resulting fields inside the airframe may be sufficient to yield strong current pulses at the inputs of sensitive internal equipment. These pulses may create disturbances and equipment failures. When the lightning phenomena is very severe, direct current effects may leave holes or even completely destroy external systems (radomes, antenna covers, ...).

Lightning protection consists mainly of external treatments, cable shielding, protection devices at equipment inputs, lightning diverters and so on. Controls

and certification tests for the lightning protection of an aircraft is always a very important and costly operation.

In this paper, we focus on very recent data obtained in flight with instrumented aircraft. These in-flight experiments have been going on since 1980, generating a considerable amount of data of help in improving our understanding of the physical phenomena of ESD and lightning-aircraft interactions. Aircraft instrumentation is briefly presented along with an analysis of the most pertinent in-flight observations.

2. Electrical and Electromagnetic effects on an Aircraft

2.1 Electrostatic disturbances [1]

Electrostatic interference is very frequent on aircraft flying in the vicinity of or through different types of clouds, and also in environments of sand or dust particles. Due to charging processes on the airframe, the aircraft potential increases rapidly, leading to corona discharges on sharp points of the structure. These corona discharges develop a train of very rapid current pulses. These cover a broad frequency spectrum. They vary the charge distribution on the airframe and, by direct coupling, set up powerful interference in the different radio navigation and communication antenna. Sometimes, very severe electrostatic effects occur on the vehicle, due to the triggering of surface discharges on dielectric parts of the structure, as may occur on radomes, windshields, antenna covers, and also on nonconductive skin panels impacted by charged particles. In these cases, severe interference is observed on radio equipment; but direct effects may also occur, such as destruction of radomes or windshield components, or destruction of de-icing systems, or receiving equipment. In the following section, we will present the main processes associated with electrostatic disturbances.

2.1.1. Charging Mechanisms

Three main mechanisms may charge an aircraft in flight: triboelectricity, field charging, and engine charging.

- ① Triboelectricity is the most efficient process affecting the electrostatic charging of an aircraft. This effect results from the contact of particles (dust, ice or snow crystals) with the aircraft skin. In the case of ice particles, the charge left on the aircraft is negative. The theory of this phenomenon has been developed by Harper [2] and confirmed by flight results obtained by Tanner [3] and Nanevicz [4]. The intensity of the charging current depends on the size of the impacting particles and on the speed with which the contact and the rupture occur.
- ② When an aircraft approaches an electrified cloud, it is immersed in an intense electric field. Electric

charges are therefore displaced by induction over the aircraft structure. Locally, the normal field may increase enough to produce electrical breakdown of the air, and a partial discharge is then established, transferring a current from the aircraft to the atmosphere. Due to lack of symmetry in the induction phenomena, it is very unlikely that a discharge of opposite sign and same intensity will be generated at the same time on any other point of the structure. Consequently, this mechanism induces a change in the self charge and in the potential of the aircraft. This becomes very intense in the vicinity of an active electrified cloud region, and may lead to the triggering of a lightning discharge from the aircraft. This point will be explained in a next section.

- ③ It has been shown experimentally that certain engines eject positive ions into the atmosphere. Two assumptions have been proposed to explain this.
 - ⇒ The electrons generated inside the combustion chamber diffuse more rapidly than positive ions towards the conductive walls of the chamber [5], and the positive ions are then ejected in the jet stream.
 - ⇒ Solid particles with a non-zero charge are carried out with the jet. This has been checked experimentally in laboratory tests on engines showing that adding a suitable particulate (Al_2O_3 for example) increases the ejected current. In modern aircraft, engines ejected currents between 50 and 400 μA have been obtained [6].

2.1.2. Discharging Mechanisms

The above mentioned charging currents increase the electrostatic potential of the aircraft with respect to the environment, while the capacitance of the vehicle remains constant in flight. As this potential cannot increase indefinitely, breakdown phenomena occur and reject charges into the atmosphere.

Two types of discharges can occur:

- ⇒ corona discharges between the vehicle and the atmosphere,
- ⇒ surface discharges between different portions of the aircraft structure.

If the vehicle capacitance C is assumed to be constant, the variation of the aircraft potential V is given by:

$$C \frac{dV}{dt} = i_c - i_d(V). \quad (1)$$

i_c is the total charging current, which does not depend on V , and i_d the total discharging current, which depends on V .

An equilibrium aircraft potential is obtained at $V = V_e$ when the following equation is satisfied:

$$i_c = \sum i_d(V_e) \quad (2)$$

Obviously, V_e depends on i_c and on the aircraft geometry.

2.1.3. Electrostatic Interference

① Radioelectric noise

As the aircraft potential becomes more and more negative, negative corona discharges are created on certain edges of the airframe. We have already mentioned that a corona current is a series of pulses having a very short rise time (5 ns) and a peak amplitude of about 10 mA; the repetition rate of the pulses is a function of the local field, and determines the mean current value. The characteristics of a typical negative corona discharge are given in the two pictures of figure 1. Picture **a** shows an isolated corona pulse and **b** the pulse repetition for a mean current of 70 μ A.

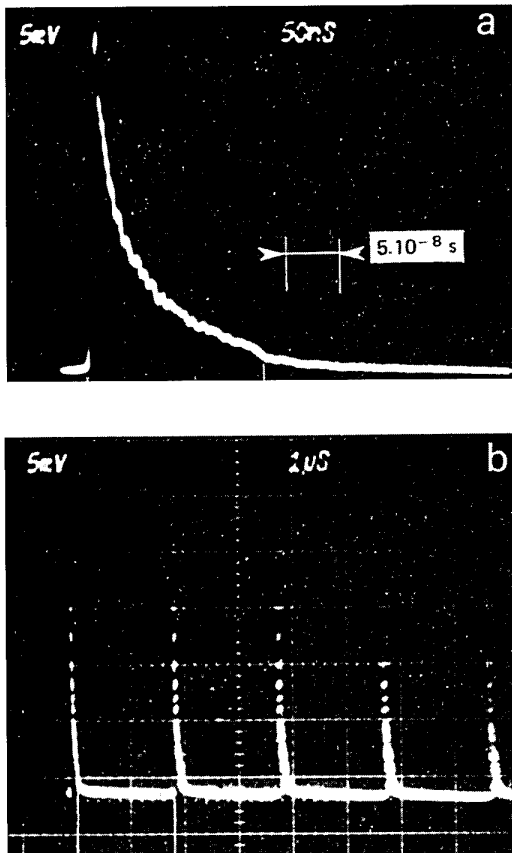


Fig. 1 - Current pulses associated with corona discharge ($i = 70 \mu$ A).

The electromagnetic radiation generated by these pulses may be capacitively coupled to an antenna and thereby disturb the avionic equipment.

The interference evaluated in term of short-circuit current $i_c(\omega)$ on a given antenna has been defined by Tanner [3] and may be given by the relation:

$$i_{cc}(\omega) = \frac{1}{V(\omega)} \int_T \vec{E}_M(\omega) \cdot \vec{J}_M(\omega) dt \quad (3)$$

- $\vec{J}_M(\omega)$ is the corona discharge current density at a local point M,
- $\vec{E}_M(\omega)$ is the radio field at the same point M, when a voltage $V(\omega)$ is applied at the antenna extremities (see [1]),
- T is the domain affected by the corona discharge.

The preceding relation can be written on the form:

$$i_{cc}(\omega) = \Phi_L(\omega) \cdot H_{LM}(\omega) \quad (4)$$

where:

$$\Phi_L(\omega) = \frac{E_L(\omega)}{V(\omega)} \quad (5)$$

is the coupling function representing the radio transmission between the antenna and a given point L on the structure.

$H_{LM}(\omega)$ is an independent function characterizing the properties of the noise source at the same point L and given by:

$$H_{LM}(\omega) = \int_T \frac{\vec{E}_M(\omega)}{E_L(\omega)} \cdot \vec{J}_M(\omega) dT \quad (6)$$

The interference $i_{cc}(\omega)$ can be reduced using static dischargers installed on the aircraft structure. The role of these dischargers (see equation 4) is mainly to:

- ⇒ reduce the $\Phi_L(\omega)$ term by a special arrangement of the discharge process versus the aircraft geometry;
- ⇒ to reduce the $H_{LM}(\omega)$ term by changing the nature of the corona discharge.

A detailed analysis of a discharger optimization is out of the scope of this paper and can be found in [1].

② Direct effects [7]

Another major source of interference is when a surface discharge occurs on a charged dielectric portion of an impacted surface, or when an arc is established between two unconnected conductive elements of the airframe.

In the first of these two cases (see Fig. 2), the discharge is formed by a bright tree-like arc channel covering the entire dielectric surface and neutralizing the initial charges deposited (picture **a**). The electrical discharge is characterized by a current pulse with a peak amplitude of about 300 A and a rise time of several nanoseconds (picture **b**). This pulse may generate severe

interference in antenna equipment in the vicinity of the discharge and may also result in direct damages like perforations or delaminations of composite materials.

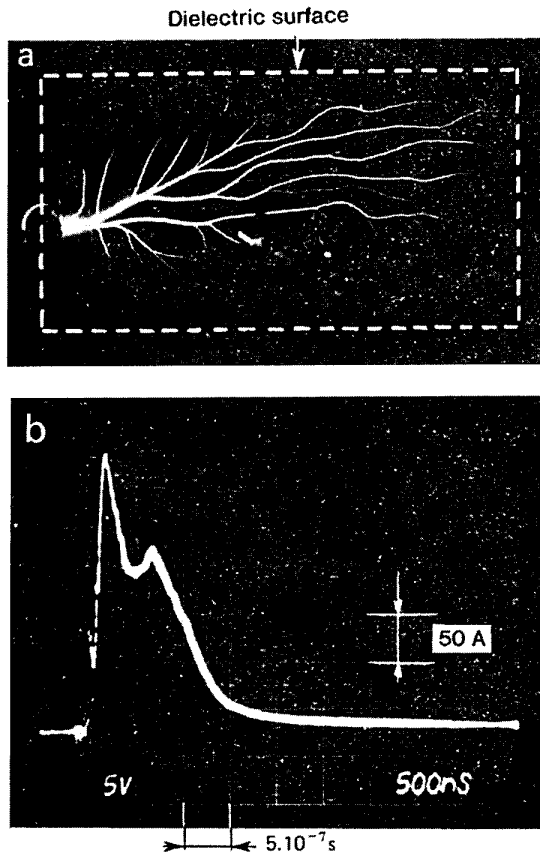


Fig. 2 - Surface discharge on a dielectric material.

In the second case of an arc between two unconnected elements, the potential difference between the two electrically isolated panels may be sufficient to create an electric arc that will also generate severe electromagnetic interference in radio equipment and direct effects on materials.

Of course, surface discharges and arcs have to be eliminated. Two successive electrostatic protections must be applied to do this. First, all the impacted dielectric surfaces of the aircraft are covered by an antistatic treatment. Second, all the isolated conductive panels or antistatic treatments are properly bonded to the airframe.

2.2. Lightning Interactions

2.2.1. Nature of the Problem [9, 10]

Lightning is one of the most severe and most unknown electromagnetic hazards to which aircraft may be exposed. Until now, aircraft were protected against the direct effects of a lightning flash, and more particularly certain essential components like radomes,

antenna covers, wing extremities, and fuel tanks, which may be directly impacted by the lightning arc. Because of the conductive properties of the essential portions of the airframe and the relatively low susceptibility of electronic equipment, the indirect effects of lightning were not considered to be as dangerous as the direct effects.

With today's new structural materials, like composites and epoxy panels, combined with the increasing role of the electronics and the greater susceptibility of electronic components, aircraft engineers now have to consider the electromagnetic effects of the lightning.

Global statistics show that, on the average, a commercial aircraft is struck by lightning every two thousand flight hours, which corresponds to approximatively one lightning flash per year per aircraft. This ratio is not so high and it is due to the fact that pilots try to avoid entering or even flying nearby thunderstorms. But in the future, the increase of airplane traffic and a major intensification of flights around airports may greatly affect lightning statistics.

When these new considerations began appearing ten years ago, most experts arrived at the conclusion that only a few characteristics concerning lightning interactions on aircraft were known. Most of the knowledge was in fact coming from actual lightning stroke data and analysis of ground observations by different laboratories. No measurements were available for aircraft struck by lightning.

This eventually led the lightning research community to decide in favor of in-flight research. From 1980 to 1988, three main experiments were carried out:

- ⇒ two were undertaken in the USA by NASA [10, 11] and the USAF [12-14];
- ⇒ the third was conducted in France under the auspices of the French DGA (General Delegation for Armament) [15, 16].

Briefly speaking, these three programs yielded essentially the same general results, and the data is very important because, after in-flight result analysis, our view of the lightning interactions with an aircraft have changed completely. In particular, we now know that the lightning flashes are usually triggered by the aircraft itself. The idea of an aircraft intercepting a pre-initiated natural discharge is not completely rejected, but its probability of occurrence is very low.

New characteristics of the lightning threat have been found, in particular the multiple burst phenomena at the beginning of the event and the multiple stroke

mechanism during the permanent phase of the lightning flash.

Specific phenomena like the sweeping mechanism have been validated in flight and observed by accurate instrumentation.

A general survey on these in-flight experiments is presented in chapter 4.

2.2.2. Electromagnetic Disturbances due to Lightning

Before going into the detail of the physical processes responsible for lightning interactions with aircraft, it is important to have a synthetic view of the different steps occurring between the incident source and the final disturbance on a given piece of airborne equipment.

These different steps are summarized by the sequence of figure 3.

① Lightning Source

After the initial attachment phase, the threat can be simplified by considering the interactions of two lightning channels connecting the aircraft with two different regions of the environment. These two channels act as quasi-conductive lines carrying discharge currents which may be permanent (part of the time) or pulsed (several sequences of recurrent current pulses).

The lightning source is defined by the time variations of the current waveform as rise time, peak value, derivative parameters di/dt , action integral, current pulses rate, period between pulses, and so forth.

For electromagnetic considerations, lightning channels have to be characterized by their geometry, conductivity, temperature, internal fields, and other parameters.

② External Response

The discharge current passing through the aircraft determines the general distribution of the electromagnetic field on the structure. This distribution is the combination of the two varying components E_e and H_e of the electromagnetic field: E_e is the electrical component normal to the surface and H_e is the tangential magnetic component. Of course, the external response cannot be obtained analytically; but the problem can be solved by numerical codes [17-20] solving the Maxwell equations in three dimensions.

③ Electromagnetic Coupling Through the Structure

Electromagnetic energy can be transferred inside by various mechanisms, such as:

- ⇒ diffusion of the current. This is very significant in the case of carbon composite materials, or generally for non-conductive panels.
- ⇒ direct coupling through aperture. This second process is at work in the case of dielectric portions of the airframe incorporating epoxy components or Kevlar, for instance.

The energy transfer can also be evaluated by numerical codes including the specific electromagnetic properties of the materials [21], the geometry of the different apertures [22], the type of panel bonding, access doors, and so forth [23, 24].

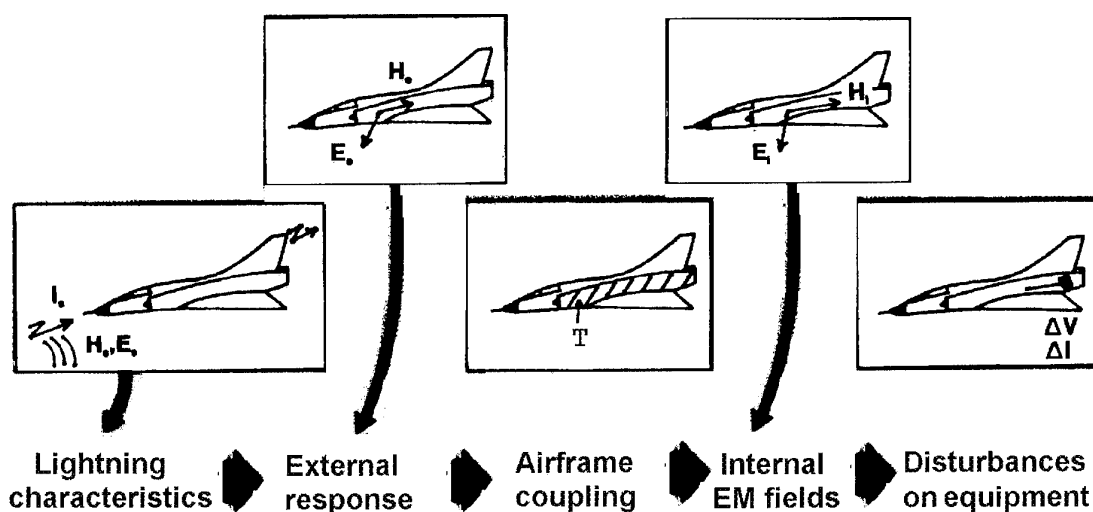


Fig. 3 - Successive steps between the lightning arc and the equipment.

④ Electromagnetic Coupling Between Internal Fields and Cables

The resulting internal electromagnetic fields act on different cables and bundles interconnecting the various electronic units of the aircraft.

How strong electromagnetic coupling is depending on the cables geometries, connector characteristics, and equipment distribution. The induced signals propagate through the cables before reaching the sensitive equipment. This kind of problem is solved by defining localized threat sources representing the interactions between the internal E_i and B_i fields and the wiring configurations. Numerical codes now exist which take into consideration this internal environment [25-28].

⑤ Interactions on a Given Unit

The induced signals propagate through the cables and reach a given unit. The reaction of the equipment may be the result of a combination of different sources.

Generally, the field threat to the equipment is given by the ΔV or Δi parameters. These are compared with the correlative ΔV_0 or Δi_0 limits, which are defined by laboratory tests. Margins also have to be taken into account, and if they are not sufficient, lightning protection has to be provided.

Lightning protection devices are generally defined and applied at different levels, for instance:

- ⇒ specific coatings and an optimized bonding of the different portions of the structure, to limit the electromagnetic coupling through the airframe;
- ⇒ shielding, to reduce the coupling between internal fields and cables;
- ⇒ arrestors, diodes, and other lightning protective devices to avoid noise or deterioration at equipment inputs.

The direct effects of the lightning flash have to be suppressed or limited at the same time by lightning diverters (i.e. for radomes, antenna covers) or specific lightning treatments on sensitive locations on the structure [29].

3. ESD Characterization

3.1. ESD Measurements

Three different categories of measurements are generally used for in-flight ESD analysis:

⇒ aircraft potential and the external atmospheric E-field. These two parameters are closely related and are determined by the same sensors.

⇒ triboelectric impact current density.

⇒ discharge currents leaving the aircraft.

⇒ Associated interference measured on a given equipment or with a spectrum analyzer.

3.1.1. Aircraft Potential and External Atmospheric E-field Measurement [30, 31]

As the aircraft is isolated in the air, the only way of measuring these two parameters is by surface electrostatic field sensors; the general measurement principle is given in figure 4. With the only external field E_0 (scheme a), the conducting body considerably changes the external E-field line configuration, which depends on the aircraft geometry and the orientation of the E-field axis versus the airframe reference axis.

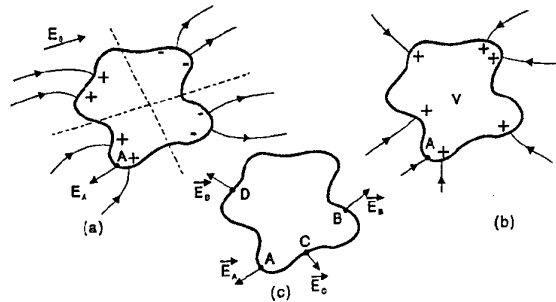


Fig. 4 - Aircraft potential and atmospheric E-field measurements.

On a point A at the conductive surface, the resulting local induced field \vec{E}_A is given by the relation:

$$\vec{E}_1 = k_{A,i} \vec{E}_i + k_{A,j} \vec{E}_j + k_{A,k} \vec{E}_k \quad (7)$$

where \vec{E}_i , \vec{E}_j and \vec{E}_k are the three components of the outside E-field \vec{E}_0 in the airframe reference axis; $k_{A,i}$ are the local aircraft geometry coefficients and represent the local enhancement of the induced field. At some place on the airframe there is a neutral line with no locally induced charge.

With the hypothesis of only an aircraft potential V, the E-field lines converge towards the airframe (see

scheme **b** on Fig. 4); the surface induced E-field on a point A is given by the equation:

$$\vec{E}_A = k_{A,V} \cdot \nabla \cdot \vec{n}_A \quad (8)$$

where $k_{A,V}$ is a geometric coefficient depending on the location of the point A and \vec{n}_A is the vector normal to A.

The superposition of two previous electrical configurations represents the general case of a global electrostatic equilibrium on the aircraft. The resulting E-field in a particular point A is given by:

$$\vec{E}_A = \sum_i k_{A,i} \vec{E}_i + k_{A,V} \cdot \nabla \cdot \vec{n}_A \quad (9)$$

To find the solution for the three components of the outside field \vec{E}_0 and for the aircraft potential, at least four different sensors are need at four different points on the airframe. The unknown parameters are then solved for by a four-equation system as follow:

$$\begin{pmatrix} E_A \\ E_B \\ E_C \\ E_D \end{pmatrix} = \begin{pmatrix} k_{A,i} & & & \\ & \ddots & & \\ & & \ddots & \\ & & & k_{D,V} \end{pmatrix} \begin{pmatrix} E_i \\ E_j \\ E_k \\ V \end{pmatrix} \quad (10)$$

or

$$\begin{pmatrix} E_i \\ E_j \\ E_k \\ V \end{pmatrix} = [k]^{-1} \begin{pmatrix} E \end{pmatrix} \quad (11)$$

$[k]^{-1}$ is a fourth-order matrix of enhancement factors k , and (E) is a fourth-order vector given by the four different sensors.

All the "k" coefficients may be obtained either by numerical codes solving the Poisson equation or by laboratory measurements carried out on a representative conductive mock-up of the airframe.

Due to accuracy problems in the solution of (11), five simultaneous measurements are needed in order to solve the problem in all flight conditions. System (11) can be solved in real time using a dedicated computer in flight. This practical approach is very useful for in-flight lightning research (see chapter 4).

3.1.2. Triboelectric Current Measurements

This current is sampled by insulating some selected areas on the impacted portions of the skin, and measuring with a current-voltage converter located between these terminals and the structure. Several current density probes may be used in order to analyze

the impact current variations as a function of the structure geometry and aircraft speed.

3.1.3. Discharge Current Measurements

As shown in the previous chapter, the aircraft potential depends on the corona emissions, which are due to local high electric fields. The discharge currents can be measured by specific instrumented wick-dischargers, each electrically connected to the structure through a low-value measuring resistor. The dynamic range of this instrumentation arrangement has to be adapted to a maximum of several milliamperes.

3.1.4. Measurement of RF Interference

The frequency spectrum of a corona discharge current or surface discharge current ranges from a few kilohertz to several hundreds of megahertz.

On instrumented aircraft, several receiving systems may be used in order to analyze the global interference domain. Generally, the following equipment is used:

- ⊗ Omega receiving system operating at 10 kHz,
- ⊗ ADF receiver operating at 250 kHz,
- ⊗ BLU receiver operating at 20 MHz,
- ⊗ two complementary receivers (VOR and ILS) tracking the interference at 130 and 330 MHz.

Typical Meteor aircraft instrumentation for ESD characterization purposes is presented in [30].

3.2. In-flight ESD Characteristics

It is impossible in this short presentation to cover all the aspects of the data obtained in-flight. Our objective is to present the essential features of the pertinent data carried out in different experiments.

Many flights have been made in various environments. Let us mention to start with that no definite electrification process has been detected in specific flight investigations of engine charging, which is considered theoretically as an efficient ESD source on aircraft. However, this mechanism, which may be efficient for missiles or space launchers, seems to be inoperative for aircraft.

3.2.1. Triboelectric Charging Current

The detection of triboelectric currents can be seen in the curves of figure 5. Curves **a** and **b** correspond to two identical lateral probes placed on the leading edges of the aircraft. The two signals SI2 and SI3 are perfectly similar, which shows that, for impact surfaces of the same type, the electrification process is very reproducible. We observe that the duration of the active

electrification process is of the order of 150 s and that the peak values detected by the probes at point A reach $50 \mu\text{A}$ which corresponds to a current density of $200 \mu\text{A.m}^{-2}$. The curve **c** shows the impact current detected by another probe located on the aircraft radome. The current variation is similar to those detected on the two lateral probes. The peak value of $69 \mu\text{A}$ at A corresponds to a current density of $108 \mu\text{A.m}^{-2}$. This calculated density is lower than that detected on the two lateral probes. This difference is explained by the aerodynamic configurations of the two situations. It is also mentioned in [3], where it is shown that the impact conditions are not the same everywhere on the aircraft. The triboelectric mechanisms depend on the dimensions of the impacting particles, and also on the curvature of the impacted surface. Curve **d** in the figure 5 gives the static E-field measured with one of the E-field sensors on the aircraft. We can already state that the aircraft potential will then follow the variation of the impact current i_c by the equation:

$$i_c = C \frac{dV}{dt} \quad (12)$$

As a whole, the triboelectric current measurements lead to the following conclusions.

- ⇒ Triboelectric phenomena is very frequent in clouds. Out of 855 minutes of flight in clouds, we observe definite triboelectric phenomena (detected currents greater than $1 \mu\text{A}$) during 388 minutes.
- ⇒ The detected currents are always negative, except for the simple case when the aircraft flies close to the ground with rain precipitations.
- ⇒ Triboelectric currents are always generated in cirrus clouds, but their level is low, typically between 25 and $60 \mu\text{A.m}^{-2}$. Tanner [3] gives figures between 50 and $100 \mu\text{A.m}^{-2}$. In cumulus clouds, the impact may become more intense and current densities exceeding $150 \mu\text{A.m}^{-2}$ are frequent. Reference [3] mentions values between 100 and $200 \mu\text{A.m}^{-2}$ in stratocumulus and $300 \mu\text{A.m}^{-2}$ in snow.
- ⇒ The maximum value, detected in a cloud of congestus type, exceeds $400 \mu\text{A.m}^{-2}$. Assuming an overall capturing surface for the whole aircraft of 8.3 m^2 , this maximum level would yield a global current of 3.3 mA .

3.3.2. Electrical Potential of the Aircraft

Curve **a** in figure 6 shows a typical aircraft potential variation when flying in clouds. On the same time scale, curve **b** shows the variation of the total discharge current as obtained by integrating all the discharger current measurements (the aircraft, in this particular case, is equipped with 30 identical instrumented dischargers).

We observe a strict coincidence between the variations of the two parameters, in particular at the singular points A (initial current increase), B (noticeable up-surge of the same current) and C (maximum potential and current).

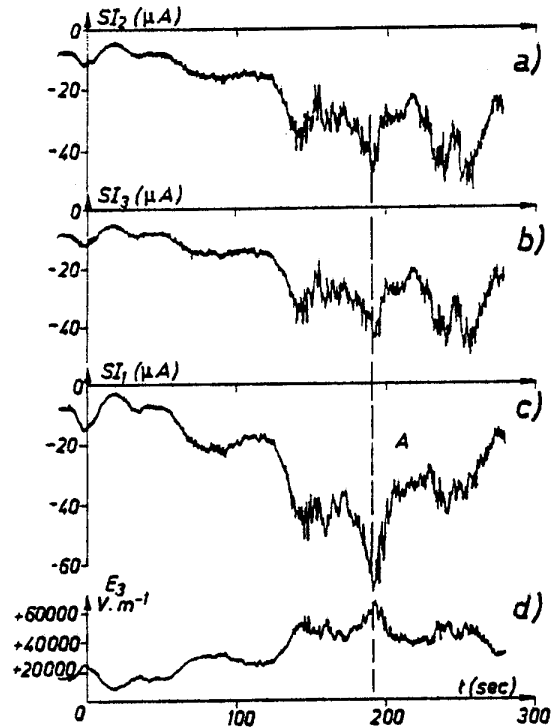


Fig. 5 -Triboelectric currents detected on aircraft.
a) left wing sensor; b) right wing sensor;
c) radome sensor; d) electric field sensor ($n^\circ 3$).

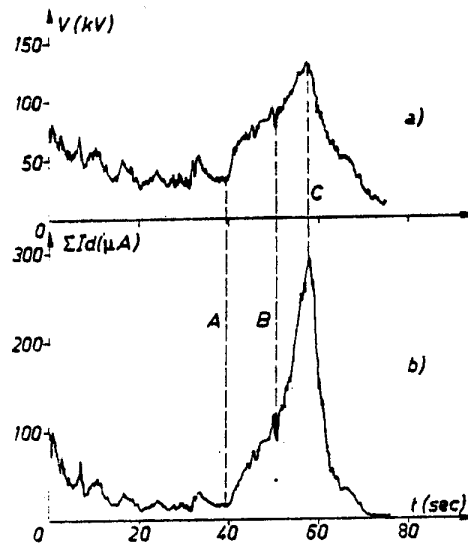


Fig. 6 -Aircraft potential variation in flight.
a) electrical potential; b) discharger currents.

The most significant parameter controlling the aircraft's electric behavior is the impact current. This current does not depend on the aircraft's potential V , since the mobility of the particles participating in the generation of this current is low. Figure 7 plots three curves giving the variation of the potential V as a function of the triboelectric current measured on a lateral probe SI2. These curves correspond to different experimental conditions characterized by local temperature and pressure, aircraft speed, and the number N of p-static dischargers.

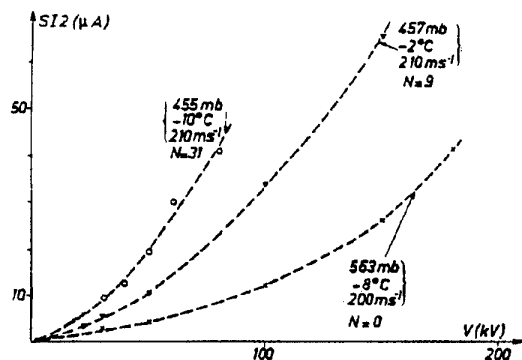


Fig. 7 - Aircraft potential and triboelectric current in flight.

We observe that the discharge efficiency, represented by the slope of the curves, depends essentially on the number N of dischargers.

A more detailed analysis of the aircraft's in-flight electrical behavior require an investigation of the operating conditions of each dischargers. Discharger efficiency can be optimized by an appropriate arrangement of p-static discharger locations on the airframe. This point is outside the scope of this paper, which presents only the essential ideas stemming from the flight data.

3.1.3. Interference Measurements

The impacting current in cirrus or alto-cumulus clouds, and the appearance of intense external electric field in extensive congestus or in cloud developments of the cumulo-nimbus type, may locally intensify a corona discharge field. If this discharge appears on a sharp point that is unprotected against RF coupling, this will entail interference in the airborne equipment, in particular the ADF or the ULF receiver.

We shall examine a typical case stressing the effect of a strong atmospheric field. In this configuration, the experimental aircraft was flying with a set of 31 p-static dischargers and with specific antistatic treatments at different points on the airframe. The aircraft flew through extensive congestus type clouds at a pressure-altitude of 640 mbar and a temperature of about 0°C.

The aircraft speed was about 200 ms⁻¹ during the experiment. This flight test is analyzed following the different recordings in figure 8.

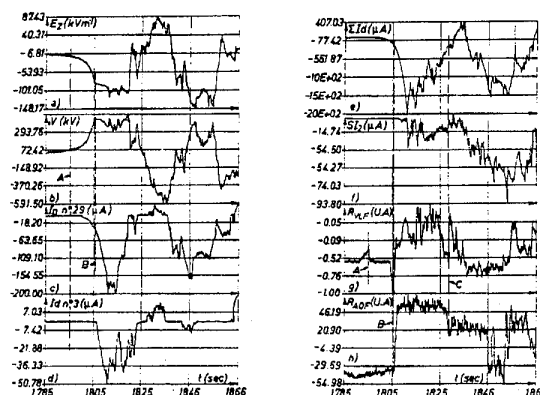


Fig. 8 - RF noise with an external field.

- a) atmospheric field; b) aircraft potential;
c) discharger n° 29 current; d) discharger n° 3 current;
e) total current, f) impact charging current;
g) RF noise at 10 kHz; h) RF noise at 200 kHz.

- ⇒ Curves **a** and **b** give the variations of the vertical component E_z of the atmospheric field and the aircraft potential respectively. Except for the sign, we observe similar variations for the two parameters. The aircraft potential reaches values of some 500 kV due to corona emissions.
- ⇒ Curves **c**, **d** and **e** are the current variation of different dischargers (n° 3 and 29) and the total current emitted by the dischargers installation. The operating thresholds of the dischargers are brought out clearly here.
- ⇒ The impact current (curve **f**) enters only very late into the evolution of V .
- ⇒ Recordings (**g** and **h**) make it possible to approximate the RF interference associated with the aircraft electrostatic state. A strong disturbance in the ADF channel (quasi saturation) appears at point B. This point B also corresponds to singular points in the variation of the aircraft potential (curve **b**). No impact current is detected at this point, and the overall discharge overall current reaches only 200 μA. We observe a desaturation in the ADF channel at point C, which also corresponds to this critical value of 200 μA for the discharger currents.

This very brief presentation of a particular event in flight shows that even with antistatic protection applied to the aircraft (installation of wick dischargers and antistatic treatments on the structure), severe interference can still occur in airborne equipment.

4. Lightning Interactions on Aircraft

4.1. Lightning Parameters Measurements [32-34]

Four global categories of measurements are needed for in-flight lightning characterization.

- ⇒ The aircraft potential and the external atmospheric E-field, as for ESD analysis. These two parameters are the essential information which define the critical environments which, in a very short period of time, lead to triggered or intercepted lightning events.
- ⇒ The lightning discharge current, when ever possible.
- ⇒ The electromagnetic field distribution of the vehicle airframe during the entire lightning flash, and particularly during the pulsed lightning current sequences.
- ⇒ The induced voltages observed on airborne equipment during these pulsed sequences.

4.1.1. Lightning Threat Characterization

Let us consider the first scheme given in figure 9. The airframe is connected to two lightning channels, which maintain the electrical contact between the aircraft and the two regions of negative and positive charge.

In principle, only one current sensor at A or B is sufficient to measure the global variation of the lightning discharge current. In fact through there are at least two physical reasons why this first hypothesis is not valid:

- ⇒ First is that the two points A and B are not unique. The lightning arcs may be connected at these two points at the beginning of the event, but one of the root channels may later move along the airframe (sweeping process illustrated in scheme b) due to aerodynamic and magnetic forces.
- ⇒ The second reason is related to the interaction of a nearby lightning discharge, with no connection between the discharge process and the aircraft. In this condition, it is possible to measure interference on the equipment without measuring the current in the airframe (scheme c).

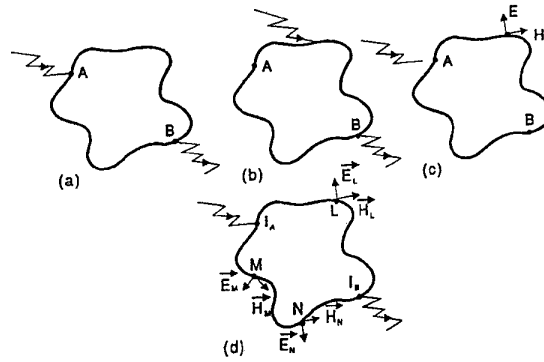


Fig. 9 - Lightning parameter measurements.

The solution to this problem is to measure the electromagnetic interactions at several locations on the airframe at the same time as the lightning current. For a given configuration of the two lightning channels, there is a unique relationship between the current in the lightning arc and the electromagnetic field measured at a given point on the structure. The electromagnetic field is detected by its two components: the electric component E normal to the local airframe surface, and the magnetic component H , which is perpendicular to the current direction.

The relationship between the current and the electromagnetic field is determined in two ways:

- ① By a 3D numerical code solving the Maxwell equations. The aircraft structure is represented numerically at the center of the calculation volume, and the two lightning channels are simulated by thin wires connecting the airframe to the boundary layers of the calculation volume. A given current waveform is applied to the wires and the global distribution of the E and H fields is calculated.
- ② By real-scale with instrumentation on the aircraft. This has to be conducted in a "quasi coaxial configuration", which means that the aircraft is located inside and along the axis of a cylindrical wiring system. A current pulse is applied, by a Marx HV generator, between an entry point on the aircraft and the return path of the coaxial system. The entry and exit points of the current may be modified in order to represent all the lightning situations encountered in flight.

A complete lightning characterization requires several cameras in order to observe the situation of the lightning arcs on the airframe. The cameras, depending on the research program and the aircraft geometries, may be installed in the cockpit, in the fuselage or in a special enclosure.

4.1.2. Interference Measurements on Equipment

One essential practical objective for all lightning programs carried out in flight is to measure the interactions with the onboard equipment. These interactions may be seen in terms of open-circuit voltage V_{oc} or short-circuit current I_{sc} at the equipment inputs. Given the current waveform $I(t)$ measured in flight, a global coupling transfer function may be calculated by:

$$T_1(\omega) = \frac{I_{sc}(\omega)}{I(\omega)} \quad (13)$$

or

$$T_2(\omega) = \frac{V_{oc}(\omega)}{I(\omega)} \quad (14)$$

The functions T_1 and T_2 may be extrapolated to expected peak $I(t)$ values in order to define the maximum threat to a given equipment unit.

A second more theoretical objective for a given piece of equipment consists of analyzing the successive coupling functions between the outside source (i.e. the current waveform), through the airframe penetration coefficient and possibly the electromagnetic material properties, the electromagnetic coupling on the wiring connecting the equipment and finally the direct coupling to the equipment itself. To further this theoretical analysis, it is very convenient to install E-field or H-field sensors inside the fuselage and induced current probes at appropriated points in the wiring system.

Given the very fast transients associated with lightning phenomena, all the sensor signals have to be transmitted to a single central acquisition system, and the measuring devices have to be connected by fiber optic links to avoid severe interference.

As an example, the photo in figure 10 shows a few of the instruments used on the Transall aircraft: I are current sensors, E and H electric and magnetic field sensors. The picture shows one of the several cameras installed at the right wing tip.

4.2. Measurements of Pertinent Lightning Parameters

Essentially, the measurements obtained in flight with the three different aircraft (Transall, F106 and CV580) are similar. The successive phases of a lightning flash can be observed from the three programs, and the two main categories of lightning events (triggered or intercepted flashes) were also detected by the three aircraft.

For these reasons, in the scope of our study of global lightning phenomenology, we can examine typical data coming independently from the three different aircraft and present a general view of the lightning-aircraft interactions.

4.2.1. Critical Environment for Lightning

It is obvious that a lightning flash can be obtained on an aircraft in a very active electrified cloud such a cumulo-nimbus. In fact, it is not necessary that the aircraft fly inside the cloud in order to be struck by a lightning discharge. Lightning phenomena may be encountered in the vicinity of a storm region or in the vicinity of cloud debris after a storm dissipation period.

In most cases (perhaps more than 95 %), the lightning flash is triggered by the aircraft itself, which means that no lightning activity would occur in the absence of the aircraft. Under these conditions, two parameters are essential in defining the triggering conditions:

- ⇒ the external atmospheric E-field,
- ⇒ the aircraft potential.

Before presenting this aspect, let us first consider how we controlled the flight path of an aircraft during our experiments, in order to be struck by lightning. A typical situation is described in the figure 11. Before the flight, the pilot and the experimenters are informed by the regional meteorological office about the storm activity in the vicinity of the airport (typically in a circle 500 km diameter around the airport). While approaching the storm, the activity is monitored on the cockpit radar

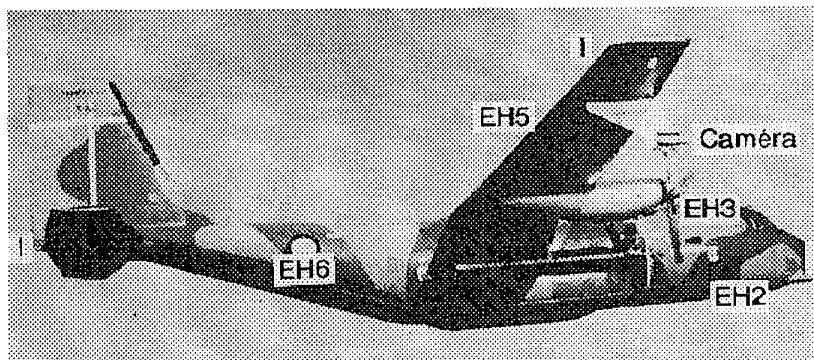


Fig. 10 - Transall instrumentation.

and the decision to penetrate the cloud is made on the basis of typical parameters like cloud base, precipitation level, cloud height, and droplet and ice crystal concentrations. Finally, the direction of the flight path when the aircraft is entering the cloud is optimized by the E-field measurements: the maximum E-field vector is located in order to obtain the maximum probability to be struck by lightning.

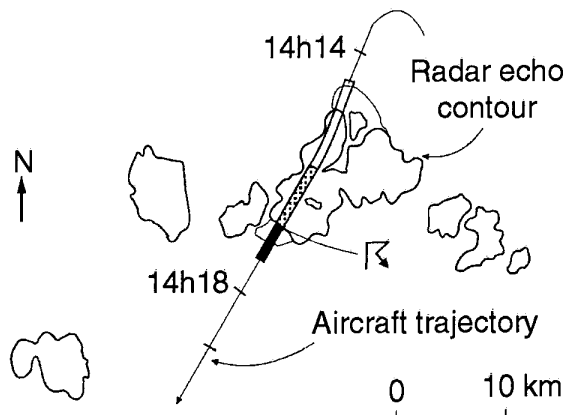


Fig. 11 - Typical cloud penetration for triggered lightning.

Figure 12 presents typical static E-field recordings observed on Transall during two triggered lightning flashes. Except for some minor differences, the global E-field sensor variations are identical. Three main periods may be defined:

- ⇒ A preparatory phase before the lightning. This phase lasts sometimes more than 10 s. The external E-field is observed to increase, from 0 and rising to 100 kV.m^{-1} . At the end of this first phase, (see example n° 1) breakdown triggering can be observed, without transformation into a complete lightning flash. When the field arrives at point A, the lightning event starts.
- ⇒ The lightning phase has a period of about 1 s (on rare occasions less than 0.2 s or more than 1.5 s). This period exhibits very fast variations in the E-field with peak to peak variations of $\pm 2 \text{ MV.m}^{-1}$. This phase will be analyzed in detail in the following sections.
- ⇒ We usually observe a third phase corresponding to some outside electrical activity, which may be either the continuation of the lightning activity (as the lightning channel is not definitively connected to the aircraft) or, if the lightning activity is completely reduced, some charge recombination or displacement may go on for several seconds. If we now consider the external E-field corresponding to point A in figure 12, we observe a critical level between 50 and 100 kV.m^{-1} , depending on the event. This is a high but not very high value; the

literature reports E-field measurements exceeding 100 kV.m^{-1} in storm region, the maximum being 400 kV.m^{-1} .

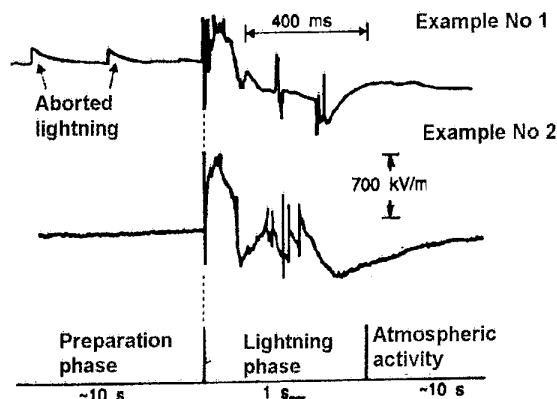


Fig. 12 - E-field variation during a lightning flash.

To begin answering, it is possible to say that the enhancement of the E-field due to the geometry of the aircraft itself is sufficient to induce a field value exceeding 30 kV.cm^{-1} at certain edges around the airframe. We remind the reader that 30 kV.cm^{-1} is the breakdown field in the air at ambient pressure and temperature. The enhancement factor is at least 30, which is very appropriate on aircraft structure geometry.

4.2.2. The Lightning Attachment

A typical lightning sequence is shown with the two curves of figure 13. These give the variations of the E-field component detected for the same event, at two different locations on the aircraft. They are the same, on the whole, which means that the E-fields detected are closely related to the aircraft potential (and not to any external E-field).

Two main phases can be identified:

- ⇒ an attachment phase at the beginning of the sequence,
- ⇒ a permanent phase for the entire duration of the lightning.

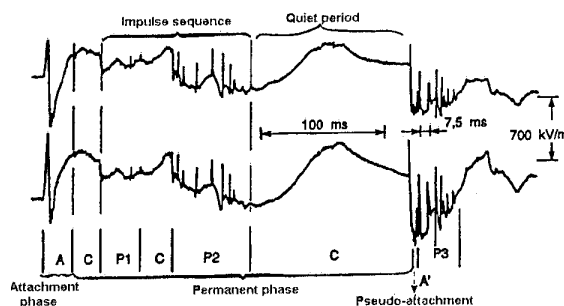


Fig. 13 - Successive phases in a lightning flash.

4.2.2.1. Attachment Phase Characteristics. As initially observed for the two curves presented on figure 13, the E-field signal is characterized by a typical signature, which is identical for all the triggered lightning flashes detected on the Transall and on the CV580. (The instrumentation on the F106 was limited to current and magnetic fields measurements).

This permanent signature seems to prove that the physical mechanisms responsible for the lightning connection on the aircraft are always the same.

The figure 14 represents the variation of the E-field signal (curve a) and of the discharge current (curve b) detected on a sensor in connection with the lightning channel, for the same period of time.

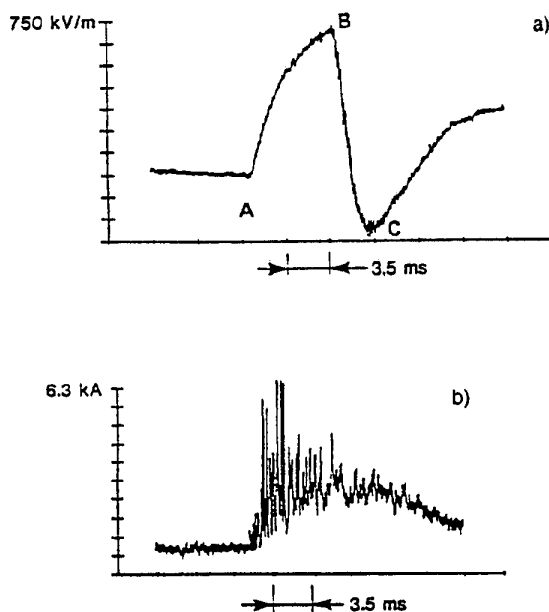


Fig. 14 - First milliseconds of attachment:
a) electric field; b) current.

The attachment signature is perfectly divided into three successive sub-phases [35]:

- ⇒ The first AB which exhibits a steady negative increase in the static E-field. The duration of this phase is roughly 4 to 6 ms. With the sensors used on the aircraft, no discharge current can be detected during this first sub-phase.
- ⇒ The second phase, BC, occurs at B, where the E-field reaches a critical negative value. This phase lasts 1 to 3 ms and corresponds to the beginning of a sequence of generally 4 to 5 successive current pulses.

- ⇒ A third phase, CD, starts when the static E-field reaches a critical positive value. This phase continues for 5 to 10 ms and is associated with the beginning of a steady current with superimposed discrete current pulses.

In the lightning simulation test procedure, this attachment phase is known as the first of the "multiple burst" sequence. We now know that a second attachment process may occur during a complete lightning flash, and that it is possible for a third attachment process to occur within a particularly long event.

It is accepted today that a multiple burst sequence consists of:

- ① Three successive current pulses bursts. These three bursts can occur in a period of 1 s with a mean duration of 0.5 s between them.
- ② Each burst consists of an average 20 successive current pulses with a constant period between 50 and 200 μ s.
- ③ Each current pulse has a peak amplitude of 10 kA, a rise time of 300 ns, and a fall time of 3 μ s.

4.2.2.2. Physical Mechanisms Associated with the Attachment Phase. The physical mechanism associated with the attachment phase is now known as the "bileader discharge process". Although the theory is still being developed by different groups worldwide, the concept of the bileader mechanism is validated and accepted.

This concept can be summarized as follows (see the three diagrams in figure 15):

- ⇒ During sub-phase AB, a positive leader starts out from a particular region of the aircraft (radome, wing tips, tail extremity). This discharge propagates from the aircraft towards a negative region of the cloud at a velocity of about 10^4 ms^{-1} and over distances of more than a kilometer. The current in this positive leader is of the order of 1 to 10 A, and of course is not detectable by the current sensors on the aircraft. Due to this current, the charges on the aircraft structure become more and more negative, and the E-field normal to the surface also increases towards the negative values.
- ⇒ At point B, the E-field reaches a critical value, which triggers a negative leader. This negative leader has an unstable propagation (the negative leader is frequently called a stepped leader) comprises a succession of current pulses. This is why the current is greater than during the positive phase AB, and the pulses are clearly detected by the sensors. During the

phase BC, the E-field varies considerably from high negative to positive values.

- ⇒ At point C, the negative and positive leaders have now propagated over long distances, the ionization processes in both channels are very efficient, the temperatures in the core channels are greater than 10 000 K, and the conductivity is ever increasing. A permanent current can now pass through the aircraft structure, which means that charges can be transferred from the two charged regions of the space now connected by the lightning arcs. In the attachment phase of a triggered lightning flash, the aircraft itself acts as a switch making contact between the positive and negative poles of a generator. The external E-field is sufficient to start and control the entire process globally.

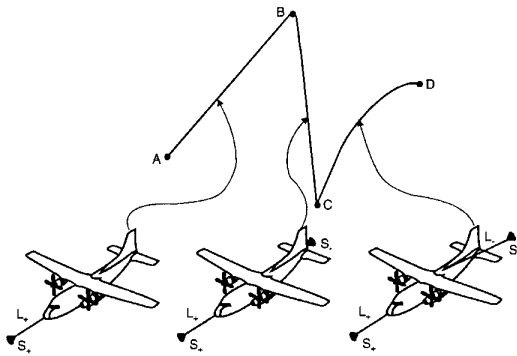


Fig. 15 - Bileader concept. S: streamer zone; L: leader zone

This new concept, which is now basically understood, is applicable not only to the aircraft lightning mechanism but also to the initiation of natural lightning inside clouds. The E-field enhancement factor is at play by way of the particles inside the cloud, such as droplets and ice particles. The conduction on these particles is sufficient to create local E-field enhancement, and this enhancement is considerably increased by the total population of particles, the integrated effect of which is large enough to trigger a bidirectional discharge. This scenario has been validated recently using an electromagnetic interferometer developed at ONERA [36, 37].

More specifically, the bileader concept has been validated in the scope of lightning and aircraft interactions. Three different experiments have been carried out (see photographs in figure 16).

- ⇒ The first was a laboratory experiment applying the concept of electrical surface discharge [38]. A small conductor C of 1 cm length, was introduced between two dielectric plates, one charged positively, the other negatively. The distance between the plate extremities is 1 m. By switching the initial floating potential of conductor C to

ground, a bileader process can be triggered, developing first a positive leader followed by a negative leader.

- ⇒ A second experiment [39] was carried out at the High Voltage Laboratory of Electricité de France at Les Renardières. The aircraft was simulated by a cylindrical conductor, 4 m long, installed in an electrical floating configuration at the middle of a 15 m gap. The gap consisted of a very large flat electrode (25 × 25 m) overhead the model and the floor of the laboratory underneath. A 5 MV pulse voltage was suddenly applied in the gap and the discharge process was followed by an image converter and by E-field sensors located on the cylinder and on the ground. The bileader mechanism was established perfectly well, yielding first a positive leader propagating towards the negative electrode and then a negative one advancing towards the ground. The measurements performed during these tests have been used extensively in order to verify the theoretical bileader model.

- ⇒ Lastly, a third experiment was undertaken at the Kennedy Space Center by ONERA, NASA, and the University of New York at Albany, in order to develop a bileader in a real environment [40, 41]. The technique has consisted in firing small rockets trailing a long conductive wire (100 m), in very active storm situations characterized by a static E-field on the ground of 6 kV.m⁻¹. When the rocket reached an altitude of about 200 m, a positive leader started out from the rocket nose and propagated up in the direction of the cloud base. This first propagation was followed a few milliseconds later, by a strong negative stepped leader, initiated at the end of the trailing wire and propagating down to the ground.

These three experiments are summarized in the three pictures in figure 16. The floating conductor C simulates aircraft airframe ranges from 1 cm (surface discharge), 4 m (HV discharge), and 100 m (lightning discharge), the propagating distance for both discharges of the bileader being 1 m, 12 m and 1000 m, respectively. These three validations show that the bileader concept applies to widely differing kinds of discharges, and the recently developed theoretical models for it are applicable in many situations.

4.2.3. Permanent Phase of Lightning

4.2.3.1. Permanent Phase Characteristics. As briefly presented above in figure 13, the attachment phase is followed by a complex permanent phase, the duration of which corresponds approximatively to the duration of the lightning flash.

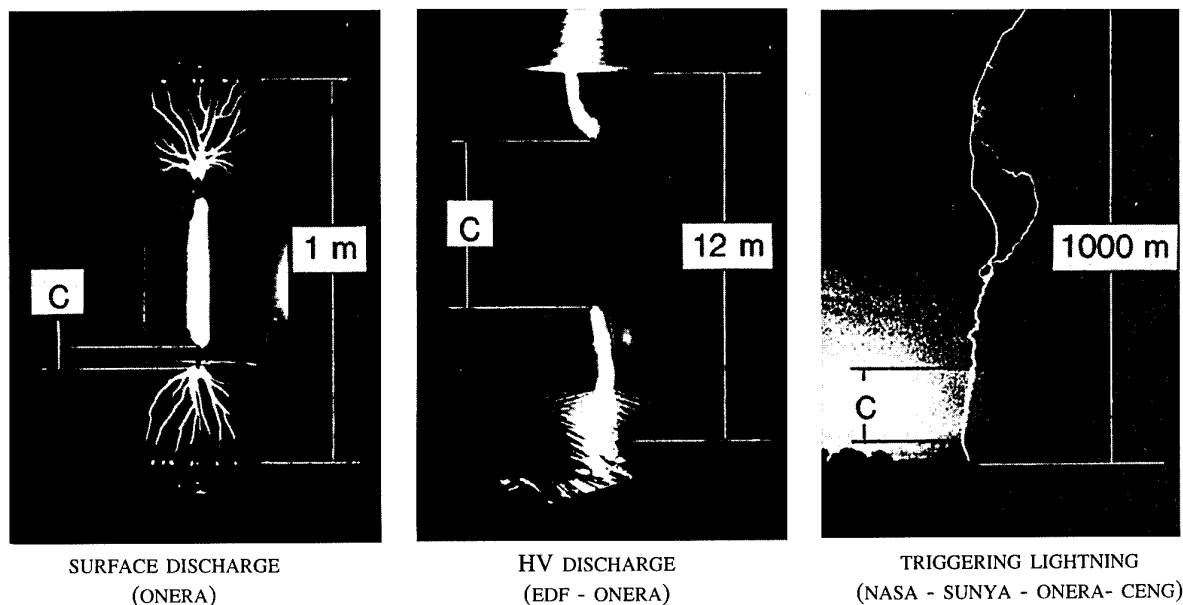


Fig. 16 - Experimental validation of the bileader concept.

The permanent phase exhibits a sequence of quiet periods (defined by C in figure 13) and active periods (defined by P_i). The periods C correspond to the charge transfers between the positive and negative regions of the environment. A roughly constant current passes through the aircraft between the two attachment zones on the airframe.

In sequences P_1, P_2, \dots, P_i , a series of fast current pulses is established. Figure 17 gives three examples of the second sequence P_2 taken from three different lightning flashes. The signatures in figure 17 correspond to E-field variations and, of course, all successive E-pulses are associated with the corresponding B-field pulses. Several characteristics of these sorts of sequences are remarkable.

- ⇒ The sequence of P_1, P_2, P_3 , and so on are very similar to the different lightning flashes detected on aircraft. This first point seems to show that lightning processes are globally the same regardless of aircraft geometry.
- ⇒ The mean time between two sequences P_i within a given lightning flash is roughly 100 ms, which is also the average time between subsequent return strokes in cloud-to-ground lightning phenomena.
- ⇒ Within a given sequence P, as shown in figure 17, the pulses are not random but seem to be distributed in intervals of about 10 ms.
- ⇒ If we go into the details of the pulse waveform, we observe two kinds of E-field pulses, and only one for the B-field signature. This indicates a charge

transfer that is always in the same direction, and also indicates repetitive connections of the aircraft structure to positive and negative charged regions.

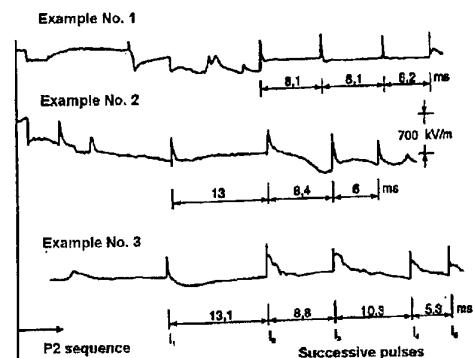


Fig. 17 - Permanent phase - Pulse sequence P_2 .

The current curve in figure 18 gives a typical current waveform associated with a pulse within a P sequence. For this example, we observe a peak value of 24 kA with a rise time of 300 ns and a decay time of a few microseconds. The rise time is so short the aircraft structure may be begin to resonate.

In the lightning simulation test procedure, this permanent phase is known as the "multiple stroke" sequence.

It is accepted today that a "multiple stroke" sequence consists of:

- ⇒ twenty-five successive current pulses. As an example a pulse distribution is given in figure 18, with five different groups of five pulses.

- ⇒ intervals of 100 ms between each group;
- ⇒ mean interval of 10 ms between pulses within a group;
- ⇒ current pulse peak value of 50 kA (200 kA for the first in the first group) with a rise time of 300 ns and a decay time of 3 μ s.

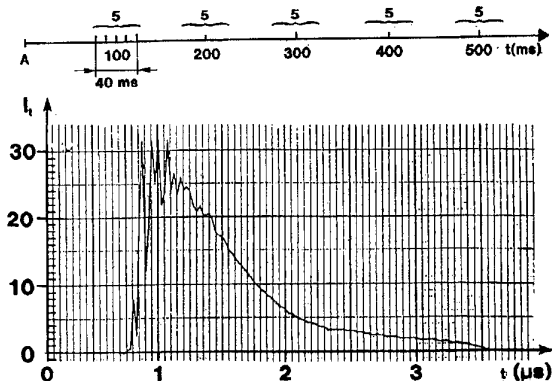


Fig. 18 - Distribution and waveform of P current pulses (NASA data).

4.2.3.2. Physical Processes in Permanent Phase [42]. In spite of very significant flight data in this field, the theoretical analysis of the physical mechanisms interacting with the aircraft during the permanent phase are not currently understood.

Two categories of hypothesis are analyzed to explain the flight measurements.

- ① The first consists in applying the principles of plasma physics phenomena to the arc channel properties to explain the quiet phase and the active period of the lightning flash. Certain specific instabilities in the plasma behavior of the lightning channel may explain the interruptions of the permanent current discharge. US Air Force and MIT Scientists are working in this direction.
- ② A second hypothesis consists in explaining these permanent phase properties in terms of the reaction of the environment itself. Briefly speaking, the idea is to interpret the successive current pulses as a connection of arcs induced in the cloud with the main lightning channel created by the aircraft. This seems to validate the two polarities of the E-field signatures and the typical waveform of the current pulses. The main problem remaining is to explain the 10 and 100 ms period intervals between pulses and between pulse bursts. Continued effort is being devoted to this subject particularly at ONERA.

4.3. Lightning Interference Observed on Equipment

The two phases of a lightning discharge result in typical interference signatures on airborne equipment. In this section, we will briefly describe our observations.

4.3.1. Attachment Phase

The interference begins at point B of attachment phase development. This is due to the appearance of the first current pulse. Thereafter, the interferences detected on the equipment depends closely on the current discharge waveform.

The situation is well defined by the three curves of figure 19. The first corresponds to the magnetic field H_1 detected on the outside surface of the airframe, where we observe, as we do for the current waveform, a succession of pulses during a period of several milliseconds. At the same time, a magnetic sensor H_{INT} inside the fuselage gives the resulting field due to the coupling transfer through the airframe. In our case, this transfer function (approximately a ratio of 20) represents the penetration of an electromagnetic field through a large carbon composite panel. There is of course a strong coincidence between the H_1 and H_{INT} pulses.

The third curve corresponds to the voltage ΔV detected during the same period of time on simulated equipment. It is clear that the interference, observed on the equipment corresponds exactly to the pulse sequence of the attachment phase; but each pulse detected on the equipment is the summation of different terms. It is possible to demonstrate in theory that the global ΔV interference is given by the relation:

$$\Delta V = A E + B \frac{dE}{dt} + C \cdot H + D \frac{dH}{dt} \quad (15)$$

This indicates that the global disturbance at the equipment inputs includes several electromagnetic coupling mechanisms that depend on the material properties, the geometry of the connecting wiring, and the impedance at the equipment inputs. Theoretically, this problem can be solved only by a numerical approach.

4.3.2. Interference during Permanent Phase

An example of a typical in-flight disturbance during the permanent phase is given in figure 20.

The sequence of curves corresponds to the same conditions as figure 19. The filtering effect due the carbon composite panel is clearly seen in the H_{INT} waveform, and the V_{cc} signature again demonstrates the complexity of the coupling mechanisms, which drive the disturbance on a given piece of equipment. In the

permanent phase, each current pulse may be considered separately. This is the multiple stroke concept.

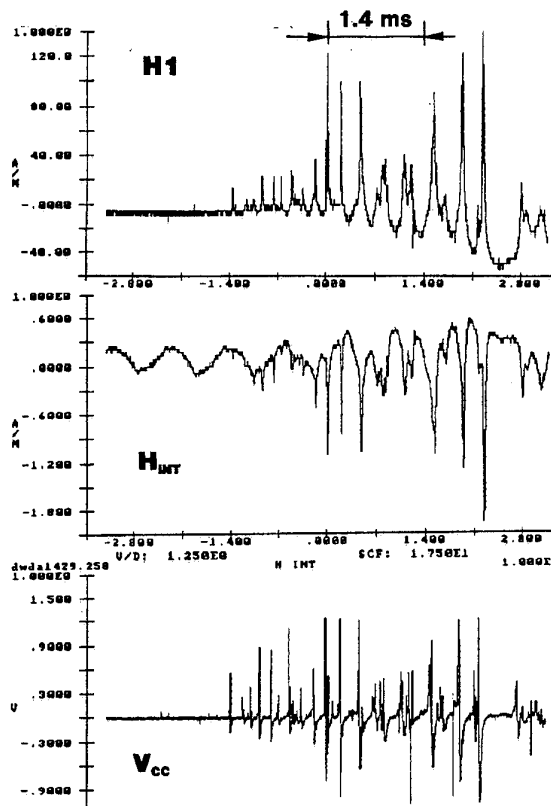


Fig. 19 - Interference on equipment during the attachment phase.

5. Conclusions

Progress has been made over the past decade concerning two electrical phenomena affecting aircraft in adverse environments.

The first is related to the electrostatic discharges that appear when triboelectric charges are captured by the airframe, or when induced charges are created under the influence of an outside atmospheric E-field. Typically, we know that an impact current density of $300 \mu\text{A.m}^{-2}$ may be encountered under certain severe conditions. A total current of several milliamperes has to be considered if we want very powerful protection against electrostatic interference. Radio navigation and communication systems, particularly in the low frequency range, are very sensitive to corona noise. Direct effects due to surface or arc discharges may cause damage on radomes, canopies or windshields de-icing systems.

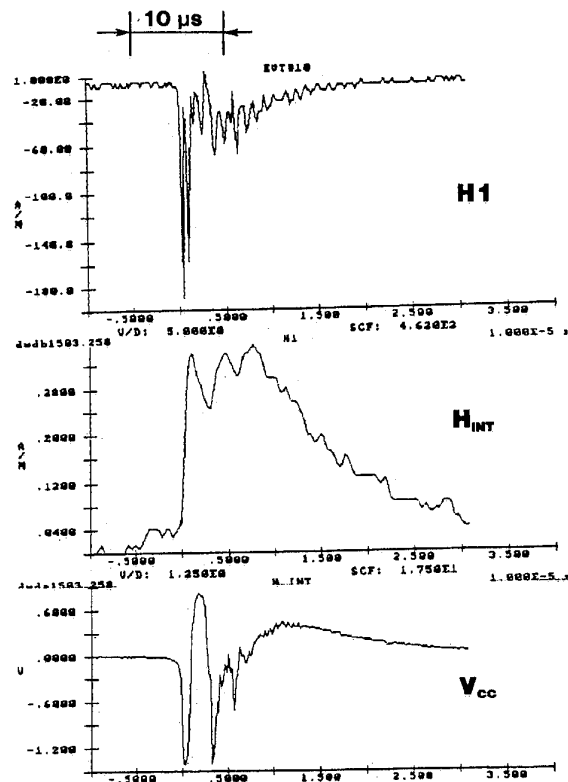


Fig. 20 - Disturbances associated with multiple stroke phenomena.

It is correct to say that a global aircraft protection against static electricity is possible today. This protection can be optimized, and the empirical methods used until recently should be changed. New methods, new protection techniques, and new controlling equipment are on the market, and can be used effectively.

The second phenomena concerns the lightning discharge. In light of the experimental campaigns carried out in flight on different aircraft, and after analysis and interpretation of the data, we arrive at a very high level of knowledge of the general mechanisms involved in a such phenomena.

This new knowledge can be summarized as follow:

- ⇒ Most of the lightning discharges affecting aircraft are triggered discharges. The aircraft itself is responsible for it. The outside atmospheric field, resulting from charge separation inside the cloud, is sufficient to create the process and to maintain a complex discharge propagation over distances of several kilometers. The critical E-field is around 100 kV.m^{-1} .
- ⇒ A lightning discharge occurs in two phases. The first is an attachment phase, which consists of the

initiation of two separate discharge processes on the aircraft. This bileader propagation is associated with the "multiburst waveform" now applied for equipment certification. The other phase is a "permanent" one consisting of successive sequences of current impulses.

This phenomena is not understood for the moment, but its characteristics are perfectly documented by flight data, validated by measurements made on three different aircraft.

This phase is associated with the "multistroke waveform" which is also recommended for equipment certification.

All this data and the related analysis are very recent. We know that work is continuing to understand some of the complex interactions between an aircraft and a lightning arc in greater depth. One of these interactions, for example, is the arc-sweeping mechanism of the lightning channel on the aircraft structure. We are just beginning to analyse this; but the consequences for aircraft lightning protection are essential. Broad discussions are getting under way, with aviation authorities (FAA, EUROCAE, CAA, DGAC) to propose international rules in this field. Effort is still needed to develop numerical tools, define protection techniques, and prepare control equipment.

References

- [1] Boulay, J.L., "Elimination des perturbations radioélectriques d'origine électrostatique sur avions", La Recherche Aéronautique, 1979-2, pp 101-120, 1979.
- [2] Harper, W.R., "Contact and frictional electrification", Oxford, Clarendon Press, 1967.
- [3] Tanner, R.L., and Nanevicz, J.E., "An analysis of corona generated interference in aircraft", Proceedings of the IEEE, 52, 1, 1964.
- [4] Nanevicz, J.E., and Tanner, R.L., "Some techniques for the elimination of corona discharge noise in aircraft", Proceedings of the IEEE, 52, 1, 1964.
- [5] Greer, P.E., "Electrostatic measurement experiment SCOUT vehicle 131-R", NASA CR 444, 1966.
- [6] Capener, E.L., et al., "Studies of ionization phenomena associated with solid propellant rockets", AIAA Paper 65-182, 1965.
- [7] Larigaldie, S., et al., "Lightning leader laboratory simulation by means of rectilinear surface discharges", J. Appl. Phys., 1982.
- [8] Boulay, J.L., et al., "Analysis of recent in-flight lightning measurements on different aircraft", ICOLSE, Oklahoma (USA), 1988.
- [9] Fischer, J.A., and Plumer, J.A., "Lightning protection of aircraft", NASA CP 108, 1977.
- [10] Pitts, F.L., "Electromagnetic measurements on lightning strikes to aircraft", AIAA 19th Aerospace Science Meeting, 1981.
- [11] Pitts, F.L., "F106 data summary and model results relative to threat criteria and protection design analysis", ICOLSE, Dayton (USA), 1986.
- [12] Rustan, P.L., et al., "Airborne measurements of the rise-time in lightning return stroke fields", ICOLSE, Fort Worth (USA), 1983.
- [13] Rustan, P.L., Moreau, J.P., "Aircraft lightning attachment at low altitudes", ICOLSE, Paris (France), 1985.
- [14] Mazur, V., "A physical model of lightning initiation on aircraft in thunderstorms", J. Geophys. Res., 4, D3, 1989.
- [15] Moreau, J.P., et al., "Transall 88. Lightning characterization program", ICOLSE, Bath (UK), 1989.
- [16] Moreau, J.P., Alliot, J.C., "Analysis of the first milliseconds of aircraft lightning attachment", ICOLSE, Dayton (USA), 1986.
- [17] Yee, K.S., "Numerical solution of initial boundary value problems involving Maxwell's equations in isotropic media", IEEE Trans. Ant. & Prop., AP14, pp 302-307, May 1966.
- [18] Rao, S.M., et al., "Electromagnetic scattering by surfaces of arbitrary shape", IEEE Trans. Ant. & Prop., AP30, 3, May 1982.
- [19] Alliot, J.C., et al., "3D computer codes developed at ONERA in time-domain and in frequency-domain to model electromagnetic interaction with a vehicle", 2nd ESA Workshop on Electromagnetic Compatibility, Noordwijk (Netherlands), December 1990.
- [20] Gobin, V., "Current injection in resistive three dimensional structure using the method of moments", ICOLSE, Bath (UK), 1989.

- [21] Gobin, V., et al., "The surface impedance: a pertinent parameter to describe finite conductivity materials in numerical codes", EMC Symposium, Zurich (Switzerland), March 1981.
- [22] Casey, K.F., "Low frequency electromagnetic penetration of loaded apertures", IEEE Trans. Elect. Compt., *EMC* 23, pp 367-377, 1981.
- [23] Sternberg, V., and Gobin, V., "Low frequency electromagnetic coupling through apertures bounded with joints. A study of overlap joints", *Annales des Télécommunications*, 48, 1-2, pp 56-70, 1993.
- [24] Gobin, V., "Modelling of electrically thick conducting shields in a three dimensional integral equation formalism", 10th EMC Symposium, Zurich (Switzerland), March 1993.
- [25] Baum, C.E., "Theory of electromagnetic interference control", *Interaction Notes*, 478, December 1989.
- [26] Parmantier, J.P., et al., "Electromagnetic coupling on complex systems: topological approach", *La Recherche Aérospatiale*, 1990-5, 1990.
- [27] Parmantier, J.P., et al., "Electromagnetic topology: junction characterization methods", *La Recherche Aérospatiale*, 1990-5, 1990.
- [28] Parmantier, J.P., et al., "Electromagnetic topology. Characterization of internal electromagnetic coupling", ICOLSE, Cocoa Beach (USA), April 1991.
- [29] Fisher, F.A., Plumer, J.A., Perala, R.A., "Lightning protection of aircraft", *Lightning Technologies Inc.*, Pittsfield, MA 01201, USA, 1990.
- [30] Laroche, P., et al., "Essais en vol pour l'étude des perturbations radioélectriques d'origine électrostatique", 37th Technical Meeting of AGARD/Avionics Panel on Electromagnetic Effects of Composite Materials upon Avionics Systems, Lisbonne, June 1980.
- [31] Boulay, J.L., and Laroche, P., "Aircraft potential variations in-flight", ICOLSE, Oxford (UK), March 1982.
- [32] Moreau, J.P., and Alliot, J.C., "E and H fields measurements on the Transall C160 aircraft during lightning flashes", ICOLSE, Paris (France), June 1985.
- [33] Boulay, J.L., "Current waveform observed during lightning strikes on aircraft", ICOLSE, Cocoa Beach (USA), April 1991.
- [34] Mazur, V., and Moreau, J.P., "Aircraft-triggered lightning: processes following strike initiation that affect aircraft", *J. Aircraft*, 29, 4, pp 575-580, July-August 1992.
- [35] Moreau, J.P., and Larigaldie, S., "Description and interpretation of aircraft lightning attachment from electric and magnetic field measurements and video observation", ICOLSE, Cocoa Beach (USA), April 1991.
- [36] Bondiou, A., Labaune, G., Marque, J.P., "Electromagnetic associated with the formation of an electric breakdown in air", *J. Appl. Phys.*, 61, 2, 1987.
- [37] Richard, P., et al., "UHF interferometric imaging of lightning", ICOLSE, Forth Worth (USA), 1983.
- [38] Larigaldie, S., "The spark propagation mechanism in ambient air at the surface of a charged dielectric. II: theoretical modeling", *J. Appl. Phys.*, 61, p 102, 1987.
- [39] Hutzler, B., Taudière, I., "Attachment process of lightning on aircraft in the light of laboratory simulations", ICOLSE, Bath (UK), 1989.
- [40] Laroche, P., et al., "Observations of preliminary discharges initiating flashes triggered by the rocket and wire technique", ICOLSE, Bath (UK), 1989.
- [41] Laroche, P., et al., "Observations of bi-directional leader development in a triggered lightning flash", ICOLSE, Cocoa Beach (USA), April 1991.
- [42] Larigaldie, S., et al., "Mechanisms of high current pulses in lightning and long-spark stepped leaders", *J. Appl. Phys.*, 72, 5, pp 1729-1739, September 1992.

ICING: ACCRETION, DETECTION, PROTECTION

John J. Reinmann*

National Aeronautics and Space Administration
Lewis Research Center
Cleveland, Ohio 44135

1. INTRODUCTION

Icing conditions present an adverse environment to aircraft. In flight, the most common icing hazards are clouds containing supercooled water droplets, clouds with mixtures of supercooled droplets and ice crystals, and freezing rain. On the ground, icing hazards include freezing rain, freezing drizzle, freezing fog, falling or blowing snow, frost, slush, and humid air.

The adverse effects of icing on aircraft operations are described below. Ice contamination on wings and tails reduces maximum lift coefficient and stall angle of attack, and increases stall speed and drag. During takeoff, ice on wings has caused wing stall and serious stability and control problems with nearly every kind and size of aircraft, resulting in pitch up, rolloff, and crash. During approach or landing, the combination of extended wing flaps and ice on the horizontal tail has caused tailplane stall, resulting in uncommanded pitchovers with some aircraft. Ice contamination on propulsion system components—such as air intakes, engine nacelles, inlet ducts, propellers, fan blades, spinners, inlet guide vanes, and helicopter rotor blades—reduces propulsive efficiency and adds to aircraft drag. For smaller fixed-wing aircraft, the combination of reduced lift, increased drag, and reduced propulsion efficiency can result in the loss of the capability for level flight, and the aircraft will execute an uncommanded descent. For helicopters, increased rotor drag caused by ice can result in required torque exceeding available engine torque, and the helicopter will execute an uncommanded descent. Iced rotors can also cause retreating blade stall, resulting in an uncontrolled rolloff. Furthermore, iced rotors will cause more rapid descents during autorotation. Pieces of ice shed from wings, propellers, rotors, or engine nacelles can cause structural damage to the airframe or engine, or cause engine flameout. Ice on aircraft instrumentation can give wrong airspeed indications or wrong engine pressure ratios that lead to improper engine power settings. Ice accretion on antennas, struts, wheels, and external stores adds weight and drag to the aircraft. Ice can cause destructive vibration of parts such as antennas and wing struts.

Anytime an aircraft flies through visible moisture at outside air temperatures below about 5 °C, there's a good chance that ice will form on the aircraft components. In-flight icing conditions normally occur from ground level up to 22,000 ft, but pilots have reported icing at altitudes as high as 40,000 to 50,000 ft. On aircraft in flight, ice forms on the leading edges of wings, tails, engine nacelles, spinners, etc. At temperatures near freezing (0 °C), in-flight ice is clear (glaze) and horn-shaped, while at colder temperatures, it is white and opaque (rime) and spear-shaped. On grounded aircraft,

freezing precipitation covers all the upper surfaces of the aircraft. Ice on grounded aircraft can take several forms: frost, wet snow that freezes, freezing rain that turns into clear ice, slush that freezes, or moisture from humid air that condenses on cold-soaked wings and freezes to clear ice.

Five methods are used to protect against ice

1. Keep water wet—apply heat continuously
2. Evaporate water—apply more heat continuously
3. Melt ice—apply heat intermittently
4. Mechanically remove ice—crack, debond, and expel the ice with pneumatic deicers or impulse deicers
5. Chemically prevent ice or melt ice—apply freezing point depressant fluids

In that ice protection systems have been used successfully since the 1940's, it would seem reasonable to expect that all the icing technology problems have been solved by now. However, new problems continually arise, because the use of new technologies in modern aircraft have a ripple effect on ice protection. Also intense global economic competition forces airplane manufacturers to optimize overall airplane performance while minimizing airplane capital costs, operating costs, and maintenance costs, and ice protection must be included in this optimization process.

The global aircraft industry and its regulatory agencies are currently involved in three major icing efforts: ground icing; advanced technologies for in-flight icing; and tailplane icing. These three major icing topics correspondingly support the three major segments of any aircraft flight profile: takeoff; cruise and hold; and approach and land. In this lecture, we will address these three topics in the same sequence as they appear in flight, starting with ground deicing, followed by advanced technologies for in-flight ice protection, and ending with tailplane icing.

2. GROUND OPERATIONS AND HAZARDS IN CONDITIONS CONDUCTIVE TO ICING

Aircraft ice contamination caused by freezing precipitation during ground operations poses a potential hazard for takeoff and subsequent flight. Airplane manufacturers do not design their airplanes to take off with ice on critical surfaces, nor does the FAA/JAR certify them to take off under such conditions. Airplane manufacturers fully support the "Clean Aircraft Concept" and warn that it is imperative not to attempt takeoff unless the pilot is certain that all critical surfaces of the aircraft are clear of ice. The Federal Aviation Regulations

*Distinguished Research Associate.

(FAR) Sections 121.629, 91.209, and 135.227 *prohibit* a pilot from taking off with ice contamination. Section 121.629 Operations in Icing Conditions states:

No person may take off an aircraft when frost, snow, or ice is adhering to the wings, control surfaces, or propellers of the aircraft.

Deicing and anti-icing fluids are available to protect aircraft from ground icing. Deicing fluids remove ice from aircraft but do not prevent refreezing. Anti-icing fluids prevent precipitation from freezing on the aircraft for a limited period of time (holdover time). The FAA requires operators to develop and use an FAA-approved aircraft ground deicing program and specifies checks and inspections to ensure a clean aircraft at takeoff.

2.1 Effects of Roughness on Wing Aerodynamics

On takeoff, the predominant effect of ice contamination is on the lifting characteristics of the wing. Figure 1 shows conventional plots of lift coefficient versus angle of attack (AOA) for a clean wing and a contaminated wing. The plots show that contamination reduces both the maximum lift coefficient and the angle of attack for maximum lift (stall angle).

Figures 2, 3, and 4 (from Ref. 1, 2, and 3, respectively) provide a comprehensive and valuable collection of wind tunnel and flight test data that quantifies the percent loss in maximum lift as a function of nondimensional roughness height, k/c . Percent loss in maximum lift is defined as:

$$\frac{100 \times (\text{maximum lift clean} - \text{maximum lift contaminated})}{\text{maximum lift clean}}$$

These last three figures present somber evidence that contamination causes a significant loss in aerodynamic performance for both slatted and unslatted wings. Unslatted wings refer to wings without leading edge devices extended. Slatted wings refer to wings with extended/deflected leading edge devices such as a slat. (In this paper, we will denote unslatted wings as "hard" wings.) Brumby's correlation for the entire upper surface covered with roughness (Fig. 2) brackets the data from all three figures and can be considered an upper limit on percent loss in maximum lift for hard wings and tails. On the last three figures, the data from Boeing, Fokker, and McDonnell-Douglas for slatted wings at higher k/c values show much lower losses in maximum lift coefficient than does Brumby's correlation.

Figure 5 (Ref. 3) shows that loss in angle of attack to stall varies nearly linearly with nondimensional roughness height, k/c . Figures 2 to 5 together contain enough information to get a representative estimate of the effects of roughness on wing or tail aerodynamics. They should prove useful to those concerned about icing problems during both takeoff and landing.

The data presented in Fig. 2 to 5 include data taken at both subscale and flight Reynolds numbers. Reference 3 presents data that demonstrates that testing must be done at chord Reynolds numbers of 5×10^6 or higher to achieve percent loss of maximum lift results representative of full-scale flight.

Figure 4 shows that even a small nondimensional roughness height of 5×10^{-4} , which is comparable to about a 0.2 mm roughness height on a small jet transport wing, can reduce maximum lift of a hard wing by 35 percent and angle of attack for maximum lift (stall angle) by about 6° . Percent increase in stall speed, the operationally more significant parameter, can be estimated as about half the percent loss in maximum lift coefficient. So for the present example, a 35 percent loss in maximum lift translates to an 18 percent increase in stall speed. For a normal takeoff run with this amount of contamination on the wings, V_2 (takeoff safety speed) would be less than stall speed, which means that the wings could not generate enough lift to take off.

Several times thus far, we have mentioned that ice contamination on the lifting surfaces (i.e., wings and tails) reduces maximum lift and stall AOA and increases stall speed and drag. Typically, a modern transport is required for certification to have about a 13 percent stall speed margin at takeoff, which is to say that its normal safe takeoff speed, V_2 , is 13 percent higher than its 1g stall speed for the clean wing takeoff configuration. Landing speeds are typically about 23 percent higher than stall speed for the clean wing landing configuration.

Although ice contamination increases form drag it does not appreciably affect drag on large transports. However, if the angle of attack is high enough to stall the wing, the wing form drag becomes appreciable and may double the aircraft drag. On smaller aircraft, ice on exposed landing gears and wing struts could contribute appreciably to airplane drag.

2.2 Effects of Ground De/anti-icing Fluids on Wing Aerodynamics

When ground deicing or anti-icing fluids are present on the wing during the takeoff run, the fluid surface becomes unstable and develops a waviness which is, in effect, a form of roughness that contaminates the wing. So, even though these fluids can protect against the large aeroperformance losses caused by ice roughness, the fluids themselves could potentially cause performance penalties during takeoff. In the 1980's and early 1990's, the Boeing Airplanes Company demonstrated both in wind tunnel tests and in flight tests that these fluids do cause measurable losses in maximum lift coefficients (Ref. 4). These results were confirmed by the von Karman Fluid Dynamics Institute in Brussels, Belgium, under a grant from the Association of European Airlines (AEA) (Ref. 5).

Remarkably, these studies demonstrated that the loss in maximum lift coefficient correlated with the boundary layer displacement thickness measured at the trailing edge of the wing's fixed element. Professor Mario Carbonaro from the von Karman Institute used this correlation to develop a cost effective Aerodynamic Acceptance Test for the qualification of Type I and Type II fluids. The test measures the growth in boundary layer displacement thickness at the trailing edge of a flat plate covered with the fluid and located on the test section floor of a specially designed wind tunnel. A correlation exists that defines an acceptable upper limit on displacement thickness over a range of temperatures. Fluids that exceed the upper limit fail the acceptance test and are rejected. (Keep in mind that the acceptable upper limit on displacement thickness is directly correlated with the acceptable upper limit on loss in maximum lift.)

Only two wind tunnel facilities are currently approved to conduct this test: one is located in Europe at the von Karman Institute and the other is in North America at the University of Quebec at Chicoutimi. References 4 and 5 discuss the Boeing and von Karman Institute aerodynamic studies on ground deicing fluids. And Ref. 6 describes the aerodynamic acceptance test and its rationale, which was approved by the Aerospace Industries of America (AIA) and the Association Europeenne des Constructeurs de Materiel Aerospacial (AECMA).

The acceptable upper limit on loss in maximum lift derives from the criterion for stall speed margin at takeoff safety speed, V_2 . The airplane manufacturers and the regulatory agencies recognized that the fluid imposed a *transitory* loss in maximum lift, since the fluid completely flows off the wing shortly after rotation (except for a very thin residual film that remains for much longer). Although authorities require a 13 percent stall speed margin for clean wings, they accepted a ten percent stall speed margin for fluid-covered wings because the fluid effect is transitory. To meet the minimum 10 percent stall speed margin, the percent loss in maximum lift coefficient must not exceed 5.24, which establishes the acceptance test criteria. We shall work through the arithmetic to show that a 5.24 percent loss in maximum lift coefficient results in a 10 percent stall speed margin. Using the rule of half, a 5.24 percent loss in maximum lift coefficient causes a 2.62 increase in stall speed. Therefore, we have the identity

$$V_{1g \text{ stall fluid}} = 1.0262 * V_{1g \text{ stall clean}}$$

The required safe takeoff speed, V_2 , is

$$V_2 = 1.13 * V_{1g \text{ stall clean}}$$

which means that the airplane takes off with a 13 percent stall speed margin when the wing is clean and dry.

Assuming no adjustment is made to V_2 for the presence of fluid on the wing (i.e., V_2 remains constant), use the first equation to substitute $V_{1g \text{ stall fluid}}/1.0262$ for $V_{1g \text{ stall clean}}$ in the second and obtain

$$V_2 = 1.13 * (V_{1g \text{ stall fluid}}/1.0262)$$

or

$$V_2 = 1.10 * V_{1g \text{ stall fluid}}$$

Thus the fluid-contaminated airplane takes off with a transitory 10 percent stall speed margin. Nearly all aircraft in the jet transport category were found to be able to accept this transitory loss in stall speed margin without any takeoff adjustments, but there were a few aircraft for which adjustments had to be made, such as by offloading passengers or cargo when fluids were used.

The Type II anti-icing fluids were designed for use on jet transports that have rotation speeds of about 110 kt, and they are not recommended for aircraft with rotation speeds below 85 kt. This is explained further in section 2.4.2.

2.3 Effects of Wing Contamination on Takeoff Characteristics

References 1 and 2 give good descriptions of the typical effects of contamination on airplane takeoff characteristics.

Fokker Aircraft engineers acquired data from wind tunnel tests of wing sections and airplane half models with roughness distributed uniformly over the entire wing upper surface and also from flight tests with simulated rime ice and sandpaper roughness on the leading edge of the wing. They made use of this data in an engineering flight simulator of the Fokker 100 (Ref. 2). Figure 6 shows the lift versus AOA curves for the clean and contaminated wing, along with stick shaker AOA and roll control boundaries. When the clean aircraft is rotated 3° per second the peak AOA was approximately 10.5°. The clean aircraft would still have about a 2.5° margin before stick shaker activation and a 5.5° margin to stall AOA. The aircraft with contaminated wings will stall at about 9°, or about 1.5° below the aircraft's target angle of attack.

Van Hengst (Ref. 2) pointed out that the clean airplane gives a slow progression of wing flow separation that starts inboard and moves toward the wing tips as AOA is increased, thereby ensuring exceptionally good roll control throughout a stall test maneuver. The manner in which a contaminated wing will stall is unpredictable and, therefore, extremely dangerous because the inherent good stalling characteristics of the clean wing are lost. Unequally distributed contamination over both wings will most likely further aggravate the situation, causing an asymmetric stall accompanied by violent roll. In addition, significant increase in drag develops during rotation as the wing goes into stall.

As Ref. 1 and 2 noted, stall of a contaminated wing is usually accompanied by either a pitch up or a pitch-down tendency of the aircraft, both of which tendencies will likely lead to over-rotation of the aircraft. A pitch-up tendency directly leads to over-rotation, driving the wing deeper into the region of stall where airframe buffet occurs. A pitch-down tendency is noticed by the pilot after rotation when the aircraft fails to gain sufficient climb rate and customary height. The pilot's normal response is to increase the elevator input, which action will over-rotate the aircraft and again lead to airframe buffet.

The moment of airframe buffet is the pilot's first indication that something is wrong. Fokker studies showed that the pilot would not notice the reduced acceleration caused by the contamination drag or the accompanying slight increase in takeoff run, and therefore, the pilot would not be alerted that something was wrong with the aircraft.

With clean wings, aircraft drag is low enough to ensure climb capability at the required climb angle at V_2 (takeoff safety speed) with one engine inoperative. However, with contaminated wings, the stalled wing may double aircraft drag, and even with all engines operative at take-off thrust, climb capability may be lost.

As mentioned above, the Fokker 100 wing is designed for flow separation to first occur inboard and then, as angle of attack increases, progress towards the wing tip. For the clean wing, inboard wing flow separation occurs at 16° AOA when maximum lift is reached, and flow separation does not affect roll control until an AOA of 19° is reached (Fig. 6). For the contaminated wing, the slow progression of flow separation towards the wing tip is lost, and uncontrollable roll may develop at an AOA as low as 10°, just 1° beyond the AOA for maximum lift of the contaminated wing.

In the Fokker 100 engineering simulator studies for a symmetrically distributed roughness of a thickness that caused

wing stall at 9°, an altered takeoff technique was found that achieved a successful simulator takeoff if the peak angle of attack were 8.5°. It was also found, however, that this was achieved at the expense of significantly increased runway distance.

Van Hengst concluded from these simulator studies that: "With the lack of any means of relating the amount of contamination in ground icing conditions to its effect on the aerodynamics of the aircraft, this flight simulation study shows that **NO TAKE-OFF SHOULD BE ATTEMPTED UNLESS IT IS FIRST ASCERTAINED THAT ALL CRITICAL SURFACES OF THE AIRCRAFT ARE FREE OF ICE, SNOW OR FROST DEPOSITS.**"

2.4 Characteristics of Ground Deicing and Anti-icing Fluids

We shall begin this section with definitions of the terms "aircraft deicing" and "aircraft anti-icing". "Aircraft deicing" is a the procedure that *removes* frost, ice, snow, or slush from the aircraft in order to provide clean surfaces. Deicing involves spraying the surfaces with hot water or hot water/glycol mixtures.

"Aircraft anti-icing" is the procedure that *protects* clean surfaces of the aircraft against the formation of frost, ice, and accumulations of snow or slush for a limited period of time (holdover time). Anti-icing involves spraying the clean surfaces with thickened glycol-based fluids that can protect against freezing precipitation for a *limited* time (holdover time). The international aviation community has accepted the AEA's coding of these deicing and anti-icing fluids as Type I and Type II, respectively. Type I and Type II fluids must meet rigorous physical, chemical, and aerodynamic acceptance specifications before they can be qualified for use in aircraft operations. Although the AEA, SAE, and ISO have cooperated to develop a comprehensive set of specifications and qualification tests for these fluids, some minor differences exists between the three organizations' specifications. Therefore the fluid is prefixed by the letters AEA, SAE, or ISO, as for example, SAE Type I or ISO Type II, etc.

Unfortunately, some confusion could develop over fluid terminology because there are also Mil Spec Type I and Type II fluids, which are similar, but not identical, to the SAE/ISO/AEA Type I fluids. These Mil Spec fluids will not be discussed herein. (For further clarification, see the discussion by M.S. Jarrell starting on p 243 of Ref. 7.)

2.4.1 SAE/ISO/AEA Type I Fluids

Type I fluids, in their undiluted (neat) formulation, usually contain a minimum of 80 percent glycol. These fluids are easily stored and handled. They are eutectic with the minimum freezing point occurring approximately at a mixture of 60 percent glycol and 40 percent water by volume. Their viscosity is a function of temperature but not of fluid shear, and therefore they are said to exhibit Newtonian behavior. Type I fluid viscosity is relatively low except at very cold temperatures, where the viscosity depends significantly on the type of glycol used. This low viscosity allows Type I fluids to readily flow off aircraft surfaces, leaving only a thin layer of protection against freezing precipitation. They have limited effectiveness when used for anti-icing purposes. Monoethylene glycol, which has been widely used in the United

States, has a low viscosity over the range of expected operating temperatures. Diethylene, triethylene, and propylene glycol-based fluids are used in Europe and are becoming more common in North America. Compared with monoethylene glycol, when these latter fluids are used undiluted, their viscosity is higher and increases faster with decreasing temperatures. If applied undiluted to the wing at the colder temperatures, their viscosities are high enough to cause unacceptably high aerodynamic penalties at takeoff. Diluted with water, these latter fluids have acceptable aero penalties; therefore, they should always be used in the diluted formulation for deicing aircraft.

2.4.2 SAE/ISO/AEA Type II Fluids

Type II fluids have markedly improved anti-icing capabilities compared with Type I fluids. These fluids contain at least 50 percent glycol in their neat form. They exhibit non-Newtonian behavior, which means that their viscosity strongly depends on shear as well as on temperature. Their viscosity decreases strongly with increasing shear stress. This non-Newtonian behavior is achieved by adding thickeners composed of long polymer chains. When the airplane is stationary and wind speeds are low, the Type II fluid film on the wing is gel-like and therefore thicker than Type I films. Its greater thickness allows it to absorb more freezing precipitation before ice crystals begin adhering to the wing. During the takeoff run and climbout (at rotation speeds over 85 kt), air flowing over the wings shears the fluid and reduces its viscosity to near that of a Type I fluid, and it readily flows off the wing.

Type II fluids are sensitive to storage tank materials and handling equipment. Therefore, special tank materials are used to prevent fluid vapors from corroding the tanks; and pumps, nozzles, and piping are designed to avoid degrading the fluid (i.e., the polymer chains must not be broken up by the shearing action of pumping and pressure drop) before it settles on the aircraft surfaces.

Type II fluids were developed for typical commercial transports that have rotation speeds of about 110 knots. During the takeoff run, high viscosity fluids, such as Type II fluids, develop a wavy surface that in effect is a form of surface roughness that degrades aerodynamic performance. The high takeoff run speeds of the large transports help shear the fluid and reduce its viscosity, and the long takeoff runs (about 25 sec) provide time for most of the fluid to flow off the wings before rotation. These fluids are not intended for commuters and general aviation aircraft whose rotation speeds are usually less than 85 knots and whose takeoff run times are about 15 sec. One commuter manufacturer found that its aircraft would have to be held on the ground for about 30 sec during the takeoff run to ensure adequate fluid runoff from the wings and tails; otherwise, the aircraft would not rotate because the residual fluid caused excessive lift loss on the tail (Ref. 8). **THE OPERATOR OF AN AIRPLANE SHOULD CONSULT THE AIRPLANE MANUFACTURER FOR RECOMMENDATIONS REGARDING THE USE OF TYPE I AND TYPE II FLUIDS.**

2.4.3 Holdover Time

"Holdover time" is the estimated time the anti-icing fluid will prevent frost, ice, snow or other forms of freezing precipitation from forming or accumulating on the protected surfaces

of an aircraft. Holdover time is estimated to be the time interval between when the fluid was applied and when ice crystals became visible in the fluid, for a given intensity and type of freezing precipitation and outside air temperature or wing surface temperature.

Tables of holdover times were first developed by the AEA on the basis of tests in the laboratory and in real winter conditions, and from years of experience of several European airlines. These holdover time tables have served as a guideline to pilots in Europe, where there have been no takeoff accidents attributable to ground icing for over 20 years. The original AEA tables have been modified by the international SAE G-12 Committee on Aircraft Ground Deicing Fluids, which had access to additional test results in real winter conditions in the United States and Canada. These adjusted tables are presented in Figs. 7 and 8 for Type I and Type II fluids, respectively (Ref. 9). While the AEA tables give only one protection time, the SAE tables give two protection times: a lower time and an upper time. This range serves to remind the user that protection times depend on many factors.

The SAE tables should not be separated from the procedures document (SAE ARP 4737), since the holdover times depend upon following the proper procedures, cautions, and caveats given in that document. The two cautionary notes given in the tables are worth repeating here:

CAUTION: The times of protection represented in this table are for general information purposes only and should be used *only in conjunction with a pre-takeoff inspection.*

CAUTION: The time of protection will be shortened in heavy weather conditions, high wind velocity and jet blast may cause a degradation of the protective film. If these conditions occur, the time of protection may be shortened considerably. This is also the case when the fuel temperature is significantly lower than OAT.

These two cautions reveal the complexity and challenge the pilot in command faces in making a final determination as to whether it is safe to take off.

2.5 FAA Rulemaking on Ground Icing

On July 21, 1992, the FAA announced that it would issue a Notice of Proposed Rulemaking that would require each airline to have an FAA-approved ground deicing program in place by the next winter (Ref. 10). The proposed rule would require airlines to provide training for pilots and other personnel on the detection of wing ice and provide for establishment of limits on how long an airplane can be exposed to snow or freezing rain before it had to be inspected or deiced again. The FAA would also change operational procedures for controlling the flow of aircraft on the ground to reduce the time aircraft have to wait in line for takeoff after being deiced. The FAA would also encourage the use of the longer-lasting AEA Type II anti-icing fluid, which is thicker and stays effective longer than Type I. The FAA would also help finance the construction of deicing pads on taxiways to further reduce the time between deicing and takeoff. For airports that historically had experienced takeoff delays due to heavy winter operations, the FAA would encourage airport,

airline, and air traffic control officials to jointly develop deicing plans tailored to their specific airport.

On November 1, 1992, revised FAR 121.629 became effective. It requires the operator to develop an FAA-approved aircraft ground deicing program and implement it when weather conditions are conducive to ground icing. *These plans are highly individualized to the particular operator at the given airport and must be approved by the FAA's Principal Operations Inspector or Principal Maintenance Inspector for the airport.*

The FAA-approved aircraft ground deicing program must include (Ref. 2, 11):

1. Procedures to determine the existence of conditions conducive to icing of aircraft on the ground.
2. Sound management, training of flight and ground crews, qualification of all affected personnel, and assignment of specific responsibilities.
3. Specific checks and inspections during the deicing process.
4. A *pre-takeoff check or inspection* within 5 min of takeoff. Using supportable holdover time tables, the operator must establish a holdover time for the applied deicing or anti-icing fluid under the existing precipitation conditions and outside air temperature.

FAR 121.629 allows operators to:

1. Develop and use FAA-approved alternative procedures such as ice detectors.
2. Elect to not operate in ground icing conditions if so stated in its Operations Specifications.
3. Dispatch and take off with slight amounts of frost (up to 3 mm) on underwing surfaces in the vicinity of cold-soaked fuel cells if approved by the FAA Aircraft Certification Office.

Operational procedures acceptable to the FAA as set out in FAR 121.629 are summarized below:

1. A pre-flight external aircraft icing check must be performed by qualified ground personnel immediately following applications of aircraft de-icing and anti-icing fluids. This check determines whether the critical surfaces are free of frost, ice or snow before push-back or taxi, and the results of the checks are communicated to the pilot in command. The aircraft should be released for take-off as soon as possible.
2. A pre-takeoff check is required within 5 min of takeoff anytime conditions conducive to ground icing exist and/or anytime the aircraft has been deiced or anti-iced and a holdover time established.
3. *If the pre-takeoff check occurs within the holdover time*, the pilot or designated crew member (co-pilot or flight engineer) normally checks from inside the cockpit or cabin, whichever provides the best vantage point. The pilot in command may require the assistance of qualified ground personnel to assist in the pre-takeoff check.

4. If the pre-takeoff check occurs after the holdover time is exceeded, the pilot in command must make a pre-takeoff contamination inspection. Depending upon the agreement between the FAA and the operator (which would take into account the type of aircraft and other factors) this inspection may range from observing the wings from some vantage point inside the aircraft to an external inspection by a licensed inspector. The FAA prefers external inspections, which might include observation from a high vantage point using binoculars, or actual touching of the aircraft surfaces.

An alternative action that could be taken if holdover time is exceeded is to re-deice/anti-ice the wings, control surfaces and other critical surfaces and establish a new holdover time.

5. An Airworthiness Directive (AD) on pre-takeoff ground icing inspections has been published for each of three specific aircraft types. Actions to be taken for these aircraft if holdover time is exceeded are as follows:

- a. On the F28 and DC-9-10 (hardwing aircraft) and on the MD 80/88 (aircraft with cold-soaked wings), conduct the check from outside the aircraft in accordance with an FAA-approved method as set forth in the AD. The operator must include a tactile check of selected portions of the wing leading edge and upper wing surface.
- b. On those aircraft for which an AD exists for pre-takeoff ground icing inspections, the manufacturer may offer alternative methods to establish that the critical surfaces are not contaminated.

For the hardwing aircraft, such methods might include: on-ground operation of the wing thermal anti-ice system; an abrasion strip which is rough when no ice is present and smooth when covered with ice, such that when an inspection rod is run over the strip, vibrations are felt when the strip is clean, but no vibrations are felt when the strip is covered with ice; a paint stripe or special reflective surface for a background that clearly shows up ice when it is present; improved lighting; surface ice detectors; or surface boundary layer flow sensors.

For cold soaked wings, existing methods include: wing tufts placed near the fuel cells such that when the tufts are probed with a long stick, the tufts will move when ice is absent, but will be frozen in place when ice is present; or surface ice detectors placed near the fuel cells.

If the FAA approves an alternative method, they will issue a replacement AD, which will define the allowable alternative inspection methods. A replacement AD has been issued for the F28 that allows the external tactile inspection to be replaced by the use of black paint stripes on the wing at selected locations in conjunction with an external visual inspection.

FAR's 125.221, 125.287, 135.227, 135.345, and 135.351 were revised and became effective December 1, 1993. They require:

1. The operator to develop and use FAA-approved, airplane type specific procedures for performing required pre-takeoff contamination checks or an approved alternate procedure for assuring the clean aircraft concept.

2. Initial and recurrent training and testing for pilots regarding procedures and ground operations in icing conditions.

3. A pre-takeoff contamination check within 5 min of takeoff.

FAR 125 and 135 allow:

1. Voluntary application of FAR 121 rules, summarized above, to FAR 125 and 135 operations.
2. Use of supportable holdover time tables with anti-icing fluids to assist in departure planning.
3. Takeoff with slight underwing frost formations if FAA approved.

As a result of these revised FAR's, FAA personnel, airline operators, traffic controllers, and airport authorities have been aggressively developing and implementing procedures to minimize aircraft takeoff hazards in icing conditions. The SAE G-12 Committee, airplane manufacturers, and fluid manufacturers have also supported the activity. These actions have resulted in significant improvements in the ground deicing/anti-icing technologies as summarized below (Ref. 11):

1. New and improved AEA/SAE/ISO Type II anti-icing fluids and procedures are now in prevalent use in North America and in Europe. If used properly, these fluids give longer protection.
2. Holdover time tables now exist that can be used in concert with other methods of assuring the clean aircraft concept. Although not yet fully validated, these tables, with proper training and guidance, can reduce flight crew confusion and workload.
3. New aerodynamic test data and experimental qualification methods ensure that deicing/anti-icing fluids do not themselves impose unacceptable aerodynamic penalties during takeoff.
4. Many operators and airports are now using either permanent or mobile deicing and anti-icing facilities located very near the departure end of runways. This method offers enormous benefits, including last minute assurances of a clean aircraft at takeoff, minimized operations time and fuel consumption, and avoidance of aircraft having to return to a maintenance or service area for re-deicing/anti-icing if ice formations were detected during pre-takeoff inspections. At many airports, where it is not yet feasible to locate spray facilities at the departure end of runways, other alternatives exist.

There is still room for improvement of the SAE holdover time tables. Better scientific methods are needed to obtain and analyze holdover time data, and to quantify the weather conditions. Ideally, the pilot needs a way to quantify the weather conditions and to put this quantified information into a computer program that will output a more accurate estimate of holdover time.

Instruments are needed that will help the pilot determine if ice has formed on the the wings at the time of the pre-takeoff check. The instruments should be able to survey the entire upper wing surface; ice detectors that sample ice at discrete points on the wing are probably not sufficient.

And finally, operators should be encouraged to locate deicing facilities near the departure end of runways so that the aircraft can be deiced, and without further delay, start the takeoff run. Fortunately, there is a trend toward airports opting for end of runway deicing when it is feasible.

3. ADVANCED TECHNOLOGY FOR IN-FLIGHT ICE PROTECTION

Even though aircraft ice protection technology matured in the 1940's, icing technology problems still continue to arise. Most of these problems have arisen either because modern aircraft have incorporated new technologies that have a ripple effect on the ice protection systems or because global economic competition has intensified the need to further optimize aircraft performance and to minimize development, capital, operating, and maintenance costs. And the aircraft ice protection system enters into these optimization strategies. In this section we briefly discuss in-flight icing and the advanced icing technologies being globally pursued by researchers, manufacturers, and regulatory agencies. Among these advanced technologies are advanced ice protection concepts and advanced computer codes.

Figure 9 shows the components of an aircraft that require ice protection.

3.1 Protection Against In-Flight Ice

Before discussing approaches to ice protection, we need to define "anti-icing" and "deicing" systems. *Anti-icing* systems prevent ice from forming either by using an evaporative system that applies enough heat to evaporate all the surface water deposited by cloud droplets, or by using a running wet system that applies just enough heat to prevent the water from freezing. With the running wet system, the water would run back in the form of rivulets that would cover the entire upper surface of the wing. To prevent the rivulets from freezing, the entire upper surface would have to be heated; but this arrangement would require far more energy than an evaporative system and would greatly complicate the design of the wing. Therefore, running wet systems are usually reserved for use on engine inlets with short duct runs. On some aircraft, anti-icing is accomplished with freezing point depressant fluids (usually mixtures of glycol and water) which are oozed out through a porous panel on the leading edge of the wing or other component.

Deicing systems allow ice to build to some prescribed thickness, and then the system is actuated to remove the ice. This is normally a repetitive or cyclic process of ice growth and ice removal. Thus, those wings and tails protected with deicing systems must be designed to tolerate the aerodynamic penalties imposed by the expected maximum thickness of ice that would accrete before actuation.

The ideal protection against icing would be to anti-ice all components that collect ice. The simplest way to do this would be to heat the surface and evaporate all the water. Unfortunately, this approach is not practical because no aircraft can economically provide the required thermal energy from the available on-board heat sources, which are hot compressor bleed air, engine waste heat, and electricity.

A more realistic approach is to protect only critical components, and design the airplane to tolerate some ice on the other components. Today's modern jet transports utilize compressor

bleed air to anti-ice engine nacelles and critical sections along the wing span. Because today's high by-pass-ratio engines can deliver only a limited amount of compressor bleed air, aircraft manufacturers anti-ice as little as 40 percent of the wing span, and allow the other 60 percent to accrete ice during an icing encounter. Reference 12 gives an illustration that shows the percentage of wing span that is anti-iced on each of Boeing's aircraft.

Jet transport manufacturers use wind tunnels to test aircraft models with simulated ice shapes attached to the leading edge of the wings and tails. From these tests they learn how the ice affects handling characteristics and stability and control, and determine which parts of the wings and tails can be left unprotected. To verify their wind tunnel results, they apply simulated ice shapes to a real aircraft and flight test it in clear air.

Some airplane manufacturers have found from their airframe integration studies that fuel burn during cruise can be reduced by eliminating the ice protection on the empennage (thus avoiding heavy and complex ducting that carries bleed air from the engines to the tail) while making the tail sections larger to tolerate the expected ice. Other manufacturers have found that the best way to reduce fuel burn is to electrothermally deice the tail, which allows them to reduce tail size, and in turn, reduce weight and drag penalties.

Business jets usually employ the same approach to ice protection as the larger jet transports, but turboprop and general aviation aircraft must employ a significantly different approach. Their power margins are so small that only their propellers and engine intake lips are electrothermally anti-iced and the remaining critical components are deiced either with expandable pneumatic boots or with electrothermal deicers.

Pneumatic boots are attractive because they require very little power, are lightweight, and are reasonably priced. One drawback usually cited for pneumatic boots is that for effective ice removal, they must not be activated until about one quarter to one half inch of ice accretes on them. This procedure prevents "ice bridging," which sometimes occurs when boots are expanded with smaller thicknesses of ice. Several inflations may be required to remove the bridged ice, during which time ice continues to accumulate on the cap and further degrades aerodynamic performance. Airplanes that are certified for flight into icing with pneumatic boots must be designed to tolerate the additional one-quarter to one-half inch of ice.

3.2 Advanced Impulse Deicers

The last decade has seen the development of alternatives to the conventional electrothermal and pneumatic boot deicers. These are the electromagnetically and pneumatically actuated mechanical impulse deicer systems: EIDI (electromagnetic impulse deicing); EEES (electro-expulsive separation system); EDI (electromagnetic deicing strip); and PIIP (pneumatic impulse ice protection) (Ref. 13). These systems produce a rapid impulse that cracks, debonds, and dynamically expels the ice. Unlike the slowly expanding conventional pneumatic boots, which rely on aerodynamic forces to remove ice, the impulse systems accelerate the iced surface up to 1000 g's, and inertially eject the ice as the surface snaps back. The inertial ejection process can remove ice layers as thin as 0.75 mm (Ref. 14). With these thinner ice layers, the

aerodynamic penalties for ice contamination are correspondingly reduced, and in addition, the ejected ice particles are very small. The small particles make the impulse deicers attractive for application to engine inlets, where ingested particles must not damage the engine components. Their power requirements are quite low—about equal to the power consumed by the aircraft's landing lights or about one percent of an electrothermal anti-icing system or ten percent of an electrothermal deicing system. Although somewhat heavier than conventional pneumatic deicers, their weights still appear competitive.

The PIIP, invented and manufactured by BFGoodrich Deicing Systems, Inc., is the only impulse system which is being applied commercially today—on only one aircraft, the Grob GF-200. The electromagnetic impulse systems have proved effective in removing ice, but their relative complexity and uncertain life expectancy have apparently discouraged any airframer from using them thus far, but manufacturers can produce them for the aviation market right now.

Lynch, et. al., have expressed concern about the aerodynamic penalties that would be imposed on jet transports by the use of the advanced impulse deicers, which can limit ice thickness to only 0.75 mm (Ref. 3). In their experimental studies on the effects of roughness on airfoil aero performance, they found that "...reductions in maximum lift capability on configurations without leading-edge devices extended are very large, even for extremely small leading-edge ice (roughness) buildups. For example, roughness heights of around 0.005 in. [0.127 mm] would result in reductions in the maximum-lift capability of 20 percent at the critical spanwise stations on the wing or tail of a representative 200-seat transport. Obviously, the concern is even greater for smaller aircraft. Increasing the leading-edge roughness size to at least 0.03 in. [0.762 mm], perhaps the minimum ice buildup that can be reliably eliminated by a deicing system, would result in losses in maximum lift capability of up to 40 percent for the 200-seat aircraft. If the wing or tail surface areas for a particular configuration are sized by maximum lift capability, then corresponding increases in surface areas would be required, with all the attendant performance penalties (drag, weight, etc.)."

For slatted airfoils, Lynch, et. al., say: "Lower percentage losses in maximum-lift capability due to leading-edge ice buildups are experienced if the ice buildup occurs on an extended/deflected leading-edge device such as a slat. The maximum penalty for the 0.03 in. [0.762 mm] ice buildup on a slat would be about 10 percent at typical landing flap settings. However, the penalty could well be near 20 percent on the wing for lower takeoff flap settings, or for a tail (without deflected flaps). Again, these penalties would all be increased for smaller aircraft."

It appears that because of the engine manufacturers' continuing quest to improve engine performance, their next generation of high by-pass-ratio turbofan jet engines will provide little or no excess bleed air for thermal anti-icing. Therefore, those involved in ice protection technology have been forced to consider efficient *deicing* systems as a possible alternative to the conventional thermal anti-icing systems. The above conclusions, by a major aircraft manufacturer, will likely create controversy and confusion about the future markets for impulse deicers—the first new ice protection concept to be demonstrated in about 40 years. This issue needs further

discussion and clarification by all the major aircraft and engine manufacturers. And perhaps there is need for flight tests of a modern jet transport with simulated roughness applied on its wings and tails to correlate two-dimensional wing section results with full-scale three-dimensional flight test results.

3.3 Physical Characteristics of Ice Accretion

As mentioned earlier, the shape of ice accreted on the unprotected portion of a wing or other component depends on the atmospheric environment (outside air temperature, liquid water content, and droplet sizes), the flight conditions (airspeed and AOA), and the component geometry (size, cross-section, and sweep). Rime ice and glaze ice were mentioned in the Introduction as two extremes of icing shapes, but actually there is a continuum of icing shapes that range from rime at the coldest temperatures to glaze at the warmest. In rime ice formation, the droplets freeze upon impact and trap air in between the frozen droplets, causing the ice to appear white and opaque. In glaze ice formation, the droplets impact the surface and form a water film that partly freezes at the droplet impact site and partly runs back along the chord to freeze farther aft. Glaze ice is clear like refrigerator ice. Between the extremes of rime and glaze, the ice shape gradually changes from a pointy shape to a single- or double-horned shape, and these in-between shapes are referred to as mixtures of rime and glaze, or as mixed icing. In the mixed regime, the ice formed near the stagnation region is usually clear glaze while the ice farther aft, where heat transfer is higher, has an opaque rime appearance. Figure 10 (Ref. 15) illustrates how total temperature affects the ice cross section when all other atmospheric and flight conditions are held constant.

Liquid water content, droplet size, and air speed also affect the ice shape, and increasing any or all of the above will increase the amount of water deposited on the surface and move the ice shape towards the glaze end of the spectrum. Increasing airspeed presents two opposing influences on ice shape: the increased convection heat and mass transfer encourages freezing while the increased kinetic heating discourages freezing. But ultimately, a speed or Mach number will be reached, beyond which kinetic heating will dominate and ice will not form. This explains why the wings of fighter aircraft are not ice protected.

Component size and shape also affect the ice shape. Relative to their size, smaller components accrete more ice than do larger components. This is illustrated in Fig. 11. This size dependence has great significance to aircraft ice protection system design requirements. For example, the wings of a C-5A aircraft are so large that only a small strip of ice would accrete on them, and as a result, the C-5A's wings do not require ice protection.

Size dependence is very important to smaller aircraft flying in icing conditions. It is frequently the case that even though the wing appears to be free of ice, the tailplane has collected enough ice to adversely affect its aerodynamics, particularly during approach and landing. To deal with this problem, pilots often look for ice accretion on the smallest object they can see, for example, the windshield wiper blade. If the windshield wiper is picking up ice, pilots know they are in icing conditions and should either turn on the ice protection systems or get out of the icing clouds.

Another parameter affecting ice shape is sweep on wings or any other component. Sweep causes spanwise flow of air along the leading edge, which in turn causes ice to form scallops or lobster tails. These ice shapes have a spanwise periodicity that has not been satisfactorily explained or predicted by analysis (Ref. 16). Although they look grotesque, their effect on aerodynamic performance may be no worse than that of the glaze horns on unswept wings. In fact it has been suggested that the scallops may act as turbulence generators and help keep the flow attached.

3.4 Advanced Computer Codes

As in every other aircraft technology area, computer codes are heavily used in aircraft icing to support design, development, and certification. Although the final proof in the icing certification process will always be through flight testing in natural icing conditions, manufacturers hope that computer code calculations can replace some of the flight testing. Icing flight testing is regarded by the entire aircraft industry as risky, costly, lengthy, and resource intensive.

Today, computer codes are used extensively throughout the aircraft industry to design ice protection systems or to predict ice accretion shapes on unprotected surfaces. For example, about 100 organizations in the United States are using NASA's LEWICE ice accretion code. Codes developed by ONERA in France and the DRA in Great Britain give comparable results and are heavily used throughout Europe. Other organizations also have ice prediction codes in various stages of development. Most of these codes are considered research codes, which means that while they are not fully validated, they are the best codes available and are very useful to those who have experience with them and understand their limitations. But, they are still being improved and validated through the development of advanced numerical methods, through the development of advanced physical models obtained from fundamental physics experiments, and through comparisons with new data from basic experiments and operational experience.

The codes most often employed in aircraft icing include 1) flow codes, 2) droplet trajectory codes, 3) ice accretion prediction codes, 4) electrothermal deicer design/analysis codes, 5) anti-icing ice protection system design codes, 6) iced airfoil aeroanalysis codes, and 7) helicopter rotor and propeller performance-in-icing codes.

3.5 Ice Accretion Predictions

Since this lecture is time-limited, we are unable to discuss the details of the computer codes. The interested reader should consult Ref. 17, which give more details and more references. In this section we will briefly discuss the LEWICE ice accretion prediction code. Figure 12 shows the modeling approach in LEWICE. The code consists of three main elements: 1) flowfield prediction; 2) water droplet trajectory prediction; and 3) ice accretion prediction. The flowfield code normally used is a potential flow panel code, although LEWICE can accommodate Navier-Stokes or Euler or compressible potential flow solvers. The droplet trajectory code uses results from the flowfield code to calculate the flux of water impinging on the leading edge region of the airfoil. The ice accretion code solves a thermodynamic energy balance and a mass balance on surface control volumes that coincide with the panel elements on the airfoil as shown on Fig. 13. LEWICE cycles through the three elements to calculate an ice shape for a given time increment or time step.

Then the flowfield is recomputed for the new ice covered airfoil, the droplet trajectories are recomputed, and a new layer of ice is computed for a time step. This process is repeated until all the of time steps add up to the total exposure time.

LEWICE is most accurate in predicting the colder ice shapes, and less accurate for the warmer ice shapes. At the colder temperatures, the droplets freeze upon impact and the accuracy of the ice shape prediction is determined primarily by the accuracy of the droplet trajectory prediction. Fortunately, droplet trajectory codes have good accuracy. At the warmer temperatures, the water only partly freezes at the droplet impact site, and the unfrozen water runs aft and eventually freezes. *At these warmer temperatures, the shape of the ice is controlled by heat transfer to the surrounding air.* The lower prediction accuracy for the warmer temperatures is attributed primarily to the lack of good heat and mass transfer prediction models for ice-roughened surfaces. Another source of inaccuracy is the limitation of the physical model of the icing process.

As just noted, central to the heat balance on the water at the warmer temperatures is the prediction of convective heat and mass transfer from the water surface to the air flowing over the surface. It is helpful to keep in mind that the air flowing over the airfoil is the sink for heat and mass. Thus, when water freezes on the surface, its heat of fusion is transferred to the surrounding air by convection heat transfer and by evaporative cooling through convective mass transfer.

The surface of ice is covered with roughness. This roughness does not affect the heat and mass transfer in the laminar boundary layer, but it does affect the transition location and the heat and mass transfer in the turbulent boundary layer. Turbulent heat transfer correlations and analytical models exist for standard sandgrain surface roughness that is about 10 percent or less of the boundary layer displacement thickness. Unfortunately, ice roughness is usually thicker than the boundary layer displacement thickness, and therefore, there are no validated correlations or analytical models for heat transfer over ice-roughened surfaces. Lacking anything better, the ice accretion prediction codes use the sandgrain roughness models and ignore the fact that they were validated only for roughness heights much less than the displacement thickness.

3.6 Basic Studies in Support of Computer Codes

In spite of their limitations, the computer codes are being used successfully by those who have had experience with them and know their limitations. Yet, it is obvious that there exists a need for further basic studies to improve the numerical techniques and the physical models of heat and mass transfer and of the ice accretion growth process. Basic numerical studies to improve the numerical stability of the LEWICE ice accretion code are being conducted at NASA Lewis. For LEWICE, it has been found that predicted warm ice shapes are sensitive to the number of time steps that make up the total exposure time. For the current version of LEWICE, about five time steps is optimal. More time steps can lead to instabilities in the ice shape, such that the results do not converge to a single ice shape as would be expected with finer and finer time increments. Bidwell (Ref. 18) has succeeded in writing a numerical algorithm that eliminates the shape instability, and his results converge to a single ice shape as time step increment is reduced.

NASA Lewis is conducting basic experimental research to better understand how ice shapes develop under various icing conditions and how ice roughness develops and affects laminar-to-turbulent transition and heat and mass transfer. One objective is to quantify ice roughness and correlate it with the cloud and flight conditions. Other objectives are to conduct experiments that will aid in developing heat and mass transfer correlations and analytical models for flow over iced surfaces and mass transfer correlations and analytical models for flow over smooth surfaces.

3.7 Experimental Icing Simulation

Good experimental icing simulation facilities such as icing wind tunnels and in-flight spray tankers are essential because they are more productive, more economical, and far safer than flight testing in natural icing conditions. Since smaller aircraft and helicopters have limited range, they must wait for the icing weather to come to their test sites. This waiting has extended icing flight trials over several winters, and has driven up the cost for icing certification. Longer-range aircraft fly long distances to where ice is forecasted, but the cost per flight hour of these aircraft is very high, and the manufacturer works hard to control these costs.

Figure 14 shows the closed-loop circuit of the NASA Lewis Icing Research Tunnel (IRT). Two unique components of the IRT are its heat exchanger that refrigerates the air and its water spray system that uses air-blast nozzles to produce supercooled clouds. The IRT can produce the desired test conditions any time of the year regardless of the weather outside. Because of its uniqueness and versatility, the IRT is one of NASA's most heavily utilized wind tunnels, logging about 1000 hr of test time annually.

4. ICE CONTAMINATED TAILPLANE STALL (ICTS)

We ordinarily associate the hazards of in-flight icing with wing ice, knowing from our earlier discussions that 2 mm thick ice roughness can increase stall speed by 18 percent and reduce stall angle by 6°. But we are not as aware that even thinner roughness on the tailplane leading edge can cause potentially catastrophic tailplane stall during approach or landing, when the wing flaps are extended. Ice contaminated tailplane stalls during approach or landing have caused some airplanes to go into a steep dive. And if this happened at low altitude, the chances of recovering from the dive were slim to none.

Figure 15 shows the catastrophic flight path and aircraft attitudes of the Vickers Viscount that crashed at Stockholm in January 1977 (Ref. 19). "The broken curve" according to Dr. Martin Ingleman-Sundberg, "shows the flight path that might have been attained, in spite of the stall, if the pilots had managed to keep the yoke back."

According to Mr. John Dow (Ref. 20), from the FAA's Small Airplanes Directorate, "Sixteen known or suspected ICTS accidents occurred worldwide to turboprop-powered transport and commuter category airplanes, resulting in 139 fatal injuries." The FAA has issued eight Airworthiness Directives (ADs) against five airplane types in commercial service in response to ICTS related accidents and incidents. Although turboprop aircraft had the highest number of ICTS accidents and incidents, the problem is not limited to a specific size or configuration of airplane. Indeed, a worldwide survey revealed that piston, jet, and non-U.S. Type Certificated

aircraft accounted for an additional twenty accidents and incidents in which ICTS was considered a likely factor.

4.1 Uncovering ICTS Problems

By early 1991, the European Joint Airworthiness Authorities (JAA) had developed and published (Ref. 21) a required flight test maneuver that they believe identifies aircraft with ICTS problems. In this maneuver, the airplane (with specified tail ice contamination) is pitched over at a prescribed pitch rate to a load factor of zero "g". If the airplane remains in control, and the stick force characteristics are within defined limits, then the airplane stability and control characteristics with ice on the tailplane are judged acceptable by the JAA. The FAA has adopted the JAA's zero "g" maneuver in principle and has required it be performed as part of the icing certification process on a selective basis to date.

Some airplane manufacturers' test pilots believe the pushover to zero "g" maneuver is too dangerous and not a maneuver that pilots would intentionally do in normal operations. But the airworthiness authorities have been successful in getting compliance from the manufacturers and believe that it is currently the best maneuver to uncover ICTS problems. Generally, the manufacturer will use a cautious approach by starting with, say, a pushover to one-half "g". And in some cases, the one-half "g" maneuver has uncovered the ICTS problem.

Although acknowledging that the zero "g" maneuver poses high risk for test pilots, aircraft operators point out that even in normal operations, if the pilot's approach was high or fast, he might push over to get to the glide slope, or if the approach was slow, he might push over to pick up speed. In either case, that would be pushing the airplane towards zero "g". The operators would like these problems to be found by the highly skilled test pilots and fixed by the manufacturer rather than be encountered unexpectedly by the journeyman pilot. But everyone agrees that it would be beneficial to better understand what happens during the pushover maneuver and to use that knowledge to develop lower risk methods to identify ICTS problems.

4.2 Screening of Turboprop Airplanes for ICTS

Two recent international workshops sponsored by the FAA have alerted the aviation community to the seriousness of ICTS. Numerous articles about ICTS have been published subsequently in magazines read by pilots. Both the FAA and the manufacturers have responded with a new and concerted effort to 1) identify the causes of tailplane stall, 2) prevent it by design, 3) discover and fix it before the airplane is certificated for icing, and 4) educate pilots on how to avoid it in flight operations,

An important recommendation that came from the first workshop was that the FAA should screen all turboprops used in Part 121 or 135 operations for susceptibility to ICTS. The FAA responded by contracting with Mr. Pete Hellsten, a consultant in aircraft design, to develop an analytical method and apply it to the thirty-one turboprop airplanes that the FAA identified in the Part 125 or 135 categories. In the study, the FAA and Mr. Hellsten analyzed cruise, approach, and landing configurations at speeds from stall to V_{FE} ; they assumed a forward center-of-gravity and made calculations for both one "g" and zero "g" load factors; and they also analyzed each of the above combination of conditions for both clean tails and

tails contaminated with standard roughness. In discussing Hellsten's work (Ref. 22) herein, we present results only for tails contaminated with standard roughness.

4.3 Wing and Tail Aero Characteristics for Approach and Landing

For the purpose of explaining his analytical approach, Mr. Hellsten used the average geometry of the 31 turboprop configurations to develop a generic or "paper" airplane. Although not an actual airplane, the generic airplane was a good representation of the study. We will use the data from Hellsten's analysis of this generic airplane to illustrate the changes in wing and tailplane operating characteristics during approach and landing (this viewpoint was first adopted by Dr. Ingleman-Sundburg in Ref. 19).

Figure 16 shows plots of wing lift coefficient versus wing angle of attack for the cruise, approach, and landing configurations. Superimposed on these plots are the operating points for cruise, approach, and landing. Starting with a cruise speed of 200 kt (point 1), the pilot decreases speed to 126 kt (point 2) while increasing the wing AOA from 2.5° to 9.5° . Next, the pilot deploys half flaps and lowers wing AOA to 7° (point 3) and then further decreases speed to 114 kt while increasing wing AOA to 9.5° (point 4). Finally, the pilot extends full flaps and lowers wing AOA to 4.5° (point 5). Eventually the pilot reduces speed and increases wing AOA while slowing to touch down.

Several aircraft responses accompany the deployment of flaps. First, when the flaps are initially deployed, say at point 2, the wing AOA has not yet changed, and the airplane is lifted because it is temporarily operating on the half-flap lift curve at an AOA of 9.5° . This effect is termed "ballooning". Second, the deployed flaps move the center of pressure farther aft on the wing, causing a nose-down pitching moment. Third, the extended flaps increase the wing downwash angle, which in turn increases the AOA on the tail and produces a greater downward force on the tail. The pilot compensates for these effects by moving the yoke to trim out the airplane. During the trim adjustment, the nose pitches down to a lower wing AOA and the tail pitches up to a higher tail AOA. During the upward motion of the tail there is an increased downward relative velocity on the tail which further increases the tail AOA. The critical moment occurs when deploying full flaps because this results in the largest trim adjustment to get to the smallest wing AOA (point 5) and, conversely, to the largest tail AOA. This is the critical point where tail stall margin is least and tail stall might occur.

The above discussion also illustrates a dilemma that the pilot can get into: If the pilot suspects that wing ice contamination has increased the wing stall speed and he increases speed to compensate, the wing AOA will decrease, but the tail AOA will increase. The increased tail AOA might possibly reduce tail stall margin to the point where a sudden downburst or nose-down pitch could stall the tail. **IT IS IMPORTANT THAT THE PILOT KNOW AND FOLLOW THE MANUFACTURER'S RECOMMENDATION IN THIS SITUATION AND FLY IT BY THE BOOK.**

By interpolating the data of Hellsten, we were able to deduce the wing and tail operating characteristics for the six points shown in Fig. 16. The wing and tail configurations for these points are given in Fig. 17. Hellsten defines the wing and tail

stall margins as $(C_{L_{max}} - C_L)$ and $(C_L - C_{L_{min}})$, respectively. These margins are given on Fig. 18 for the six points on Fig. 16. (Figure 18 also shows stall margins for the zero "g" analysis, which will be discussed later). As expected, the tail stall margin is least at point 5 but does not seem excessively small. It would be difficult to draw any conclusions from the results shown in Fig. 18 about the susceptibility of this generic airplane to ICTS. These stall margins, however, are for the trimmed airplane and do not account for transients such as the nose down pitch rates or downgusts or control inputs that might temporarily increase tail AOA and push the lift margin to zero or negative.

Just as the JAA had found that the zero "g" flight test maneuver was the best discriminator of ICTS, Hellsten also found that his calculated response of an aircraft to the zero "g" maneuver correlated best with the airplane's actual ICTS history. Hellsten's study of the thirty-one turboprops showed that when his analysis predicted that an airplane had a negative or just slightly positive tail stall margin for the zero "g" maneuver, that airplane was likely to be susceptible to ICTS. During the pitchover maneuver, the wing loading is zero (zero lift) and the large nose-down pitching moment coming from the flaps is balanced by a large download or negative lift on the tail. The predicted tailplane configurations, lift coefficients, and stall margins during the zero-"g" maneuver are shown in the bottom of Fig. 18 for three airspeeds: V_{stall} , $1.3 \cdot V_{stall}$, and V_{FE} . The predicted stall margins for the zero "g" maneuver range from a low of 0.04 at V_{stall} to a high of 0.07 at V_{FE} . The tailplane was contaminated with standard roughness. These slightly positive stall margins put the generic airplane in the susceptible range for ICTS.

The results of Hellsten's screening analysis are summarized in Fig. 19, which is a histogram of the calculated tailplane stall margins for each of the 31 airplanes during the zero "g" maneuver for standard roughness contamination on the tail (Ref. 23). Hellsten's analysis predicted that eighteen of the 31 turboprop airplanes had stall margins that were either negative or just slightly positive. Of these 18 airplanes 13 have known histories of ICTS. The remaining 13 airplanes outside the susceptible range (meaning they have substantial positive stall margins) have no histories of ICTS. These findings gave the FAA confidence that they were heading in the right direction with this screening process. The FAA is currently working with the manufacturers of these 18 potentially susceptible airplanes to verify the methodology developed by Hellsten.

The question naturally arises as to whether certain design features distinguished airplanes that are not susceptible to ICTS. Hellsten found that those airplanes having no history of ICTS problems either had properly trimmed movable horizontal stabilizers or had tails with inverted camber. But, Dow cautioned that not all aircraft with movable tailplanes or cambered tails were free of ICTS problems. Hellsten also observed that the more effective wing flap systems (i.e., more Fowler motion) cause more nose-down pitching moment, thus requiring more negative lift on the tail to trim out the flaps and thereby driving the tail further toward stall. Although the use of movable stabilizers or cambered tails appear to be steps in the right direction, Hellsten cautioned that there is no simple answer to what works or doesn't work. The designer must go through the details of the design.

4.4 Stick Forces Caused by Stall of Fixed-Incidence Tailplanes

In a number of turboprop ICTS incidents or accidents, it was found that after the pilot extended full flaps, the stick lurched forward with such force that the pilot, or both the pilot and co-pilot, had to use all their strength to pull it back (on large turboprops, as much as 400 lb were required). This occurred on airplanes with fixed incidence tailplanes that had aerodynamically balanced elevators without power boosting. When the tailplane stalled, the separated flowfield redistributed the pressure over the elevator and caused an enormous downward hinge moment on it (Ref. 19). The problem is not a complete loss of elevator authority when the tailplane stalls, but rather the problem is the inability to detect the stall (stick lightening or vibration or tail buffeting) soon enough and to muscle the stick back so that the elevator is moved from the down to the up position. Even though the tail is stalled, it apparently can develop sufficient downward lifting force to prevent a dive.

4.5 Operating in Known or Suspected Icing Conditions

If you are in known or suspected icing conditions, you must be keenly aware of the deleterious effects of ice contamination on both wing and tailplane aeroperformance and the resulting reduction in airplane handling qualities and stability and control. Keep in mind that because the tailplane is smaller than the wing, ice can accumulate on the tail before you can actually see it on the wings or elsewhere; and relative to its size, the tailplane ice coverage will be thicker and extend farther aft than the ice on the wing (see Fig. 10). The bottom line is that the tail will accumulate more ice and be less tolerant of it than the wing. Also, on airplanes equipped with pneumatic boots for ice protection, remember that the smaller leading edge radius of the tail renders the tail boot less effective than the wing boot in removing ice. Thus the tail boot may have to be exercised more often than the wing boots; BUT HERE YOU SHOULD FOLLOW THE AIRPLANE AND PNEUMATIC BOOT MANUFACTURER'S RECOMMENDATIONS.

Several recommendations came from the two tailplane icing conferences and from subsequent articles published in pilot magazines. Some recommendations involved operational strategies that should help prevent an ice contaminated tailplane stall or help recover from one. There is an important caveat to any recommendation or guideline published here or elsewhere: **READ YOUR AIRPLANE FLIGHT MANUAL AND FOLLOW THE AIRPLANE MANUFACTURER'S RECOMMENDATIONS; THEY OVERRIDE ANYTHING THAT IS PRINTED HERE.**

The following partial, but representative, list of the guidelines for avoiding or recovering from ICTS was published recently by Manningham (Ref. 24):

After checking with the manufacturer and the FAA, consider the following guidelines to avoid tailplane icing and its worst consequences:

Know the level of icing for which your airplane is certified and never intentionally fly into icing conditions which exceed that level.

Never fly in known icing conditions with any anti-icing or deicing components inoperable.

When you observe ice on the wing, assume that there is even more ice on the tail and that it will have a more profound effect.

Use pneumatic boots and other deicing and anti-icing components strictly according to manufacturer's recommendations. Hangar tales and rumors never provide better operating procedures than those who make and test the equipment. If you have a question, talk to the manufacturers directly.

In icing conditions, make the landing approach with something less than full flaps. Half flaps or less are about right. Ask your manufacturer. Check the applicable ADs [Airworthiness Directives]. [Have a firm hold on the stick, and if your airplane has a fixed incidence tailplane with aerodynamically balanced elevators and no power boosting, anticipate the possibility that it could lurch forward with great force.]

In icing conditions be circumspect about adding speed for the final approach to compensate for ice on the wings. Every knot of speed added to prevent wing stall is a knot closer to tail stall... Fly the approach by the numbers if your airplane is one of those at greatest risk. [Adding speed lowers wing AOA and raises tail AOA, thus reducing tail stall margin to the point where a sudden downburst or nose-down pitch could stall the tail.]

If you do encounter pitch problems on final approach in icing conditions, muscle the elevator to the position you want, and it will provide adequate control to avoid a pitchover. The problem is not elevator authority but hinge moment and, therefore, control forces that you can overcome with muscle.

Be alert and wary during flap changes. Make final flap selection at least 1,000 ft above ground level so that any uncommanded pitchover will occur with enough altitude to recover.

If you experience an uncommanded pitchover during or shortly after flap selection, immediately return the flaps to the previous setting.

If the aircraft is high and fast on final approach, go around and try again. Several uncommanded pitchovers have been reported by pilots who attempted to slow rapidly with max flaps.

Tailplane icing is a real and serious threat to all airplanes, but especially to mid-sized, propeller-driven airplanes. Conversely, tailplane icing need not threaten your flight safety if you: (1) are aware of the potential, (2) limit final flap settings in icing conditions, and (3) maintain vigilance during the final approach.

It takes just the right combination of a number of factors that can momentarily increase the tail's AOA and trigger a tail stall. These factors include tail ice accumulation (and, maybe, not very much of it), deployment of flaps, higher airspeeds, low airplane AOA, nose-down pitch, forward center of gravity, headwind gusts, sideslips, downdrafts, etc. But by studying the above guidelines AND FOLLOWING THE

AIRPLANE AND ICE PROTECTION MANUFACTURER'S RECOMMENDATIONS, you should be well prepared to cope with ICTS.

We will conclude this section on ICTS by repeating Manningham's succinct advice:

The classic tail icing pitchover occurs on final approach as the flaps move to an increased setting. Appropriate pilot action is to use all necessary force to pull back on the yoke while returning the flaps to their previous setting. If you can remember the contents of this paragraph, you will have retained virtually all of the important information regarding tail icing.

REFERENCES

1. Brumby, R.E.: The Effect of Wing Ice Contamination on Essential Flight Characteristics. Paper No. 2 in AGARD-CP-496, Dec. 1991.
2. van Hengst, J.: Aircraft De-Icing and Future Technical Developments—An Aircraft Manufacturer's Point of View. Wingtips (Fokker Aircraft), No. 26, Sep. 1993.
3. Lynch, F.T.; Valarezo, W.O.; and McGhee, R.J.: The Adverse Aerodynamic Impact of Very Small Leading-Edge Ice (Roughness) Buildups on Wings and Tails. Paper No. 12 in AGARD-CP-496, Dec. 1991.
4. Hill, E.G.; and Ziertzen, T.A.: Flight and Wind Tunnel Tests of the Aerodynamic Effects of Aircraft Ground Deicing/Anti-Icing Fluids. AIAA Paper 91-0762, Jan. 1991.
5. Carbonaro, M.: Aerodynamic Effects of De/Anti-Icing Fluids, and Description of a Facility and Test Technique for their Assessment. Paper No. 18 in AGARD-CP-496, Dec. 1991.
6. Anon.: Aerodynamic Acceptance Test for Aircraft Ground Deicing/Anti-icing Fluids. Boeing Commercial Airplanes Document No. D6-55573, Mar. 1992.
7. Jarrell, M.S.: SAE Type I Aircraft Deicing/Anti-Icing Fluids. Report of the FAA International Conference on Airplane Ground Deicing, Reston, VA, U.S.A., May 28-29, 1992.
8. Ellis, N.; Lim, E.; Teeling, P.; and Zhu, S.: Wind Tunnel Tests of Aerodynamic Effects of Type I & II Ground De/Anti-icing Fluids on Small Transport & General Aviation Aircraft During Takeoff. AIAA Paper 91-0763, Jan. 1991.
9. Anon.: Aircraft Deicing/Anti-Icing Methods with Fluids, for Large Transport Aircraft. Society of Automotive Engineers (SAE) Aerospace Recommended Practice Document No. SAE ARP4737, Oct. 1992.
10. Farrar, F.: FAA Announces Action to Prevent Ice on Aircraft. FAA News Release FAA 36-92, July 21, 1992.
11. Adams, R.I.: Personal communication.
12. Cozby, D.E.: Ice Protection/Detection. Report of the FAA International Conference on Airplane Ground Deicing, Reston, VA, U.S.A., May 28-29, 1992.
13. Bond, T.H.; and Shin J.: Advanced Ice Protection Systems Test in the NASA Lewis Icing Research Tunnel. NASA TM-103757, May 1991.
14. Shin, J.; and Bond, T.H.: Surface Roughness Due to Residual Ice in the Use of Low Power Deicing Systems. AIAA Paper 93-0031, Jan. 1993. (Also, NASA TM-105971, Jan. 1993.)
15. Olsen, W.A.; Shaw, R.J.; and Newton, J.: Ice Shapes and the Resulting Drag Increase for a NACA 0012 Airfoil. NASA TM-83556, Jan. 1984.
16. Reehorst, A.L.: Prediction of Ice Accretion on a Swept NACA 0012 Airfoil and Comparisons to Flight Test Results. AIAA Paper 92-0043, Jan. 1992. (Also, NASA TM-105368, Jan. 1992.)
17. Potapczuk, M.G.; and Reinmann, J.J.: Icing Simulation: A survey of Computer Models and Experimental Facilities. Paper No. 5 in AGARD-CP-496, Dec. 1991. (Also, NASA TM-105192, Oct. 1991.)
18. Bidwell, C.: Personal communication
19. Ingelman-Sundberg, M.: Why Icing Causes Tailplane Stall. Air Line Pilot, Jan. 1992.
20. Dow, J. Sr.: Presentation at Ice Contaminated Tailplane Stall Program, FAA-NASA Planning Meeting. NASA Lewis Research Center, May 2-3, 1994.
21. Cattaneo, G.: Evolution Reglementaire en Matiere de Certification des Avions Civil en Conditions Givrantes. Paper No. 4 in AGARD-CP-496, Dec. 1991.
22. Hellsten, P.: Aerodynamic Analysis of Susceptibility to Ice-Induced Tailplane Stall. Conference Proceedings of International Tailplane Icing Workshop II, San Jose, CA, U.S.A., Apr. 21-23, 1993.
23. Dow, J. Sr.: Actions in Progress. Conference Proceedings of International Tailplane Icing Workshop II, San Jose, CA, U.S.A., Apr. 21-23, 1993.
24. Manningham, D.: Tails of Woe. Business & Commercial Aviation, Jan. 1993.

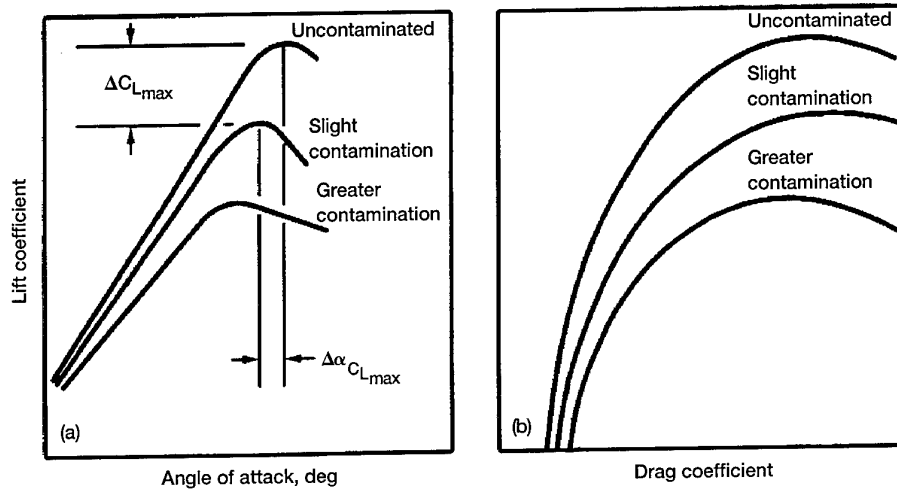


Figure 1.—Effect of wing ice contamination on lift and drag coefficients (ref. 1). (a) Lift coefficient. (b) Drag coefficient.

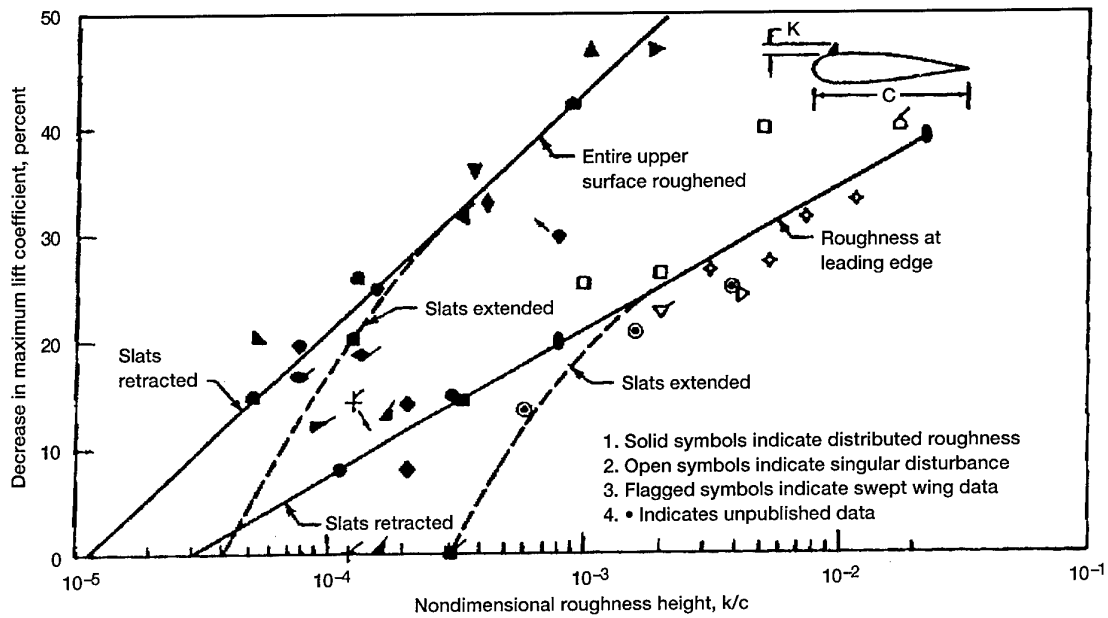


Figure 2.—Correlation of the effect of wing surface roughness on maximum lift coefficient (ref. 1).

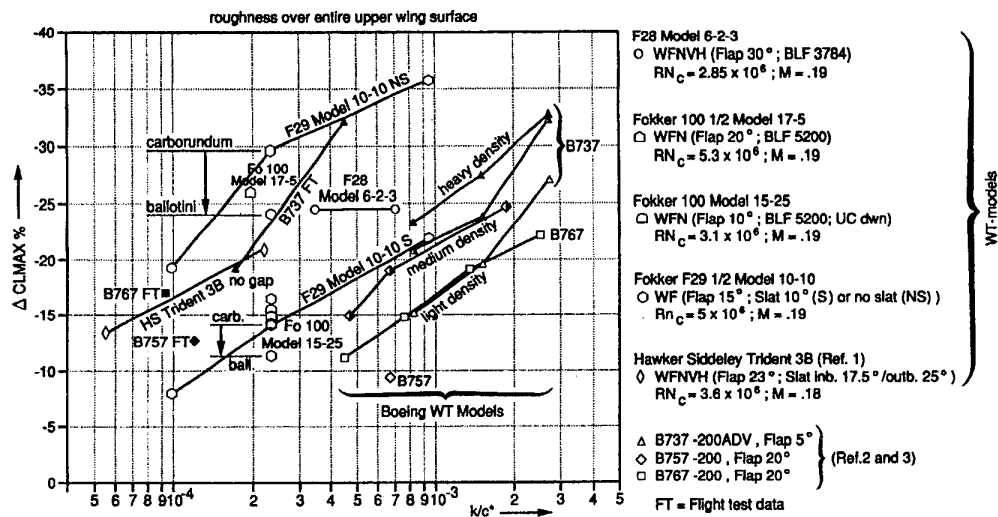


Figure 3.—Effect of roughness on maximum lift coefficient (ref. 2).

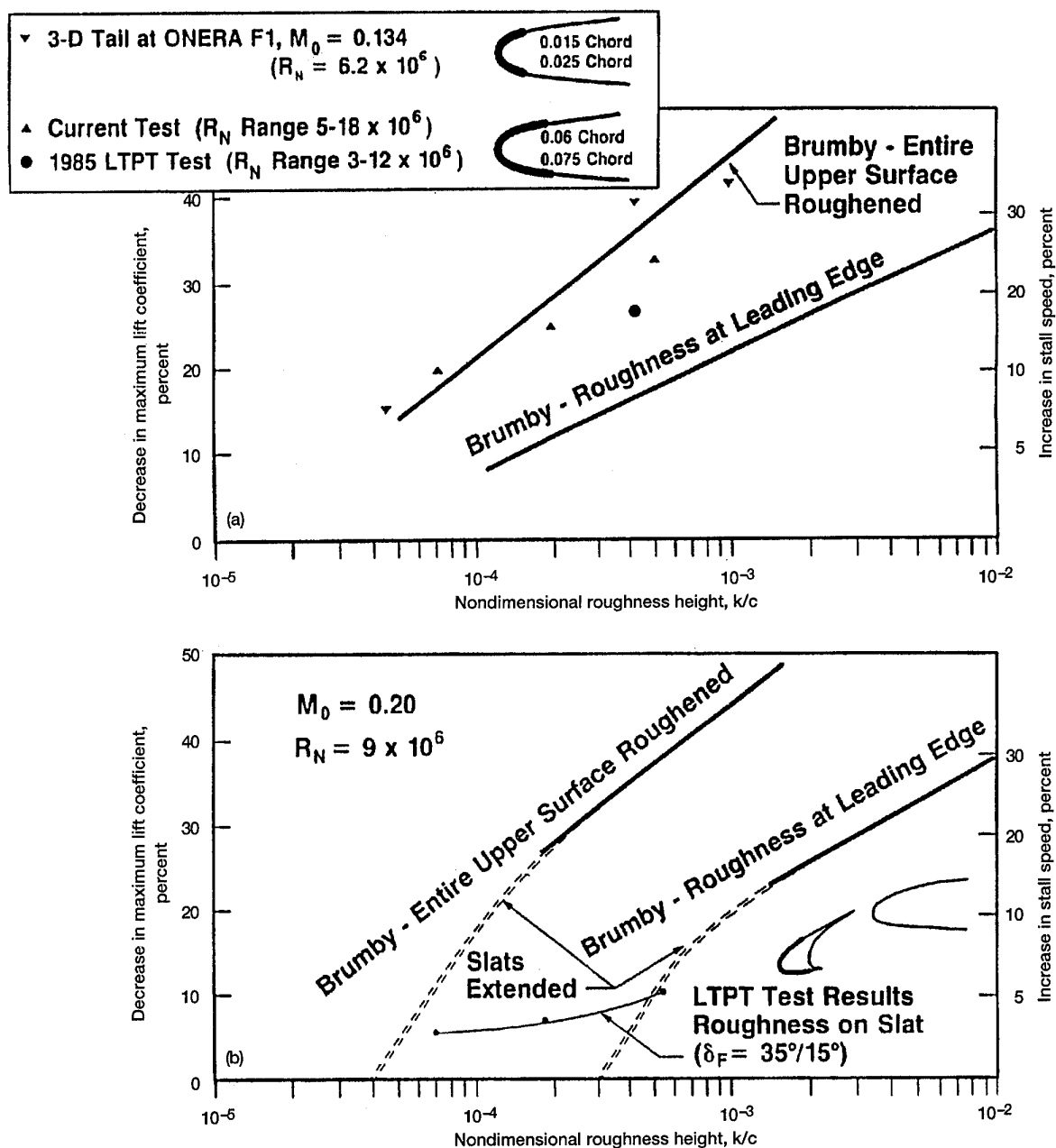


Figure 4.—Effect of roughness on maximum lift (ref. 3). (a) Single element airfoil and tail. (b) Four element airfoil.

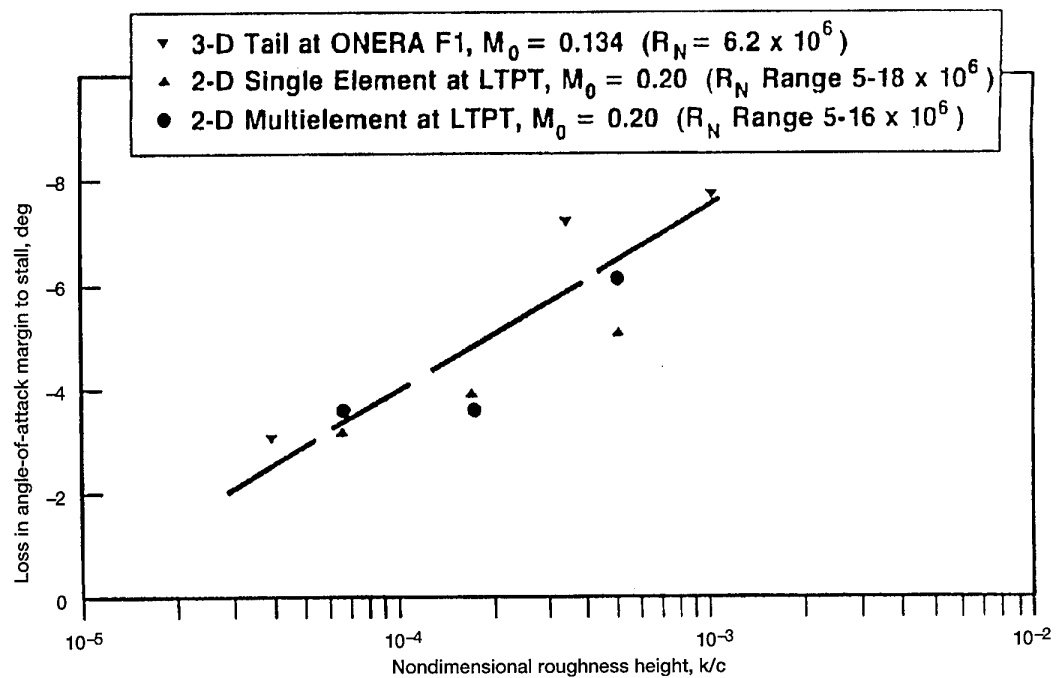


Figure 5.—Effect of roughness on loss of angle-of-attack margin to stall (ref. 3).

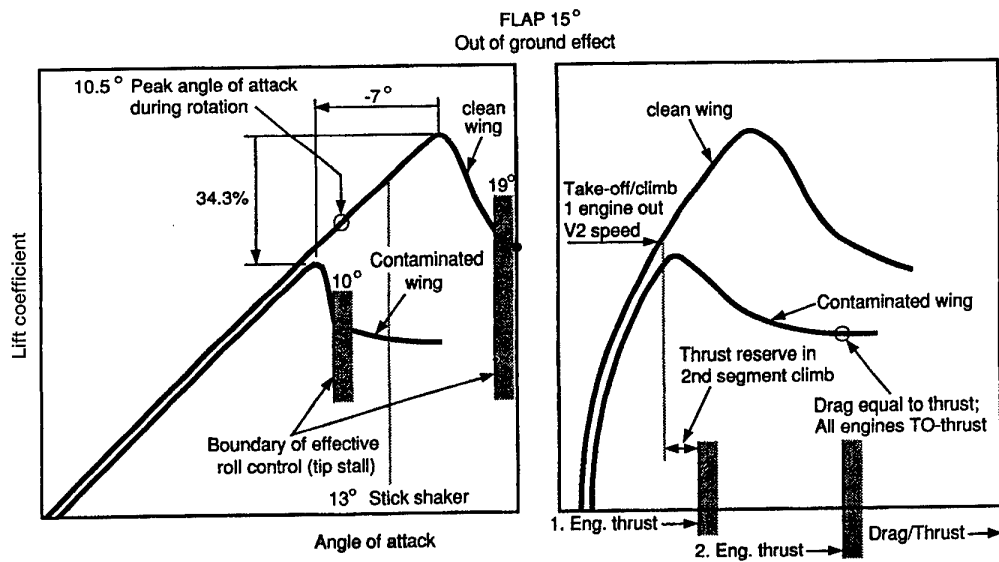


Figure 6.—Effect of wing contamination on aircraft lift and drag (ref. 2).

THE RESPONSIBILITY FOR THE APPLICATION OF THESE DATA REMAINS WITH THE USER AND SHOULD ONLY BE USED IN CONJUNCTION WITH THE SAE METHODS DOCUMENT (SEE CAUTIONS)

FP of SAE Type I Fluid Mixture Must be at least 10 °C (18 °F) below OAT

OAT		Approximate Holdover Times Under Various Weather Conditions (hours:minutes)				
°C	°F	Frost	Freezing Fog	Snow	Freezing Rain	Rain on Cold Soaked Wing
0 and above	32 and above	0:18-0:45	0:12-0:30	0:06-0:15	0:02-0:05	0:06-0:15
below 0 to -7	below 32 to 19	0:18-0:45	0:06-0:15	0:06-0:15	0:01-0:03	
below -7	below 19	0:12-0:30	0:06-0:15	0:06-0:15		

°C = Degrees Celsius
°F = Degrees Fahrenheit
OAT = Outside Air Temperature
FP = Freezing Point

CAUTION: THE TIMES OF PROTECTION REPRESENTED IN THIS TABLE ARE FOR GENERAL INFORMATION PURPOSES ONLY AND SHOULD BE USED ONLY IN CONJUNCTION WITH A PRE-TAKEOFF INSPECTION.

CAUTION: THE TIME OF PROTECTION WILL BE SHORTENED IN HEAVY WEATHER CONDITIONS. HIGH WIND VELOCITY AND JET BLAST MAY CAUSE A DEGRADATION OF THE PROTECTIVE FILM. IF THESE CONDITIONS OCCUR, THE TIME OF PROTECTION MAY BE SHORTENED CONSIDERABLY. THIS IS ALSO THE CASE WHEN THE FUEL TEMPERATURE IS SIGNIFICANTLY LOWER THAN OAT.

Figure 7.—Guideline for holdover times anticipated for SAE Type I fluid mixture as a function of weather conditions and OAT (ref. 9).

THE RESPONSIBILITY FOR THE APPLICATION OF THESE DATA REMAINS WITH THE USER AND SHOULD ONLY BE USED IN CONJUNCTION WITH SAE METHODS DOCUMENT. (SEE CAUTIONS)

OAT		SAE Type II Fluid Concentration Neat-Fluid/Water (Vol %/Vol %)	Approximate Holdover Times Under Various Weather Conditions (hours:minutes)				
°C	°F		Frost*	Freezing Fog	Snow	Freezing Rain	Rain on Cold Soaked Wing
0 and above	32 and above	100/0	12:00	1:15-3:00	0:25-1:00	0:08-0:20	0:24-1:00
		75/25	6:00	0:50-2:00	0:20-0:45	0:04-0:10	0:18-0:45
		50/50	4:00	0:35-1:30	0:15-0:30	0:02-0:05	0:12-0:30
below 0 to -7	below 32 to 19	100/0	8:00	0:35-1:30	0:20-0:45	0:08-0:20	
		75/25	5:00	0:25-1:00	0:15-0:30	0:04-0:10	
		50/50	3:00	0:20-0:45	0:05-0:15	0:01-0:03	
below -7 to -14	below 19 to 7	100/0	8:00	0:35-1:30	0:20-0:45		
		75/25	5:00	0:25-1:00	0:15-0:30		
below -14 to -25	below 7 to -13	100/0	8:00	0:35-1:30	0:20-0:45		
below -25	below -13	100/0	Use of SAE Type II for anti-icing below -25 °C (-13 °F) must maintain 7 °C (13 °F) buffer, and the fluid shall conform to the lowest operational use temperature/aerodynamic acceptance limitation (see para. 6.3.1.1.2). Consider use of SAE Type I where SAE Type II fluid cannot be used.				

°C = Celsius
 °F = Degrees Fahrenheit
 OAT = Outside Air Temperature
 VOL = Volume
 * = For maintenance purposes

CAUTION: THE TIMES OF PROTECTION REPRESENTED IN THIS TABLE ARE FOR GENERAL INFORMATION PURPOSES ONLY AND SHOULD BE USED ONLY IN CONJUNCTION WITH A PRE-TAKEOFF INSPECTION.

CAUTION: THE TIME OF PROTECTION WILL BE SHORTENED IN HEAVY WEATHER CONDITIONS. HIGH WIND VELOCITY AND JET BLAST MAY CAUSE A DEGRADATION OF THE PROTECTIVE FILM. IF THESE CONDITIONS OCCUR THE TIME OF PROTECTION MAY BE SHORTENED CONSIDERABLY. THIS IS ALSO THE CASE WHEN THE FUEL TEMPERATURE IS SIGNIFICANTLY LOWER THAN OAT.

Figure 8.—Guideline for holdover times anticipated for SAE Type II fluid mixture as a function of weather conditions and OAT (ref. 9).

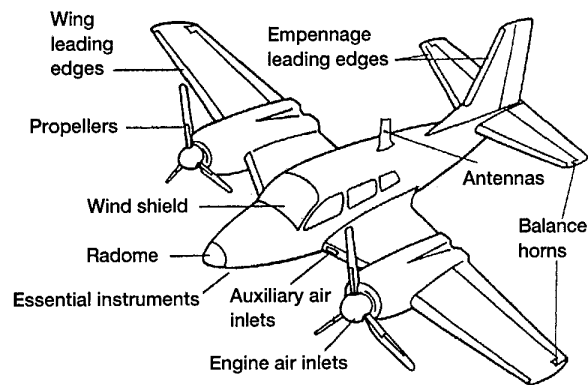


Figure 9.—Aircraft ice protection.

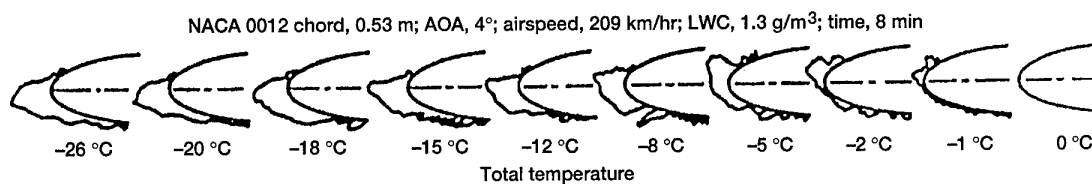
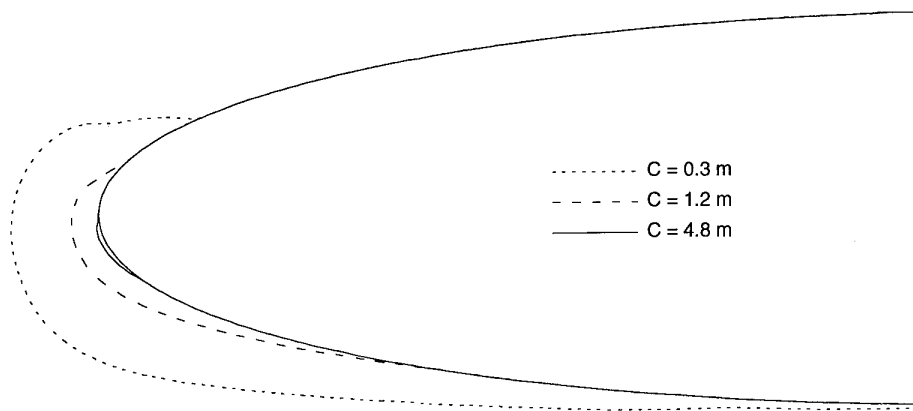


Figure 10.—Effect of total temperature on ice shape development (ref. 15).



NACA 0012 airfoil; AOA, 4° ; airspeed, 252 km/hr; LWC, 0.35 g/m^3 ; MVD = $20 \mu\text{m}$; time, 10 min

Figure 11.—Effect of airfoil size on ice coverage.

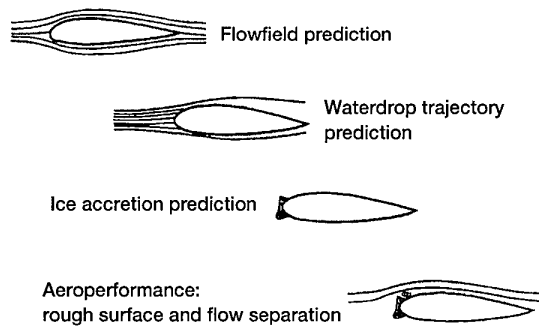


Figure 12.—Ice accretion modeling approach.

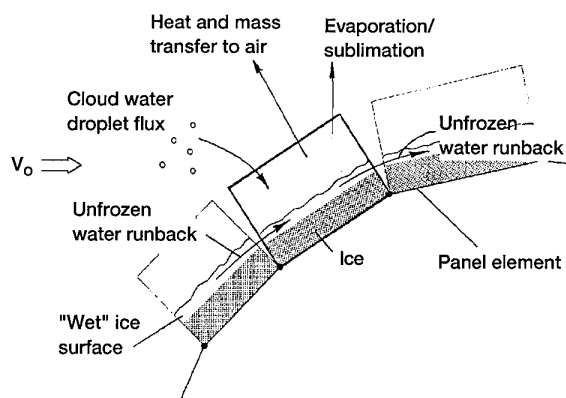


Figure 13.—Control volume approach for ice accretion model.

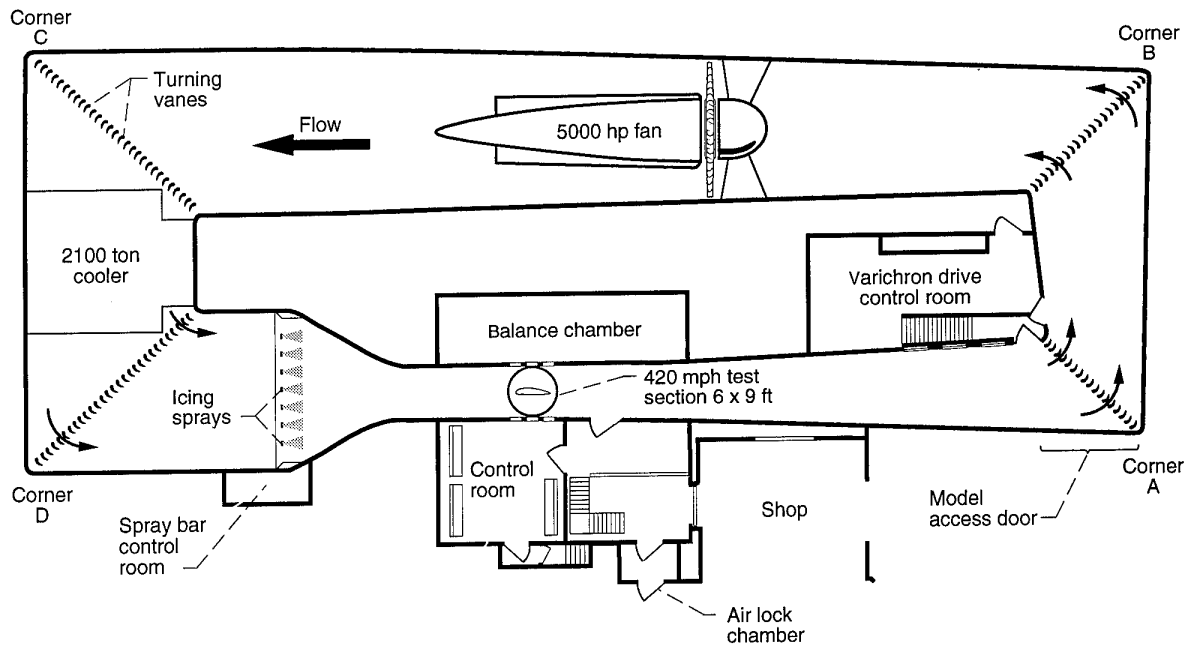


Figure 14.—Schematic of the NASA Lewis Research Center Icing Research Tunnel (IRT).

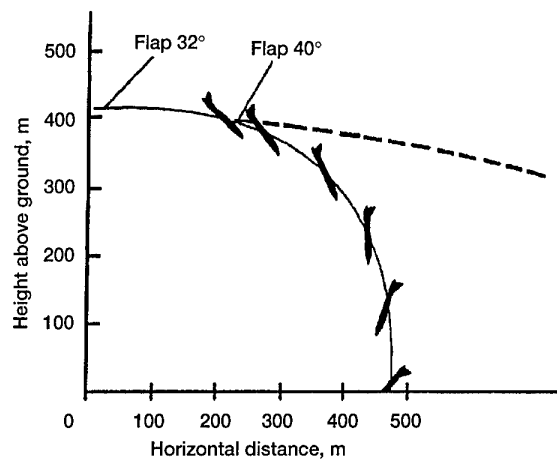


Figure 15.—Catastrophic flight path of Vickers Viscount accident in Stockholm, Sweden on January 1977 (ref. 19).

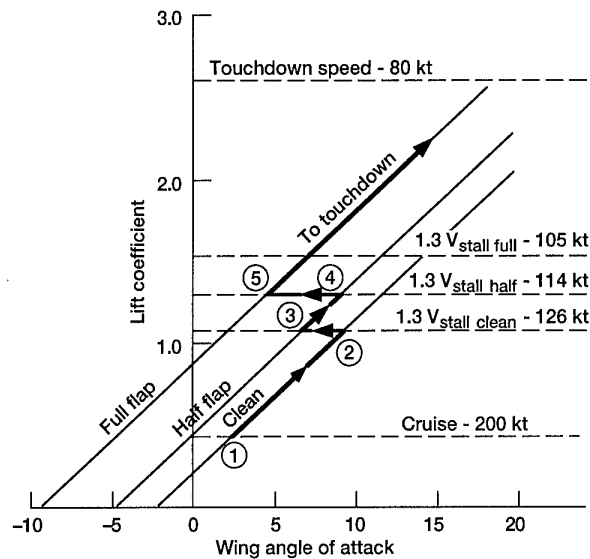


Figure 16.—Angle-of-attack conditions for P. Hellsten's generic turboprop airplane (ref. 22).

	Condition (fig. 16)	Flaps	Wing AOA, deg	Wing downwash, deg	Tail AOA, deg	Elevator deflection, deg	Tail, C_L	Airspeed, kt
Trimmed aircraft	1	Clean	2.3	1.4	-1.5	2.3	0	200
	2	Clean	9.5	3.8	3.1	-3.4	0.04	126
	3	Half	7.0	3.8	-2.0	1.1	-0.07	126
	4	Half	9.5	4.8	-0.2	-0.8	-0.05	114
	5	Full	4.4	4.8	-4.9	3.1	-0.22	114
	6	Full	18.1	9.6	4.2	-7.5	-0.075	80
Zero "g" pushover	VFE	Full		0	-14.8	15.1	-0.29	145
	$1.3 V_s$	Full		0	-15.8	16.3	-0.29	105
	V_s	Full		0	-17.3	18.3	-0.29	80

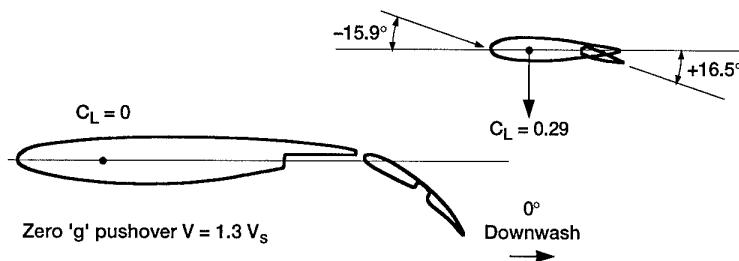


Figure 17.—Wing and tail configurations for the flight conditions shown on figure 16 (ref. 22).

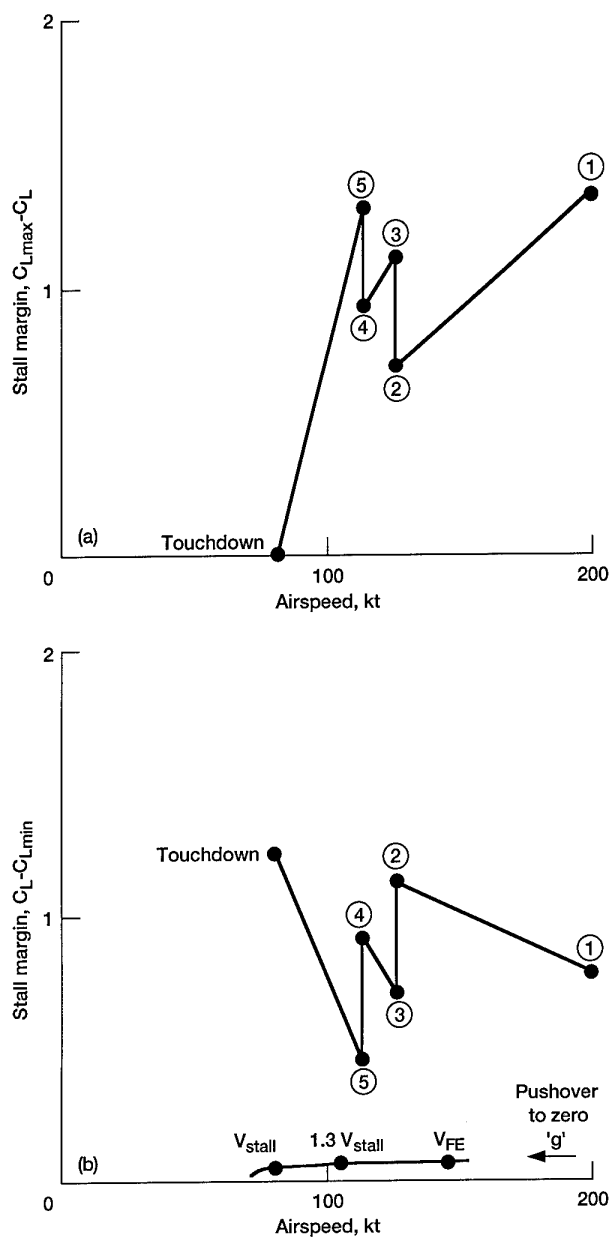


Figure 18.—Stall margins for the flight conditions shown on figure 16 and for the pushover to zero 'g' maneuver (ref. 22). (a) Wing. (b) Tail.

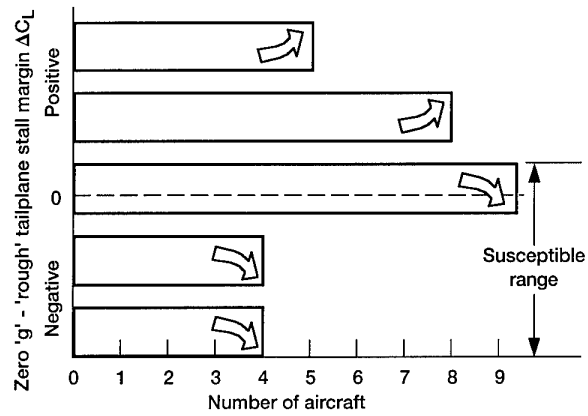


Figure 19.—Predicted zero 'g' 'rough' tailplane stall margins for thirty-one Part 121/135 Turboprop Aircraft (ref. 23).

Wind Shear and its effects on aircraft

A A Woodfield

Aviation Research Consultant

9 Colworth Road

Sharnbrook

Bedford MK44 1ET, United Kingdom

Abstract

Wind Shear has been responsible for several major accidents and many incidents during landing and take off. In aviation terms, wind changes that cause flight path deviations (wind shear) are mainly those occurring over distances between about 150 and 3000m, i.e. approximately 3 to 40 sec. at approach speeds. General characteristics of many forms of wind shear are described together with measured data on the probability of meeting headwind shears of different magnitudes. This is followed by analysis of the basic response of aircraft to both horizontal wind changes and downdraughts, and discussion of aircraft sensitivity to wind shear. Several recorded examples of wind shear in both normal operational and accident scenarios are presented. The relevance of different ways of quantifying wind shear severity is examined, including a calculation of height loss that can be used when a wind shear is fully defined, and the 'F' factor, which is used with reactive wind shear measuring systems. Some insight into the probabilities of false or missed warnings with each system is derived using the measured probability data. A brief outline is given of the relevant characteristics of different wind shear prediction and detection systems. The lecture concludes with a study of the ways in which pilots can be trained and assisted to survive most wind shear encounters and, hopefully, avoid those which could be catastrophic. It is concluded that, given appropriate training and aircraft systems, it is possible to survive encounters with nearly all those wind shears that caused fatal accidents in previous years. New predictive detection systems offer the possibility to warn an aircraft before it attempts to penetrate those extremely rare wind shears that are beyond its performance capability.

1. INTRODUCTION

Large changes in horizontal wind or downdraughts can have dramatic effects on the flight path of an aircraft. If these changes occur at low altitude then the aircraft may well strike the ground

unintentionally with possibly catastrophic consequences for crew and passengers. Since the early 1970's such short term changes in wind have been known as Wind Shear, and a series of major accidents in the USA in which over 500 people lost their lives has resulted in several intensive studies of these types of events.

Wind shear events that cause difficulties to aircraft are usually very localised and often short lived. They are also generally invisible unless special sensors are used or another aircraft has flown through the event. Thus it is very difficult to find ways of avoiding severe wind shear and all possible means must be employed together to assist in the detection of wind shear. Most airports and aircraft are not equipped to detect and avoid severe wind shears and it is essential to help pilots and aircraft respond appropriately when they encounter such events.

Three main areas need to be addressed to help reduce the probability of wind shear accidents and these were the basis of proposals for an Integrated Wind Shear programme identified by a special committee on Low-Altitude Wind Shear and Its Hazard to Aviation set up jointly by the US National Academy of Sciences and the FAA¹ in 1982. These are:

- a Understanding the characteristics of wind shear and its effects on aircraft
- b Detecting and categorising the severity of wind shear
- c Helping the pilot through improved training, displays and aircraft performance and control.

Each of these areas needs to be considered to present a balanced view of wind shear and its impact on aircraft operations.

Several major accidents² in the USA between 1975 and 1985, where wind shear was the cause or a significant factor, led to the establishment of major research efforts in that country. Many of these wind

shear accidents were attributed to downbursts in the vicinity of thunderstorms, which later became known as microbursts. However, large wind shear is not always associated with thunderstorms. Of 24 wind shear accidents and incidents between 1964 and 1982 in the USA, or involving US carriers outside the USA, about 50% probably include thunderstorm microbursts as a factor (Ref.1). Wind shears are also a world wide phenomena and certainly not peculiar to the USA. It is a group of natural phenomena that have been present since the earth's atmosphere achieved its present form. One of the earliest documented aircraft accidents that was almost certainly caused by wind shear occurred to a Douglas DC3 near Bowling Green, Kentucky on 28 July 1943³.

Research programmes in many countries since 1976 have resulted in a number of developments in knowledge, training methods and aircraft systems. As a result the probability of major accidents from Wind Shear is now considerably reduced.

Wind shear has become such a well known potential cause of aircraft accidents in the past 20 years because:

- a the widespread use of Flight Data recordings in accident analysis has made it possible to identify wind shear as a factor,
- b operations in bad weather are now commonplace, and
- c the volume of commercial flight operations is increasing rapidly.

This presentation on wind shear is divided into four main sections that explore

- a What is Wind Shear?

This presents descriptions and examples of wind shear, discusses the main causes of different types of wind shear, and presents statistics on the probability of encountering wind shear of different levels of severity.

- b Aircraft Response to Wind Shear.

The behaviour of an aircraft in wind shear is examined and the relative importance of various aircraft performance characteristics is identified. The section concludes with several examples of aircraft encounters with wind shear.

- c Detecting and quantifying Wind Shear.

Discussion of ways of classifying wind shear severity that are relevant to aircraft performance is followed by consideration of various methods of detecting and measuring wind shear.

- d Helping the pilot.

After introducing the issues that need to be addressed to help pilots that encounter wind shear, there are further sub-sections on cockpit displays, training needs and the behaviour of autopilots.

2. WHAT IS WIND SHEAR?

2.1 Definition of Wind Shear

Before continuing it is advisable to define wind shear in the context of aviation operations, as it has slightly different connotations for meteorologists[#]. It can be defined in general terms⁴ as:

'Any change of wind or downdraught causing a change of flight path that requires significant pilot action for recovery'

The words 'change of wind' are particularly significant as steady winds, or variations in headwind caused by changes of aircraft direction in steady winds, are not wind shears because they do not change an aircraft's flight path through the air.

Wind shear is part of a continuous spectrum of atmospheric disturbances ranging from Turbulence through Wind Shear to Local Weather. Each of these can be related to the duration or spatial length of the events for aviation purposes, viz.

Turbulence

Disturbances that require little or no pilot action to maintain the desired flight path within acceptable limits. These are generally short duration events lasting less than about 3 sec.

Wind Shear

Disturbances that require significant pilot action to maintain a flight path within acceptable limits. These events are typically of between 3 and 40 seconds duration.

[#] Meteorologists usually associate wind shear with a change in wind velocity with altitude.

Local Weather

Long term and large scale wind variations that do not change the flight path, although they will affect navigation, touch down, etc.

The two basic components of wind shear are changes in wind along the flight path and perpendicular to the flight path. Each of these affect aircraft in different ways. Various forms of wind shear will include different proportions, magnitudes and phasing of these components.

2.2 Description of main classes of wind shear and their causes

It is important to remember that wind shears come in an infinite variety of wind changes, duration and magnitude and they are usually accompanied by significant turbulence. However, it is convenient to show simple stylised wind changes when describing examples of wind shear arising from different causes, although in reality these are as likely to be encountered as is the 'average man'.

Wind shear arises from two basic causes

- a Wind flowing past large natural or man-made objects, or
- b wind changes generated by thermal gradients and discontinuities in the atmosphere.

Local topography, such as hills and mountains, local surface conditions, such as the presence of large volumes of water, and the level of solar energy, which is primarily related to Latitude, will all contribute to both basic causes. Thus particular airports tend to be prone to particular types of wind shear.

It is appropriate to identify 8 basic types of wind shear starting with some that are general for all airports, then considering some that relate to local conditions, and finishing with some related to strong thermal activity, which is particularly characterised by thunderstorms.

2.2.1 Boundary layer shear

Drag of the surface of the earth and its rotation reduces the speed of wind and changes its direction as height is reduced near the ground. This effect is particularly noticeable below about 300ft. The gradient increases with higher wind speeds. However, wherever there is wind, a boundary layer shear is always present and expected by pilots. The rate of change of wind speed in such a shear is not

usually a major problem; at least for winds within the maximum that any particular aircraft can tolerate for safe manoeuvring on the ground.

Thus this type of shear is not of practical interest when studying potentially hazardous wind shears. However, boundary layer shear produces a negative increment to headwind shear on landing, and a positive increment during take-off as both usually occur into wind. This biases the probability distribution of headwind shears between approach to landing and take off.

2.2.2 Low level jet

In the presence of a strong temperature inversion, i.e. where temperature increases with height, there is usually a sharp discontinuity in temperature gradient at the top of the inversion layer. On descending into such an inversion the wind will often increase very sharply at the top of the layer and then decrease steadily to a much lower speed near the ground where measurements will be made for airport Air Traffic Control systems. These winds are known by the meteorological term of 'low level jets'. Such inversion layers are quite common at night with clear skies and light winds, when surface temperatures drop rapidly, and they usually extend to about 800 - 1500ft altitude above the ground.

This means that the strongest shear is well above ground level and pilots have ample time to recover from any flight path disturbances before landing.

Measurements of a low level jet encountered during an approach to San Francisco⁵ show a headwind component increasing from 17 to 34 kn as the aircraft descends about 50 ft from 1200 ft above ground. The surface wind was only about 10 kn. Whilst this is a significant wind shear of 17 kn at about 4.2 kn/sec, it is a headwind increase and well clear of the ground. For both these reasons it was not a problem.

In general, low level jets will produce an increasing headwind unless the surface wind is so light that the landing runway is not into wind, in which case it is likely that the low level jet will be either weaker or at a higher altitude, and thus less significant. In most cases low level jets are not very likely to cause significant wind shear problems.

2.2.3 Large scale gusts

As wind strength increases there is a corresponding increase in the probability of encountering random turbulent gusts with a duration greater than about

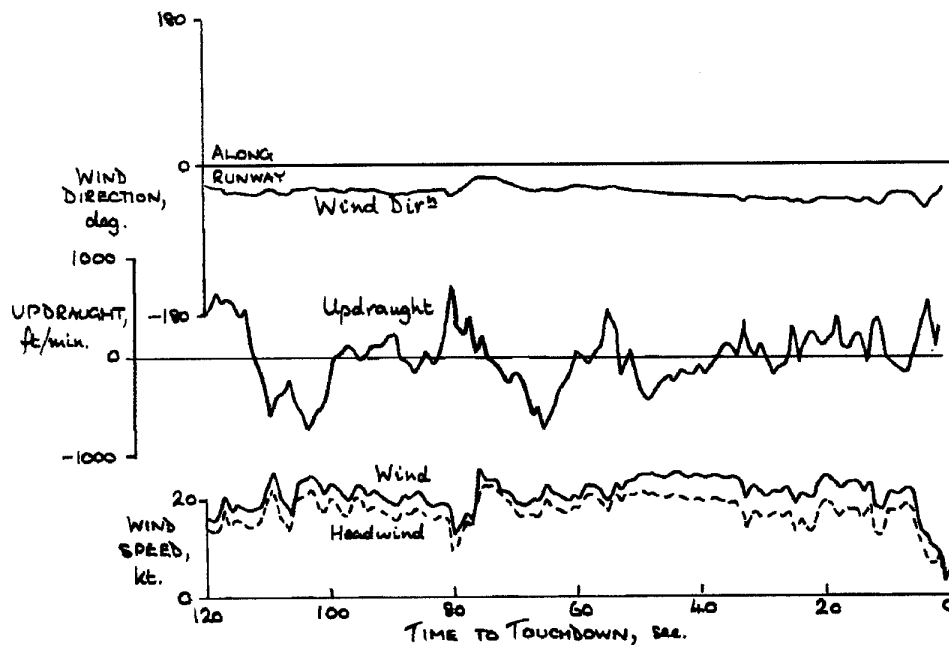


Fig.1: Large gust Wind Shear at Chicago (Ref.5)

3 sec. This will be further increased by the presence of such features as distant groups of very tall buildings or rugged terrain, which will increase the general level of turbulence in relation to the wind speed. Such gusts will not be obviously related to any particular topographical feature.

Pilots tend to take account of the possibility of encountering wind shear of this nature by increasing their approach speed by a proportion of the wind strength in strong winds. However a large gust can be a problem if it is encountered during particularly critical manoeuvres such as the landing flare.

Occasionally these gusts may be associated with quite moderate wind speeds as in the example recorded during a landing at Chicago ⁶, Fig.1, where a gust reduced a headwind of 20 kn by over 15 kn in about 5 sec just from the start of the landing flare. The result was a very firm landing because the loss of airspeed virtually cancelled the usual lift increment expected in the landing flare.

2.2.4 On-shore wind

Airports close to large water areas will experience on-shore winds during the day if the land becomes significantly warmer than the water (or the reverse effect in cold climates where the water is often warmer than the land). Such on-shore winds occur

in a shallow layer close to the ground that may extend to around 300 - 600 ft altitude. An example of this type of wind at San Francisco is shown in Fig.2 (Ref.6, Fig.4b). The significantly cooler air near the ground is characteristic of an on-shore wind.

Because the wind is close to the ground it will be measured by the airport and aircraft will be approaching into any significant wind. Thus any change in headwind will appear as an increase during an approach, and a decrease during take off. Usually the shear will be far enough above the ground to avoid significant problems. Also pilots will be well aware of the likelihood of encountering on-shore winds at airports near large areas of water. Thus these wind shears are not likely to cause significant problems.

2.2.5 Topographical disturbances

In moderate and strong winds the airflow around large hills, mountains, cliffs or down large valleys can be very different from the mean wind and change dramatically with small changes in position relative to the objects. There can also be large localised eddies. Even large man-made objects close to runways, such as hangars and multi-storey car parks, can produce significant local disturbances.

In general the size of any disturbances will relate to the size of the object that is its cause, and effects will decay with distance because of mixing induced by turbulence that is always present and related to wind strength.

Two particularly significant types of topographical disturbances are large changes in wind speed and direction as an aircraft leaves or enters a shielded region of relatively light wind, and vortices, sometimes referred to as rotors, that are shed from sharp edges such as cliffs, or generated in the lee of steep hills.

Airports that suffer from these effects are well known to pilots. Some prime examples are Hong Kong (Kai Tak), Gibraltar, Nice, and Anchorage.

These effects can be severe and often limit operations from airports when winds exceed certain speeds from particular directions. In general the most severe effects are from vortices (rotors), particularly because these energetic wind shears dissipate relatively slowly and can be carried by the wind into the approach and take off flight paths of aircraft.

An example of such topographical wind shears in a wind of about 30 kn at Anchorage, Alaska, is discussed in the examples of aircraft responses to

wind shear in Section 3.5 below. Another example was an accident involving a BAe ATP twin turbo-prop aircraft that struck and damaged a wing tip during take off from Sumburgh Airport in the Shetland Isles, UK in a 55 kn wind ⁷.

2.2.6 Frontal shear

Significant changes of wind speed and direction can occur across synoptic weather fronts and the storm fronts surrounding thunderstorms. Synoptic weather fronts are usually gentle changes over several kilometres. Storm fronts are often much more abrupt, can be severe, and often appear in generally calm conditions. They can be some kilometres away from the thunderstorm that causes them.

An example of a storm front recorded during a landing at Calcutta is shown in Fig.3 (Ref.5, Fig.4). In this case the wind change across the front resulted in a change in headwind of about 14 kn in 4 sec. Although the change in total wind speed was only from about 3 to 10 kn, the change of direction was about 150° and this resulted in a shear of about twice the size of the wind speed change.

About 30% of the 24 USA investigations of wind shear accidents and incidents between 1964 and 1982 (Ref.1) probably involve frontal shear.

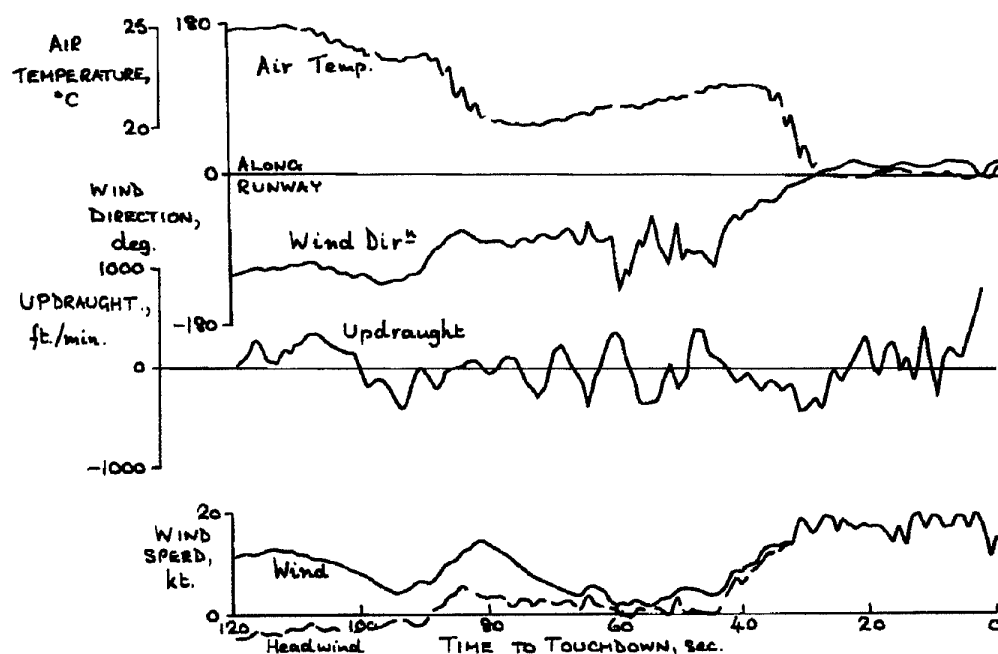
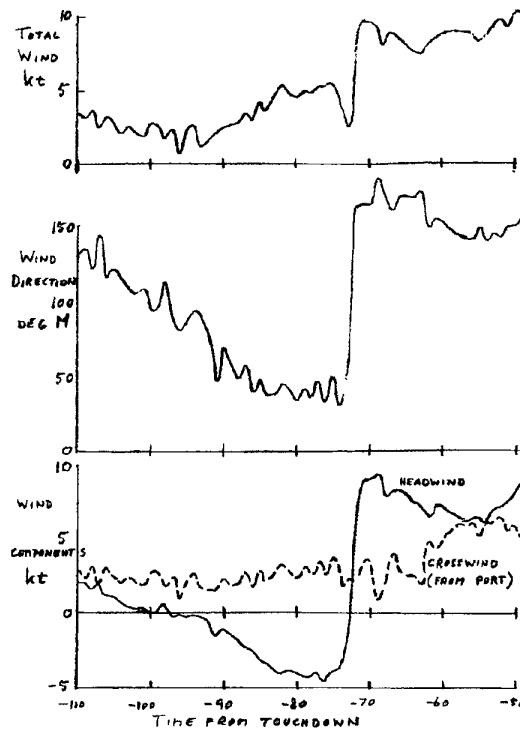
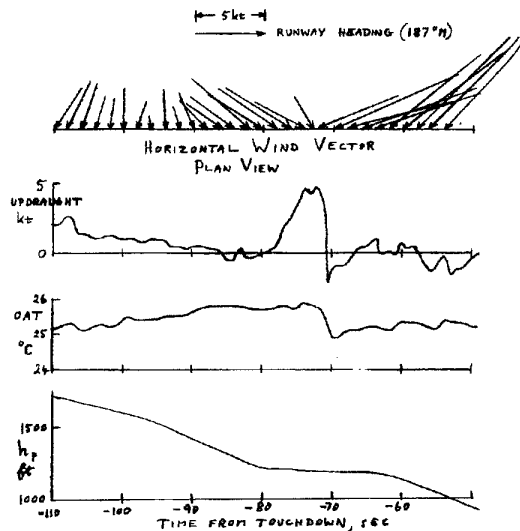


Fig.2: On-shore wind at San Francisco (Ref.5)

Fig.3: Frontal shear at Calcutta
(Ref.6)



2.2.7 Thunderstorm microburst (downburst) shear

This type of shear results from strong localised downflows in the region of thunderstorms and typically have a diameter of between about 0.5 and 2Km and a lifetime of around 15 minutes from starting to form to disappearing. Wind speeds up to 50 kn in opposing directions have been recorded near the periphery of such events. This would result in a horizontal wind shear of 100 kn.

The first record of such downbursts as a cause of an accident was Fujita's analysis⁸ of the accident to Eastern Airlines Flt. No. 66, a B727 aircraft, at John F Kennedy Airport, New York on 24 June 1975. At that time downbursts were described as the downflow of a continuous stream of air being deflected by the ground to give a mixture of horizontal and vertical winds, i.e. similar to the flow of a jet of water striking a horizontal surface.

Further investigation, including the international Joint Airport Weather Studies (JAWS) trials in Denver, USA during 1982 sponsored by NASA, FAA and NCAR, have now established that such downbursts are the airflow around approximately horizontal vortex rings that are fed by a series of pulses from the thunderstorm and then decay once these pulses cease. This vortex ring structure, Fig.4,

conserves energy, dissipates relatively slowly and requires much less total energy to generate extreme velocities than the previous downflow jet model.

A research team from the UK Royal Aerospace and Royal Signals and Radar Establishments (both establishments are now part of the UK Defence

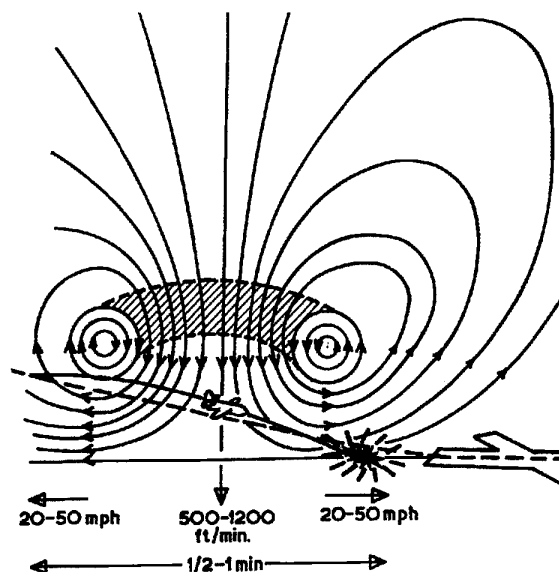


Fig.4: Vortex ring microburst flow pattern

Research Agency) took part in the JAWS programme using a heavily instrumented HS (now BAe) 125 aircraft. Using information from ground based Dual Doppler Weather Radar the HS125 was guided to intercept about 20 different microbursts in the Denver area during a 3 week period. Recordings during one of these penetrations, which took place about 1000ft above the ground (6400ft barometric altitude), are shown in Fig.5. There are three main features to note about this penetration.

The most obvious is the reduction in headwind of about 35 kn in 5 sec. (about 600m distance) This was preceded by an increase of about 25 kn and followed by a smaller increase of about 10 kn.

Another feature is the change in pitch attitude needed to maintain height. This is a direct measure of vertical winds and the maximum change of about 6° corresponds to a maximum downdraught of 24 kn (approximately 2400 ft/min or 12 m/sec). This is greater than the maximum climb rate of most light aircraft with best climb speeds below about 120 kn, and more than 50% of the best climb rate of

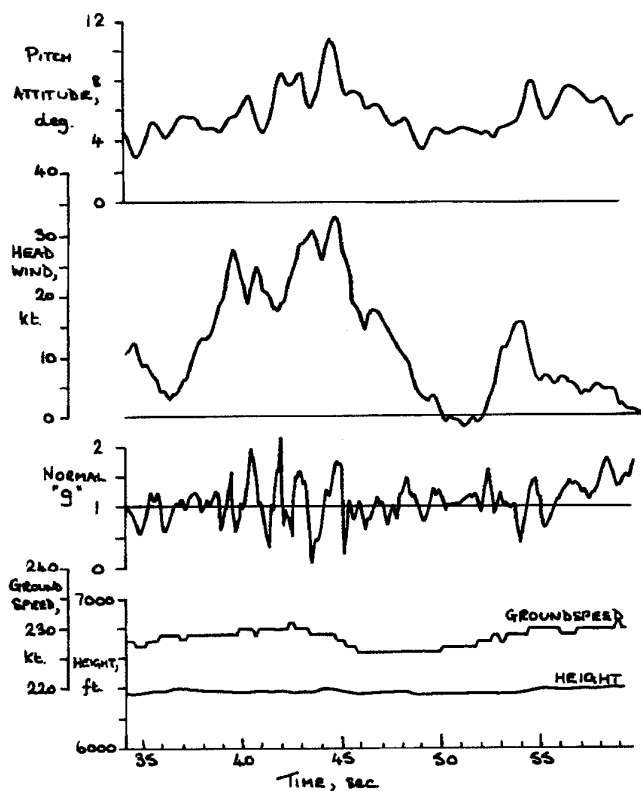


Fig.5: Microburst recorded by the RAE HS125 during the JAWS program

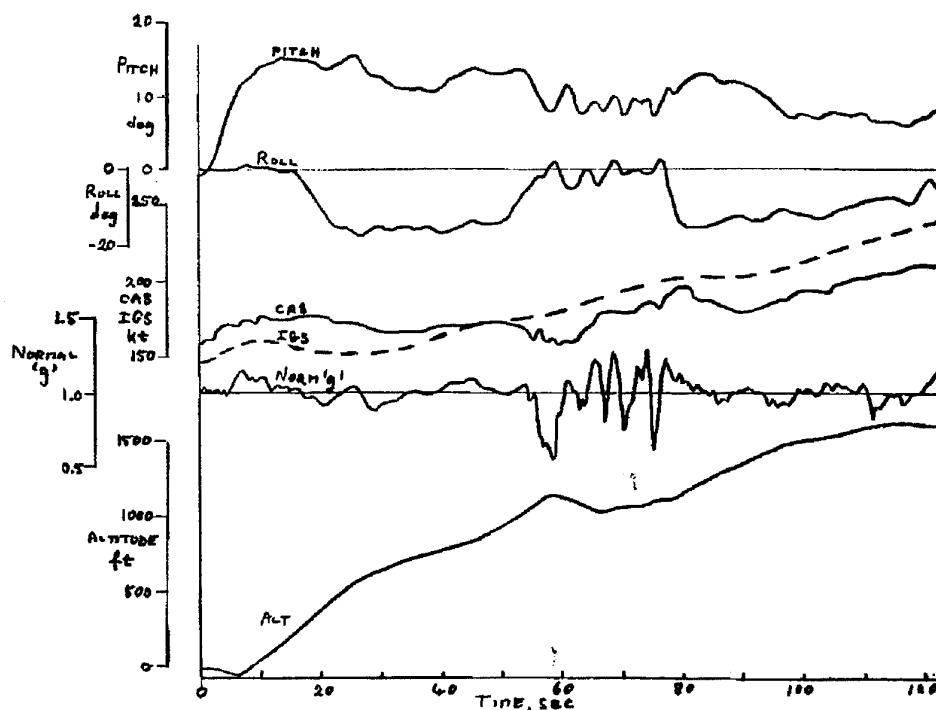


Fig.6: Microburst wind shear during take-off from Chicago

larger jet transport aircraft, which have maximum climb rates between about 3000 and 4500 ft/min.

The third notable feature is the large range of excursions in Normal acceleration, which vary by ± 1 g at a frequency of about 1 Hz (wavelength about 100m) in the region of the microburst. This corresponds to short period fluctuations in angle of attack in response to rapid changes in downdraught. The range of ± 1 g corresponds to downdraught fluctuations of ± 12 kn (approximately 1200 ft/min or 6 m/sec.). These short period fluctuations do not have a significant effect on the flight path of an aircraft, but large changes in Normal acceleration provide both a clue to the presence of severe wind shear and also tend to make it difficult for pilots to interpret their situation clearly. It is particularly important to represent this turbulence when training pilots to identify and respond correctly to wind shear using simulators, and also when testing airborne wind shear detection and warning systems.

Positive evidence supporting the vortex ring model of microbursts was obtained from the Flight Data Record of a take off of a B747 from Chicago which passed over the top of a microburst, Fig.6. In this case the downdraught is still present but the aircraft passes above the vortex ring and the change in headwind is reversed with an initial decrease followed by a large increase and then a decrease.

Several records, including those for the accident to a Delta Airlines L-1011 on the approach to Dallas-Fort Worth Airport on 2 August 1985, have shown the presence of smaller secondary ring vortices. This was also suggested in the HS125 records by some of the smaller fluctuations in headwind. Any such secondary vortices will combine with the main vortex in ground effect.

The meteorological conditions that generate the pulses which produce vortex rings are not clearly understood. In many cases microbursts are produced under relatively innocuous looking cloud well away from the dark heart and main precipitation regions of a thunderstorm. They generally seem to be associated with some precipitation although this can be so light that it evaporates before reaching the ground. (A condition known as Virga, where precipitation can be seen descending part way to the ground.) In most cases there is no visual evidence of vortex rotation as a ring in the cloud above a microburst, and this suggests that the base of the cloud may provide the discontinuity that is required to turn a pulse into a vortex ring. Occasionally there is a lighter grey

circular area in the cloud above the place where a microburst had been. There is also no correlation of microburst severity with the intensity of weather radar echoes as shown in Fig.7 from the JAWS programme.

If the surface of the ground is dry and dusty then the presence of a microburst is shown clearly by dust blowing rapidly outwards from the centre of a circle and then rising quite abruptly and almost vertically towards the cloud base.

Like other forms of wind shear, microbursts come in all shapes and sizes. There are small innocuous microbursts as well as severe ones. Vortex rings can be produced that are inclined relative to the ground and distorted by sloping ground and varying ground surface temperatures. These effects distort the symmetry of wind shear across the microburst.

Microbursts can produce severe wind shear in the absence of significant winds at nearby measuring sites, and they have been responsible for about 50% of the wind shear accidents investigated by the USA between 1964 and 1982. Thus they are certainly one of the more important types of wind shear.

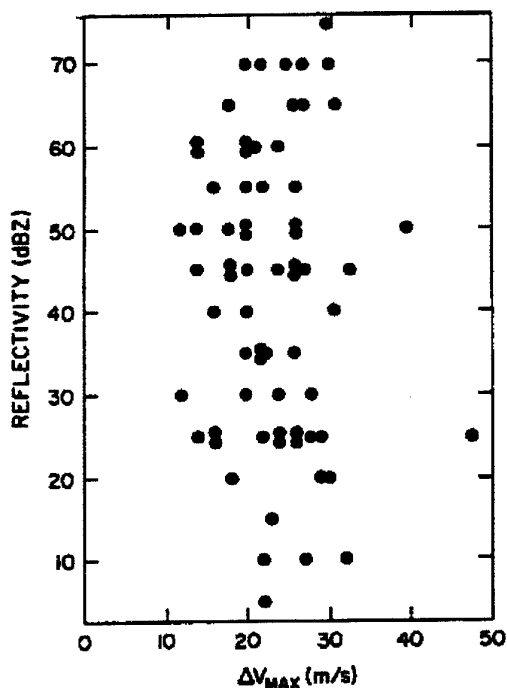


Fig.7: Radar reflectivity in JAWS microbursts

2.2.8 Tornadoes

Another severe wind event that is associated with thermal gradients in the atmosphere is the tornado.

Tornadoes are the most severe localised wind events that can be experienced close to the ground and have extremely large wind gradients. Below cloud they are very easy to see and will be avoided by anybody on the ground who can move out of their way, as well as by any aircraft flying in the area.

However the strong rotation of a tornado extends into the cloud above and it often tilts towards a horizontal axis of rotation. The vortex of a tornado increases in core diameter with height above the ground and this will reduce the peak velocities and gradients. However, velocities and gradients will still be extremely large with velocity changes of hundreds of knots over a distance of a few hundred metres.

A tornado top in cloud will be invisible although it may appear as a strange echo on weather radar. Any aircraft happening to pass through it will experience very severe gusts or wind shear which can be beyond the structural design cases specified for aircraft. An aircraft would be extremely unfortunate to encounter the top of a tornado. However at least one case has been recorded around 1980 where an airliner flying over the Netherlands encountered a tornado top which was so severe that the wings were torn off the aircraft.

Fortunately the probability of such an encounter is extremely low, and it is unlikely that another case will occur for many decades. This type of event and its probability have to be considered when formulating structural design requirements. It is not usually included in wind shear studies, where the main concern is loss of height rather than structural failure.

2.3 Probability of encounter

The aviation community has had to come to terms with probabilities of failure in a more formal way than most other forms of human endeavour. Balancing risks is part of our daily life, e.g. in relation to driving vehicles, vaccination against disease, etc. In aviation we attempt to specify targets for acceptable probabilities of catastrophe so that designers can make and test practical aircraft and systems. For civil aviation a typical failure probability for a critical system will be less than 1 in 10^9 landings or flight hours. This is chosen because accident rates through human error and unforeseen events are around 1 in 10^7 and thus only about 1 in 100 accidents will occur through events that can be foreseen.

Knowledge of the probability of encounter is important when considering wind shear so as to establish the levels that should be used for training, and to assist in determining the likely false alarm rate of wind shear warning systems. Information on

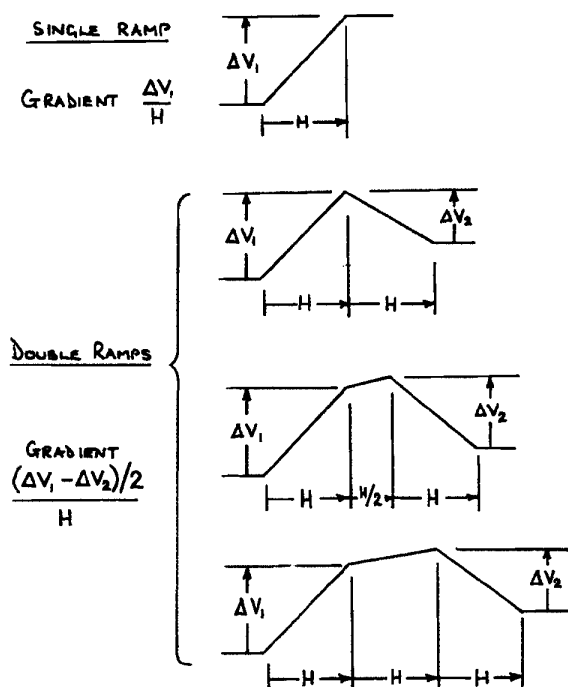


Fig.8: Ramp patterns for wind shear analysis (Ref.5)

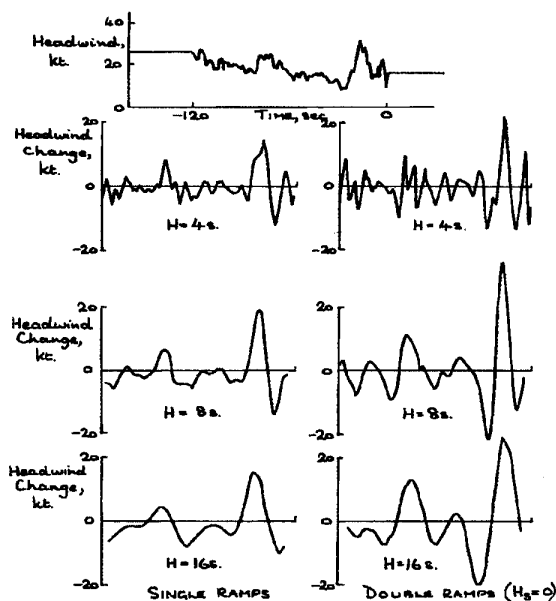


Fig.9: Examples of filter outputs for different ramp patterns of wind shear (Ref.5)

probabilities of encounter can also be used to verify that proposals for categorising wind shear severity relate to known incidents and accidents in a way that is consistent with their observed frequency of occurrence.

It might be imagined that wind shear would be a different class of atmospheric disturbance from general turbulence. Also, that different types of wind shear would have different probability distributions of magnitude.

The Royal Aerospace Establishment, RAE (now part of the Defence Research Agency) with the co-operation of British Airways (BA) and the UK Civil Aviation Authority, examined the final 2 minutes from the Flight Data Recordings of every approach and landing of the BA B747 fleet in normal operations for about 12 months. Data was analysed to calculate all the headwind shears that were encountered. Overall statistics were obtained for various airports, and for larger wind shears a full analysis was made of the Flight Data Records of these approaches to identify aircraft flight path deviations, pilot control activity, and any associated downdraught shears. Data for about 10000 approaches were analysed (Ref.6) after eliminating records with suspect sensor data. The statistical discrete gust analysis procedure⁹ identified single and double ramp patterns of headwind change, Fig.8, with basic time units of 4, 8 & 16 sec. Fig.9

shows the filter output from a typical approach. Wind shears are identified by peaks and troughs in the filtered data. This type of analysis method is needed to identify discrete events. Normal frequency analysis methods are unsuitable for identifying wind shear because they tend to smooth out discrete events. Such methods are only appropriate for continuous records, where the sample is part of an infinite record with the same spectral characteristics.

The 10,000 landings provided over 100,000 identified headwind shears of all types and sizes. When normalised in the same way as the RAE have normalised turbulence¹⁰, then all the data collapsed into one family, Fig.10. This normalisation of the headwind shear uses

$$\frac{\Delta V_x}{L^{1/3}}$$

where ΔV_x = headwind change, and

L = the ramp length of the wind shear

Frequency of occurrence is normalised in terms of occurrences per ramp length travelled.

The data in Fig.10 includes all types of wind shear, and different combinations of headwind change and shear duration or length. Particular airports have

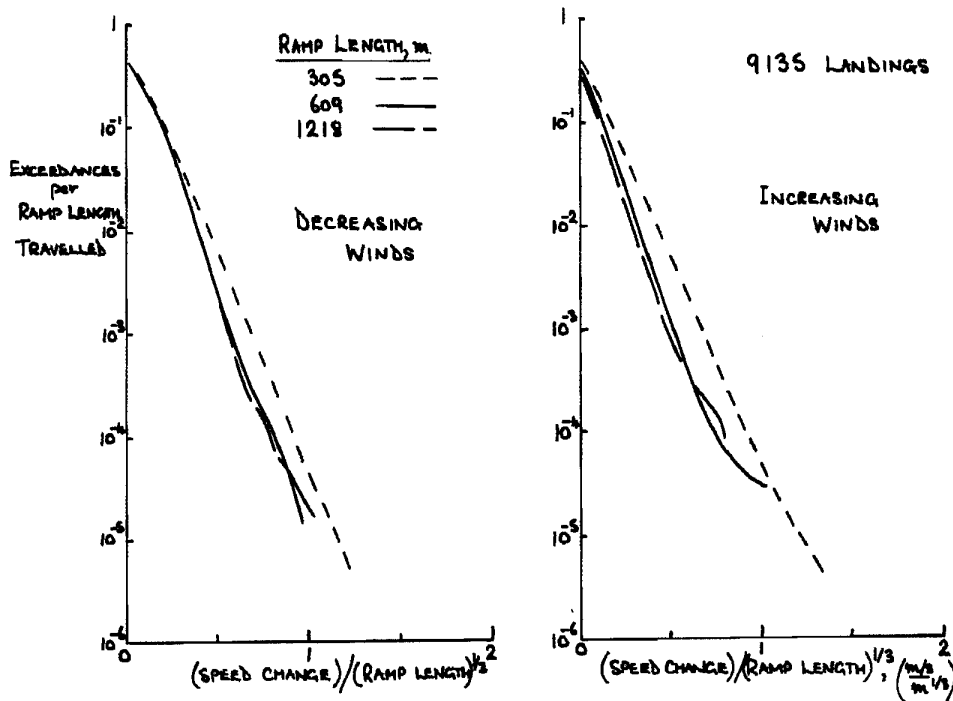


Fig.10: Probability of single ramp headwind shear (Ref.5)

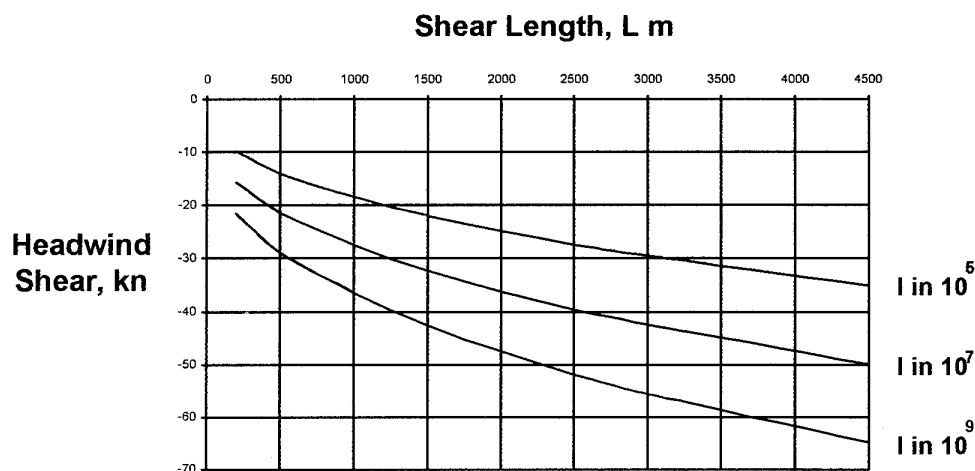


Fig.11: Constant probability lines of decreasing headwind shear as functions of shear strength and length

different slopes of probability against magnitude reflecting their local terrain, proximity to large masses of water, and general climate. Typically the airports most susceptible to wind shears have wind shears about 30% larger at a given probability level than airports that are least susceptible to shear. Most importantly, the slope of the frequency distribution curve is well defined and is consistent with an exponential probability distribution. From this it is possible to extrapolate with confidence to establish realistic levels for the most severe headwind shear that needs to be considered, i.e. 1 in 10^9 landings.

For a single ramp shear of 1500m length, such as that encountered at New Orleans in the microburst that caused the take off accident to a Pan American B727 on 9 July 1982¹¹, a 1 in 10^9 probability world wide would be a headwind change of 46 kn. (The New Orleans example has a change of headwind of 40 kn in 1500m and would correspond to about the 1 in 10^8 probability level for the headwind shear component.) Fig.11 shows the probability of encounter for different headwind shear lengths and wind speed changes. Headwind shears with greater than 60 kn change of wind speed have been measured using Doppler weather radar, they are either

extremely unlikely to be encountered or would be over longer lengths, which is less significant in terms of aircraft behaviour. This unique set of probability data provides a sound basis for selecting appropriate levels of headwind change and event length for practical training of pilots and testing of systems.

Close to the ground it is not possible to encounter significant downdraughts without significant headwind shear because the ground deflects downdraughts and creates horizontal shear. This is clear in the examples of large shear encounters shown in Section 3.5, where significant downdraughts accompany all three examples. Statistical information on the probability distribution of downdraughts at various levels of headwind shear is needed to complete the definition

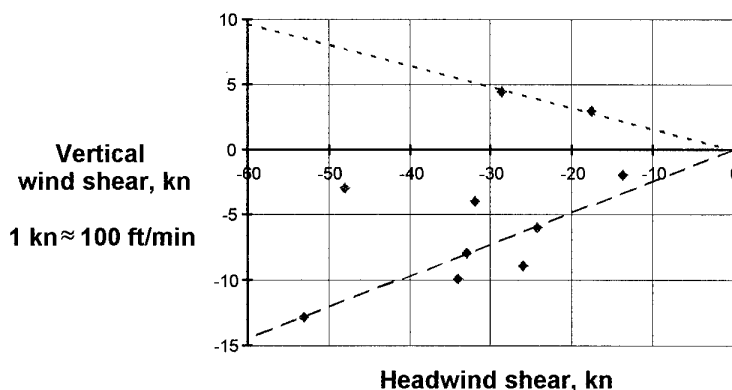


Fig.12: Examples of average vertical wind shear associated with headwind shear

of encounter probabilities. However, in practice this would require considerably more data than the 10000 landings, and much more intensive data analysis.

A practical approach to defining downdraughts associated with large headwind shears, which are the most relevant combination to consider when defining wind shear severity boundaries and training conditions for simulators, is to take the few measured examples, Fig.12, and assume that these are representative of the levels of downdraught most commonly associated with a given headwind shear. In many situations, such as topographical disturbances and microbursts, any downdraughts will be related directly to headwind shear. The majority (8 of the 10 examples) have downdraughts associated with decreasing headwind shear, i.e. reinforcing the hazard, but there are 2 examples of an updraught associated with decreasing headwind shear. The median line through the more hazardous quadrant where both V_x and V_z are negative has a slope of 0.24. This line passes through the largest recorded wind shear encounter, which caused the crash of the L-1011 Tristar at Dallas/Fort Worth Airport in August 1985. The two points just below the line are the wind shears that caused the crash at John F Kennedy, New York in 1975 and a microburst measured by the RAE HS125 at Denver, Colorado during the 1982 JAWS programme (Fig.5).

3. AIRCRAFT RESPONSE TO WIND SHEAR.

Wind shear has a duration of typically between 3 and 40 sec which is long in relation to the dynamic responses of pilots. Thus pilot control actions are always going to play an important part in the response to a wind shear. These control inputs will be of two basic types:

- a stabilising inputs to dampen oscillations.
- b performance inputs to achieve the necessary flight path or maximum performance.

Stabilising inputs in the longitudinal plane to control pitch attitude and speed will continue to be primarily the pitch control inputs that stabilise the lightly damped phugoid mode¹² of the aircraft with controls fixed. The phugoid mode has a long period of many seconds and is easily controlled by small pitch control inputs to maintain constant pitch attitude. This is the normal way of flying aircraft.

Some early studies of the effects of wind shear looked at the response of an aircraft with controls fixed¹³. However, without controlling pitch attitude, the response is dominated by large oscillations of the lightly damped phugoid mode, where speed and height are exchanged at almost constant energy. This oscillation will not be present in practice because it is easily suppressed by a pilot or autopilot. Thus it is impossible to obtain a meaningful measure of the response of an aircraft to wind shear without including pitch stabilising control inputs¹⁴. The simplest case is to consider an aircraft with perfect pitch attitude stabilisation, i.e. pitch attitude remains constant. The two references (Refs. 13 & 14) show the phugoid response to wind shear and then the response of a piloted simulation to the same wind shear. In the simulation the height excursions of the aircraft were dramatically less because phugoid motion was suppressed by the pilot in the normal way.

When an aircraft is stabilised in pitch then the characteristic dynamic modes in the longitudinal plane become

- a a strongly convergent exponential angle of attack mode with a time constant in approach and take off conditions given approximately by

$$\frac{V}{2g} \cdot \frac{C_L}{a}$$

where g = acceleration due to gravity,
 a = lift curve slope per radian,
 V = true airspeed,

$$C_L = \text{Lift coefficient} = \frac{W/S}{0.5\rho \cdot V^2},$$

$$W/S = \text{Wing loading, and}$$

$$\rho = \text{air density.}$$

For most aircraft this results in a time constant of around 0.5 - 1 sec.

- b an exponential speed (or flight path) mode that is usually close to neutral stability during approach and take-off.

3.1 Response of an aircraft controlled in pitch

The longitudinal equations of motion of an aircraft are significantly simplified if pitch attitude is assumed to be constant, and this is a practical and appropriate assumption for pilot response to wind shear in the initial stages. Even in later stages

during an encounter when a pilot may decide or need to change pitch attitude, the change will be smooth and it will be a reasonable approximation, when considering changes in flight path, to ignore the effects of angular rate and acceleration in pitch.

A consequence of stabilising in pitch is that speed stability becomes almost neutral for approach and take off conditions. Ground speed will not be significantly affected by changes in headwind caused by wind shear, but only by thrust changes. This further simplifies the equations of motion, although it should be noted that airspeed will be affected by headwind changes.

The other important control input during a wind shear encounter is thrust change. However, for potentially hazardous wind shear the thrust will fairly rapidly be increased to its maximum as soon as a pilot identifies the severity of the particular wind shear. Thus the most significant parameters for thrust control will be the delay in applying maximum thrust, and the maximum thrust increment that is available.

With the above assumptions the equations become very simple and it is easy to identify the influence of aircraft parameters on response to wind shear. These equations have been developed in Ref. 4.

Considering first the effect of both (a) headwind shear and (b) downdraughts without any throttle or pitch attitude change, then the change in flight path angle due to the wind shear is

a Headwind shear, ΔV_x

$$\Delta\gamma = \frac{C_L}{a} \cdot \frac{\Delta V_x / V \cdot \left(2 + \Delta V_x / V\right)}{\left(1 + \Delta V_x / V\right)^2}$$

where $\Delta\gamma$ = change in flight path angle (+ve upwards)

This is an asymmetric expression and loss of headwind has a much greater effect than the same increase in headwind. An example of the change in flight path angle for a typical approach condition with $C_L = 1$, $a = 5$ and $V = 120$ kn is shown in Fig.13. The asymmetry is very marked with a 40 kn increase in headwind shear required for a

5 deg. climb yet only a 20 kn decrease gives a 5 deg. dive.

Increasing the approach airspeed of an aircraft at a given weight by 20% (the dashed line in Fig.13) reduces its Lift Coefficient as well as increasing the airspeed and dramatically reduces dive angles at large shears with over 50% reduction when there is a headwind shear of -50 kn. On the other hand a lower approach speed at the same Lift Coefficient such as that for an aircraft with lower wing loading would increase the dive angle. An aircraft with a higher Lift Coefficient, e.g. higher wing loading and the same approach speed, will have greater dive angles. The trend towards more aerodynamically effective wings that operate at higher Lift coefficients is increasing the susceptibility of more recent aircraft designs to headwind shear.

b Downdraughts, $-V_z$

$$\Delta\gamma = \frac{V_z}{V}$$

where V_z = updraught,

which is the usual convention.

This is a linear and symmetric function and values for the same condition as above, i.e. $V = 120$ kn, are shown in Fig.14.

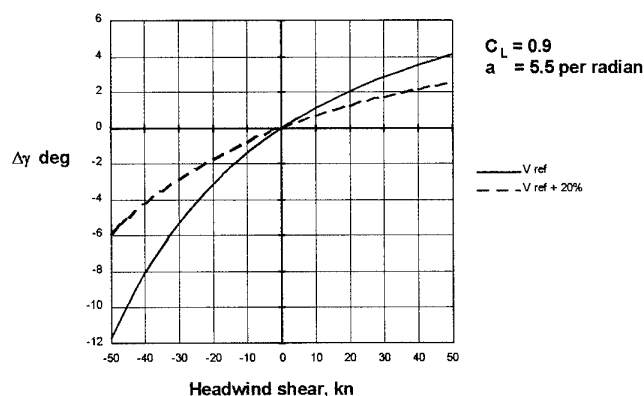


Fig.13: Change of climb angle, $\Delta\gamma$, with Headwind shear

It is important to note that both types of shear result in a change in flight path angle. This change will be reached quite quickly because of the short time constant of the angle of attack response, and it is a satisfactory approximation for performance calculations to assume that flight path changes are instantaneous with changes in headwind and downdraught. If no corrective action is taken by the pilot the wind shear will result in a permanent change in flight path angle. In practice, once the wind shear is identified then action will be taken to increase thrust and the usual affect of adverse wind shear will be a loss of height relative to the desired flight path.

All control inputs, other than stabilising pitch motion, are aimed at changing the aircraft flight path angle to compensate as far as possible for the effects of wind shear. The first instinctive control action is to increase thrust. A change of thrust has a direct effect on flight path

$$\text{angle } \Delta\gamma = \sin^{-1}\left(\frac{\Delta X}{W}\right) \approx \left(\frac{\Delta X}{W}\right)$$

where ΔX = increase in engine thrust.

This may be followed by a deliberate change in pitch attitude, θ . This will initially produce a change in angle of attack and thus lift. Then the stable angle of attack mode will wash out the increase in angle of attack and convert it to a

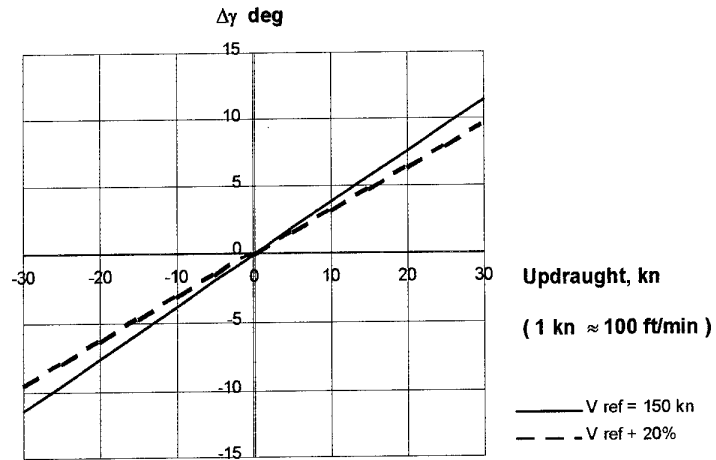


Fig.14: Change of climb angle, $\Delta\gamma$, with Updraught

change in flight path angle. Thus

$$\Delta\gamma = \Delta\theta$$

3.2 Potential loss of height in a headwind shear

The primary hazard from a wind shear encounter near the ground is that a loss of height can result in the aircraft hitting the ground. Thus potential height loss from the desired flight path is a direct measure of that hazard and independent of the type of aircraft.

Using the simple relationships between wind shear and control input effects on flight path from the previous section it is possible to estimate height loss for a variety of control strategies. In terms of

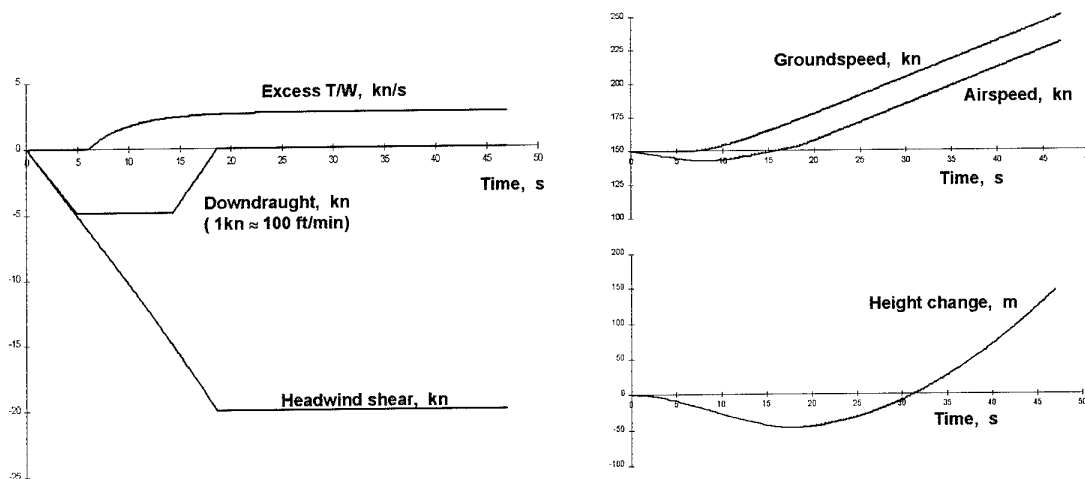


Fig.15: Example of aircraft response to a wind shear with both headwind and downdraught components

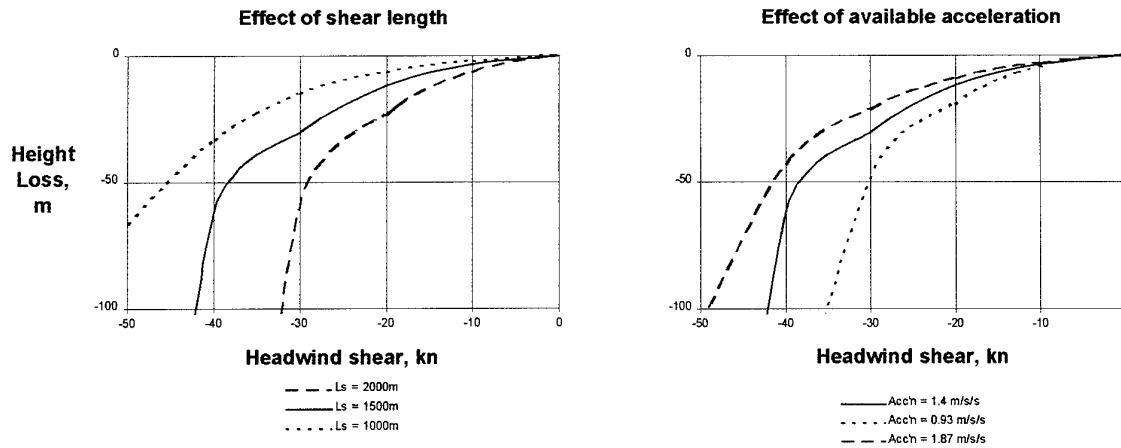


Fig.16: Effects of Shear Length and Available Acceleration on Height loss in Headwind shear

defining the severity of a particular wind shear, it is proposed that a good control strategy for responding to moderate wind shears should be used. This will describe shear severity in a consistent and relevant way.

A suitable strategy is to maintain constant pitch attitude and apply full thrust once the wind shear has been identified as significant. Thus the only control input in this case will be a thrust increase. Control variables will be the maximum available longitudinal acceleration at full thrust, A , the delay, T sec., in applying the throttle and the subsequent dynamic build up of thrust in response to the throttle change. In this case a first order response will be assumed with a time constant, τ

sec. A typical time history of the response to a simple wind shear is shown in Fig.15.

From ref.4 it can be shown that in non-dimensional terms the height change, H_x , is related as

$$\frac{H_x \cdot A \cdot \rho \cdot a}{W/S} = f \left[\frac{\Delta V_x}{V}, \frac{A \cdot L_x}{V^2}, \frac{A \cdot T}{V}, \frac{A \cdot \tau}{V} \right]$$

where A = maximum available acceleration

ρ = air density

(Non-dimensional parameters provide a useful way of reducing the total number of independent variables in physical equations, and highlighting associations between variables.)

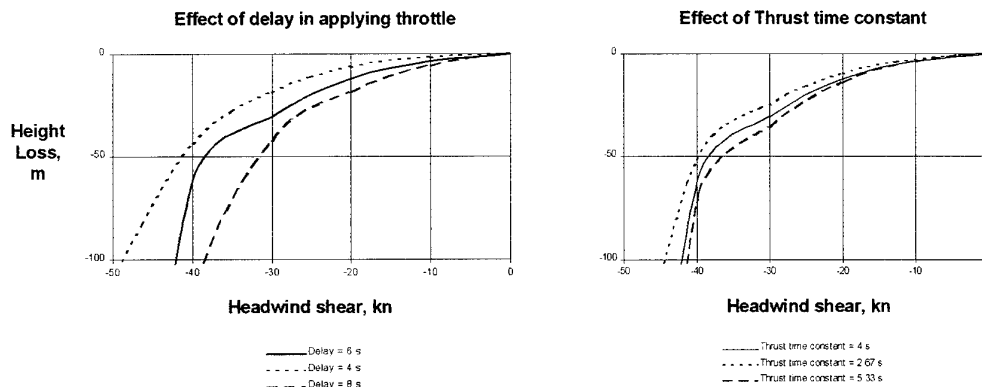


Fig.17: Effects of Throttle time delay and Thrust time constant on Height loss in Headwind shear

It is shown in Figs.16 & 17 (developed from Ref.4, Figs.2 & 3), where each variable is changed by $\pm 1/3$, that potential height loss is less sensitive to variation in available acceleration, A , and delay in applying throttle, T , than it is to a headwind shear. Varying the thrust time constant, τ , has the least effect. Sensitivity to changes in the delay before applying throttle, T , decreases significantly as the delay increases, Fig.17, and it is not necessary to use delay times of less than 6 seconds when estimating potential hazards. Thus it is acceptable to choose relevant constant values for available acceleration, and the thrust delay and response times in order to estimate the potential height loss for a particular combination of aircraft and headwind shear. At large negative magnitudes of ΔV_x the height loss increases rapidly because the aircraft has to reduce pitch attitude to avoid exceeding the stall warning value of angle of attack.

In a severe wind shear a pilot will also change pitch attitude and this will significantly change the actual height loss. However, such pitch attitude changes can vary significantly depending on the actual circumstances of a wind shear encounter. Potential height loss at constant pitch attitude provides the most consistent measure of wind shear severity.

3.3 Potential loss of height in a downdraught

The relationship between downdraught and height change, H_z , is

$$H_z = \frac{1}{V} \cdot \int V_z \cdot dx$$

where x = horizontal distance along flight path

It is expressed in terms of distance because the variation of the updraught, V_z , for a given shear is constant in space regardless of the speed of the aircraft.

The effects of thrust changes are already included in the potential height change in a headwind shear, and the overall potential height change will be the sum of the headwind and downdraught changes.

3.4 Influence of aircraft performance parameters, flight speed and control inputs on height loss in wind shear

As may be expected, the available acceleration, A , has a major effect on the potential height change. The other major aircraft performance parameters are

wing loading, W/S , and lift curve slope, a . Lift curve slope does not vary much between most types of transport aircraft. Thus wing loading is the more important parameter. An increased wing loading at the same airspeed, which is typical of the trend to more aerodynamically effective wings, will increase the potential height change due to headwind shears proportionally; although it will not affect the potential height change due to downdraughts.

Flight speed is a major parameter in potential height change for both headwind and downdraught shears. In downdraughts the potential height change is always reduced in proportion to the increase in flight speed. In headwind shear the relationship is more complex, but an increase in flight speed will reduce significantly the effect of encountering severe shears.

In considering response to wind shear and suitable control strategies, it is interesting to note the effect of pitch attitude changes. Normal pilot training emphasises the importance of maintaining airspeed at a suitable margin from the level flight stall speed to avoid the rapid loss of height that occurs once the aircraft cannot generate enough lift to maintain level flight. A consequence of this single minded

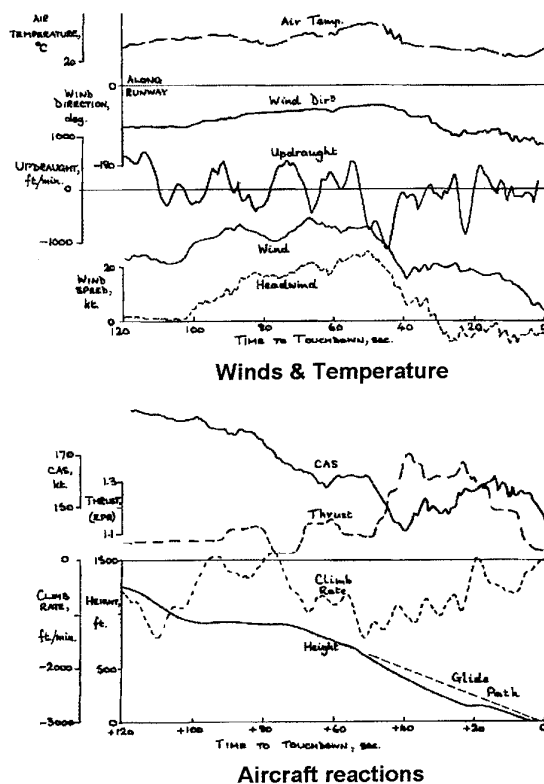


Fig.18: Wind shear at Melbourne

attention to airspeed has been that pilots have tried to regain airspeed lost during headwind shear encounters by reducing pitch attitude to increase longitudinal acceleration. However it is shown above that decreasing pitch attitude will reduce the flight path angle, and this will immediately increase the rate of descent and the height loss.

Such a response near to the ground will increase the hazard, and it is a sad fact that many of the accidents before 1985 could have been avoided if the pilot had not reduced pitch attitude in an attempt to regain airspeed.

Increasing pitch will be generally beneficial during any wind shear encounter. However it is important not to stall and the overriding concern must be to remain just below stall warning. This is indicated by various means on different aircraft, but it is not indicated by airspeed except when an aircraft is in steady level flight. It is possible to control an aircraft and remain below stall warning at speeds below the level flight stall speed, but in such cases the normal acceleration will be less than 1g.

3.5 Examples of wind shear encounters

Detailed analysis of a variety of different types of strong wind shear events experienced during 10000 landings world-wide by the British Airways B747 aircraft are presented in Ref.6. Other analyses available are related to accidents¹⁵, but these usually contain less, or more often, no information on accompanying turbulence, temperature

variations, etc. which are all important to the performance of an aircraft and a pilot's appreciation of the situation.

Three examples of wind shear are presented here. The first two are taken from the BA B747 analysis and the last from analysis of an accident at New Orleans, USA in 1982. In the encounter at Melbourne, Fig.18, the aircraft experienced a loss of 30 knots of headwind over 25 sec. together with large downdraughts of around 800 ft/min at the beginning and end of the headwind shear. Despite applying almost full thrust the aircraft lost 120 ft before passing through the shears and recovering in the final 20 sec before touch down. The 4°C temperature reduction in the shear region would be beneficial in terms of available engine thrust. The general change in wind direction and the associated change in air temperature suggests that the shears were associated with a front.

The second example, Fig.19, is from an aborted approach at Anchorage, and probably due to rotor flow caused by the local terrain in the moderately strong 25-30 kn wind. Fluctuations in wind strength, direction and vertical winds are very large. The strength varies between a few knots and 30 kn, while direction changes by about 180° and updraughts vary up to ± 1000 ft/min. Such large fluctuations are typical of rotor conditions. The pilot wisely decided to go-around after sinking 150 ft below the glide path for a second time. It is, perhaps, not too unusual to find that the Ground

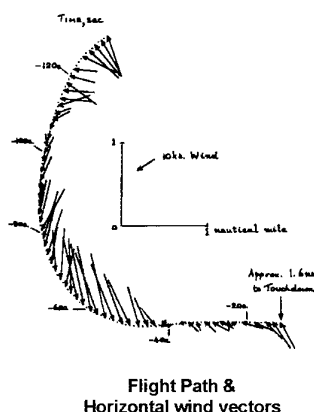
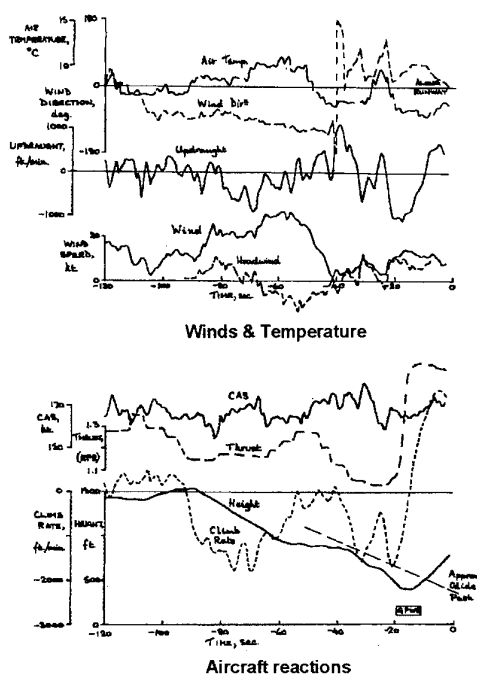


Fig.19: Wind shear at Anchorage

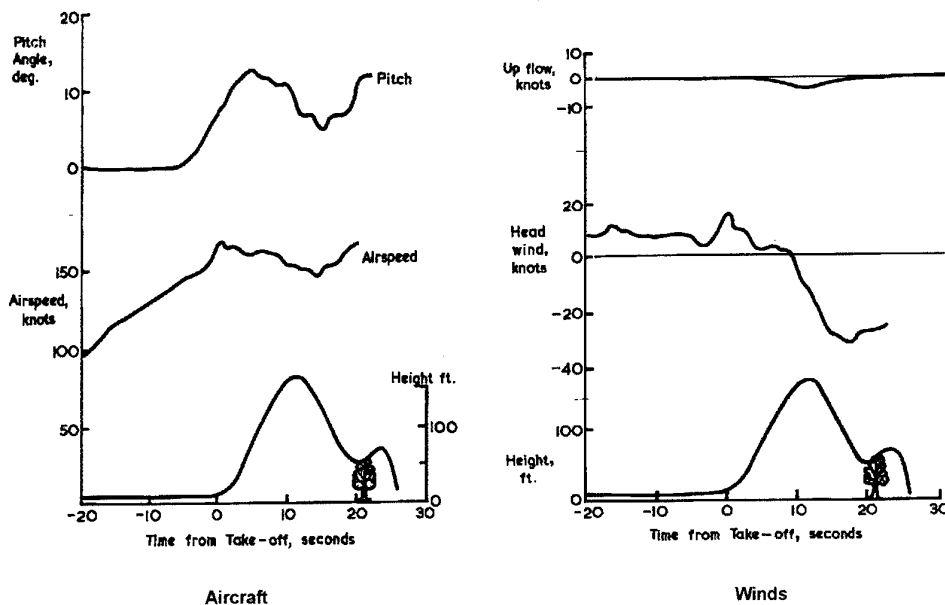


Fig.20: Microburst accident at New Orleans
9 July 1982

Proximity Warning System operated shortly *after* he applied full thrust!

Both these examples illustrate the very dynamic behaviour of both horizontal and vertical winds in real life wind shear situations. Only rarely will wind shear be clearly identifiable as a particular type, because there will usually be significant turbulence present. It is not unusual to have combinations of shear types together in the same area at one time.

The third example, Fig.20, comes from analysis of the PanAm take-off accident at New Orleans in 1982. After a small initial gain in headwind, the aircraft encountered a loss of headwind of 40 kn in 17 seconds and a downdraught peaking at about 350 ft/min. Despite an initial rate of climb of over 1000 ft/min, this microburst wind shear led to an irrecoverable rate of descent of over 1000 ft/min and impact with trees and then the ground. It is interesting to note that the aircraft would not have crashed if the pilots had maintained pitch attitude and used the additional available lift up to stall warning. However, without relevant training, which was not available at that time, it would have been an unusual reaction for a pilot faced with a rapid fall in airspeed. It is estimated from the data of Ref.15 that the reduction in pitch attitude resulted in an increase in the height loss by about 110ft, Fig.21, out of the total loss of

about 260ft below the normal take off flight path. Increasing pitch attitude would have reduced the height loss.

4. DETECTING AND QUANTIFYING WIND SHEAR

4.1 Classification of wind shear severity

In Section 3 above the idea of potential height change was introduced as a measure of wind shear severity. It was shown that response to headwind

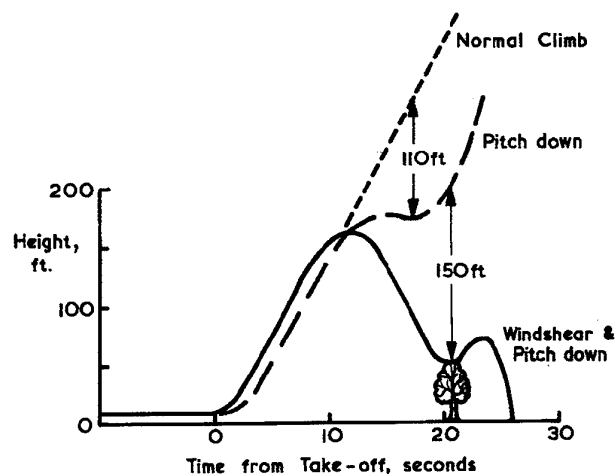


Fig.21: Contributing factors in the
New Orleans accident

shears is primarily a function of two shear parameters, i.e. the total wind change, ΔV_x , and the physical length over which the wind change occurs, L_x , and three aircraft parameters, i.e. wing loading, maximum available longitudinal acceleration, and airspeed. Response to downdraughts was shown to be the integral of the downdraught with distance along the flight path, i.e. again a function of the wind and the length of the shear, divided by airspeed.

It is thus possible to derive a severity scale based on the wind shear characteristics alone and then particular aircraft responses can be directly related to the wind shear severity. A B747 with relatively high wing loading and approach speed would be expected to react to shears in a significantly different way to the reaction of a twin turbo-prop airliner with much lower wing loading and a lower approach speed. Thus a given aircraft type will have its own set of wind shear limits. This is illustrated diagrammatically in Fig.22 where the severity of aircraft response is related to different levels of shear strength depending on the wing loading,

approach speed and available acceleration of the particular aircraft.

As an example consider the effects of wind shear at a typical B747 condition with a wing loading of 3500 newton/m² (73 lbf/ft²), a maximum available acceleration of 1.4 m/s², and an approach speed of 150 kn (77 m/s), Fig.23. This corresponds approximately to the BA B747 conditions during the study of world wide landings, and it is possible to identify occasions when the effects of wind shear could be classified as moderate or strong. These are marked on Fig.23 for comparison with contours of potential height loss. The three squares are strong shear examples where significant flight path deviation is present, and the diamond is a case of moderate shear.

To calculate contours of constant potential height loss it is necessary to define a form of wind shear that includes a relationship between headwind and downdraught shears. Section 2.3, Fig.12, suggested that the average downdraught was typically 0.24 times the headwind shear, and the form of wind shear shown in Fig.15 is suggested for calculating

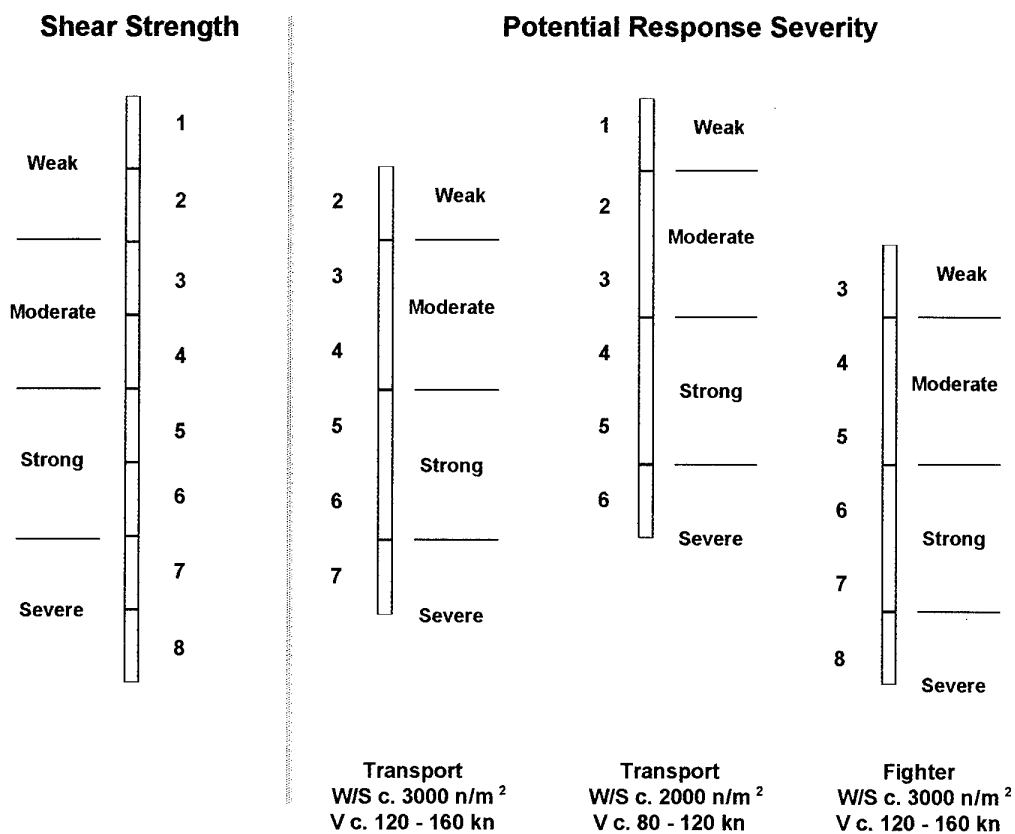


Fig.22: Illustration of possible relationships between Response Severity and Shear strength for different aircraft

potential height loss.

There is good correlation between the small number of measured cases and the bands of Moderate and Strong shear indicated in Fig.23. The Height Loss contours of 50m and 100m seem to form appropriate boundaries for these regions.

A line also appears in Fig.23 indicating where headwind shear will cause this aircraft to reach its stall warning boundary in 1'g' flight. This means that for part of the encounter the aircraft will have to reduce pitch attitude to avoid stalling, and for this period of time its lift will be less than its weight. The effects of this pitch reduction and loss of lift are included in the calculation of potential height loss. This is why the 100m height loss contour has quite a steep gradient until it passes out of the stall warning region.

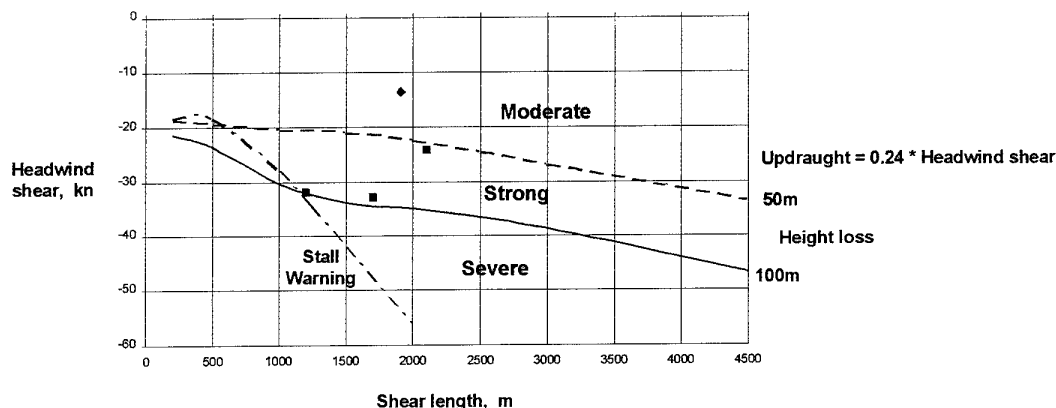
Another test of the appropriateness of 50 and 100m height loss contours for separating severity regions would be to compare them with the potential height losses of aircraft and shears that resulted in accidents. Calculations for the John F Kennedy, New York accident conditions suggest that the potential height loss was 80m, and the New Orleans accident conditions give 50m. It is now known that both accidents could have been avoided using the procedures that are now taught to pilots. In this light the potential height losses would both have been 'Strong' wind shear responses, which seems appropriate. The potential height loss of 50m for

the New Orleans case is also close to the loss of 46m (150 ft) that was due to the wind shear without any change in pitch attitude.

The accident at Dallas/Fort Worth in 1985 had very high headwind shear of 53 kn and average downdraught of about 1300 ft/min. For these severe conditions, which would include a significant period at the stall warning boundary, the potential height loss is an enormous 1100m. This aircraft could not be expected to survive the encounter with this wind shear.

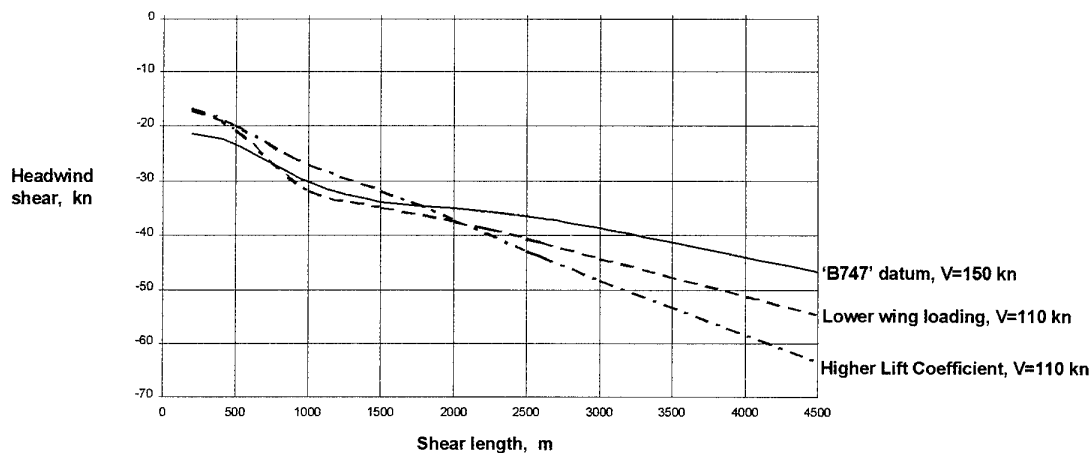
The values of potential height loss contours defining the boundaries between levels of wind shear response severity should remain the same for all aircraft, although the shear conditions for a given height loss will vary with aircraft performance parameters.

Contour lines for 100m height loss for changes in Wing loading and in Lift Coefficient are presented in Fig.24. In each case the single parameter has been changed so as to reduce the reference speed to 110 kn from 150 kn. Compared with the 'B747' datum case, the aircraft with lower wing loading is more responsive to wind shears less than 750m long; is slightly less responsive to lengths between 750m and 1750m, and is significantly less responsive at greater lengths. The aircraft with higher Lift Coefficient is more responsive at lengths less than 1750m and less responsive at greater lengths.



Aircraft characteristics (B747 type): Approach speed 150 kn.,
Lift coefficient 0.9, Available acceleration 1.4 m/s/s
Throttle time delay 6 s., Thrust time constant 4s

Fig.23: Potential Height Loss contours of a 'B747 type' aircraft for different shear conditions



Aircraft characteristics as Fig. 23, except where stated

Fig. 24: Effects on the 100m Potential Height Loss contour of changing Wing loading and Lift coefficient

The differences reflect the greater response of these aircraft to headwind shears and the increased ratio of available acceleration to the square of speed, which improves the response to longer shears. (Available acceleration is constant and speed is reduced.) However, the differences are not very large for shear lengths less than 2000m.

Calculation of the potential height loss for any particular aircraft is straightforward where the overall characteristics of the shear are known, i.e. the total headwind shear, the average downdraught and the length of the shear. Such measurements of a wind shear are available from ground based sensors such as Doppler Weather Radar, and could be obtained from forward looking sensors on an aircraft. When these wind shear measurements are available then characteristics for a nominal datum transport aircraft could be used to generate a general measure of wind shear severity that pilots can compare with their particular aircraft's response levels (Fig. 22).

A growing number of aircraft are equipped with wind shear systems which provide a measure of the wind shear that has very recently been experienced by the aircraft. The delay is a few seconds and is inevitable because wind shear measurement involves the differentiation of airspeed. A period of a few seconds is needed to attenuate any short wavelength turbulence and avoid excessive noise in wind shear measurements. These measures of the current wind shear state do not provide the information needed to calculate potential height

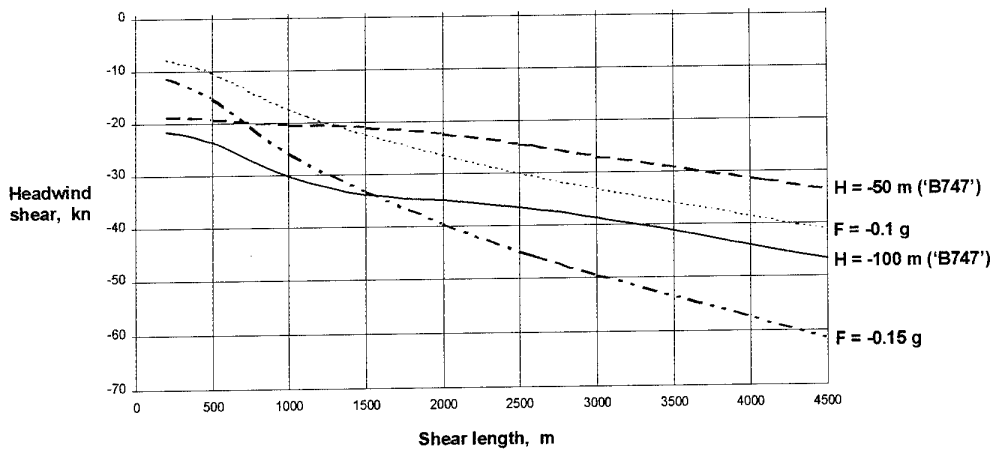
loss until after the aircraft has passed through the wind shear.

A different measure of wind shear severity has been developed for use with such 'instantaneous' measuring systems. The 'F' factor, as it is known¹⁶ is given by

$$F = \frac{dV_x/dt}{g} + \frac{V_z}{V}$$

The two terms are flight path angles, which are equivalent to the accelerations in 'g' units that need to be exerted to counteract the headwind and downdraught shear at any instant. If these accelerations could be generated instantaneously throughout the duration of a wind shear then there would be no deviation of flight path. The 'F' factor has the advantage that it can be calculated on-line during penetration of a wind shear and does not need to know the duration of the wind shear[#].

[#] 'F' factor is often derived by differentiating the total energy of an aircraft using airspeed for the kinetic energy term. This is not physically correct because energy can only be calculated within a frame of reference that is moving at a constant velocity. An accelerating frame of reference, such as that when wind shear changes airspeed, does not instantaneously change the energy of an aircraft. It changes the forces produced by the aircraft and these will eventually change its energy state.



$$\text{Updraught} = 0.24 * \text{Headwind shear}$$

Fig.25: Comparison of Potential Height Loss and 'F' factor contours for different shear conditions

Contour lines for the greatest magnitude of the 'F' factor in the nominal wind shears used for the 'B747' calculations of potential height loss are shown in Fig.25. 'F' factor lines of -0.1 and -0.15 g are shown together with the potential height loss lines for 50 and 100m for the 'B747' case. (N.B. The 'F' factor is mainly dependent on wind shear characteristics and its own filter time constant apart from the aircraft speed in the downdraught term.)

It is not surprising that potential height loss contours differ significantly from constant 'F' factor contours in Fig.25. The 'F' factor has no knowledge of the length of the shear nor its maximum values of headwind shear or downdraught. The 'F' factor is a useful approximation to the flight path angle change caused by wind shear at any point during an encounter. It will reach a maximum for the nominal wind shear form of Fig.15 when the downdraught first reaches a maximum (plus the time constant delay). Usually this will be much later than the 6 second delay used to calculate potential height loss, e.g. with an aircraft speed of 150 kn the 'F' factor will reach a maximum after 6 seconds, including a 4 second filter delay, if the shear length is > 620m.

If a given level of the 'F' factor is used to provide a wind shear alert, then the chosen level must be a compromise. For short duration wind shears the alert will be reached while the potential height loss is low. For long wind shears the alert will not sound until large height loss is already present (or the pilot

has already taken action). However, in the absence of more complete information about a wind shear, the 'F' factor does provide useful guidance to pilots about a large variety of wind shears. The 'F' factor is also useful as a term in any autothrottle system, where it will operate continuously to reduce the effects of wind shear.

4.2 Detection systems

Detection systems can be separated into two groups. Predictive warning systems measure conditions around an airport or well ahead of an aircraft and predict the conditions that an aircraft will encounter. Reactive measurement systems measure the wind conditions that an aircraft is encountering or conditions very close to the aircraft that will be encountered within a few seconds.

4.2.1 Predictive Warning systems

Before considering different types of predictive systems it should be remembered that wind shears are dynamic events which move, grow and decay with time. Prediction of their behaviour for one or two minutes can be quite reliable. Beyond that time the accuracy of the prediction falls rapidly and soon becomes little more than a warning to take care without any reliable indication that a wind shear will be encountered or any measure of its strength.

The most successful predictive system is Dual Doppler Weather Radar such as those used during the JAWS program¹⁷, which can measure headwind shears longer than about 500m. They can have

sufficient volumetric coverage to make a good estimate of downdraughts using continuity and energy equations. These measurements can be used to calculate wind shear severity using potential height loss methods and can follow the growth, decay and movement over the ground of wind shears. Wind shear data from radar can be available within seconds with suitable processing and data-link systems. These weather radar are used primarily for a wide range of weather measurements for forecasting. By locating such radar in appropriate positions near major airports it is possible to use them for wind shear measurement and prediction.

Other ground based systems have been tried such as the use of anemometers and direction vanes at a series of locations on and around airports, as in the Low Level Wind Shear Alerting System. This system has been used at several USA airports, but despite some improvements in alerting algorithms it is always going to be difficult to locate anemometers where they will feel the effects of significant wind shears. Many microburst and topographical rotor types of wind shear are less than 1Km in size, and it is not practical to locate and maintain anemometers with such a close spacing to cover all the approach and take off areas at an airport. Anemometer systems can be useful for detecting frontal shears, but can fail to identify many important wind shears.

One possible predictive wind shear system that has not been exploited could be based on measurements by preceding aircraft. In many of the major wind shear accidents in the USA the shear that caused the accident has often been experienced as a significant disturbance by preceding aircraft. Data measured by 'F' factor systems, or by analysing any other combination of accelerometers, angle of attack and air data measurements such as those provided for Flight Data Recording, could be analysed to give complete information about any wind shear that an aircraft has encountered. With the increasing use of 'data links' such information could be automatically signalled to the ground and up-linked to following aircraft if the wind shear was above a given strength. This data could be available almost immediately and provide information on conditions only one or two minutes ahead of the next aircraft. Such a system would certainly have given timely warnings to the aircraft involved in the JFK and Dallas/Fort Worth accidents if it had been available.

Finally there are investigations into fitting aircraft with medium range, i.e. several kilometres, wind shear detection systems such as pulsed laser radar (lidar) or infra-red radiometer systems. The intention is to assess the severity of wind shears in an aircraft's path. Lidar systems are the most reliable, but it is arguable that the expense, size, and complexity of these systems will limit them to large transport aircraft (at least initially). This is particularly true for a predictive system where the data may not be reliable enough to justify the expense of what may be a significant number of unnecessary 'go-arounds'. Transport aircraft are unlikely to encounter a wind shear that is beyond their capability to penetrate safely more than about 1 in 10⁸ landings. It seems unlikely that the installation of medium range lidar systems can be justified for wind shear alone, unless some other practical use is found that makes such a system economically desirable.

4.2.2 Reactive systems

Reactive systems will generally describe conditions as the aircraft penetrates a wind shear and the only delays will be the few seconds needed to filter turbulence from any underlying wind shear.

By definition it is not possible to use reactive systems to avoid wind shear. Thus it is important that such systems provide reliable quantitative data that can be used for warning systems, and, probably more importantly, to drive autothrottle and other relevant autopilot modes.

In principle any Inertial or Doppler navigation system that calculates winds could be used as a source of wind shear data. In practice such systems are heavily filtered to provide values of average winds for navigation purposes. Short and medium term wind changes are deliberately masked and the data would be less useful for navigation purposes if filtering was reduced. Thus wind shear systems are usually designed to be responsive to medium term wind changes and filter out short term turbulence and steady winds.

Most wind shear measuring systems on aircraft rely on measurements of normal and longitudinal acceleration, true airspeed and angle of attack to derive the 'F' factor, which is then used to drive a warning system and can be used as a signal to an autothrottle. An approximate value of the 'F' factor can be derived using pitch attitude rather than angle of attack¹⁸, and if both pitch attitude and angle of attack are used then it is possible to identify the

headwind and downdraught shears separately. In general it is preferable to use the signal from such inertially based systems to drive the autothrottle. A slow increase in the 'F' factor can produce a large disturbance before any warning level is reached. If the signal goes to an autothrottle then some of the necessary throttle action will be taken before the warning is reached. Height loss will be significantly less than taking action after the threshold is reached and an alarm triggered.

More timely information about an approaching wind shear can be obtained if a laser radar (lidar) is fitted to an aircraft¹⁹. This can measure airspeed along its line of sight at some distance from an aircraft and use this rather than the aircraft's normal air data system for calculating winds. Because any winds will be changing with time there is an optimum range for making such measurements. If the range is too close there will not be a worthwhile time lead before the aircraft encounters the wind. If the range is too large there will be an increasing uncertainty about the measured wind due to changes with time after the measurement. Dynamic oversensitivity will not be a problem because true winds are measured and not predictions based on rate information, such as those that are generated by lead/lag filters. An example of lidar measurements of the microburst wind shear in Fig.5 is shown in Fig.26. The lidar airspeed clearly leads the aircraft's measurement of airspeed by several seconds.

The difference between lidar measurements and on-

board air data, Fig.26, can be used to estimate a smoothed headwind gradient. This gives a true instantaneous gradient, and, if the flight time to the measuring point of the lidar is around 4 seconds or greater, any effects of turbulence will be attenuated. If the flight time is too great then the gradients of significant short length wind shears will also be attenuated. Thus the optimum focal length for a Continuous Wave Lidar is that corresponding to about 4 seconds flight time. This distance will be the minimum range required for any pulsed lidar system.

The width of the lidar spectrum, Figs.26 & 27, at any instant is also a measure of headwind shear gradient because the lidar is measuring winds at all points along its line of sight, although there is a large variation in signal strength which peaks at the focus. However, comparing airspeed differences with spectral width in Fig.26 suggests that differencing provides a more reliable estimate of gradient. This may be caused by effects of turbulence on the spectra shapes.

Lidar measure airspeed along their line of sight, but, by using a conical scanning motion combined with measurements of the angle of attack and pitch rate of the aircraft, it is possible to calculate vertical wind differences between the laser scanning position and the aircraft. The 'F' factor derived from this data will lead any data derived solely from the normal on-board systems by the flight time to the lidar measuring point, i.e. around 4

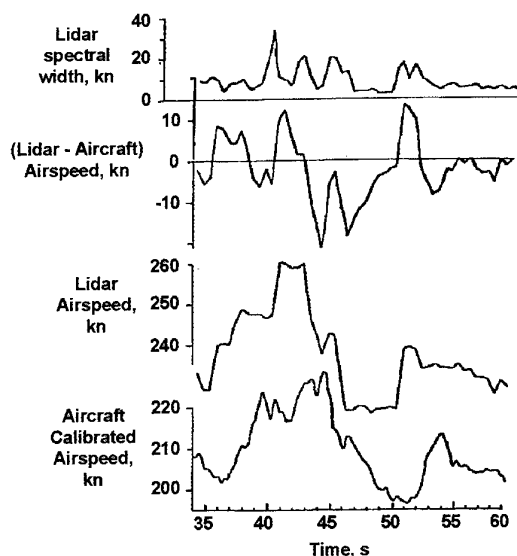


Fig.26: Lidar measurements of the microburst of Fig.5

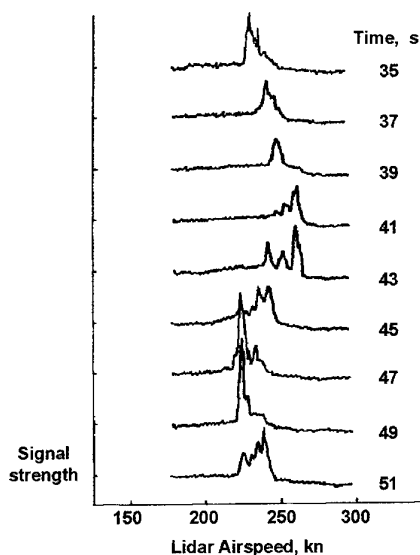


Fig.27: Lidar spectra during a microburst encounter (Fig.26)

seconds. This is a very significant lead, and also helps to improve the effectiveness of any autothrottle using 'F' factor inputs.

However, even these close range lidar will be expensive and complex systems and it is likely that they will not be used commercially unless there is a financial incentive. One possible incentive could be to use an efficient autothrottle system based on lidar information which could minimise throttle action without compromising response to genuine large deviations. Such an autothrottle would reduce thermal cycles during approaches and increase engine component life.

5. HELPING THE PILOT

5.1 Guiding principles for operations where wind shear may be present

Wind shears occur frequently, and come in all shapes and sizes. However, potentially hazardous wind shear is a very rare event and training, displays, and systems to assist the pilot must be appropriate and automatic (or 'instinctive' to apply).

On-board wind shear warning systems without any forward projection are relatively late in providing an alarm because an aircraft must be part way through a shear before its magnitude can be assessed. Also, because of the rarity of severe wind shear and the use of 'instantaneous' gradient measurements, it is almost inevitable that wind shear warning systems will generate false alarms, particularly from short duration wind shears with large headwind gradients, and will miss some significant shears, particularly long duration shears with significant downdraughts. In many cases a pilot will be responding to a shear before an alarm sounds. However, there is a need for warning systems to provide clear confirmation of the presence of a potentially hazardous shear to pilots who may be distracted by other problems or confused by apparently conflicting behaviour of their aircraft. (This is similar to the situation with Ground Proximity Warning Systems (GPWS), which should not be needed if pilots were able to absorb and understand everything that is happening during an approach in difficult circumstances. Pilots are frequently already taking appropriate action before a GPWS alarm sounds, but it is there to help on those few crucial occasions when action is not being taken.)

Guidance from regulatory bodies, such as the FAA, and from ICAO emphasises that pilots should avoid

encounters with severe wind shear wherever possible. This is good advice, but unfortunately there are likely to be few occasions where reliable advance warning of severe wind shear can be provided. The only systems able to provide reliable quantitative advice are Doppler Weather Radar sending continuous information to Air Traffic Controllers or over data links to aircraft, and any data on encounters by immediately preceding aircraft. Any information from other systems is likely to be too imprecise or old to do anything more than alert a pilot to the possible presence of severe wind shear. Thus avoiding wind shear is rarely likely to be a practical proposition.

Not only are reliable predictive systems unlikely to be available, but most wind shear warning systems in aircraft are unlikely to be entirely reliable nor can they always be expected to provide timely warnings. Only warnings from on-board short range lidar offer the possibility of being timely and reliable at all airports and in all conditions, but these are unlikely to be in widespread use (at least for some years to come). Thus it is essential that pilot training prepares them to respond appropriately in wind shear. Because of the rarity of severe wind shear and the need for prompt and appropriate action by pilots, any flying techniques should be appropriate to all types and sizes of wind shear. There will be a better chance of pilots using these techniques instinctively if they are valid for any situation where there is a significant downwards deviation from the intended flight path at low altitude.

Such techniques should not require any special wind shear displays or information, but should be able to be applied using normal cockpit display information. Only in this situation can pilots be expected to respond 'instinctively', because the technique needed to respond to a potentially hazardous 'severe' shear will be a direct extension of the technique that they will have used during previous encounters with many 'moderate' and a few 'strong' shears.

In summary the most important principle is that response to wind shear must be handled by automatic flight systems and 'instinctive' responses by pilots based on appropriate general flying techniques and normal cockpit displays. A wind shear warning system should be provided, but no special wind shear displays should be presented.

5.2 Cockpit displays

Despite the recommendation to avoid special wind shear displays there have been many investigations over the years into providing continuous wind shear information on separate instruments, or with additional information on rate of climb or airspeed instruments. The main features will be described briefly, if only to indicate why many are not particularly appropriate.

Special wind shear displays have shown a parameter, usually closely related to the 'F' factor on a dial or strip instrument. In principle this is more helpful than a threshold exceedance alert system because it provides continuous information on the development of a shear. Unfortunately this presupposes that a pilot will be including such an instrument in his normal scan pattern during an approach (or take off). In practice this is unlikely because for most flights the instrument will not provide any useful information.

Wind shear and throttle activities change the climb gradient, or Specific Excess Power, capability of an aircraft. This can be indicated on the Rate of Climb instrument by a second needle²⁰. For example, during an approach, if the second needle indicates a greater sink rate than that of the aircraft, then more thrust will be need to be applied. If this action is not taken then the sink rate will increase to that shown by the second needle. Unfortunately the rate of climb instrument is not part of the primary scan pattern of pilots. It is mainly used to adjust the mean power over a period of several seconds. Thus it suffers from inattention in the same way as any dedicated wind shear display. The other problem is that the rate of climb increases with speed for a given gradient. This means that if a higher approach speed is selected to reduce the effect of a shear then the difference between the two needles gets greater rather than smaller.

Incorporating wind shear information on the airspeed instrument²¹ overcomes any problems of lack of attention as this instrument is a crucial part of the primary scan pattern of pilots. There is a direct relationship between airspeed changes and headwind shear, and also with climb gradient changes. Unfortunately there is no direct relationship with the effects of downdraughts, but these are generally accompanied by headwind shear. The most direct and easily interpreted representation of headwind shear is obtained through a second needle or bug showing ground speed (or more precisely an equivalent ground

speed corrected for relative density such that it can be compared directly with the Calibrated Airspeed signal). In the absence of significant shear the two needles will move together with only a gentle drift and small oscillations from turbulence and boundary layer shear. In the presence of significant shear the needles will converge or diverge quite rapidly, with the ground speed remaining almost constant initially. This large change will alert the pilot to the presence and the magnitude of a wind shear. This type of display has no significant disadvantages other than the need to avoid confusion between the needles. A pilot could get into difficulties if the ground speed was used as the reference speed on an approach instead of airspeed.

The instruments that are most useful during an encounter with wind shear are the Airspeed, pitch attitude indication on the ADI, and the Rate of Climb, together with the Stall Warning System. Airspeed and rate of climb will identify the problem, which will usually be a reducing airspeed and increasing sink rate (or reducing climb rate during take off). Then appropriate throttle action and control of pitch attitude, both visually and on instruments, can be used together to respond to the shear. Presentation of 'Go-around' director information related to wind shear on the ADI can be particularly helpful, particularly in poor visibility conditions.

Most current display studies are concentrating on including appropriate responses to wind shear in existing director modes on the ADI.

5.3 Training

Nearly all the major wind shear accidents, with the probable exception of that at Dallas/Fort Worth in 1985, could have been avoided if the pilots had taken appropriate action at the time they started to apply significant thrust to counteract the effects of the wind shear. However, prior to 1985, all the pilots were responding in the way that they were trained to respond, and were trying to recover from a large loss of airspeed by increasing thrust and reducing pitch attitude. Clearly there was something wrong or missing from the way that pilots were being trained.

It seemed unlikely that training was wrong as it had developed from decades of experience. So what was missing?

The primary training rules relating to approach and landing were

- a maintain an airspeed near or above the reference speed to avoid the possibility of stalling. (Reference speed is set at around 1.2 to 1.3 times the 1'g' stalling speed)
- b use throttle to adjust the mean rate of descent (sink rate)
- c use pitch attitude to control the mean airspeed.

From these it is clear that increased throttle and reduced pitch attitude would be appropriate responses to a falling airspeed and increasing sink rate. If an aircraft is well clear of the ground or the wind shear is only moderate, then this technique will be satisfactory. However it involves significantly greater loss of height during recovery than more optimum techniques, and this can be catastrophic if the aircraft is close to the ground.

It may seem obvious, but to counteract increasing sink rate and avoid hitting the ground it is necessary to temporarily increase the vertical force (lift and component of thrust normal to the ground) on the aircraft. The lift increase can be obtained by increasing airspeed at constant angle of attack, or increasing angle of attack at constant airspeed, or a suitable combination of both. Increasing thrust will give very little component normal to the ground in most cases, but it is the means for increasing airspeed (or at least reducing any loss of airspeed due to the shear) to generate more lift.

Angle of attack, α , is related directly to the pitch attitude, θ , and the flight path angle, γ , viz.

$$\alpha = \theta - \gamma$$

Thus the immediate effect of reducing pitch attitude is to reduce the angle of attack and hence the lift. This will increase the sink rate.

From this it would seem that the most appropriate response to increasing sink rate from *any cause* would be to increase pitch attitude and apply thrust to increase airspeed. However, increasing sink rate implies an increasingly negative flight path angle and this together with increasing pitch attitude could rapidly increase the angle of attack towards the stall angle. Thus the practical recommendation to respond to increasing sink rate is to maintain pitch attitude and increase thrust. If this is not sufficient to achieve the desired reduction in sink rate by the time that full thrust is applied, then pitch attitude should be increased until stall warning is

reached. In this condition the aircraft is producing the maximum vertical force available.

Sink rate needs to be controlled as soon as possible because the height loss in recovering from a given sink rate with a given vertical force is proportional to the square of the sink rate. It is possible to use the training rules to recover from moderate sink rates where the additional height loss can be negligible. In a severe shear the difference in techniques can make several hundreds of feet difference to the height loss.

The apparent discrepancy between this advice on recovery from increasing sink rate and airspeed loss and the training rules is at the heart of the long running debate about whether throttle controls sink rate and pitch attitude controls speed or vice versa. The answer is that both methods should be used. The training rules are appropriate for controlling mean conditions, i.e. trimming the flight condition, and the recovery advice is appropriate for responding to transient disturbances. Thus if the approach condition needs a long term adjustment use the training rules, but if a significant temporary disturbance occurs then use the recovery advice. In practice some pilots will already be using this combination of techniques, but others will have kept more closely to the training rules.

One significant addition to training is that pilots need to learn that the 1'g' stalling speed is meaningless in the context of a major wind shear encounter where normal 'g' can be varying by $\pm 1'g'$. The only true indication of proximity to the stall is given by the stall warning, and in extreme conditions it is necessary to use all the performance that the aircraft can provide even if this means going as far as stall warning. It is no good keeping money in reserve for the future if you are going to starve to death today!

Wind shear training programmes are now available on most airline training simulators²². This provides a practical means of demonstrating and training pilots in the use of the recovery techniques, and of the dangers inherent in reducing pitch attitude. Unfortunately the general principles of recovery from undesirable sink rates are not currently taught as part of basic flying training. If this does become common practice then specific wind shear training will become less important, although wind shear provides a powerful means of demonstrating the benefits of using the correct techniques.

5.4 Autopilots

Autopilot modes are designed to maintain particular flight parameters constant without intervention by a pilot, or to perform a particular activity such as the landing flare or a 'go-around' manoeuvre. Pilots will expect autopilots to respond appropriately during a wind shear encounter, and are likely to be slower to recognise any problems because of these expectations. Thus it is essential that autopilots should take the most appropriate actions during a wind shear encounter. Three autopilot modes are particularly relevant and these are

- a Autothrottle, which is designed to maintain airspeed constant,
- b Coupled approach, which is designed to maintain the instrument approach path (This usually works together with the autothrottle mode)

Autopilot modes usually have limited authority over the control inputs that they can make. This prevents unwanted large disturbances to the aircraft in the event of a sensor failure or large spurious signal. Unfortunately a wind shear can produce real signals that are large and could exceed limiting thresholds for an autopilot. This would cause the autopilot to stop functioning and require immediate intervention by the pilot to continue responding to the wind shear.

This can be a particular problem with thrust response to autothrottle demands where sufficient authority to provide maximum thrust is needed for some strong and severe wind shears.

It is also very desirable that any autothrottle should respond to deviations in sink rate as well as airspeed, and that it should increase airspeed above its reference value until any deviation in sink rate is eliminated. Unless such terms are present, e.g. through an 'F' factor input, it is important to override any autothrottle mode during an encounter with strong or severe wind shear. A good recovery depends on achieving airspeeds above the reference value.

In a fully coupled approach mode with flight path and speed control it is important that the autothrottle includes wind shear terms ('F' factor). It is also important that any speed error inputs to pitch control are biased by an 'F' factor term to prevent reductions in pitch attitude during any encounter with a significant wind shear.

In general, unless autopilot modes include appropriate inputs of wind shear conditions such as the 'F' factor, their response will be significantly worse than optimum pilot control although this may very well only become apparent in encounters with large wind shears. During encounters with more moderate wind shear the response of the autopilot will be adequate and the small extra height loss compared with an optimum response will not be evident.

Usually it is better for the pilot to override autopilot modes as soon as there is any suggestion that sink rate is becoming undesirably high.

Sophisticated flight control systems such as those in the Airbus 320 and other modern aircraft can be a great help during a wind shear encounter if they provide reliable angle of attack control to avoid stalling. In such situations a pilot should be able to apply full thrust and full back stick to recover from a severe wind shear and the aircraft's control system will hold the maximum safe angle of attack.

6. CONCLUSIONS

Severe wind shear with both headwind changes and downdraughts can be a hazard during landing and take off of aircraft. The paper has summarised much of the knowledge gained following a series of major accidents in the 1970's and early 1980's where wind shear was recognised as the probable cause.

Of the various causes of wind shear, those arising from winds over rugged terrain, those created by storm fronts, and microbursts in the vicinity of thunderstorms are responsible for most of the encounters between aircraft and strong or severe wind shear. Routine operations in all-weather have increased the probability of encountering a severe wind shear, and improvements in the aerodynamic effectiveness of modern aircraft wings tend to increase height loss during encounters with headwind shear.

However, data obtained from analysing wind shear encountered during about 10000 landings around the world by the British Airways B747 fleet indicate that the probability of encountering an unsurvivable wind shear is very low, i.e. of the order of less than 1 in 10^8 landings. Data from a small sample of large wind shears indicates that downdraughts are typically about 0.24*(Headwind shear).

A simplified method of estimating the response of an aircraft to wind shear has been developed based

on flight at constant pitch attitude, which is shown to be a close approximation to normal controlled flight for disturbances lasting longer than a few seconds. Potential height loss during a wind shear encounter is shown to depend on flight speed, wing loading, available acceleration at full thrust and the delay in starting to apply thrust, including a small effect due to the engine thrust response time constant. The effects of headwind and downdraught shears on an aircraft are rather different and downdraught response is independent of wing loading.

Calculations of potential height loss for a 'B747' type of aircraft and comparison with data from the British Airways world-wide landings suggests that height losses of 50m and 100m may be appropriate boundaries between Moderate & Strong and Strong & Severe wind shear respectively. Height loss is not linear with the magnitude of the shear, e.g. it doubles with between 40% and 60% increase in the magnitude of headwind shear where stall warning is not reached.

Potential height loss is an appropriate measure of the hazard posed by a wind shear when its character is fully defined in terms of wind magnitudes and length. An alternative measure is the 'F' factor which defines the 'instantaneous' magnitude of a wind shear. This, by its very nature, will tend to overestimate the severity of short duration shears with large headwind gradients and underestimate (and provide a late warning) for long duration shears with modest yet potentially hazardous downdraughts. However, 'F' factor signals are appropriate as inputs to an autothrottle to reduce height loss during a wind shear encounter.

Predictive wind shear measurement and forecasting systems have been demonstrated and those based on the use of Dual Doppler Weather Radar, or on information from preceding aircraft, are likely to be reliable. However any predictive system will need to be very reliable if it is to be used by pilots as a basis for 'go around' decisions. Wind shear varies significantly in magnitude with time and moves with the local wind so it is difficult to forecast encounter severity for 30 to 60 seconds ahead to give sufficient time for avoidance action by a pilot. Forecasts will be useful for Severe wind shear when it is wise to take avoiding action, but wind shear that is less than Severe can be safely penetrated using appropriate flying techniques. Dual Doppler Weather Radar are unlikely to be available at many airfields, and encounters by preceding aircraft

cannot be expected on many occasions. Thus there is a need for systems on aircraft to assist and warn pilots during wind shear encounters.

In many situations pilots will recognise wind shear as rapidly as on-board warning systems, but such systems are still valuable to alert pilots who may be distracted by other happenings and to confirm that the wind shear is part of the cause of any unusual behaviour of the aircraft. 'F' factor systems are available and use accelerometer and air data signals to estimate the current value. Lidar systems, which look ahead of the aircraft by about 4 seconds, have been tested and provide much more timely measurements of the 'F' factor for any wind shear.

Autothrottles and other autopilot modes can have inappropriate responses in wind shear if they restrain speed increases that are essential to minimise height loss, and if they can reduce pitch attitude during recovery. There may also be additional delays before a pilot takes appropriate recovery action if limits are exceeded and an autopilot switches off during an encounter. Autothrottle systems with 'F' factor inputs are more helpful during a wind shear encounter. Flight control systems with automatic stall avoidance will make it easier and safer for a pilot to fly to the maximum safe angle of attack when this is needed to achieve maximum lift.

Special wind shear instruments or other displays to the pilot of wind shear situations are not appropriate because of the rarity of severe events, and the importance of pilots reacting correctly in an instinctive and timely fashion. Pilot actions in response to an encounter with a rare severe wind shear should be the same as those used during more frequent encounters with moderate and strong shears.

Flying technique changes are the most useful way of countering the effects of wind shear. Before the early 1980's the emphasis was on thrust to control flight path, pitch attitude to control speed, and maintaining a good speed margin from the 1'g' stalling speed. This is sound advice for maintaining average conditions, but inappropriate when faced with transient disturbances. It led to pilots reducing pitch attitude to try and regain speed in wind shear encounters, and this significantly increased the loss of height. The appropriate response to transient disturbances with increased sink rate is to increase thrust in an attempt to maintain or increase speed and maintain pitch attitude, or if necessary increase pitch until stall warning is reached. This flying

technique is now taught on piloted simulators with wind shear models, and is the appropriate technique to reduce sink rate in any situation.

All the major accidents attributed to wind shear in the USA since around 1970, with the exception of the accident at Dallas/Fort Worth in 1985, would not have occurred if the above technique had been taught and used.

Very large wind shear events can still be encountered during normal operations. However, with today's knowledge about wind shears, their causes, characteristics, probability of encounter, the response of aircraft, detection systems, improved autopilots and, above all, improved flying techniques and pilot training aids, the probability of accidents from encounters with wind shear has been dramatically reduced.

References

- 1 "Low-Altitude Wind Shear and Its Hazard to Aviation", National Research Council, National Academy Press, 1983
- 2 William G Laynor, "Summary of Windshear Accidents and views about Prevention", SAE 861697, SAE Transactions - Aerospace, Vol.95, 1986
- 3 Report of the USA Civil Aeronautics Board, American Airlines Inc., DC-3, NC 16014, near Bowling Green, Kentucky, July 28, 1943. File No. 3525-43
- 4 A A Woodfield, "Classification of Wind Shear Severity", AGARD Flight Mechanics Panel Conference on "Flight in Adverse Weather Conditions", Gø1, Norway, 8-11 May, 1989. AGARD CP 470, September, 1989
- 5 A A Woodfield & J F Woods, "Wind shear from Head wind measurements on British Airways B747-236 aircraft - Initial results", RAE Tech. Memo. FS 409, June, 1981
- 6 A A Woodfield & J F Woods, "Worldwide experience of Wind Shear during 1981-1982", AGARD Flight Mechanics Panel Conference on 'Flight Mechanics and system design lessons from Operational Experience', AGARD CP No. 347, 1983
- 7 "Report on the accident to British Aerospace ATP, G-BTPE at Sumburgh Airport, Shetland Isles, on 23 December 1991", The Department of Transport, Air Accidents Investigation Branch, Aircraft Accident Report 6/96, December 1992
- 8 T T Fujita, "Spearhead echo and downburst near the approach end of a John F Kennedy airport runway, New York city", University of Chicago, SMRP 137, 1976
- 9 A Haynes, "Description of a program developed for the analysis of windshears experienced during aircraft approach to landing", RAE Tech Memo FS 321, March 1980
- 10 J G Jones, "The application of worst case analysis to aircraft gust response assessment. A Statistical Discrete gust Theory progress note", RAE Technical Memorandum FS 321, 1980
- 11 "Aircraft Accident Report - Pan American World Airways, Clipper 759, N4737, Boeing 727-235, New Orleans International Airport, Kenner, Louisiana, July 9, 1982", National Transportation Safety Board, NTSB-AAR-83-2, March 1983
- 12 B Etkin, "Dynamics of Flight", Chap. 6, John Wiley & Sons, New York, 1959
- 13 B S Turkel & W Frost, "Pilot-Aircraft System Response to Wind Shear", NASA Contractor Report 3342, 1980
- 14 W Frost, B S Turkel, & J McCarthy, "Simulation of Phugoid Excitation due to Hazardous Wind Shear", AIAA 20th Aerospace Sciences Meeting, AIAA-82-0215, January 1982
- 15 T T Fujita, "Microburst Wind Shear at New Orleans International Airport, Kenner, Louisiana on July 9, 1982", University of Chicago, SMRP Research Paper 199, January 1983
- 16 R Bowles & R Targ, "Windshear detection and avoidance: Airborne systems perspective", 16th Congress of the International Council of the Aeronautical Sciences, Jerusalem, Israel, 1988

- 17 C Kessinger, M Hjelmfelt & J Wilson, "Low-level microburst wind structure using Doppler Radar and PAM data", AMS 21st Conference on Radar Meteorology, Edmonton, Alberta, Canada 19-23 September 1983.
- 18 R A Greene, "Airborne detection of Low-level Wind Shear", J. Aircraft, Vol.16, No.12, December 1979
- 19 A A Woodfield & J M Vaughan, "Using an airborne CO₂ CW Laser for free stream airspeed and windshear measurements", Conference on Flight Test Techniques, AGARD CP-373
- 20 R M Griffin, "Study of Displays for Manual Speed and Flight Path Control in Windshear", Smiths Industries RID 1656, 1979
- 21 S L Gale & Alison White, "Windshear detection using the Airspeed Indicator: A piloted simulation study", RAE TR 87039, June 1987
- 22 A A Woodfield, "Severe Wind Shear. Measurement and modelling for airline pilot training.", RAeS Conference on "Data Issues for Flight Simulators - An on-going problem?", 10-11 November 1993

HEAVY RAIN EFFECTS

by

R. Earl Dunham, Jr.,
NASA Langley Research Center
Mail Stop 156A
Hampton, VA 23665-5225, USA

SUMMARY

This paper summarizes the current state of knowledge of the effect of heavy rain on airplane performance. Although the effects of heavy rain on airplane systems and engines are generally known, only recently has the potential aerodynamic effect of heavy rain been recognized. In 1977 the United States Federal Aviation Administration (FAA) conducted a study of 25 aircraft accidents and incidents which occurred between 1964 and 1976 in which low-altitude wind shear could have been a contributing factor (reference 1). Of the 25 cases (23 approach or landing and 2 take-off) in the study, ten cases had occurred in a rain environment, and in five cases these were classified as intense or heavy rain encounters. These results led to the reconsideration of high-intensity, short-duration rainfall as a potential weather-related aircraft safety hazard, particularly in the take-off and/or approach phases of flight.

This paper describes the phenomena of heavy rain, discusses the analytical and experimental methods that have been used to evaluate the aerodynamic performance penalty associated with heavy rain, and assesses scaling issues involved in extrapolating subscale testing results to a full size vehicle. Small scale and large scale test results are presented. The data indicate a reduction in maximum lift capability with increasing rainfall rate and an associated decrease in the angle of attack at which maximum lift occurs. It would appear that normal aircraft operations would not be affected by heavy rain since most operations avoid angles of attack near stall. However, if the heavy rain encounter occurs during a severe low altitude wind shear then the piloting procedures used to counter the wind shear effects may result in operating at a higher than normal angle of

attack. A simulation study of the combined effect of a simultaneous heavy rain and strong wind shear is shown. The results indicate that the additional performance degradation associated with the heavy can produce a significantly more hazardous wind shear encounter situation.

NOMENCLATURE

C_d	section drag coefficient
C_D	drag coefficient
C_l	section lift coefficient
C_L	lift coefficient

INTRODUCTION

Heavy rain has several effects on aircraft operations that need to be considered. They include the influence on the performance of engines and air data sensors, erosion of painted or composite surfaces, weather radar operation, and the overall aerodynamic performance of the airplane. Engines are certified to operate at water ingestion rates during aircraft cruise conditions that exceed the world record rain fall rate and current air data sensors are designed to minimize the effect of rain. Erosion resistant paints and composites have been developed. At this time the effect of heavy rain on weather radar performance has not been completely characterized. Evidence seems to indicate that in extremely heavy rain a layer of water over the radome may attenuate the radar signal and seriously limit its range. Such a reduction in the performance of the radar would result in the radar only detecting nearby rain shafts while not being able to see intense rain further away.

Only recently has the effect of heavy rain on airplane performance been addressed. The influence of rain on airfoil performance has

long been thought to be insignificant. Previously the primary hazards associated with airplane operations in heavy rain were the loss of visual reference during landing and take-off conditions. Until the late seventies the recognition of weather-related safety hazards to aircraft performance and operations had included clear-air turbulence, lightning, icing, hail, low-altitude windshear, and microburst. The latter two phenomena have long been recognized as hazards to aircraft landing and take-off operations. In 1977 the United States Federal Aviation Administration (FAA) conducted a study of 25 aircraft accidents and incidents which occurred between 1964 and 1976 in which low-altitude wind shear could have been a contributing factor (reference 1). Of the 25 cases (23 approach or landing and 2 take-off) in the study, ten cases had occurred in a rain environment, and in five cases these were classified as intense or heavy rain encounters. These results led to the reconsideration of high-intensity, short-duration rainfall as a potential weather-related aircraft safety hazard, particularly in the take-off and/or approach phases of flight.

This paper is an summary of the most recent work conducted by the NASA and others to study the influence of heavy rain on airfoil performance. The overview includes results of recent attempts to measure high-intensity, short-duration rainfall, a discussion of some of the earlier analytical investigations of rain effects on airfoils, a review of some promising experimental methods for evaluating rain effects, and some important scaling considerations for extrapolating model data. The potential effect of heavy rain on airplane aerodynamic performance is quantified in a simulation study and the results discussed.

THE CHARACTERISTICS OF HEAVY RAIN

In order to develop analytical models and conduct experimental studies on the effect of rain on airfoil performance, the phenomenon of naturally occurring precipitation needs to be understood. An understanding of the drop size distribution associated with heavy rain, the frequency of occurrence, and the range of

rainfall rates is required in order to assess hazard potential for aircraft operation.

Two quantities generally used to describe rain are rainfall rate (R) and liquid water content (LWC). Rainfall rate is the linear accumulation depth at ground level per unit time and liquid water content is the mass of liquid water per unit volume, usually expressed as g/m^3 . An additional parameter for quantifying rain is the rain drop size distribution. In the absence of a vertical wind velocity, the LWC is directly related to the rainfall rate and the drop size distribution. The relationship is uniquely dependent on the type of storm and the intensity level of the storm. In 1947 Marshall and Palmer (reference 2) collected data which showed that the size distribution of rain in a cloud could be estimated using an exponential expression of the form:

$$N(D) = N_0 e^{-ID}$$

where $N(D)$ is the drop size distribution (density function) in terms of the number of drops per cubic meter of air per unit interval, D is the drop diameter, and $I = nR^m$, where n , m , and N_0 are empirically determined constants and R is rainfall rate. Data from Marshall and Palmer indicated that $N_0 = 8000$, $n = 4.1$, and $m = -.21$ for the light continuous rain. More recent studies (references 3 and 4) have shown that the values of N_0 , n , and m are dependent upon storm type and intensity. Reference 3, for example, suggests that the distribution in heavy thunderstorm-type rain is best characterized by $N_0 = 1400$, $n = 3.0$, and $m = -.21$.

For a given drop size distribution the liquid water content can be calculated since it is the integrated sum of the mass of each drop multiplied by the number drops of each size per unit volume as follows:

$$\text{LWC} = \int_0^{\infty} \rho_w \frac{\pi}{6} D^3 N(D) d(D)$$

where: ρ_w = density of water

When the integration is performed this expression becomes

$$\text{LWC} = \frac{N_0 \rho_w \pi}{I^4}$$

substituting $I = nR^m$

then
$$LWC = \frac{N_0 \rho_w \pi}{n^4 R^{4m}}$$

When the suggested constants of Marshal and Palmer are substituted for light continuous rain the following equations results:

$$LWC = .08894 R^{.84}$$

For storm rain conditions the constants of Joss and Waldvogel yield the following equation:

$$LWC = .054 R^{.84}$$

These equations for the relationship of liquid water content and rainfall rate are plotted and shown in figure 1.

The range of rainfall rates that an airplane could expect to encounter varies from light rain of 5-10 mm per hour (.2-.39 in/hr) up to very large rainfall rates. The ground-level world record rainfall accumulation of 30.5 mm (1.2 inches) in one minute was measured in an intense afternoon thunderstorm on July 4, 1956, (ref. 5). The volume of rain accumulated in the one minute time interval is equivalent to a rainfall rate of 1830 mm/hr (73.8 in/hr). In 1978 Jones and Sims (reference 6) reviewed data on instantaneous rainfall rates. The probability distribution data collected by Jones and Sims, measured over time constants of 1- and 4-minute accumulations at ground level, are useful for determining the potential for encountering a given rainfall rate. They analyzed data collected over a one-year period on recording weighing-bucket rain gages placed throughout the world. Gages from maritime subtropical (Southeastern USA, Vietnam, Marshall Islands, Japan), continental temperate (Midwestern USA, Alaska), maritime temperate (England, France, West Germany, Northwestern USA), and mid-latitude interior (Israel, Southwestern USA) regions were used. Figure 2 is a summary of the averaged zonal frequency distribution curves obtained. The probable number of minutes a given rainfall rate (or greater) can be expected in a given climatological zone can be obtained from figure 2 by converting the ordinate from percent to a fractional portion of time and multiplying by the number of minutes in a year (5.2596×10^5). The Jones and Sims data indicate that for about two minutes every year in the maritime subtropical zone, a rainfall rate greater than

200 mm/hr (8 in/hr) could be expected at any location.

More recently Melson (references 7 and 8) reviewed the methods of obtaining instantaneous rainfall rates from tipping buckets (Jones and Sims, reference 6) and determined that this measurement technique masks the short-duration (less than a minute), high-intensity rainfall characteristics associated with thunderstorms. Melson's technique acquires data over very short time constants, as short as one sample per second. Data were acquired at 6 geographical sites: Darwin, Australia; Seattle, Washington; Denver, Colorado; Kennedy Space Center, Florida; Hampton, Virginia; and Wallops Island, Virginia. His measurement technique has verified the existence of high-intensity rainfall at ground level (reference 8). Over 7,000 events have been measured above 100 mm/hr since the test program began in 1988. The maximum rainfall rate measured of 720 mm/hr (28.3 in/hr) occurred for just under ten seconds at NASA Wallops Flight Facility in 1990. In figure 3 the data are presented as percentages of the total number of measurements indicating that one quarter percent of the events measured were above 508mm/hr (20 in/hr). The rainfall rates above 508mm/hr (20 in/hr) were sustained up to 10 seconds per event.

Most of the work on rainfall intensity and duration has been done by ground based measurements. Some limited in-flight data would indicate (within regions of convergence in a thunderstorm) the potential existence of extremely high localized liquid water which is dispersed by winds before it impacts the ground.

ANALYTICAL WORK

The computation of airfoil performance, including viscous effects near stall, is by no means a mature technology, and it is even more uncertain in a rain environment where these computations must be made for a two component, two-phase flow field. An idealization of rain drop interaction with an airfoil is shown in figure 4. Drop interactions include drop trajectories with respect to

streamlines, drop splash-back ejecta in regions of near oblique drop encounters, and splash-back ejecta coupled with water film "runback" interaction with the air boundary layer. Gaining a detailed understanding of the physical phenomena and developing an accurate mathematical model poses a unique aerodynamic challenge which has not yet been accomplished, although several efforts have been directed at describing certain aspects of the problem.

The effect of rain on the aerodynamic performance of an airplane was addressed analytically as early as 1941 by Rhode (reference 9). His analysis indicated that drag increases associated with the momentum of a DC-3 aircraft encountering a rain cloud with a water mass concentration of 50 g/m^3 (equivalent to approximately 1270 mm/hr or 50 in/hr) would cause an 18 percent reduction in airspeed. Rhode considered such an encounter to be of a short duration and of little consequence to an aircraft flying at 1524m (5000 feet).

Since low visibility take-offs and landings were not routine in 1941, the consequences of a heavy rain encounter during these phases of flight was not considered. However, for a modern day transport such an airspeed loss during take-off or landing would be significant. In the intervening years a great deal of work had gone into calculating the motion of water drop particles in the flow field about an airfoil (references 10 to 14); however these efforts were directed at calculating water drop trajectories and impingement on the airfoil for purposes of estimating ice accretion. The influence of liquid water on the airfoil performance was not calculated. The influence of rain on airplane performance was addressed again in 1982 when Haines and Luers (reference 15), under contract from NASA, evaluated the effect of rain on aircraft landing performance.

The Haines and Luers study was an attempt at refining the study of Rhode to estimate the effects of rain on a modern-day airplane. Their analysis not only included the calculation of the impact momentum of the raindrops, but also estimated the increase in

skin friction drag by equating the water layer waviness and raindrop crater effects on the airfoil surface to an equivalent sand grain roughness. Using empirical data for roughness effects on airfoil lift they calculated the rain effect on the lift and drag of a 747 transport. Their analysis estimated a 2 to 5 percent increase in drag and a 7 to 29 percent reduction in maximum lift with associated reductions in stall angle from 1 to 5 degrees for rainfall rates from 100 to 1000 mm/hr (3.94 to 39.37 in/hr). These predictions, of course, constitute a substantial loss of performance.

In 1984 Calarese and Hankey (reference 16) studied droplet drag acting as a body force in the Navier-Stokes equations. This analysis neglects the interface effects of droplet splashing, cratering, and water-layer formation. Their analysis produced a pressure distribution for an NACA 0012 airfoil for the limiting cases of a very fine rain (small drop size and a drop Reynolds number much less than 1) and for a coarse rain (large drop size and large Reynolds number). For the coarse rain little change in airfoil pressure distribution was noted. For the fine rain, significant changes in pressures were predicted which showed a small increase in lift with increasing water spray concentration.

In 1985, Kisielewski (reference 17) performed a three-dimensional Euler analysis to investigate the effects of momentum and energy exchange between the rain and the flow field. He concluded that the rain had little effect on the calculated lift produced by a simple airfoil. Both Calarese and Hankey and Kisielewski concluded that the major influence of rain on airfoil performance was probably dominated by viscous effects of the water droplet splashing and its subsequent interaction with the air boundary layer, but these effects were not modeled in their analyses.

EXPERIMENTAL METHOD

The experimental investigation of rain effects on the aerodynamics of airfoils or aircraft systems is a technical challenge as difficult as

investigating the effects analytically. A full-scale flight test investigation would require that performance measurements be made on an airplane while in a severe rainstorm. In addition to the hazard to the test pilot, extraction of accurate performance measurements and environmental parameters would be very difficult. Because of the variability of natural rain, repeatable conditions would be difficult if not impossible to obtain. Scale model tests of the effects of rain present a different set of challenges in that they require the simulation of properly scaled rain conditions. The three types of tests which have been used for investigating the effects of rain are (1) a rotating arm in which a model is placed at the end of a counterbalanced rotating beam, (2) conventional wind tunnels, and (3) a track in which the model is propelled down a straight track segment.

Rotating arm facilities have been quite useful for studying single-drop impact dynamics (references 18 and 19). Airfoil performance measurements have not been attempted with the rotating arm facility because the centrifugal effects on the water film would influence the results. Wind tunnels and track facilities are considered to be the best methods of obtaining airfoil performance data, and in both methods the technique for simulating rain and developing scaling relationships presents the areas of greatest difficulty. For the wind tunnel the difficulty lies in obtaining a uniform distribution of the water with a minimum of influence on the tunnel flow conditions. For the track the water manifolding and nozzle distribution becomes elaborate and extensive in order to cover the test area.

NASA has developed test techniques and procedures and conducted a series of wind-tunnel tests in the NASA Langley 14- by 22-Foot Subsonic Tunnel. The tests were conducted in the closed test section with dimensions of 14.5 feet high (4.42m) by 21.75 feet wide (6.63m) by 50 feet long (15.24). A photograph of a typical test set-up and a schematic of the test technique developed are shown in figures 5 and 6. The model hardware was located in the aft bay of the test section aligned laterally with the tunnel centerline.

The water spray distribution manifold, shown in figure 7, was located approximately 10 wing chord-lengths upstream of the model location and directed the spray horizontally at the model while aerodynamic force measurements were obtained. The shape and location of the spray manifold were selected to minimize the interference effect on tunnel freestream conditions and to allow time for the stabilization of the accelerating water droplets. The manifold was aligned approximately 6 inches (15.24cm) above the chord plane of the model to account for gravity effects on the water droplets. Comparisons of model aerodynamic data in and out of the simulated rain environment were made with the spray manifold in position at all times.

SCALING ISSUES

In 1985, Bilanin (reference 20) addressed the subject of scaling for model tests of airfoils in simulated rain. The complexity of the scaling problem was reduced by an analysis which indicated that thermodynamics effects of condensation and evaporation would make a small change in lift curve slope (less than 3%) even for very heavy rainfalls. By ignoring these thermodynamic effects, the scaling problem could be treated as illustrated in figure 4 where a subsonic airfoil is operated in a two-component flow field. The actual surface of the airfoil is assumed to be smooth so that surface roughness is not a parameter.

The dimensional variables which control the aerodynamics force (F) generated on the airfoil are:

<u>Symbol</u>	<u>Variable</u>	<u>Units</u>
ρ_a	density of air	ML ⁻³
ρ_w	density of water	ML ⁻³
γ_a	kinematic viscosity of air	L ² T ⁻¹
γ_w	kinematic viscosity of water	L ² T ⁻¹
$\sigma_{w,s}$	surface tension water-solid	MT ⁻²
$\sigma_{a,s}$	surface tension air-solid	MT ⁻²
$\sigma_{w,a}$	surface tension water-air	MT ⁻²
D	volume average drop diameter	L
λ	mean spacing between drops	L
c	airfoil chord	L
U_∞	flight speed	LT ⁻¹
α	angle of attack	radians

A nondimensional analysis of these variables shows that the nondimensionalized aerodynamic force on the airfoil is a function of nine nondimensional groups as follows:

$$\begin{aligned} \text{Group 1} &= \frac{cU_\infty}{\gamma_a} & \text{Group 2} &= \frac{cU_\infty}{\gamma_w} \\ \text{Group 3} &= \frac{\rho_w U_\infty^2 D}{\sigma_{w,a}} & \text{Group 4} &= \frac{\sigma_{w,s}}{\sigma_{w,a}} \\ \text{Group 5} &= \frac{\sigma_{a,s}}{\sigma_{w,a}} & \text{Group 6} &= \frac{\lambda}{c} \\ \text{Group 7} &= \frac{D}{c} & \text{Group 8} &= \alpha \\ \text{Group 9} &= \frac{\rho_a}{\rho_w} \end{aligned}$$

The first two groups are simply the Reynolds numbers of the air and water respectively. The third group is the Weber number which is the ratio of inertial forces to surface tension forces. Groups four and five preserve the scaling of surface energy interaction. Groups six and seven dictate that droplet spacing and mean diameter must be scaled with the airfoil. Groups eight and nine dictate that for similar results the scaled tests must be conducted at the same angle of attack and with fluids preserving the density ration of air to water.

It is unlikely that scale model tests can be conducted while preserving all of the parameters. For example, simply increasing test velocity while decreasing model scale allows Reynolds number to remain unchanged. The Weber number, however, is a squared function of velocity and must change since the drop diameter can only be changed linearly with scale in order to preserve the seventh scaling parameter. Since all of these parameters cannot be preserved from full scale to model scale, the sensitivity of the wet airfoil aerodynamic force to each of these parameters must be assessed.

It should be noted that the geometric scaling of the rain (variables six and seven) requires that liquid water content be conserved between full-scale and model-scale testing. However, since liquid water content is to be preserved in model testing, and the drop diameter is to be scaled, the distribution of drops must then be different for model testing

than for full-scale testing. In natural rain the rain rate, liquid water content, and drop distribution are uniquely related. Because of drop distribution distortions due to scaling relationships rainfall rate in model testing is a less meaningful term than is liquid water content. A useful term is obtained by defining an "equivalent full-scale rainfall rate" based on the liquid water content. For most of the model tests the liquid water content is quite high. In natural rain at high liquid water content most of the mass is contained in drops larger than 1mm, and these larger drops have fall velocities from 7 to 10 m/s (23 fps to 33fps). Since rainfall rate is the integrated product of liquid water content and drop velocity, for ease of calculation, an average drop velocity of 9 m/s (29.5 fps) was chosen and for the model test an equivalent rainfall rate was defined as the product of LWC and the average drop velocity.

WIND TUNNEL TESTS RESULTS

Exploratory tests were conducted on a wing with an NACA 0012 airfoil section fitted with a simple, full-span trailing-edge flap at Reynolds Number of 1.7×10^6 (reference 21). The wind-tunnel rain simulation system used for the NACA 0012 tests produced LWC values ranging from 13 to 22 g/m³. A 15 percent reduction in the maximum lift capability of both the cruise and landing configurations of the airfoil model were measured in the simulated rain environment independent of the LWC. A sample of the data is shown in figure 8. The exploratory small-scale wind-tunnel results confirmed the existence of a performance penalty in a simulated rain environment.

Following these tests, an investigation was conducted to determine the severity of the rain effect on an airfoil geometry which was representative of typical commercial transport wing sections as a function of rainfall intensity and to explore the importance of surface tension interactions of water as a scaling parameter (reference 22). The airfoil model was an NACA 64-210 with leading-edge and trailing-edge high-lift devices tested in cruise and landing configurations. The model had a rectangular planform and was supported

between two endplates in an attempt to represent a two-dimensional flow field (figure 9). The basic airfoil chord was 76.2 cm (2.5 feet) and the span between the endplates was 2.44 m (8 feet). Details of the airfoil cruise and landing configurations tested are shown in figure 10. The high-lift devices consisted of a leading-edge slat deflected at a fixed angle of 57° and a trailing-edge double-slotted flap deflected at a fixed angle of 35.75° .

These tests were also conducted in the Langley 14- by 22-Foot Subsonic Tunnel for Reynolds numbers of 1.8×10^6 , 2.6×10^6 , 3.3×10^6 based on airfoil chord. The rain simulation system produced liquid water concentrations ranging from 16 to 47 g/m³. As shown in figure 11, a 25 percent reduction in maximum lift capability with an associated 8° decrease in the angle of attack at which maximum lift occurs was measured for the high-lift configuration at the highest water mass concentration of 46 g/m³. For this data set the Reynolds number was 2.6×10^6 , the Weber number was 270, and the drop diameter to wing chord ratio was .0018.

In general, the NACA 64-210 data indicated the same trends as the data for the NACA 0012 airfoil model. Both airfoil sections exhibited significant reductions in maximum lift and increases in drag for a given lift condition in the simulated rain environment. The most significant difference between these two airfoil sections was the sensitivity of the NACA 64-210 airfoil section to LWC. As noted previously the NACA 0012 performance losses in the rain environment were not a function of LWC. Although reductions in maximum lift capability and corresponding increases in drag were measured for both the cruise and high-lift configurations of the NACA 64-210 airfoil model, the high-lift configuration was more sensitive to the rain environment than the cruise configuration. The data indicated a reduction in maximum lift capability with increasing liquid water concentration and an associated decrease in the angle of attack at which maximum lift occurs. One surprising result of this test was that the results did not seem to be a strong function of Weber number. The tests reported in reference 22 varied the Weber

number by adding an agent that reduced the surface tension of the water. However no significant changes in test results were found for a factor of four variation in Weber number for the same tests conditions.

Similar tests of heavy rain effects on a two dimensional airfoil were conducted by Tang (reference 23) in a 1.5m blowdown wind tunnel at the Canadian National Research Council Institute for Aerospace Research. His test model consisted of a modified NACA 652-215 airfoil with a leading edge slat and a two element trailing edge fowler flap. The results in terms of lift reductions and drag increases were similar to those noted in the NASA tests. Reference 23 shows data taken for two airfoil surface treatments. One was for an epoxy painted surface and the other was for a bare metal surface. The bare metal surface was not as smooth as the epoxy painted surface and the water tended to bead more readily on the painted surface. This would indicate that there was a significant difference in the surface tension characteristics between the painted and bare surface. Since the contact angle for the water drops on the two surfaces was not reported the amount of difference in surface tension could not be ascertained. The results of reference 23 indicates that the difference in surface tension resulted in a small but measurable difference in the performance degradation associated with the heavy rain unlike the results of the reference 22 which showed no measurable effect. The surface tension effect measured in reference 23 was small and amounted to only about a 3% difference.

Campbell and Bezos (reference 24) conducted a test using an NACA 23015 airfoil section to evaluate the time required for a wing immersed in rain to achieve a steady state condition. They reported that the transition time for the wing to achieve a steady state condition encountering simulated heavy rain to be less than two to three seconds in most cases. These transition times are small when compared to the short duration high intensity ground-based rainfall measurements reported by Melson.

LARGE-SCALE TEST RESULTS

In order to determine to first order if there were significant rain scaling effects, the NASA Langley Research Center and the FAA supported the development of a large-scale ground testing capability for evaluating the effect of heavy rain on airfoil lift. Figure 12 is a photograph of the facility which was equipped to acquire aerodynamic data on large-scale wing sections immersed in a simulated natural rain environment. A wing section was mounted on a test vehicle and propelled along a track through a highly-concentrated rain environment. The simulated rain was produced by a series of spray nozzles suspended above the track. This technique provided a more realistic rain simulation than could be produced in a wind tunnel. The test vehicle was propelled into an environment which exemplifies an airplane flying into a rainstorm.

The generation of the rain environment in the vertical direction allows the water droplets to achieve the proper droplet size distribution and terminal velocities found in severe rainstorms. The outdoor rain simulation system developed for this investigation produced rainfall conditions from 50.8 to 1016 mm/hr (2 to 40 in/hr). The details of the design, development, and operation of the NASA Langley Research Center Aircraft Landing Dynamics Facility (ALDF) for large-scale heavy rain effects testing are described in references 25, 26, and 27. Although the ALDF was designed to test full-scale aircraft landing gear at operational velocities on a variety of simulated runway surfaces, its operating characteristics facilitated the conversion to a large-scale aerodynamic performance testing facility with minimal modifications to the test carriage and track test section. The ALDF is composed of three components: a test carriage, a propulsion system and an arrestment system. A high-pressure jet of water is directed into a turning bucket on the back end of the carriage to provide carriage thrust. Once the peak velocity is attained, the carriage coasts the remaining 1800 feet (548.6m) to the arrestment system. The large-scale wing section was mounted above the central open bay area of the

carriage 22 feet (6.71) above the track as shown in figure 13.

The wing section had an NACA 64-210 airfoil section with a rectangular planform and was mounted between circular endplates. The wing was equipped with leading-edge and trailing-edge high-lift devices deployed to simulate a landing configuration (figure 14). The ALDF wing chord was chosen to be 10 feet (3.05m), which corresponds to a scaling factor of 4 when compared to the wind-tunnel model chord of 2.5 feet (76.2cm). The wing span was constrained to a width of 13 feet (3.96m) by the model location chosen. The wing surfaces were painted with commercially available aircraft paint to model the wing surface/rain interaction properly. The wing angle of attack, which was set prior to launch, remained fixed during a test run, and was varied between runs from 7.5° to 19.5° in 2° increments.

The ALDF Rain Simulation System (RSS) was located approximately 800 feet (152.4m) downstream of the propulsion system (figure 15) and provides uniform simulated rain over an area 30 feet wide (9.14m), centered over the track, by 500 feet (9.14m) long. The system consisted of three commercially manufactured irrigation pipes positioned length-wise along the track in 100-foot (30.5m) sections which were supported at both ends by a structural support frame. One leg of this frame was piping which allowed the flow of water to travel from the water/air supply system up to the three irrigation pipes. Feeding off each irrigation pipe was an array of nozzles whose spacing was dependent upon the desired rainfall rate.

The majority of the rain effects data were obtained at the maximum rain rate of 40 in/hr (1016mm/hr) for an angle-of-attack range of 7.5° to 19.5°. For this rain condition the drop size to model chord ratio was .0009. This rain condition was chosen because it closely approximated a previously tested wind-tunnel condition and met one of the test objectives to investigate the significance of scale effects. A photograph of the carriage exiting the 40 in/hr (1016mm/hr) rain condition is shown in figure 16. Aerodynamic data were also obtained for rainfall rates of 9 (22.9cm) and

19 in/hr (48.3cm) for an angle of attack range of 9.5° to 19.5° . These rain conditions have a much higher probability of occurrence than the 40 in/hr (1016mm/hr) rain intensity as indicated by references 4 and 6.

Dynamic pressure was measured by a standard aircraft pitot-static tube mounted on a forward extremity of the carriage. In addition to data on the wing and carriage, the measurement of wind speed and direction at the rain simulation system location are recorded along with temperature and barometric pressure. Because the carriage was decelerating, the Reynolds number varied from 11×10^6 to 18×10^6 . The Weber number also varied from 320-510.

The time dependent data were averaged to provide a single lift coefficient for each angle of attack. The lift coefficient versus angle of attack data exhibit the same general characteristics as the previous wind-tunnel results. The rain effect is to reduce the maximum achievable lift coefficient and to reduce the angle of attack for stall. The data shown in figure 17 for the airfoil in the rain environment reflects the fact that the wing has stalled prior to 13.5° angle of attack and attained its highest observable lift at 11.5° angle of attack. A reduction of lift capability of at least 15 to 20 percent is reflected in the data shown in figure 17 for the 40 in/hr rain condition.

COMPARISONS OF LARGE AND SMALL SCALE DATA

Despite the previously noted difficulties, the wind-tunnel technique appears to provide a valid estimate of the effects of heavy rain at full scale conditions (reference 26). The lift coefficients predicted for the ALDF large-scale configuration using the wind-tunnel data are shown in figure 18 along with the ALDF large-scale data acquired at the same test conditions. The two sets of data for the dry wing agree quite well. The ALDF lift-curve slope and maximum lift measured show excellent correlation to the wind tunnel lift performance for that condition. There appears to be a reasonable degree of correlation between the two data sets for the 40 in/hr

(1016mm/hr) rain condition. The data shown in figure 18 indicates that the wet wing attains its highest observable lift at approximately the same angle of attack (between 10° and 11.5°) in both the large scale and wind tunnel tests.

Comparisons of the angle of attack for maximum lift and of the percent lift loss in the various rainfall conditions in the wind tunnel and at large scale are shown in figures 19 and 20. Based on the comparisons available between the limited large-scale results and the wind-tunnel results, the difficulties in precisely simulating the rain environment in the wind tunnel do not have a first order effect on the impact of the test results. It appears that, to first order, rain scale effects are not large and that wind-tunnel results can be used to predict large-scale heavy rain effects.

EFFECTS ON FULL SCALE AIRCRAFT

The results of the large scale testing and the wind tunnel tests were used in reference 28 to estimate the effects of heavy rain on a full scale airplane. For this study, the rain effects were applied to a Boeing 737-100 airplane. The experimental data were utilized as an approximation to two dimensional data and the data were integrated in the spanwise direction over the planform of the airplane. Although the vortex lattice method used to compute the wing loading is not an accurate representation for a multi-element flap high lift system, the wet aerodynamics was modeled as a change in the lift and drag with liquid water content from the integrated dry baseline aerodynamic model obtained with the vortex lattice method. An example of the results of this modeling is shown in figure 21. This figure shows the decrease in maximum lift coefficient and stall angle of attack and the drag increase associated with the heavy rain effects. Figure 22 shows the effect of heavy rain on the climb performance of the airplane in a landing configuration as a function of liquid water content. These reductions and performance degradations noted in figures 21 and 22 are not a serious hazard unless combined with other performance degradation hazards such as a strong wind shear.

Figure 23 from reference 28 shows the results of the effect of heavy rain combined with a wind shear. The wind shear modeled had a maximum outflow of 37 knots at an altitude of 120 feet (36.58m) and a radius of 2,391 feet (728.8m). This represents a wind shear which has caused aircraft accidents. The rain was a step input when the aircraft was within the 2,391 foot (728.8m) microburst radius. The wind shear was located 4000 feet (1219.2m) from the intended landing point. The wind shear recovery procedure modeled the Federal Aviation Administration (FAA) recommended procedure. When the shear was encountered the throttles were moved to take-off power and the airplane was pitched to an initial attitude of 15 degrees. The pitch attitude was limited throughout the shear encounter to a value corresponding to the airplane's stick shaker angle. The results indicate that if the correct wind shear procedure is applied during the wind shear encounter the aircraft can safely recover from the shear if rain is not present. Increasing the rain rate (liquid water content) decrease the margin of safety and at very heavy rain rates (large liquid water contents) the combined hazard presented by rain and wind shear is not recoverable.

CONCLUDING REMARKS

The preliminary findings of the large-scale testing would seem to support earlier wind-tunnel studies of the effect of very heavy rain on airfoil performance. Extremely heavy rain of 40 in/hr (1016mm/hr) produced a reduction in maximum achievable lift coefficient of at least 15 to 20 percent and an approximate reduction in the angle of attack at which the maximum observed lift occurred of 4° to 6°. Results of these small-scale studies had shown that a two-phase flow environment representing a high-intensity rainfall reduced the maximum lift by as much as 20 percent and increased the drag. Additionally, the stall angle was reduced 4 to 8 degrees in the heavy rain environment. The simulated rain seems to have little influence on the lower angle-of-attack airfoil lift performance characteristics. The severity of the effect is airfoil- and configuration-dependent and is

most severe for high-lift configuration airfoils, i.e., leading-edge and trailing-edge devices deployed. Based on the wind-tunnel and large-scale results, it would appear that normal aircraft operations for transport aircraft would not be affected by heavy rain since most operations avoid high angle of attack maneuvers. However, if the heavy rain encounter occurs during a severe low altitude wind shear then the piloting procedures used to counter the wind shear effects result in operating at a higher than normal angle of attack. Analysis has shown that the combined effects of heavy rain and wind shear may significantly reduce the capability of an aircraft to successfully escape the combined hazards.

REFERENCES

1. Low-Altitude Wind Shear and Its Hazard to Aviation. National Academy Press. Library of Congress Catalog #83-63100, 1983.
2. Marshall, J. S. and Palmer, W. McK. : The Distribution of Raindrops with Size. *Journal of Meteorology*, Volume 5, 1948, pg. 165- 166.
3. Joss, J. and Waldvogel, A. : Raindrop Size Distribution and Sampling Size Errors. *Journal of the Atmospheric Sciences*, Volume 3, 1969, pg 566-569.
4. Markowitz, Allan H.: Raindrop Size Distribution Expressions. *Journal of Applied Meteorology*, Volume 15, September, 1976, pg. 1029-1030.
5. Riordan, P.: Weather Extremes Around the World. Earth Sciences Laboratory, TR-70-45-ES, January 1970.
6. Jones, D. M. A. and Sims, A. L.: Climatology of Instantaneous Rainfall Rates. *Journal of Applied Meteorology*, Volume 17, August 1978, pg. 1135-1140.
7. Melson, W. E., Jr.: Heavy Rain Characteristics and Ground Measurement Comparisons. Presented at the WHO IAHS 8th International Workshop on

Precipitation Measurement, December 1989.

8. Melson, W. Edward, Jr.: Observation and Comparison of Rainfall Measured at a High Sample Rate. Proceedings of the American Meteorological Society, 71st Annual Meeting, January 13-18, 1991, New Orleans, Louisiana.
9. Rhode, Richard V.: Some Effects of Rainfall on Flight of Airplanes and on Instrument Indications. NACA TN 803, April 1941.
10. Bergrun, Norman R.: A Method of Numerically Calculating the Area and Distribution of Water Impingement on the Leading Edge of an Airfoil. NACA TN1397, 1947.
11. Bergrun, Norman, R.: An Empirically Derived Basis for Calculating the Area, Rate, and Distribution of Water-Drop Impingement on Airfoils. NACA Report 1107, 1952.
12. Dorsch, R. G. and Brun, R. J.: A Method for Determining Cloud-Droplet Impingement on Swept Wings. NASA TN2931, 1953.
13. Morsi, S. A., and Alexander, A. J.: An Investigation of Particle Trajectories in Two-Phase Flow Systems. Journal of Fluid Mechanics, Volume 56, 1972, page 193-208.
14. Bragg, M. B.: A Similarity Analysis of the Droplet Trajectory Equation. AIAA Journal, Volume 20, December 1982, pg. 1681-1686.
15. Haines, P. A. and Luers, J. K.: Aerodynamic Penalties of Heavy Rain on Landing Aircraft. NASA CR 156885, July 1982.
16. Calarese, W. and Hankey, W. L.: "Numerical Analysis of Rain Effects on an Airfoil," AIAA-84-0539, AIAA 22nd Aerospace Sciences Meeting, Reno, NV, January 1984.
17. Kisielowski, Keith: A Numerical Investigation of Rain Effects on Lift using a Three-Dimensional Split Flux Vector Form of the Euler Equations, Master Thesis, Department of Aerospace Engineering, Mississippi State University, May 1985.
18. Feo, A.: Single Drop Impact Studies. AIAA 87-0257, AIAA 25th Aerospace Sciences Meeting, Reno, NV, January 1987.
19. Bilanin, A. J.; Quackenbush, T. R.; Feo, A.: Feasibility of Predicting Performance Degradation of Airfoils in Heavy Rain. NASA CR 181842.
20. Bilanin, A. J.: Scaling Laws for Testing of High Lift Airfoils Under Heavy Rain. AIAA-85-0259, January 1985.
21. Dunham, Jr., R. E. : Potential Influences of Heavy Rain on General Aviation Airplane Performance. AIAA-86-2606, September, 1986.
22. Bezos, Guady M.; Dunham, Jr., R. Earl; Gentry, Jr., Garl, L.; and Melson, Jr., W. Edward: Wind Tunnel Aerodynamic Characteristics of A Transport-Type Airfoil in a Simulated Heavy Rain Environment. NASA TP-3184, August 1992
23. Tang, F. C.: Experimental Investigation of Heavy Rainfall Effectg on A 2-D High Lift Airfoil. AGARD CP-496, December, 1991.
24. Campbell, B. A. and Bezos, G. M.: Steady-State and Transitional Aerodynamic Characteristics of a Wing in Simulated Heavy Rain. NASA TP 2932, August 1989.
25. Taylor, J. T.; Moore, C. T., III; Campbell, B. A.; and Melson, W. E.: The Development of a Facility for Full-Scale Testing of Airfoil Performance in Simulated Rain. AIAA-88-0055, January 1988.

26. Bezos, G. M.; Campbell, B. A. and Melson, W. E. Jr.: The Development of a Capability for Aerodynamic Testing of Large-Scale Wing Sections in a Simulated Natural Rain Environment. AIAA 89-0762 January 1989.
27. Campbell, B. A.; Bezos, G. M.; Dunham, R. E., Jr.; and Melson, W. E., Jr.: Operational Considerations for Aerodynamic Testing of Large-Scale Wing Sections in a Simulated Natural Rain Environment. AIAA 89-0485, January 1990.
28. Vicroy, Dan D.: The Aerodynamic Effect of Heavy Rain on Airplane Performance. AIAA 90-3131, September 1990.

List of Figures

- Figure 1.- Liquid water content as a function of rain rate (Dana figure 1)
- Figure 2.- Climatology of instantaneous rainfall rate (as defined by 1 and 4 minute accumulations) (Dana figure 20)
- Figure 3.- Distribution of rainfall rates measured for less than 10 seconds (Dana figure 4)
- Figure 4.- Illustration of flow phenomena associated with rain drops impinging on an airfoil (Figure 3 von Karman)
- Figure 5.- Rain spray manifold and wind tunnel model mounted in the Langley 14-by 22-Foot Tunnel (Dana figure 5)
- Figure 6.- Typical wind tunnel test set-up for simulated rain effects studies (Dana figure 6)
- Figure 7.- Close-up view of the rain spray manifold used in the 14-by 22-Foot Tunnel rain effects studies (Dana figure 7)
- Figure 8.- Lift and drag coefficients measured on a NACA 0012 wing model with a 30% chord flap deflected 20° while subjected to several water spray concentrations (Dana figure 9)
- Figure 9.- Photograph of 64-210 model mounted in the wind tunnel (Dana figure 10)
- Figure 10.- A cross-section view of the cruise and high lift configuration of the NACA 64-210 airfoil used in the rain effects wind tunnel studies (Dana figure 11)
- Figure 11.- Effect of simulated rain on a NACA 64-210 airfoil with leading edge slat and double slotted trailing edge flap (Dana figure 12)
- Figure 12.- Aerial view of the outdoor facility used to conduct large scale aerodynamic rain effects tests (Dana figure 13)
- Figure 13.- Photograph of the wing model mounted on the test carriage (Dana figure 14)
- Figure 14.- Close-up view of large scale wing section mounted to the test carriage (Dana figure 15)
- Figure 15.- Aerial view of the outdoor rain simulation system (Dana figure 16)
- Figure 16.- Carriage exiting the rain spray system during a simulated 40 in/hr rainfall (Dana figure 17)
- Figure 17.- Lift coefficient measure during the large scale rain effects tests during a no rain condition and a simulated 40 in/hr rainfall (Dana figure 18)
- Figure 18.- A comparison between wind tunnel and large scale tests of a high lift configuration for similar simulated rainfalls (Dana figure 19)
- Figure 19.- Measured effect of rain on stall angle of attack (Dana figure 20)
- Figure 20.- Measured effect of rain on maximum lift (Dana figure 21)
- Figure 21.- Modeled effect of rain on the aerodynamics of a Boeing 737-100 airplane in a landing configuration (Flaps 25° and landing gear down) (Vicroy figure 11)
- Figure 22.- Effect of rain on the climb performance of a Boeing 737-100 airplane (Vicroy figure 13)
- Figure 23.- Effect of rain on the wind shear escape performance of a Boeing 737-100 airplane in a landing configuration (Vicroy figure 21)

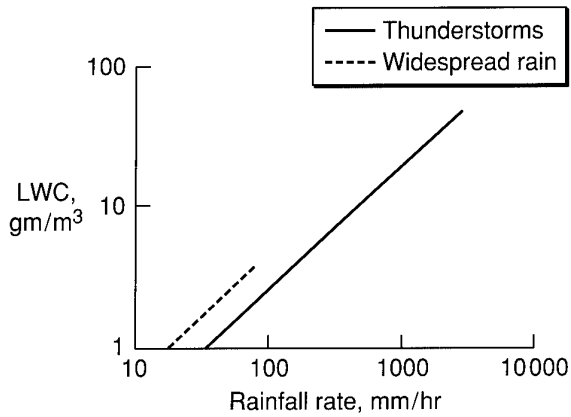


Figure 1 - Liquid water content as a function of rain rate

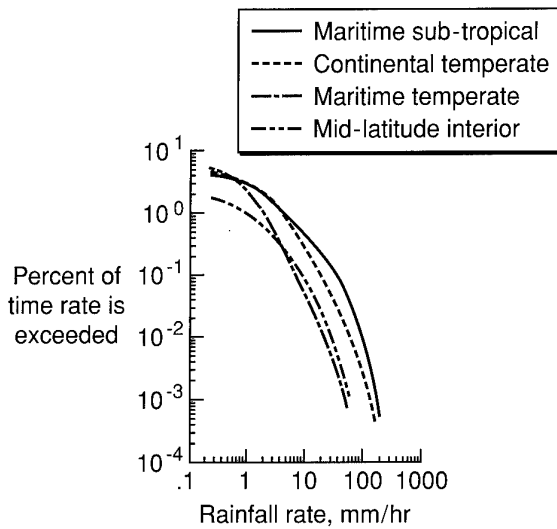


Figure 2 - Climatology of instantaneous rainfall rate (as defined by 1- and 4-minute accumulations)

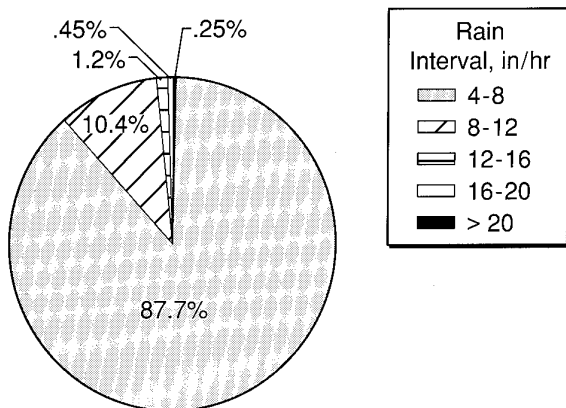


Figure 3 - Distribution of rainfall rates measured for less than 10 seconds

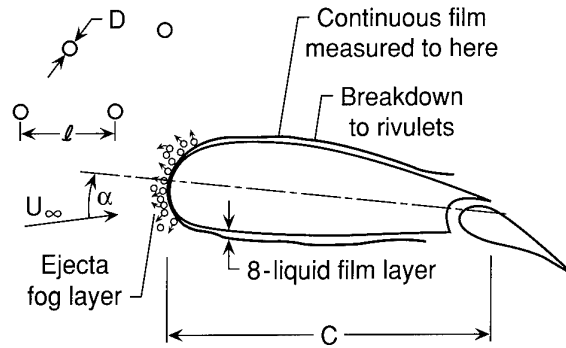


Figure 4 - Illustration of flow phenomena associated with rain drops impinging on an airfoil

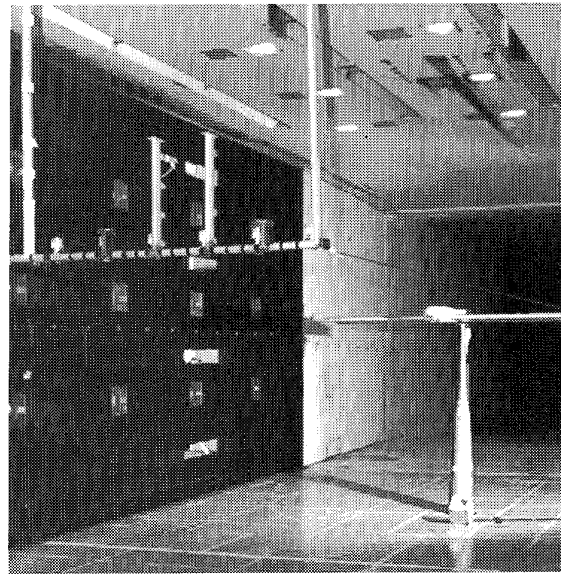


Figure 5 - Rain spray manifold and wind tunnel model mounted in the Langley 14- by 22-Foot Tunnel

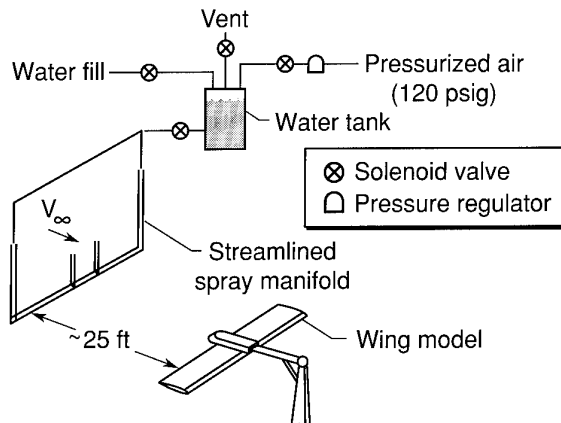


Figure 6 - Typical wind tunnel test set-up for simulated rain effects studies

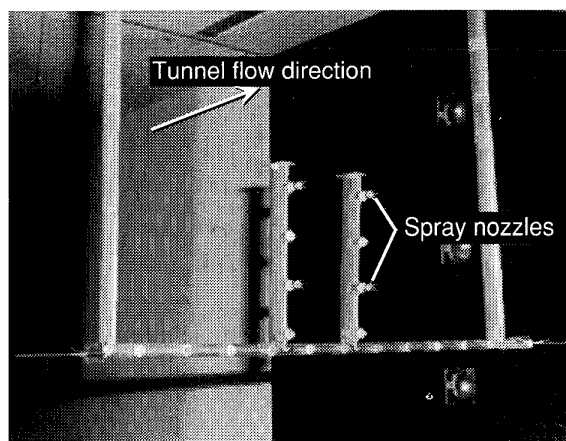


Figure 7 - Close-up view of the rain spray manifold used in the 14- by 22- Foot Tunnel rain effects studies

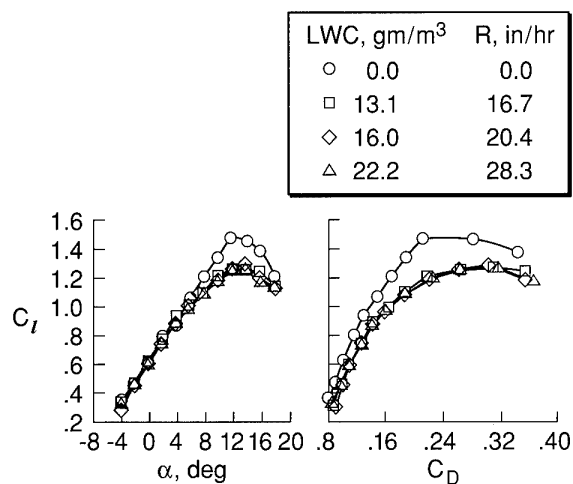


Figure 8 - Lift and drag coefficients measured on a NACA 0012 wing model with a 30% chord flap deflected 20° while subjected to several water spray concentrations

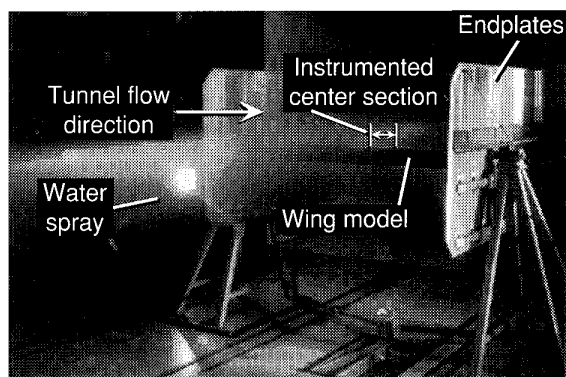


Figure 9 - Photograph of 64-210 model mounted in the wind tunnel

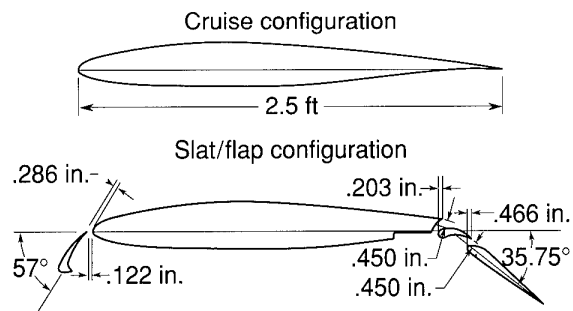


Figure 10 - A cross-section view of the cruise and high lift configuration of the NACA 64-210 airfoil used in the rain effects wind tunnel studies

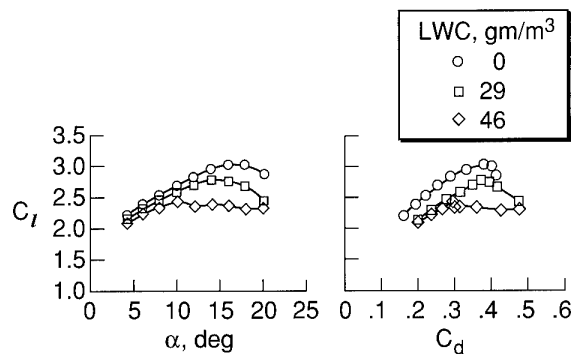


Figure 11 - Effect of simulated rain on a NACA 64-210 airfoil with leading edge slat and double slotted trailing edge flap

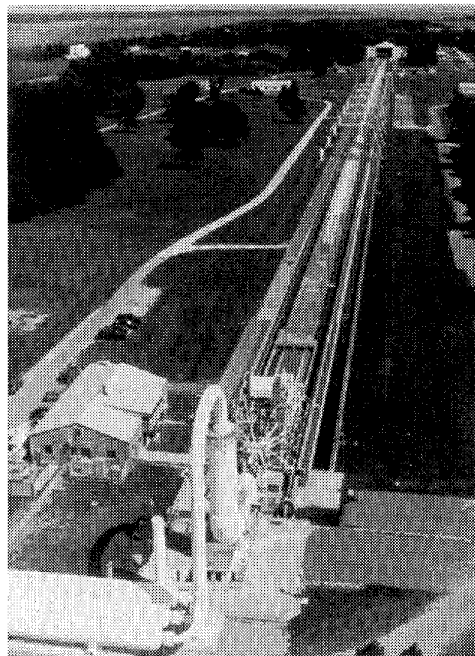


Figure 12 - Aerial view of the outdoor facility used to conduct large scale aerodynamic rain effects tests

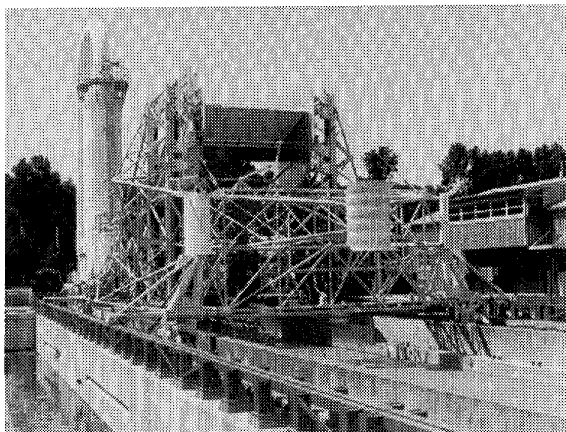


Figure 13 - Photograph of the wing model mounted on the test carriage

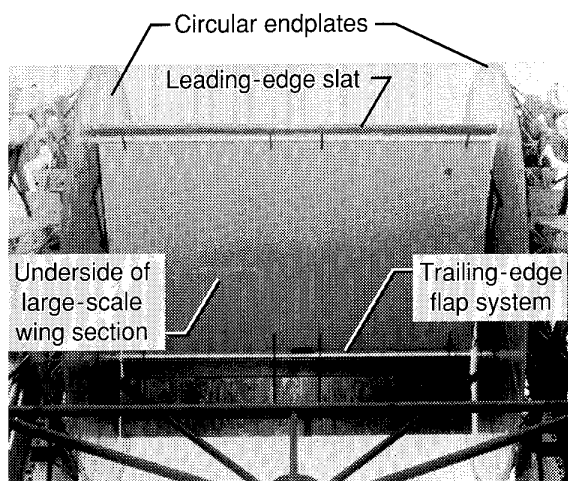


Figure 14 - Close-up view of large scale wing section mounted to the test carriage

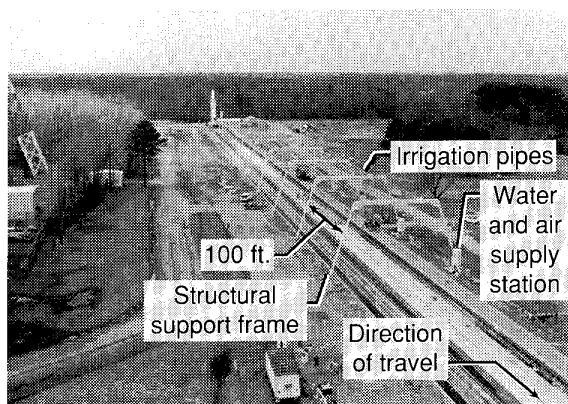


Figure 15 - Aerial view of the outdoor rain simulation system

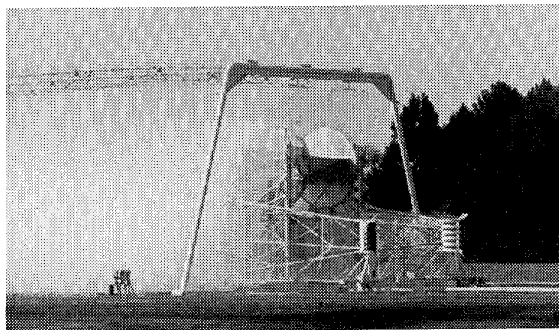


Figure 16 - Carriage exiting the rain spray system during a simulated 40 in/hr rainfall

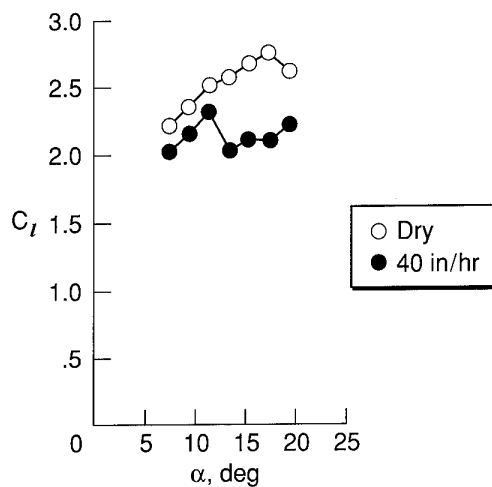


Figure 17 - Lift coefficient measure during the large scale rain effects tests during a no rain condition and a simulated 40 in/hr rainfall

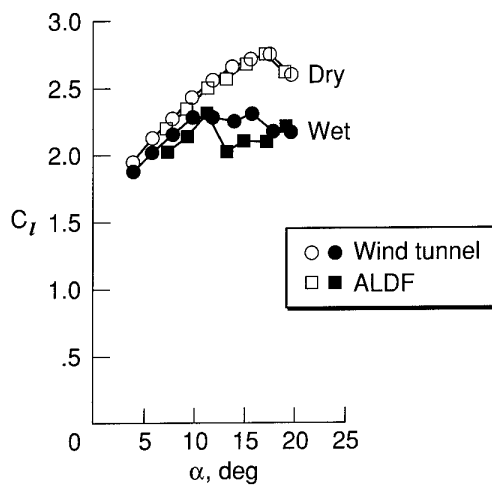


Figure 18 - A comparison between wind tunnel and large scale tests of a high lift configuration for similar simulated rainfalls

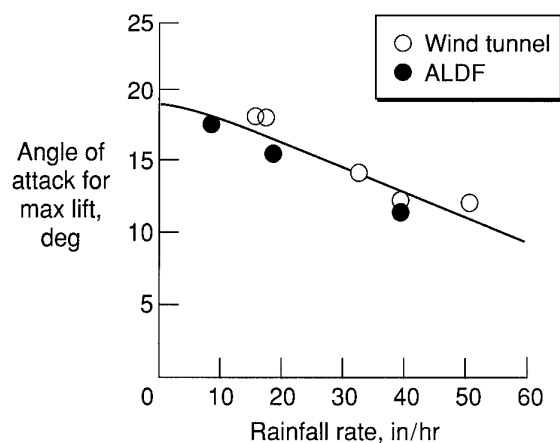


Figure 19 - Measured effect of rain on stall angle of attack

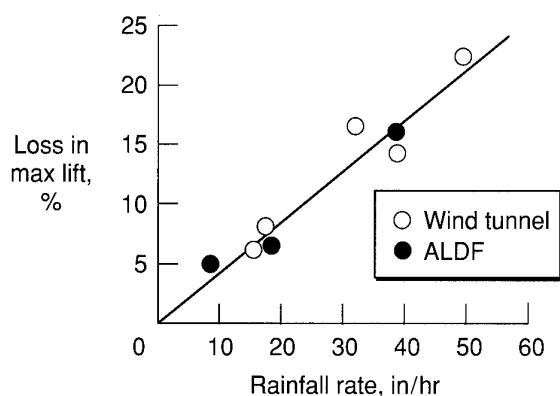


Figure 20 - Measured effect of rain on maximum lift

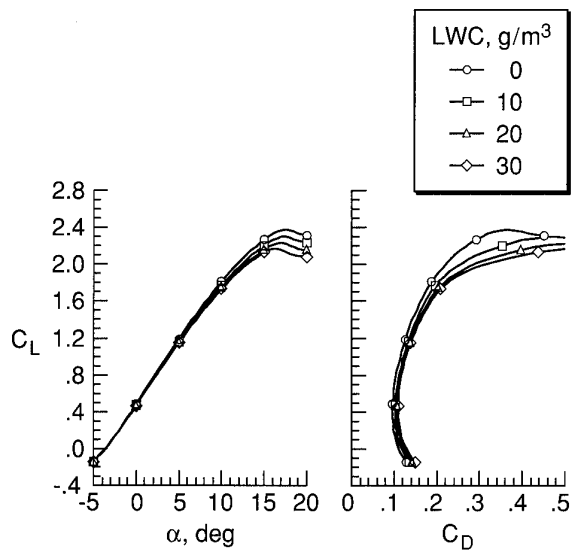


Figure 21 - Modeled effect of rain on the aerodynamics of a Boeing 737-100 airplane in a landing configuration (Flaps 25° and landing gear down)

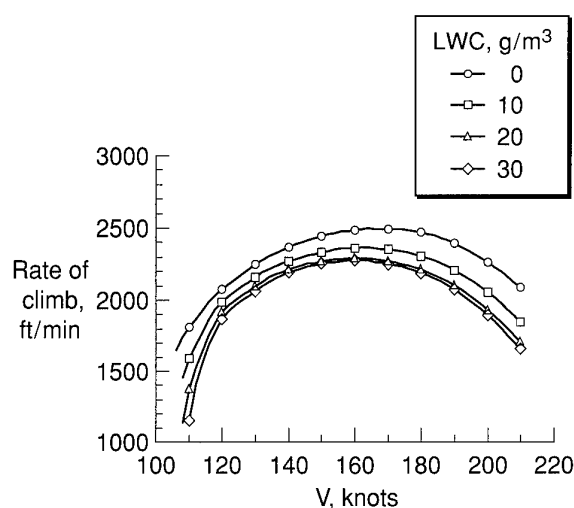


Figure 22 - Effect of rain on the climb performance of a Boeing 737-100 airplane

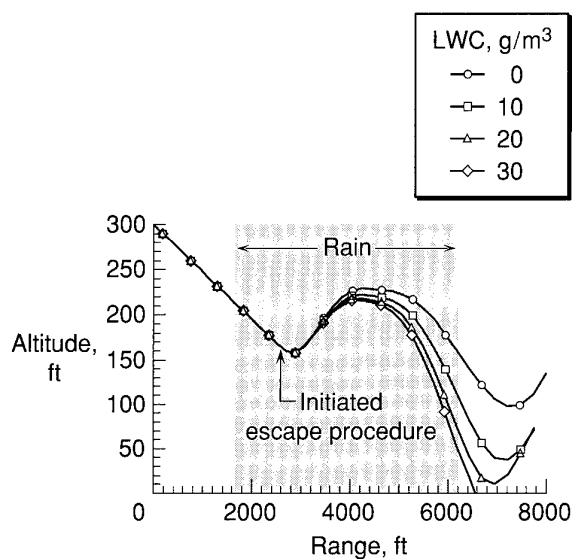


Figure 23 - Effect of rain on the wind shear escape performance of a Boeing 737-100 airplane in a landing configuration

TURBULENCE ENGINEERING MODELS, AIRCRAFT RESPONSE

by

Manfred Swolinsky
Institute of Flight Guidance and Control
Technical University of Braunschweig
Hans-Sommer-Str. 66
38106 Braunschweig
Germany

Abstract

This paper covers problems of flight in a turbulent atmosphere. A realistic simulation of aircraft behaviour in turbulent air requires different engineering models. On one hand, this means a mathematical description of random turbulence or short scale gusts. For simple problems, a computation of the turbulence velocity vector only at the trajectory of the aircraft is sufficient. In cases of detailed investigations, the generation of a 3-dimensional spatial turbulence field is necessary. Additional real time requirements imply special approaches, such as the realization of a matrix wind model.

On the other hand the description of the interaction between turbulence or short scale gusts and aircraft may require complex aerodynamic models especially if the gust scale and the aircraft scale are in the same order of magnitude. The presented multi point or lifting surface models consider the wind vector at several points along the wing span under real time constraints.

Based on simulation results and flight test data, the dynamic aircraft response is discussed. Single gust effects are demonstrated by examples of cross flights through the up-draft of a powerplant cooling tower.

Nomenclature

\bar{c}	mean wing chord
c_L	lift coefficient
c_D	drag coefficient
D	drag
$E(\Omega)$	energy spectrum of turbulence
H	altitude
\dot{H}	vertical speed ($= -w_{Kg}$)
\ddot{H}	vertical acceleration ($= -\dot{w}_{Kg}$)
I_y	moment of inertia about y-axis
K	gust response factor
K_g	FAR-gust response factor
L	lift, length scale,
	rolling moment
L_u, L_v, L_w	integral scale of turbulence
	velocity components
\bar{M}	pitch moment
m	aircraft mass
n	gust load factor
q	pitch rate
R_r	roughness factor
R_{ij}	correlation matrix
S	wing area
s	half wing span
T	thrust
T^*	time constant
u, v, w	velocity components

W	airplane gross weight
α	angle of attack
α_w	wind angle
γ	flight path angle
λ	wave length
μ_g	mass factor
θ	pitch angle
ρ	air mass density
σ	rms-value of stochastic variables, angle between thrust line and body fixed axes
τ	time shift separating two points
ω	angular velocity
Ω	angular velocity vector
$\Omega(\Omega_1, \Omega_2, \Omega_3)$	wave number vector
ξ	vector separating two points
$\psi(\tau)$	KÜSSNER-function
$\Theta(\Omega_1, \Omega_2, \Omega_3)$	matrix of three dimensional spectra function
$\Psi(\Omega_1, \Omega_2)$	matrix of two dimensional spectra function
$\Phi(\Omega_1)$	matrix of one dimensional spectra function

1. Introduction

The description of aircraft behaviour in a turbulent atmosphere represents a complex task. In spite of the continuously growing computing power of simulation systems, a complete mathematical model of aircraft motion in a turbulent wind field is still out of reach. This is even more so the case when real-time requirements are to be fulfilled with regard to the use of flight simulators. The development of approximate solutions in the form of simplified engineering models in such cases is essential. The type and size of the simplifications and approximations are obviously dependent on the problem definition and boundary conditions. According to what is being dealt with; whether qualitative approximations, design and layout problems with the structure or with the flight control systems, state estimation or parameter identification, a decision must be made as to which model solutions are most appropriate:

linear	-	non-linear models
ridged	-	flexible aircraft
steady	-	unsteady aerodynamics
mass-point	-	multi-point model

and if, e.g., ground effect, engine/propeller influence must be taken into account. Parameter identification, in particular, reacts very sensitively to model errors and for this reason, requires very detailed, extensive models.

The question of model quality is posed not only in reference to the aircraft and the description of its aerodynamic qualities, but also in reference to the turbulent wind velocity fluctuations affecting the aircraft. Special requirements for the turbulence model result from the type of aerodynamic model used. Whereas, for a mass-point model, the turbulence components are only to be calculated at the center of gravity of the aircraft continually along the flight path (one dimensional turbulence model), for multipoint models or panel methods of three-dimensional turbulence models, sufficient spatial resolution is required.

When simplified aerodynamic or flight simulation models are being used, it is important to know where the limits of each of the model solutions are, and what type of errors can be expected under certain conditions. In this article, these questions, in addition to others, shall be examined and illustrated through the use of examples.

2. Description of Atmospheric Turbulence

2.1 Random Turbulence

To an observer, the earth's atmosphere appears chaotic. Turbulent disturbances occur in all scales and sizes, from the smallest vortex in the area of a millimetre to planetary waves of 1000 km wavelength. In order to classify the variety of turbulence, each type of motion can be assigned a characteristic length L and a characteristic time T . In doing this, L can be, e.g., a vortex diameter or the horizontal or vertical extension of the disturbed atmospheric motion phenomenon and T can be the average length of time of such a phenomenon. The quotient L/T yields a characteristic velocity V , which is to be assigned to the corresponding motion phenomenon. In the diagram or framework illustrated in Fig. 2.1, it is possible to classify all types of atmospheric motion. On the abscissa, all possible characteristic lengths, L from 1 mm up to ca. 40,000 km (earth's circumference), are displayed logarithmically, whereas on the ordinate, the characteristic velocity V is plotted in logarithmic calibration. Lines of the same characteristic time T are recorded below an angle of 45°. The turbulent motion phenomena which are present in the atmosphere are indicated here through the use of different symbols, which give an indication as to the cause of their origins. The L-zone up to 1000 m, which is also referred to as the zone of micro-scale-turbulence, is relevant in reference to the application in flight technology and aircraft reaction to turbulence.

The turbulent types of motion referred to with an M indicate the mechanical turbulence. It originates in a shearing process of the basic flow, e.g., in the planetary boundary layer ($0 < H < 1000\text{m}$) or, at times, near the tropopause, in layers that are several hundred meters thick and marked vertical wind shear (jet stream) as Clear Air Turbulence (CAT). Additionally, mechanical turbulence occurs as a result of orographic influences (roughness of terrain, hills, valleys, villages, individual impediments). The dimension of turbu-

lence due to roughness of terrain is somewhat larger than the turbulence from shearing process.

The characteristic length of mechanical turbulence extends over a number of orders of magnitude (from $L=1\text{ mm}$ to 10 m). Here, very small vortices result only to a small extent from shearing process from roughness of terrain, but even more from the decay of larger vortices. From the point of view of energy, one may speak here of the energy cascade. Here, that the M-symbols of the mechanical turbulence group themselves around a correlation line $VL^{-1/3}$ up to the vortex dimensions from fragments of millimetres is recognizable, where molecular dissipation is already active (symbol m). Strictly taken, this rule is only valid for isotropic turbulence. However, the measurement results show that the turbulence even in the planetary boundary layer with vortices becoming smaller becomes more isotropic and the complies increasingly well to the said procedure.

In the micro-scaled turbulence zone, turbulence from a completely different origin can be found; namely, that of thermic turbulence (in Fig 2.1 marked with symbols τ and t). It extends over an even larger characteristic length zone than the mechanical turbulence. Often a more detailed division is undertaken in small scale thermic turbulence (τ) and thermal cells (t). Whereas the vertical and horizontal extension for small areas of thermic turbulence has a ratio of 2:1, this ratio amounts to about 10:1 for the thermal cells, which means that the heated air which is rising over the earth's surface is concentrated in very narrow regions.

Although no exact definition is provided here, the micro scale turbulence zone, which is defined from a meteorological point of view, is relevant for aeronautical applications.

Normally, the air flow the atmosphere are separated into a mean flow and additional turbulent fluctuations. As a result it is possible to write in components

$$\begin{aligned} u &= \bar{u} + u' \\ v &= \bar{v} + v' \\ w &= \bar{w} + w' \end{aligned} \quad (2.1)$$

In meteorology, the averages $\bar{u}, \bar{v}, \bar{w}$ are normally arrived at by taking the mean over a period of time of 10 - 30 min. Fig. 2.2 illustrates the division of the average wind and turbulent fluctuation values for the example of the u-component of a vertical wind profile.

How can the spatial-temporal development of turbulence be mathematically described? The corresponding motion equations are based on the non-linear Navier-Stokes and continuity equations. Suitable solutions can only be attained only for a few simple special cases. The set of equation has been proven unsolvable for practical applications and the associated complex boundary conditions for the realization of a realistic, turbulent, three-dimensional, temporally and spatially varying flow field. For this reason, the mathematical

description of turbulence should be limited to statistical and probabilistic solutions.

These statistical qualities can be expressed with spectral power density and auto-correlation functions.

A 3x3 correlation matrix is obtained for a spatial, time variable turbulence field in which the turbulence component u_i is a function of the space coordinates x_1, x_2, x_3 and for which time is t :

$$R_{ij}(\xi, \tau) = u_i(\underline{r}, t) \cdot u_j(\underline{r} + \xi, t + \tau).$$

Through a four-dimensional FOURIER integral of $R_{ij}(\xi, \tau)$, the related 3x3 turbulence - spectrum-matrix $\Theta_{ij}(\Omega, \omega)$ is obtained. The parameter Ω represents spatial frequency or wave number [rad/m] and ω angular velocity [rad/sec] (further details, e.g. at Ref. [2.1]). A series of simplified assumptions are made for the practical applications:

- Turbulence is a stationary process, which means that at least over limited periods of time and on the condition that the meteorological conditions do not change, the statistical values are temporally independent.
- Turbulence is homogenous. The statistic qualities are not altered by a shift in the coordinate systems. However, this is valid optimally for limited spatial segments.
- When the principle of the stationary state and homogeneity are present, the time and ensemble averages can be exchanged (ergodic qualities).
- Turbulence is isotropic, which means that its statistical properties are independent of the orientation of the coordinate axes. This signifies, for example, that the mean square of the three turbulence components are equal.
- The turbulent velocity fluctuations are normal- or Gaussian-distributed. This quality is fulfilled - if at all - most likely for short measurement periods (4 minutes).
- If the velocity of the vehicle is distinctly larger in comparison to the turbulence velocities, turbulence can be treated as a "spatially frozen" velocity field, according to the "Taylor Hypothesis".

These qualities are not ideally fulfilled in the atmosphere. However, above the planetary boundary layer they are sufficiently fulfilled in limited segments. This idealization considerably simplifies the mathematical treatment of turbulence.

The covariance matrix is dependent only on the spatial difference between two points ξ_i and the matrix of the power density function on the wave number vector Ω . Ref. [3.3] provides the turbulence spectrum for isotropic conditions:

$$\Theta_{ij}(\Omega_1, \Omega_2, \Omega_3) = \frac{E(\Omega)}{4\pi\Omega^4} (\Omega^2 \delta_{ij} - \Omega_i \Omega_j) \quad (2.2)$$

with δ_{ij} as KRONECKER-Delta and

$$\Omega = \sqrt{\Omega_1^2 + \Omega_2^2 + \Omega_3^2}$$

The scalar quantity $E(\Omega)$ describes the turbulence energy spectrum function. Fig. 2.3 illustrates the shape of the energy spectrum as

a function of the wave number magnitude Ω in double logarithmic plot.

The range of turbulence production is joined with the inertial subrange, in that the energy density decreases proportionally $\Omega^{-5/3}$ and the energy from the large vortices is transferred to small vortices (energy cascade). For wavelengths in the millimetre range ($\Omega \approx 50000$ rad/m), the turbulence energy dissipates in the form of frictional heat. The energy density decreases here even more sharply. Heisenberg gave an energy decrease $\sim \Omega^{-7}$ for this subrange.

There are several model formulas for the description of energy density in the production and inertial subrange. The most well known and models most used for aeronautical applications are the DRYDEN and v. KARMAN formulas. Both approach the production range through constant power density. In the case of v. KARMAN, this constant power density changes over from above $\Omega_L = 1/L$ to $\Omega^{-5/3}$ -law, whereas DRYDEN applies a decrease here $\sim \Omega^{-2}$. This results in a lower energy density for high wave numbers for the DRYDEN spectrum, and a somewhat higher energy density at the transition between the production and inertial subrange. In comparison with the variability of measured spectrums, the difference can be considered minimal. The DRYDEN model is frequently preferred, as it is much more simple to practically realize. Both formulas will be briefly presented in the following.

The corresponding energy spectrum functions $E(\Omega)$ result in

DRYDEN

$$E(\Omega) = \frac{16}{2\pi} \sigma^2 L \frac{(L\Omega)^4}{[1 + (L\Omega)^2]^3} \quad (2.4)$$

v.KARMAN

$$E(\Omega) = \frac{55}{9\pi} \sigma^2 L \frac{(aL\Omega)^4}{[1 + (aL\Omega)^2]^{17/6}} \quad (2.5)$$

$a = 1.339$ (v.KARMAN - constant)

If inserted in equation (2.2), the three-dimensional spectral power density of turbulence $\Theta_{ij}(\Omega_1, \Omega_2, \Omega_3)$ result for both formulas. In this case, three-dimensional means that the corresponding components of the turbulence velocity vary along the entire three coordinate axes.

For investigations of the influences of turbulence on aircraft motion under the simplified assumption that the turbulence velocities along the vertical axis do not vary, a limitation to the equations of the two-dimensional spectrum $\Psi(\Omega_1, \Omega_2)$ results, which can be determined through integration with regard to Ω_3 .

$$\Psi_{ij}(\Omega_1, \Omega_2) = \int_{-\infty}^{\infty} \Theta_{ij}(\Omega_1, \Omega_2, \Omega_3) d\Omega_3 \quad (2.6)$$

Detailed information about the complete formulas can be found, e.g., in Ref. [3.3]

A one-dimensional spectral power density function is obtained through further integration with regard to Ω_2

$$\Phi_{ij}(\Omega_1) = \int_{-\infty}^{\infty} \Psi_{ij}(\Omega_1, \Omega_2) d\Omega_2 \quad (2.7)$$

As the majority of the data which is collected from experiments is generated in the form of one-dimensional spectrums, and additionally, because in this case a turbulence simulation is relatively easy to realize, one-dimensional spectrum are very common in flight simulation. Depending on the wave number Ω_1 , the v. KARMAN and DRYDEN formulas can be illustrated as follows:

$$\begin{array}{c} \text{--- DRYDEN ---} \quad \text{--- v. KARMAN ---} \\ \text{--- Longitudinal component ---} \\ \Phi_{11}(\Omega_1) = \frac{\alpha_w^2}{\pi} \frac{2L}{[1 + L^2 \Omega_1^2]} \quad \Phi_{11}(\Omega_1) = \frac{\alpha_w^2}{\pi} \frac{2L}{[1 + (aL\Omega_1)^2]^{5/6}} \\ (2.8) \qquad \qquad \qquad (2.9) \end{array}$$

$$\begin{array}{c} \text{--- Vertical and lateral component ---} \\ \Phi_{33}(\Omega_1) = \frac{\alpha_w^2}{\pi} \frac{L(1 + 3L^2 \Omega_1^2)}{[1 + L^2 \Omega_1^2]^2} \quad \Phi_{33}(\Omega_1) = \frac{\alpha_w^2}{\pi} \frac{L(1 + \frac{8}{3}(aL\Omega_1)^2)}{[1 + (aL\Omega_1)^2]^{11/6}} \\ (2.10) \qquad \qquad \qquad (2.11) \end{array}$$

$$\Phi_{22} = \Phi_{33} \quad a = 1.339$$

According to (Ref. 3.3), typical values for L in altitudes above the planetary boundary layer are in the order of magnitude of 1500 m. For design purposes, a value of $L = 750$ m is given in (Ref. 2.2). Fig. 2.4 illustrates a representation of the power density spectrums of the vertical component, according to v. KARMAN and DRYDEN, in comparison to measurement results.

The ideal and real relationships diverge more and more from each other with increasing proximity to the ground in the planetary boundary layer, especially with regard to the isotropic conditions. This means that the cross correlation function and the cross power density do not disappear between longitudinal and latitudinal components. However, an increasing isotropic behaviour can be observed with increasing propagation factor for one-dimensional spectrums.

A series of model formulas exist for behaviours for which ideal conditions are not fulfilled. In Ref. [2.3], a model for simulation of non homogeneous turbulence is published. The modelling of non-Gaussian distributed turbulence is described, e.g., in Ref. [2.4]. However, in many cases, approximate stationary state, homogeneity and Gaussian distribution can be assumed for limited horizontal turbulence patches.

Information about the dependence of the model parameters variance and integral scale from meteorologists, and orographic conditions are necessary for the development of a simulation model. A multitude of empirical data about this is available. In Fig. 2.5, the dependence of the variance of the turbulence velocity σ_w on the average wind velocity and the stability of the atmosphere is illustrated. The RICHARDSON-number is used as a measure of

stability representing the relative importance of buoyancy and shear.

Furthermore, σ_w is dependent on the roughness of the terrain.

$$\sigma_{w, \text{rough}} = R_T \cdot \sigma_{w, \text{water}} \quad (2.11)$$

Some values for the roughness factor R_T are given in Table 2.1 (adopted from PRITCHARD et al. (1965)).

terrain structure	R_T
water	1.0
field	1.1
forest	1.15
flat mountains	1.3
high mountains	1.4

Table 2.1

Fig. 2.6 illustrates the dependence of the integral scale from the altitude above the ground and the stability of the atmosphere. In Fig. 2.7, the relationship of the integral scale of the horizontal component ($L_u, L_v = L$) to those of the vertical component is illustrated, namely as a function of the altitude. In this way, the model parameters determine the turbulence spectrums for the v. KARMAN or DRYDEN formulas depending on essential influence parameters.

The practical realization of a turbulence simulation program for one-dimensional spectrums is relatively easy to construct and can also be implemented for real-time requirements. This is especially valid for the DRYDEN spectrum. It can be generated with Gaussian distributed white noise of constant power density and the form filter in the time domain which is diverted from the PDS of turbulence. Fig. 2.8 illustrates the structure of a simple turbulence calculation model.

The v. KARMAN model results in a somewhat larger computing effort, as the noise generator and the form filter generate in the FOURIER domain and are retransformed through an inverse FOURIER transformation in the time or spatial domain.

Substantial real-time difficulties occur during the simulation of a three-dimensional spatial turbulence field, especially in connection with a costly flight simulation model (multipoint/panel method). Ref. [2.5] and [2.6], in adoption of proposed solutions of Ref. [2.7], have realized a simulation model of spatial turbulence fields in three steps.

- In the first step, dimensionless, complex turbulence velocities are generated in the frequency domain by filtering of normally divided random numbers. In this way, the distance between two turbulence values is described through dimensionless spatial frequencies. The spatial grid space refers to the integral scale and is, as a result, dimensionless.

- In the second step, the entire field produced in the frequency zone undergoes an inverse triple FOURIER transformation, so that afterwards, a spatial turbulence field with real dimensionless turbulence velocity is available.

- Beginning in the third step, the specific physical turbulence velocities are calculated with regard to roughness-, stability- and wind velocity dependent variances in the flight simulation program. Here the dependence of the integral scale from the altitude above ground can be regarded through the variation of the distance between the matrix elements. Additionally, a superimposition of the turbulence is possible with variable mean wind velocity components.

In order to avoid real-time problems, it is advisable to precompute the processes described in steps 1 and 2 before the real time simulation run and to store them as dimensionless matrix wind fields. The associated amount of storage can be reduced in that the application of a method of images on the block boundaries connects multiple closely bordering turbulence boxes. In this way, if necessary, only each of the smaller zones in close proximity to the aircraft can be held in RAM and adapted corresponding to the flight path through transfer from the hard-disk (see Fig. 2.9).

Fig. 2.10 includes an illustration how to save storage capacity by restriction on a typical matrix shape for a take-off and landing area in case landing approach investigations.

As an instantaneous picture or a time slice of the dynamically developing turbulence field is saved, data can also be utilized from extensive meteorological simulation programs with the assistance of the matrix turbulence field method (as it is in many cases available (e.g., Ref. [2.8])).

At the end of this chapter the comment is made that in addition to the mentioned model formulas for the turbulence spectrums according to DRYDEN and v. KARMAN, other models also exist, which definitely appear to be appropriate for aeronautical applications. Here, the formula according to KAIMAL (see Ref. [2.9]), which is characterized by dimensionless spectrums and makes possible the adaptation to various meteorological boundary conditions, is given special mention.

All of the models mentioned have in common that they do not realistically describe turbulence acceleration respectively velocity gradients. The spectrum of the turbulent acceleration can be calculated, e.g. for the one-dimensional turbulence spectrum, through the multiplication of the velocity spectrum with the square of the wave number. Consequently, the acceleration spectrum for small wave numbers exhibits an increase proportional to Ω^2 . In the inertial subrange an increase proportional to $\Omega^{1/3}$ (v.KARMAN) or a constant power density (DRYDEN) exhibits, as shown in Fig. 2.11. The variance of the acceleration is proportional to the integrated PDS of the velocity. The integral does not converge and as a result produces infinitely large values. In practical realization, the variance of the turbulence acceleration is determined by the sample time of the simulation computer or the noise generator. As the examination of the dissipation zone ($\Omega_1 \sim 5000 \text{ rad/m}$) with a decrease of the spectrum proportional to Ω^{-5} is not practical, the sampling frequency of the simulation program, also in consideration of this state of affairs, is to be selected.

2.2 Discrete Gusts

The so-called one-minus cosine shape is the most important among the discrete gusts. This is, for example, defined according to US Federal Aviation Regulations, Part 25, for gust load analysis. A further known type of gust, the step gust, has more reference character as a "worst case" and has hardly any practical importance.

An attempt will be made to explain the question of a realistic connection to the one-minus cosine gust, among other ways, through the identification of this type of gust in time signals of stochastic turbulence, as illustrated in Fig. 2.12. In reality, however, comparable vertical wind profiles are also definitely encountered as discrete gusts. This shall be illustrated through the use of measurement results from flights through updraft of power plant cooling tower. The rise of vapour from cooling towers can lead to a considerable vertical gusts. Calm wind conditions are especially relevant (horizontal wind velocities $0 < V_w < 3 \text{ m/s}$) during unstable atmosphere. During an absolute horizontal calm, rotation symmetrical vertical wind profiles occur (compare Fig. 2.13), which can be described which means of a two-dimensional one-minus cosine gust. The updraft profiles often take on asymmetrical shapes with increasing horizontal wind velocities. That means a steeper gradient on the lee side in comparison to the windward side. A sample of results from a flight measurement program, (using research aircraft, type DO 128), concerning cooling tower of a high powered nuclear power plant is illustrated in Fig. 2.14. In this case the average horizontal wind velocity amounted to about 3 m/s.

The updraft profiles often take on asymmetrical shapes with increasing horizontal wind velocity. The effects of the updraft were detectable up to an altitude of 2000 m above the cooling tower. The measurements had to be discontinued at an approximate altitude of 580 m above the cooling tower due to high gust effects on the measurement aircraft. In this case, the maximum gust velocity amounted to ca. 18 m/s, or relative to the upwardly directed surrounding flow almost 20 m/s at a wavelength of 170 m ($L_m = 85 \text{ m}$). This corresponds to about double the exhaust speed of the vapour at the top of the cooling tower (10.6 m/s). According to theoretical investigations by the Institute for Technical Thermodynamics of the University of Karlsruhe, the maximum velocity of the rising of vapour can be expected to be at about 250 m above the top of the cooling tower. Fig. 2.15 illustrates the obtained measurement results (maximum updraft velocity as a function of the altitude above the cooling tower) in comparison to the theoretical investigations. The width of the fluctuation can be attributed to two effects. First, a flight exactly through the center of the vapour could not always be accomplished. Secondly, during the rise of vapour from cooling towers of this capacity, unsteady effects are exhibited, which are expressed as pulsing of the vapour flow. Although in the present case horizontal wind velocities of $V_w \sim 3 \text{ m/s}$ were on hand, the mean updraft profiles can, in part, be re-

constructed with a one-minus cosine formula (see, e.g., Fig. 2.16). In other cases, asymmetrical formulas have proven to be more suitable.

Very extensive simulation models are being developed at the Institute of Technical Thermodynamics of Karlsruhe (Ref. [2.10], [2.11]) in order to reconstruct the interaction of several cooling tower vapour clouds. Fig. 2.17 illustrates a result of the simulation of the superposition of two updraft with a horizontal wind - component V_w at 2 m/s in longitudinal cross section. A two-dimensional representation of the vertical gust profile at an altitude of 580 m above the cooling tower is illustrated in Fig. 2.18. It becomes clear that these gust velocity distribution can no longer be approximated with simple model formulas, but must be integrated into the flight simulation model as a result of numerical simulation, using a spatial matrix wind model.

Cooling tower updraft can definitely be of relevance with regard to flight safety and operation, especially when they are located in the take-off and landing approach sectors of airports.

3. Modelling the Aircraft Dynamics

3.1 Fundamental Equations for the Longitudinal Motion

The motion of an ridged aircraft can be described with a second order system of six nonlinear, coupled, differential equations. This equation system is relatively complex and is used for detailed, precise simulation or calculations. Various simplifications can be undertaken for fundamental or qualitative investigations, which are generally distinguished by improved clarity.

The most clearly noticeable effect of gusts on an aircraft appears in the vertical axis. Vertical gust loads are primarily caused by vertical gusts and play an important role in aircraft design.

For this reason, the following details are mainly confined to the response to vertical gusts and the response behaviour of the aircraft in the vertical plane. First, it shall be assumed that a uniform gust or turbulence distribution is present along the wingspan (one-dimensional turbulence). Under these assumptions and with the neglect of the elastic degrees of freedom, one may limit oneself to the mathematical description of the longitudinal motion of the ridged aircraft. The kinematics, forces and moments of the longitudinal motion are sketched in Fig. 3.1. The geometry of the velocity components of the wind vector V_w yields the relationship to the wind angle α_w .

$$\sin \alpha_w = \frac{-w_{wg}}{V} \cos \gamma - \frac{u_{wg}}{V} \sin \gamma \quad (3.1)$$

For small angles equation 3.1 can be simplified

$$\alpha_w = -w_{wg}/V \quad (3.2)$$

Wind angle α_w is part of the flight path angle γ :

$$\gamma = \gamma_a + \alpha_w \quad (3.3)$$

The forces which take effect are the aerodynamic forces lift L and drag D , thrust force T and aircraft weight W . To satisfy the balance of forces of an unsteady aircraft motion, d'ALEMBERT forces must be defined. For the assumption of a ridged aircraft structure, the problem can be reduced to a solution of vehicle mass center. With the flight path velocity vector and angular velocity vector

$$\underline{V}_K = [u_{Kx}, 0, 0]^T \quad \underline{\Omega} = [0, \dot{\gamma}, 0]^T \quad (3.4)$$

and supposing a constant aircraft mass m , the resulting force equations in the flight path fixed coordinate system are

$$m \dot{u}_{Kx} = L \sin \alpha_w - D \cos \alpha_w - W \sin \gamma + T \cos(\alpha - \alpha_w + \sigma) \quad (3.5)$$

$$-m \dot{u}_{Kx} = -L \cos \alpha_w - D \sin \alpha_w + W \cos \gamma - T \sin(\alpha - \alpha_w + \sigma) \quad (3.6)$$

The influence of wind and turbulence is expressed by the wind angle α_w . For a constant moment inertia, the moment equation in the aircraft symmetrical plane can be described by

$$I_{yy} \ddot{\Theta} = \underline{M}^A + \underline{M}^T \quad (3.7)$$

\underline{M}^A presents the resulting aerodynamic moment and \underline{M}^T the thrust moment, both related to the center of gravity. The equations (3.5) - (3.7) are nonlinear differential equations of the aircraft motions, which can be solved by numerical integration. The equations can be further simplified and linearized for small angle values.

In conventional aircraft configurations the tail plane is in the flow field of the wing. The wing induced downwash in the tail region results a reduced angle of attack at the tail plane α_{tail} expressed by the downwash angle ϵ_{tail} . Alterations of the flow condition at the wing meet with a delay time r_H/V at the tail plane.

The description of the dynamic effects at the tail plane is of great importance for the investigation of realistic moment alterations resulting from small scale turbulence and gusts. Essentially, three effects in the model should be taken into account (fig. 3.2).

- stationary angle of attack and downwash delay
- wind delay during the occurrence of wind-angle α_w
- dynamic induced angle of attack at the tail from the pitch motion of the aircraft.

Various solution formulas exist for the examination of the delay (which occurs due to the propagation time between the wing and the tail plane) of the gust effect on the tail. These solution formulas can be used depending on the gust wavelengths and are described in

Ref. [3.1], [3.2], [3.3] as 1-point or 2-point gradient models and time delay models.

In the following the question of how much the full equation system (3.5.) - (3.7.) is to be taken into account should be considered, in order to determine the gust response behaviour, especially with regard to the calculation of the gust load factor.

The most simple mathematical description illustrates the mass point model which, as a plunge only motion, is the basis for gust load determination for the aircraft design method for a long period. Here, the pitching degree of freedom and the force balance in x-direction are omitted. This leads to the simple, well-known equation from the earliest gust load studies, for the maximal vertical additional gust load factor Δn :

$$\Delta n = \frac{\rho V S}{2W} C_{La} \Delta w_{wg} \quad (3.8)$$

In the most unfavourable circumstance, Δw_{wg} represents a step gust. This is not of very practical importance, although it is often used as a reference value for the reactions to other types of gusts. In more realistic cases of a discrete vertical gust, the aircraft experiences a heave or plunge motion w_{kg} while flying through the gust, which reduces the alteration of the angle of attack: $(\Delta \alpha_{eff} = (\Delta w_{wg}(t) - w_{kg}(t)))$. This effect is taken into account through the gust response factor K , which is defined by the relationship of the maximum gust load factor of real gusts to maximum load factor of step gusts. Gust factor K is a function of the mass factor μ_g , as well as the gust wavelength (as a general rule a half of a wavelength or a gradient distance L_m is used) in relation to the mean wing chord \bar{c} .

$$\mu_g = \frac{2m}{\rho S \bar{c} C_{La}} \quad (3.9)$$

Fig. 3.3 illustrates the progress of the K -factor over the mass factor for various relationships L_m/\bar{c} for a one-minus cosine gust. As a sample aircraft with $\mu_g = 30$ and with a gust wavelength of $2L_m = 60\bar{c}$, the maximum gust load factor, as a result of a one-minus cosine gust, amounts to about 72.5% of the maximum value of a step gust of the same gust amplitude. Furthermore, the progress of the FAR-gust factor K_g is recorded and is defined as follows:

$$K_g = \frac{0.88 \mu_g}{5.3 + \mu_g} \quad (3.10)$$

This empirical factor produces somewhat lower values than the analytical solution for the mass point model. This shall be briefly discussed later.

In case of random turbulence stimulation the gust response of the aircraft can be described by means of spectral and correlation methods. If the transfer function of the mass point model between the vertical acceleration and the vertical turbulence velocity is indicated as $F_{\ddot{H},w}(j\omega)$, the power density spectrum of the vertical acceleration is illustrated as follows:

$$\Phi_{\ddot{H}}(\omega) = \Phi_{wW}(\omega) \cdot |F_{\ddot{H},wW}|^2 \quad (3.11)$$

Here, Φ_{wW} illustrates a one-dimensional simplified DRYDEN spectrum of the vertical turbulence component.

$$\Phi_{wW} = \frac{2\sigma^2 T_W}{1 + T_W^2 \omega^2} \quad (3.12)$$

The squared transfer function can be expressed with the relationship:

$$|F_{\ddot{H},wW}|^2 = \frac{\omega^2}{1 + T^2 \omega^2} \quad (3.13)$$

$$T = \frac{2m}{\rho V_r S C_{La}}$$

The relations are illustrated in Fig. 3.4 in the form of a diagram. It is apparent that the maximum vertical acceleration in the area of $1/T < \omega < 1/T_W$ results. The variance of the vertical acceleration can be determined with the PARSEVALIAN theorem:

$$\sigma_{\ddot{H}}^2 = \frac{1}{2\pi} \int_{-\infty}^{\infty} \Phi_{\ddot{H}}(\omega) d\omega = \frac{1}{T^2} \frac{1}{1 + T_W/T} \sigma_{wW}^2 \quad (3.15)$$

Substantial limiting quantities for the variance of the vertical acceleration are the parameter airspeed V , wing loading m/S , gust intensity σ_w and integral scale L_w . Fig. 3.5 illustrates a qualitative analysis of the effect of the parameter on the spectrum of vertical acceleration as a function of the angular velocity ω .

A gust factor for random gusts can also be defined similarly to that of a discrete gust:

$$K = \frac{\sigma_{\ddot{H},random}}{\sigma_{\ddot{H},step}} = \sqrt{\frac{\mu_g}{\mu_g + L_m/\bar{c}}} \quad (3.16)$$

In Fig. 3.6, the K -factors for the gust types 1-cos and ramp with $L_m = L_R = 30$ are compared with the gust factors for stochastic gusts ($L_w = 30\bar{c}$). The lowest gust loads result at the base of random gusts. However, the gradient distance, the gust wave length and the integral scales can not be directly compared with each other.

3.2 Consideration of the Pitch Motion

When evaluating the results obtained up to now, one must not fail to consider that, with the use of the mass point model, marked simplifications are underlying, which alone allow a qualitative analysis.

More exact results require the examination of the degrees of freedom which have, up to now, been neglected. With the use of the example of a model of the longitudinal motion of a twin engine commuter aircraft (mass = 5 to, $\mu_g = 30$), under the influence of a one-minus cosine gust, the differences between a mass point model "Plunge Only", a "Plunge/Pitch"

motion model and a complete model of longitudinal motion shall be illustrated. Fig. 3.7 shows the transfer function (magnitude and phase shift) for three different models. The typical amplitude magnifications and the strong phase alteration of the phugoid motion can only be recognized during full longitudinal motion. In the area of the phugoid frequency, relatively large deviations result for the mass point model (Plunge only) and the Plunge/Pitch model. In the typical turbulence or short scale gust zone; in the zone of "fast period motion" and above it, a good concordance between the complete solution and the Plunge/Pitch model can be recognized.

In Fig. 3.8, a different form of illustration was chosen in which the gust factor K ($K = n_{1-\cos' \max} / n_{\text{step}' \max}$) is applied for the mass point model in comparison to the plunge/pitch model at the gust gradient distance L_m / \bar{c} referring to the mean wing chord. The Plunge/Pitch model results in clearly lower vertical acceleration values. At $L_m = 12.5 \bar{c}$, they are 87% of the mass point model and at $L_m = 45 \bar{c}$ they are ca. 52%. The differences become smaller and smaller for very large gust wavelengths (in reference to mean wing chord).

The gust load reduction through the consideration of the pitching degree of freedom can be explained with a physical demonstration. Due to the downward pitching of the aircraft when flying into the gust (caused by the natural stability), the change in angle of attack is lowered and with it, the load factor. Additionally, as can be seen in Fig. 3.9, the maximum load factor is reached earlier than with the mass point model (for $L_m / \bar{c} > 10$).

The FAR gust factor K_g , which is recorded at $L_m = 12.5 \bar{c}$ is especially emphasized. For the example of $\mu_g = 30$, K_g assumes a value of 0.74, which is fairly close to gust factor K of the plunge/pitch model. The influence of the pitch motion is obviously also taken into account for this empirical factor, K_g .

3.3 Airplane Models for Nonuniform Spanwise Turbulence and Gusts

In the preceding section, conditions were examined which had as their basis uniform discrete or random gust along the wingspan of the aircraft. This is also the case for the "design load requirements". The situation can be compared to a flight through a spanwise uniform wave formation (see Fig. 3.10 a). In reality, a three-dimensional gust or turbulence field looks fundamentally different: the gusts or turbulence velocities also vary along the wingspan of the aircraft (Fig. 3.10 b) and in vertical direction. This has a considerable effect on the aircraft's behaviour in the wind field. The differences in comparison to the case of one-dimensional turbulence effect the reaction in the aircraft lateral motion, as well as the vertical load factor. Solutions using correlation methods were already reported in the 50's for the calculation of lifting forces and rolling moments occurring in a two-dimensional turbulence or gust field (e.g., in Ref. [3.5]). The results of the investigation in Ref. [3.6] show a fundamentally higher gust load for the uniform spanwise gust

model than in the case of the nonuniform model. Ref. [3.7] illustrated that the effects mainly depend on the ratio of wingspan and gust wavelength (sinusoidal gust) respectively integral scale (random gust). Fig. 3.11 shows a comparison between two-dimensional and one-dimensional lift covariances (random) or lift coefficients (sinusoidal) as a function of the geometrical parameter s/L or s/λ_y . An increasing gust alleviation effect is recognizable for the two-dimensional case with increasing wingspan and decreasing integral scale or wavelengths.

Various model formulas are available for the consideration of the influence of two-dimensional turbulence or nonuniform spanwise and longitudinal gusts, which can be adapted for real time flight simulation. In a first approximation the changes in gust velocity in a longitudinal and cross direction are described by means of a gradient model (Ref. [3.8], [3.9]). In this formula, four plotted points are used (two each on the longitudinal and transverse axes) in order to define different gust gradients in the center of gravity of the aircraft (Fig. 3.12). The deviation of the induced rolling moment for the 4 point model was determined from an exact reference solution, dependent on the relationship of gust wavelength to half wingspan (Fig. 3.13). An error in the rolling moment calculation less than 10% requires a gust wavelength which is at least six times greater than the half wingspan (Ref. [3.11]). The gradient model can also be considered as a special case of other general procedures, such as, e.g., the power series method (Ref. [3.10]) or the panel or multipoint method. The lifting surface models shall be briefly explained as being representative of this procedure. Here, the wing (in some cases also the tail plane) is replaced by a number of elementary wings, which are each characterized by a system of consecutive horseshoe vortices (Fig. 3.14). The vortex system induces a flow field which must fulfil the requirements of the kinematic flow conditions of the lifting surface theory under the influence of the airspeed V . It leads from the integral equation of the lifting surface theory to the calculation of the vortex distribution on the flow surface. In support of the TRUCKENBRODT-procedure, Ref. [3.11] has chosen $\bar{c}/4$ line of the wing and the trailing edge to fulfil kinematic flow conditions (Fig. 3.15). Local circulations γ_v and pitching moments μ_v can be determined for each section v with known local angle of attack α_i in each plotted point i . The aerodynamic coefficients of the wing c_L and c_D result, as well as moment coefficients. In order to calculate now aerodynamic forces and moments for the entire wing-tail combination, the influence of the delayed additional velocities which are induced at the tail plane is taken into account through a vortex model.

When a certain type of aircraft is to be very exactly reconstructed from the aerodynamics determined from flight test data and wind tunnel measurements, it is advisable to use a combination of a non-linear center of gravity model, which refers to the average wind in the aircraft center of gravity, and those from the additional forces and moments determined from the panel model. This procedure can also be used under real time requirements in flight

simulation. The amount of computation time is naturally dependent on the capacity of the computer system being used. When using a simulation computing system, for example on the basis of a VAX 4000-300, the dependence of the computing time per simulation cycle displayed in Fig. (3.16) is obtained from the number of wing sections (cycle frequency 20 Hz). For 31 wing sections, a burden of 94% for one computation cycle resulted for the entire simulation program, including turbulence and aerodynamic models. The number of necessary wing sections is dependent on the relationship of the gust wavelength to the wingspan. In the case of the gust wavelength being equal to the wingspan, the procentual errors displayed in Fig. (3.17) result for the rolling moment. For 31 sections, an error of ca. 1% is obtained.

3.4 Unsteady Lift

The results examined in the previous chapter are based on the assumption that a change in the angle of attack results in a change in lift without any time delay. However, this is strictly speaking only valid when the change in the angle of attack takes place sufficiently slowly, as it does in the case of large gust wavelengths in relation to average wing depths (quasi steady conditions). If, however, the gust scale is in the order of magnitude of the aircraft scale or lower, the change in lift of the change in angle of attack follows with the corresponding delay. In Fig. 3.18, this effect is illustrated for the approach of a wing or a horizontal elevator in a step gust. This effect can be expressed by the KÜSSNER function [3.13] as illustrated in Fig. 3.19. The WAGNER function, which is also included, describes the delay in lift due to aircraft motion (Ref. [3.14]). The wing motion effect, however, shall not be further discussed here for reasons of clarity.

H.G. KÜSSNER defined a function $\psi(t)$ as a solution formula for the mathematical description of unsteady lift. The KÜSSNER-function is defined

$$\Delta L = L_{\alpha} \psi(t) \alpha_{W\infty} \quad (3.17)$$

KÜSSNER's formula refers back to very complex functions, which can be approximated fairly well by the superimposition of exponential functions (Ref. [3.15]).

$$\psi(\tau) = (b_0 + b_1 e^{-\beta_1 \tau} + \dots + b_n e^{-\beta_n \tau})$$

$$\tau = \frac{2V}{\bar{c}} t \quad (3.18)$$

The coefficients β_i and b_i are essentially dependent on the aspect ratio and the Mach number. In the first approach, the KÜSSNER-function can be described in simplified form

$$\psi(\tau) = 1 - e^{-t/T^*} \quad (3.19)$$

as is illustrated in Fig. 3.20. Here, T^* is the time constant.

Simple transfer functions can be derived from this KÜSSNER-function, with which the temporal progress of the aerodynamic forces for any (discrete or stochastic) gust disturbances can relatively easily be calculated, as far as the dynamic qualities of the gust disturbances are known.

Using the first approach according to equation 3.19 the transfer function $F(s)$ for unsteady aerodynamic forces is as follows:

$$F(s) = \frac{L_{\alpha}}{1 + Ts} \quad (3.20)$$

$$\text{where } s = \text{LAPLACE-operator, } T = T^* \frac{\bar{c}}{2V}, L_{\alpha} = \frac{\rho}{2} V^2 S C_{A\alpha}$$

The alleviation of gust loads at high turbulence frequencies results, along with the decreasing energy density in the inertial subrange, due to the low-pass effect of the unsteady aerodynamic forces. The decisive value is the relationship of the integral time scale $T (=L/V)$ of the turbulence velocity to the KÜSSNER time constants (Fig. 3.21). Quantitative results shall be demonstrated with the example of a commuter aircraft ($\mu_g = 30$, $m = 5$ to, $m/S = 170 \text{ kg/m}^2$) for discrete one-minus cosine gusts. Here, both the wing and the tail plane were separately calculated with unsteady lift influence. KÜSSNER's time constant for the wing is equal to $T_{K, \text{wing}} = 0.038 \text{ s}$, and that for the tail plane is $T_{K, \text{tail}} = 0.024 \text{ s}$. In this case, as can be seen in Fig. 3.22, a gust alleviation occurs at half gust wavelengths of lower than $10 \bar{c}$. Additionally, for small wavelengths, the penetration depth into the gust for which the maximal vertical acceleration occurs, is changing. The corresponding transfer function is displayed these conditions in the frequency range (Fig. 3.23).

4.1 Flight Test Data from Cross Flights in Atmospheric Turbulence

Much turbulence data and many turbulence spectrums were collected during flight tests in the region of the planetary boundary layer, as well as in the layer 1-2 km above it. In many cases considerable deviations from the idealized conditions named in section 2 occurred. The example shown in Fig. 4.1 is the result of a flight under heavy wind conditions ($V_w = 20 - 27 \text{ m/s}$ at an altitude of 990 m, correspondingly 910 m above ground. The wind components are plotted, as well as the essential state parameters of the longitudinal motion. One may recognize from the vertical wind component that random turbulence is superimposed from thermal cells. The three thermal zones exhibit upwind velocities of between 4 and 6 m/s. The accompanying effects in the aircraft reaction are easily identifiable, e.g., in the downward pitching motion and in the vertical acceleration, which exhibited values up to 4 m/s^2 . The power density spectrum of the vertical acceleration, along with the vertical wind component, is naturally also effected by the head wind component, which exhibits very substantial changes. With the exception of noticeable ef-

fects, such as, e.g., thermal influences, aircraft reactions during flight through atmospheric turbulence can not be assigned to individual turbulence components. An investigation of the corresponding transfer functions and the comparison with accompanying model formulas is not possible.

4.2 Cross Flights through Vertical Gusts of Cooling Tower

Flying through cooling tower vapour in low wind conditions shall serve as an example of the response behaviour of aircraft in discrete small-scale vertical gusts. There is a good possibility to attach wind disturbance and aircraft reaction. In Fig. 4.2, a sample of the vapour velocity profile of the already mentioned cooling tower flight test program is illustrated at an altitude of 580 m above the top of the cooling tower. The aircraft responses expressed by signals of the measured aircraft parameters angle of attack, altitude, vertical velocity, vertical acceleration, pitch angle and pitch rate are also illustrated. A maximum change in angle of attack of 10.5° is recognizable during the flight through the vertical velocity field. In case of a step gust of the same magnitude a change of angle of attack $\Delta\alpha$ of 16.3° would have resulted. Due to the climbing velocity of the aircraft in combination with a certain vertical wind profile ($L_m = 90$ m), only the differences between the gust velocity and climbing velocity of the aircraft are effective. At the point of α_{max} , a change in angle of attack of roughly 10.7° results from the difference between $-w_{gust} = 14.3$ m/s and $\dot{H} = 2$ m/s at an air speed of 65 m/s. This coincides fairly well with the measured value. The aircraft experiences a change in altitude of just under 6 m, largest vertical velocity changes of about +5.5 m/s /- 4 m/s and a maximum additional load factor in a center of gravity of +/- 1.22 g.

The degree of pitching freedom shall now be discussed. Due to static stability, the aircraft pitches downwards about 12° shortly after flying into the gust, whereas the negative gradient of the gust generates a pitch up motion. In the pitching phase, the pitch rate reaches a maximum value of $-17.5^\circ/s$. If the combination of pitching and lifting motions are considered, the typical type of motion of the short period motion can be recognized. In this way one can imagine a motion with a virtual axis of rotation in front of the aircraft's nose (Fig. 4.3). This results, with regard to the portion of rotation acceleration, that passengers in the rear part of the aircraft experiencing more vertical acceleration than the passengers on the front seats or the pilots. The rise of the additional load factor for the passenger area farthest back amounted to between 10% and 20%, in various investigated cases with different types of aircraft.

For those cases from the results of the cooling tower program in which the upwind profiles could be approximated with one-minus cosine

functions, the maximum vertical acceleration was determined and applied to the maximum accelerations that would occur in the case of step gusts of the same gust strength. These gust factors that were reported as such, were compared with K-factors from simulation calculations with models of simplified plunge only motion and plunge/pitch motion. Fig. 4.4 illustrates the result of this comparative calculation applied above the relationship of half wavelengths to the mean wing chord. The measurement results display, in principle, the same tendency as the Plunge/Pitch model. However, for wavelengths above $L_m = 50\bar{c}$, the measured gust factors deviate increasingly from the model result and approach an average course between the plunge only model and the plunge-pitch model. Therefore, the plunge/pitch model leads to favourable gust load values. It must, however, be taken into account that updraft profiles of cooling tower vapour clouds are turbulent velocity profiles. With increasing gust wavelength, the relatively high gradients of turbulent fluctuations differentiate increasingly from the average gradients of the vertical wind. Only the average upwind profiles are included, however, in the model calculation.

5. Concluding Remarks

Based on the simplified plunge motion of the mass-point model, it shall be shown how extensions and improvements of the engineering model lead to the establishment of smaller, more realistic gust loads. Gust alleviation effects occur when the degree of pitching freedom is considered, when the spanwise varying turbulence velocities (2-D and 3-D turbulence) are considered, as well as a result of non steady lift effects. Aeroelastic influences can also lead to a reduction of the gust load. They were, however, not examined here for reasons of clarity.

The mentioned reduction effects are basically dependent on the parameters, wing chord and wingspan, respectively, in relation to the gust wavelength or integral scale of the turbulence, as well as on the mass factor.

The type of aerodynamic model selected also defines the requirements for the turbulence model. Multipoint aerodynamic models or panel methods require at least two-dimensional spatial turbulence models.

The topic of the reaction of aircraft under turbulent and gust influences, including the modelling of aircraft dynamics and atmospheric turbulence, is very extensive and provides sufficient material for several semesters of classes. For this reason, only a general overview could be given in the available space, a few special aspects mentioned and references to some of the many publications made which are available on this topic in large quantities on an international level.

REFERENCES

- [2.1] F. Wippermann
Die "Scales" als ein erstes
Ordnungsprinzip
für alle Turbulenzvorgänge in der
Atmosphäre
PROMET, Heft 1/2 1971
- [2.2] F. M. Hobbilit
Gust Loads on Aircraft: Concepts and
Applications
AIAA Education Series, 1988
- [2.3] M. Perlmutter, W. Frost, G.H. Fichtl
Three Velocity Component, Nonhomogeneous
Atmospheric Boundary-Layer Turbulence
Modeling
AIAA Journal, Vol.15, No.10, out 1977
- [2.4] P. M. Reeves, G. S. Campbell, V. M. Gan
R. G. Joppa
Development and Application of a
Non-Gaussian Atmospheric Turbulence
Model for Use in Flight Simulators
NASA CR-2451, Sept. 1974
- [2.5] V. Gollnick
Erstellung und Bewertung eines drei
dimensionalen Matrixluftturbulenzmo-
dells für die Flugzeugsimulation
Internal Report Inst. für Flugführung,
TU Braunschweig, 1994
- [2.6] S. Lindemann
Vergleichende Untersuchungen zur
Flugzeugbewegung in einem Turbulenzfeld
Internal Report, Inst. für Flugführung
TU Braunschweig, 1993
- [2.7] C. Campbell, V. Sanborn
A Spatial Model of Wind Shear and
Turbulence
Journal of Aircraft, Vol.21, No.12,
Dec. 1984
AIAA Paper 84-0277
- [2.8] S. Raasch, D. Etling
Numerical Simulation of Rotating
Turbulent Thermal Convection
Beitr. Phys. Atmosph., Vol. 64, No. 3,
Aug. 1991, pp. 185 - 199
- [2.9] J.C. Kaimal, J. J. Finnigan
Atmospheric Boundary Layer Flows
Their Structure and Measurement
Oxford University Press, 1994
- [2.10] T. Flassak
Ein nicht-hydrostatisches mesoskaliges
Modell zur Beschreibung der Dynamik der
planetaren Grenzschicht
Fortschr. - Ber. VDI, Reihe 15, Nr.74
VDI-Verlag, Düsseldorf
- [2.11] W. Egler
Mathematische Modellierung der
Ausbreitung von Kühlturmschwaden in
der Atmosphäre
ortschr.-Ber. VDI, Reihe 7, Nr. 59,
VDI-Verlag, Düsseldorf
- [2.12] K.-U. Hahn, T. Heintsch, B. Kaufmann,
G. Schänzer, M. Swolinsky
Wind Models for Flight Simulation
AGARDograph No.301, 1990
- [3.1] J. Krüger
Untersuchungen zu analytischen
Näherungslösungen für den Einfluß von
Vertikalböen auf die Flugzeuglängs-
bewegung Internal Report, Inst. für
Flugführung, Technical University
Braunschweig, 1988
- [3.2] G. Schänzer
Einfluß von Böenstörungen auf die
Flugzeuglängsbewegung
Dissertation
Techn. Univ. Braunschweig, 1969
- [3.3] B. Etkin
Dynamics of Atmospheric Flight
John Wiley & Sons, Inc., 1972
- [3.4] S. O. Rice
Mathematical Analysis of Random Noise
Bell System Techn. Journ., Vol. XXIII,
No. 3, July 1944, pp 282 - 332, and
Vol. XXIV, No.1, Jan. 1945, pp 46 - 156;
- [3.5] J.M. Eggelston et al.
Theoretical Calculation of Power
Spectra of Rolling and Yawing Moments
on a Wing.
In Random Turbulence, NACA-Rep. 1321
- [3.6] J.P. Crimaldi, R.T. Britt, W.P. Rodden
Response of B-2 Aircraft to Nonuniform
Spanwise Turbulence
Journal of Aircraft, Vol. 30, No. 5,
Sept. - Oct. 1993
- [3.7] G. Schänzer
Lift and Rolling Moment of a Finite
Wing due to Sinusoidal and
Stochastic Turbulence.
Institut für Flugführung,
TU Braunschweig, 1993
- [3.8] R. Brockhaus
A mathematical multi-point model for
aircraft motion in moving air
Z. Flugwiss. Weltraumforschung 11
pp 174 - 184, 1987
- [3.9] B. Etkin
Turbulent Wind and Its Effects on Flight
Journ. of Aircraft, Vol.18, No.5.,
May 1981
- [3.10] J.C. Houbolt, R. Steiner, K.G. Pratt
Dynamic Response of Airplanes to
Atmospheric Turbulence Including
Flight Data on Input and Response
NASA TR R-199, June 1964
- [3.11] T. Heintsch
Beiträge zur Modellierung von Wirbel-
schleppen zur Untersuchung des Flug-
zeugverhaltens beim Landeanflug
Dissertation an der Fakultät für
Maschinenbau und Elektrotechnik
TU Braunschweig, 1994
- [3.12] W. Kindel, T. Heintsch, B. Kaufmann
Three Dimensional Teal Time Models
for the Interaction between Wind and
Aircraft
International Conference Flight
Simulation"
Zhukovsky, Moskau Region, Russia,
August 11-16, 1992
- [3.13] H.G. Küssner
Zusammenfassender Bericht über den
instationären Auftrieb von Flügeln
Luftfahrtforschung 13, pp 410 - 424
(1936)
- [3.14] H. Wagner
Über die Entstehung des dynamischen
Auftriebs von Tragflügeln
Dissertation, Charlottenburg, 1924
- [3.15] G. Schänzer
Abschätzung von stochastischen
Böenlasten unter Berücksichtigung
instationärer Luftkräfte.
Z. Flugwiss. Weltraumforsch. 9
(1985), Heft 3

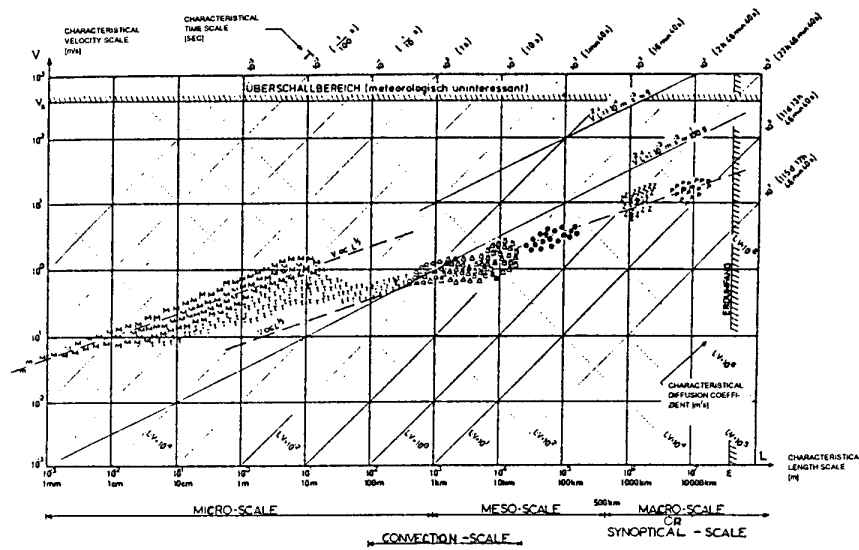


Fig.2.1 Classification of atmospheric turbulence scales [2.1]

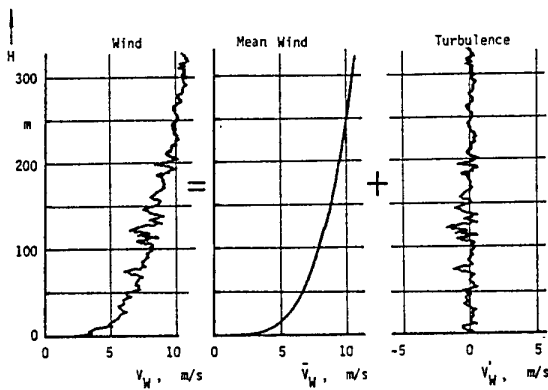


Fig.2.2 Separation of mean wind and turbulence

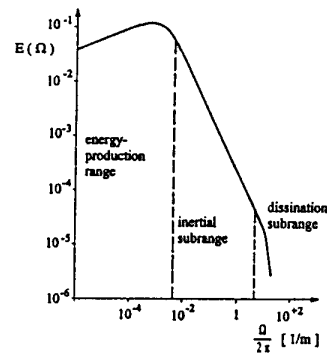


Fig.2.3 Basic energy spectrum function

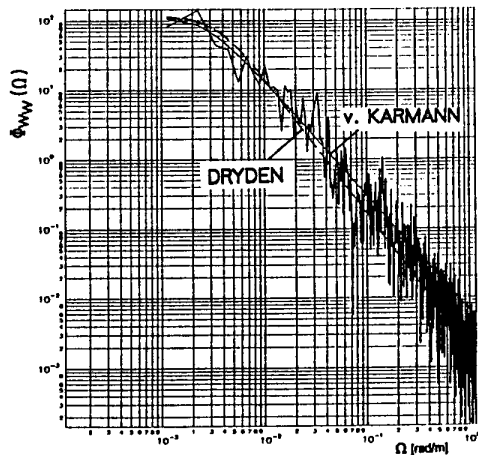


Fig.2.4 Comparison of one-dimensional v.KARMAN- and DRYDEN PDS with measured spectrum

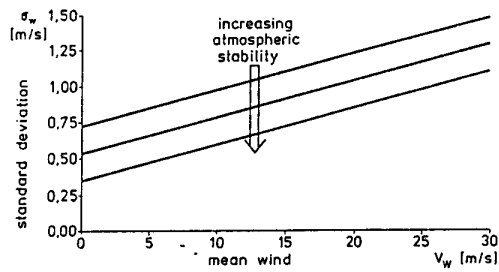


Fig. 2.5 Standard deviation of turbulence velocities versus mean wind speed [2.12]

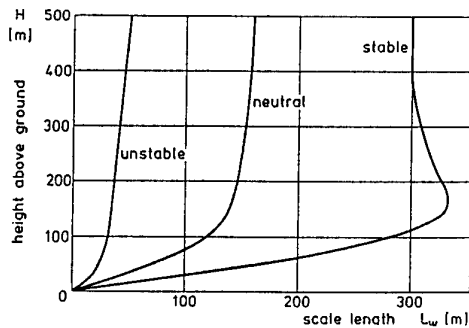


Fig.2.6 Integral scale versus height above ground [2.12]

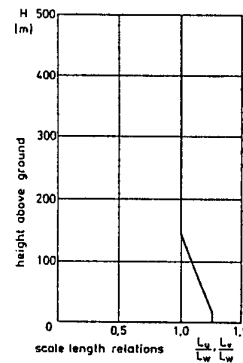


Fig.2.7 Relation of integral scale for horizontal and vertical turbulence components

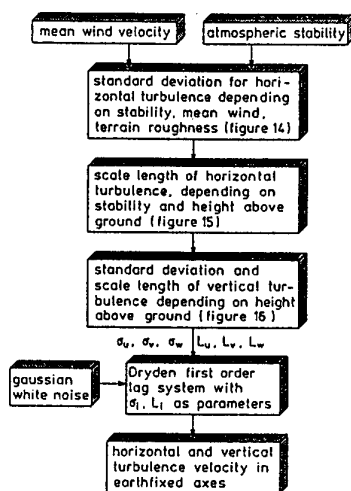


Fig.2.8 One-dimensional turbulence simulation model [2.12]

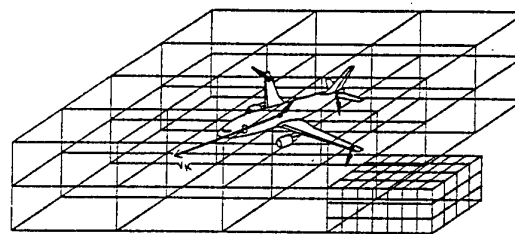


Fig.2.9 Aircraft in the wind-boxes of a matrix-wind model [3.12]

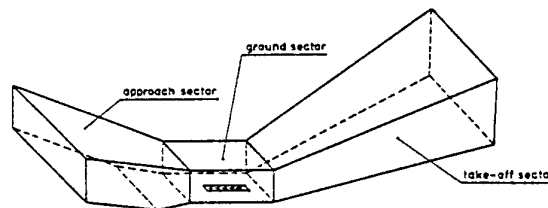


Fig.2.10 Typical take-off and landing area of the matrix wind model [3.12]

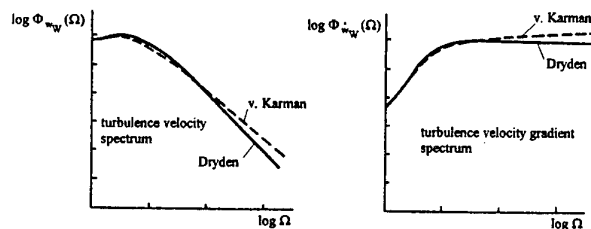


Fig.2.11 Power density spectra of turbulence velocity and acceleration

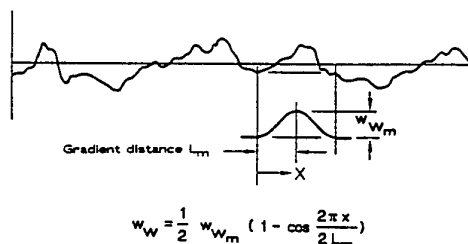


Fig.2.12 Idealization of the gust structure [2.2]

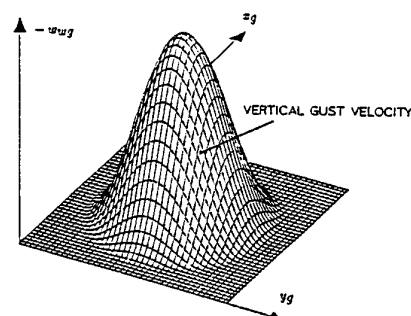


Fig.2.13 Two-dimensional one minus cosine gust

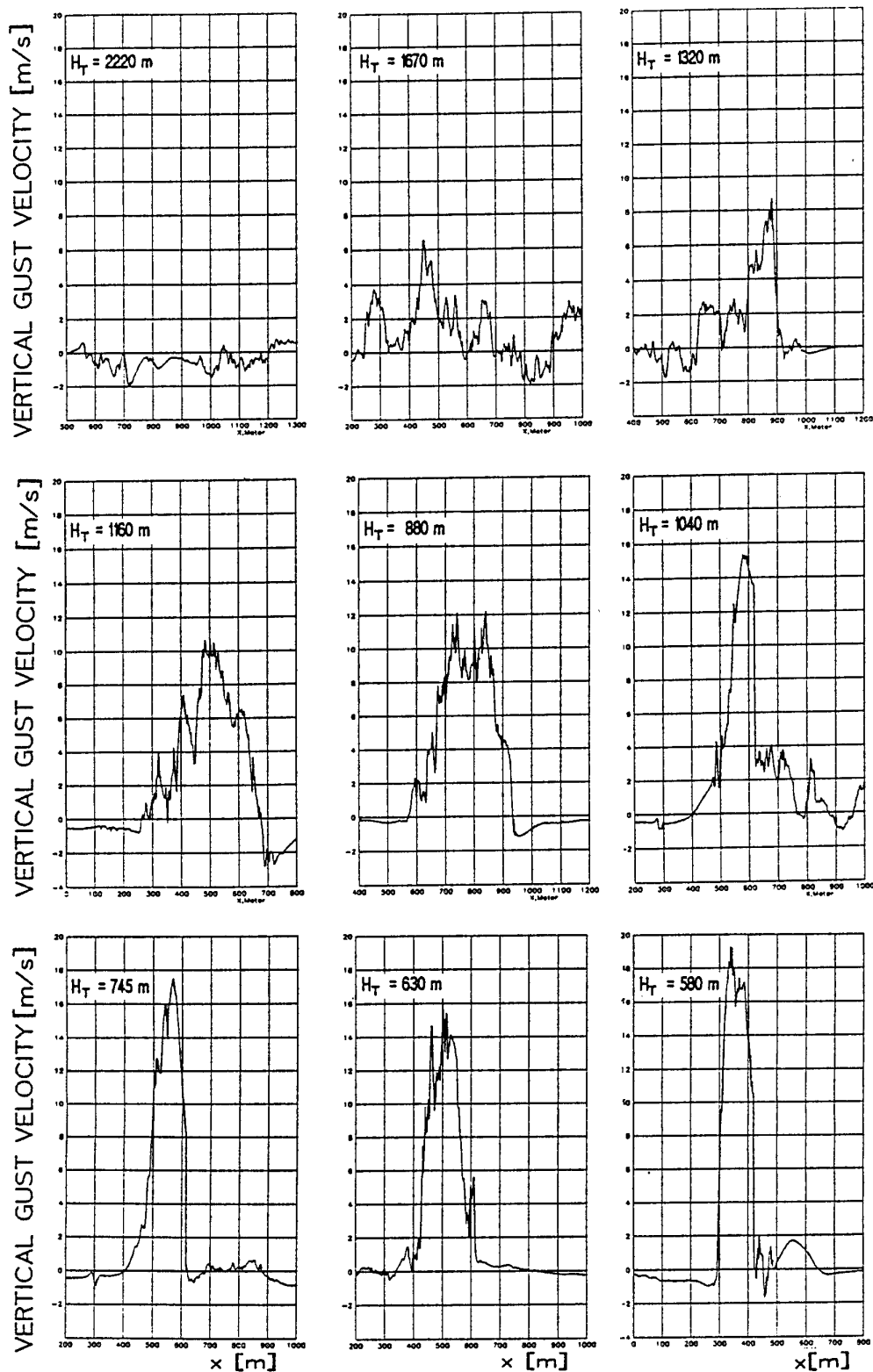


Fig.2.14 Updraft shapes at different height above a cooling tower from flight tests

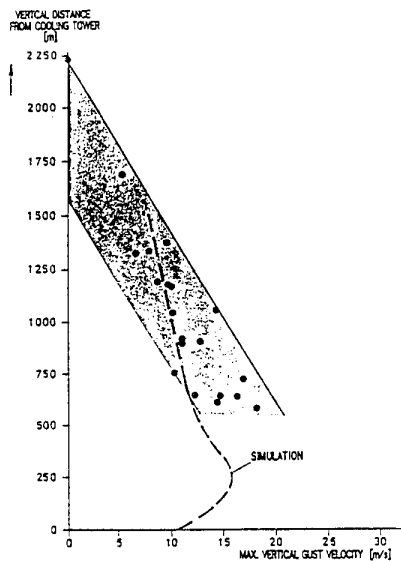


Fig.2.15 Maximum updraft velocity at different vertical distances from the cooling tower

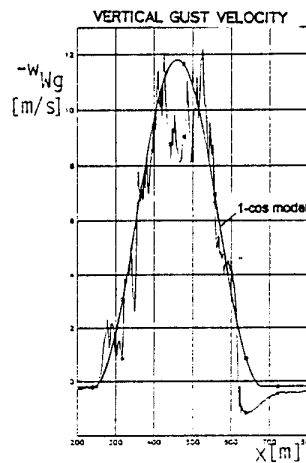


Fig.2.16 Approximation of a cooling tower updraft

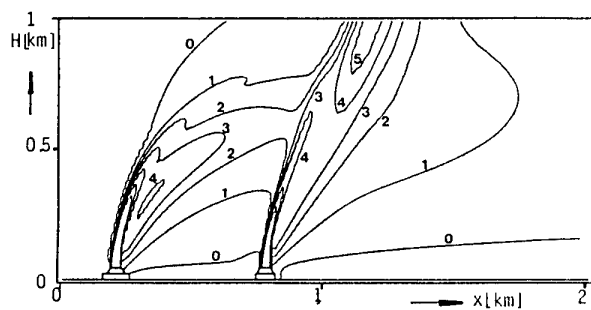


Fig.2.17 Longitudinal section of superposed cooling tower vapour

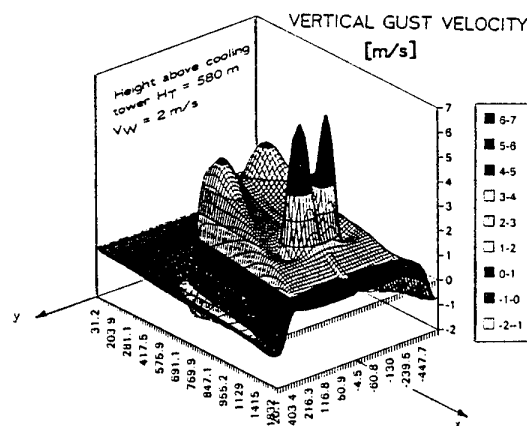


Fig. 2.18 Two-dimensional representation of superposed updraft velocities

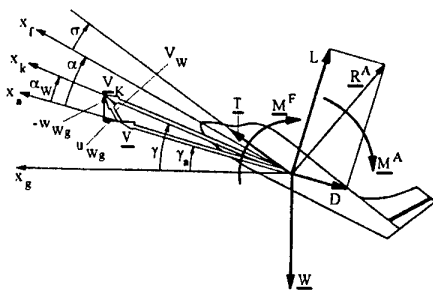


Fig.3.1 Angle definition, velocities, forces

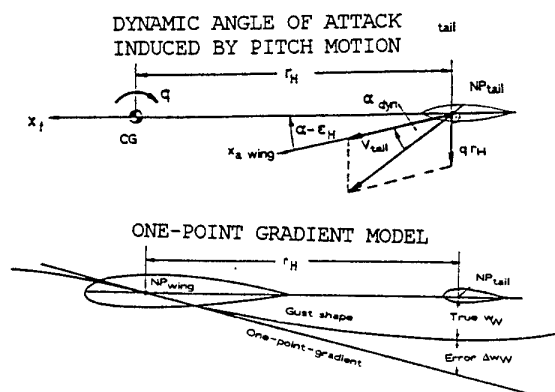
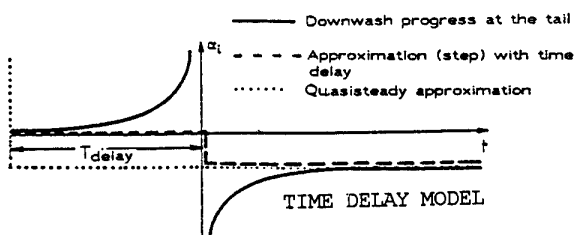


Fig. 3.2 Models for wing - tail effects

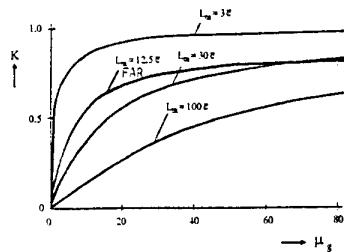


Fig.3.3 K-factor depending on mass factor and wave-length/mean chord relation

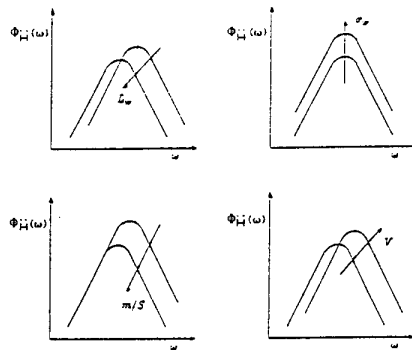


Fig.3.5 Influence of different parameters on the PDS of the vertical acceleration

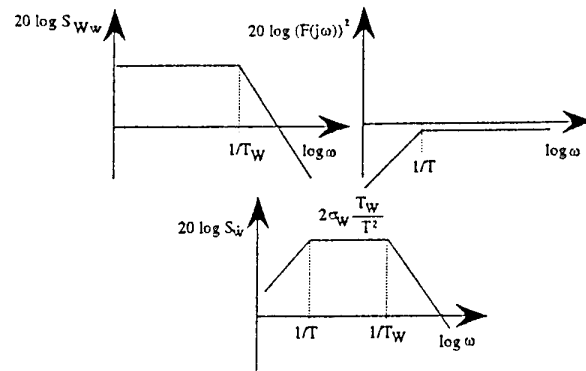


Fig.3.4 PDS of the vertical acceleration composed of turbulence spectrum and aircraft transfer function

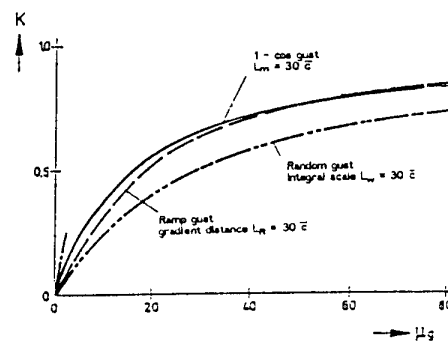


Fig.3.6 Comparison of maximum vertical acceleration for different gusts related on a step gust

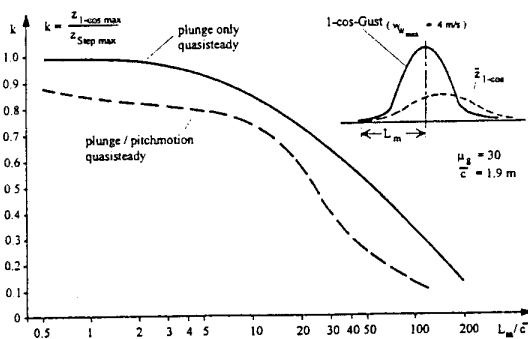


Fig.3.8 Example of K-factors depending on wave length/wing mean chord relation for plunge only and pitch/plunge model

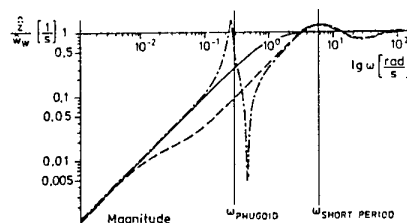


Fig.3.7 Transfer function of different aircraft models [3.1]

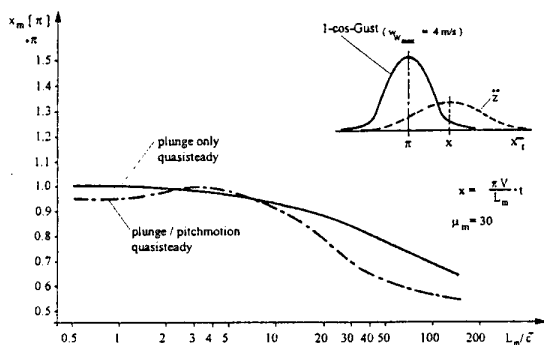
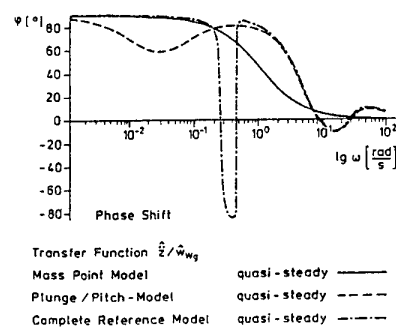


Fig. 3.9 Location of the maximum acceleration in relation to the gust velocity maximum



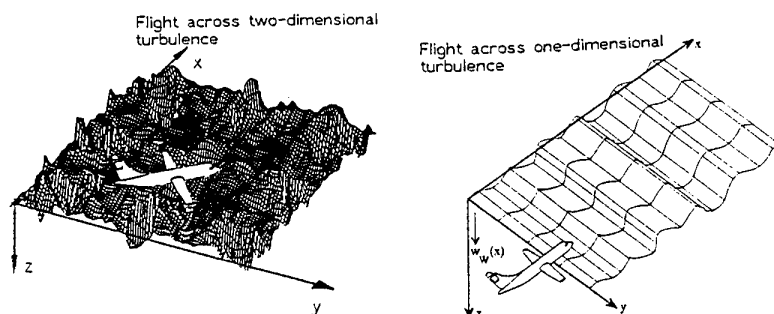


Fig.3.10 Sketch of cross flights in one-dimensional and two-dimensional turbulence

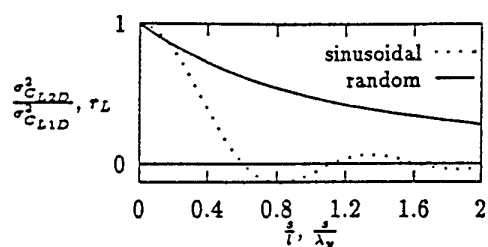
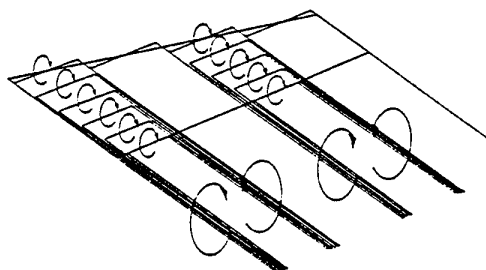
Fig.3.11 Comparison of two-dimensional to one-dimensional lift variance ratio (random $\sigma_{CL2D}^2/\sigma_{CL1D}^2$) and lift coefficient ratio (sinusoidal : r_L), [3.7]

Fig.3.14 Replacing the wing by elementary wings

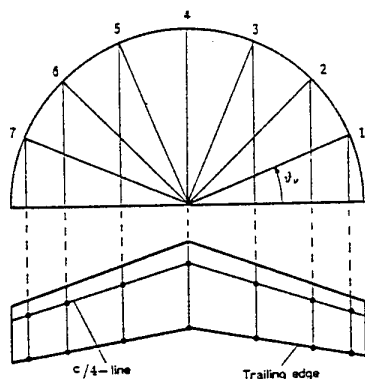


Fig.3.15 Determination of the reference points according TRUCKENBRODT procedure

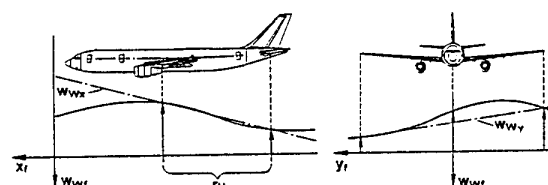


Fig.3.12 Four-point gradient model

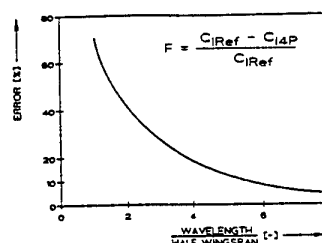


Fig.3.13 Error in rolling moment of the four-point model (from Ref. [3.11])

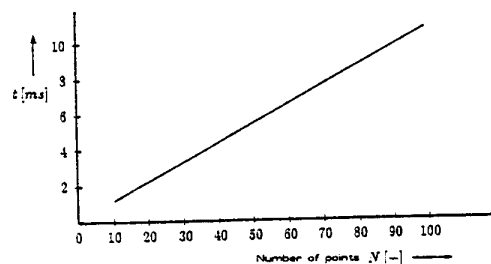


Fig.3.16 Required computing time per simulation cycle depending on the number of reference points [2.6]

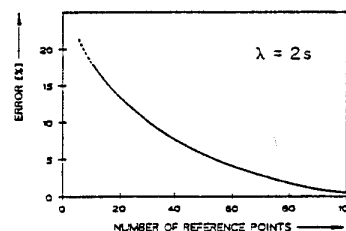


Fig.3.17 Error in rolling moment depending on the number of reference points [3.12]

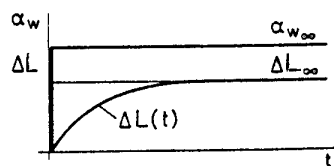


Fig.3.18 Time delay in lift during a step gust

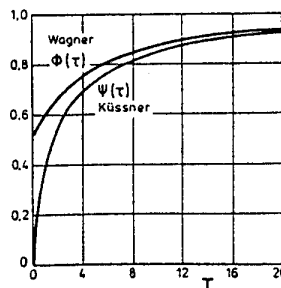


Fig.3.19 Time histories of KÜSSNER and WAGNER functions [3.15]

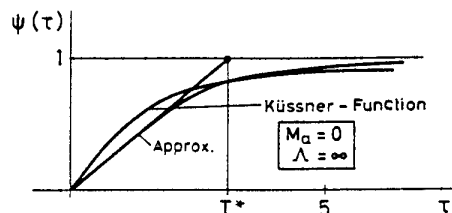


Fig.3.20 KÜSSNER function and approximation [3.15]

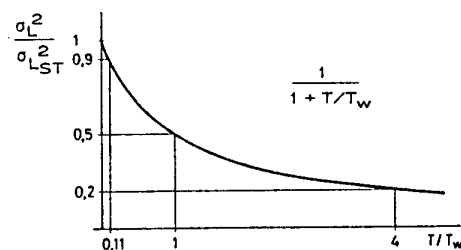


Fig.3.21 Gust alleviation depending on unsteady lift [3.15]

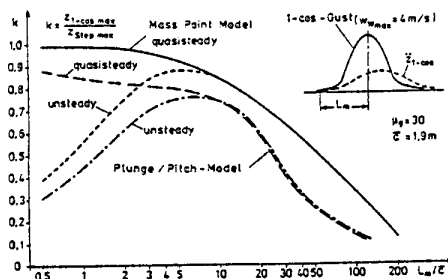
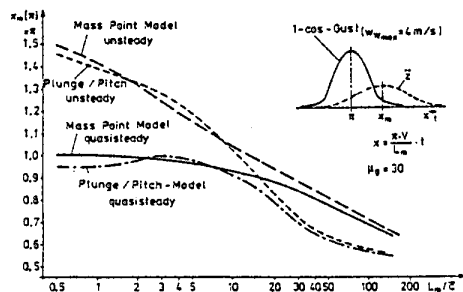
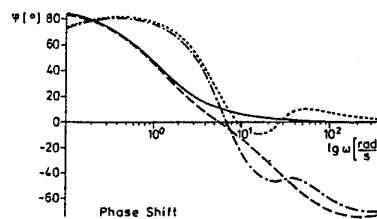
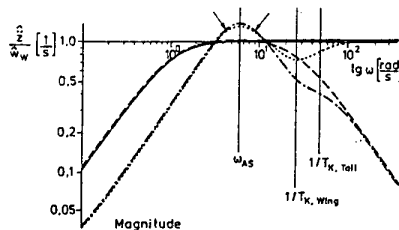


Fig.3.22 Gust response factor depending on the ratio wave length / mean wing chord



Transfer Function $\frac{Z}{w_g}$
Mass Point Model quasi-steady:—; unsteady:---
Plunge / Pitch - Model quasi-steady:—; unsteady:---

Fig.3.23 Unsteady lift effect expressed by the transfer function [3.1]

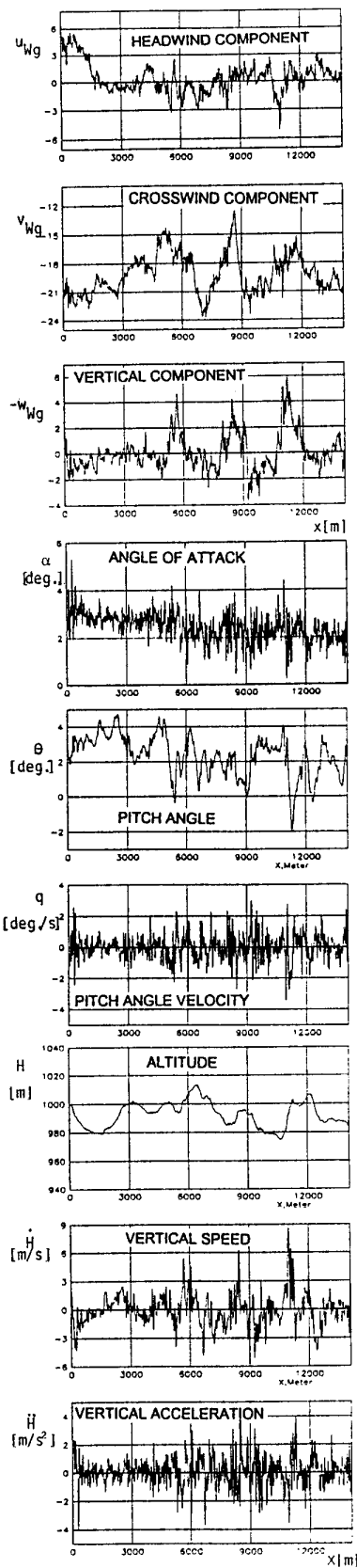


Fig.4.1 Sample of flight test results during flight in turbulence

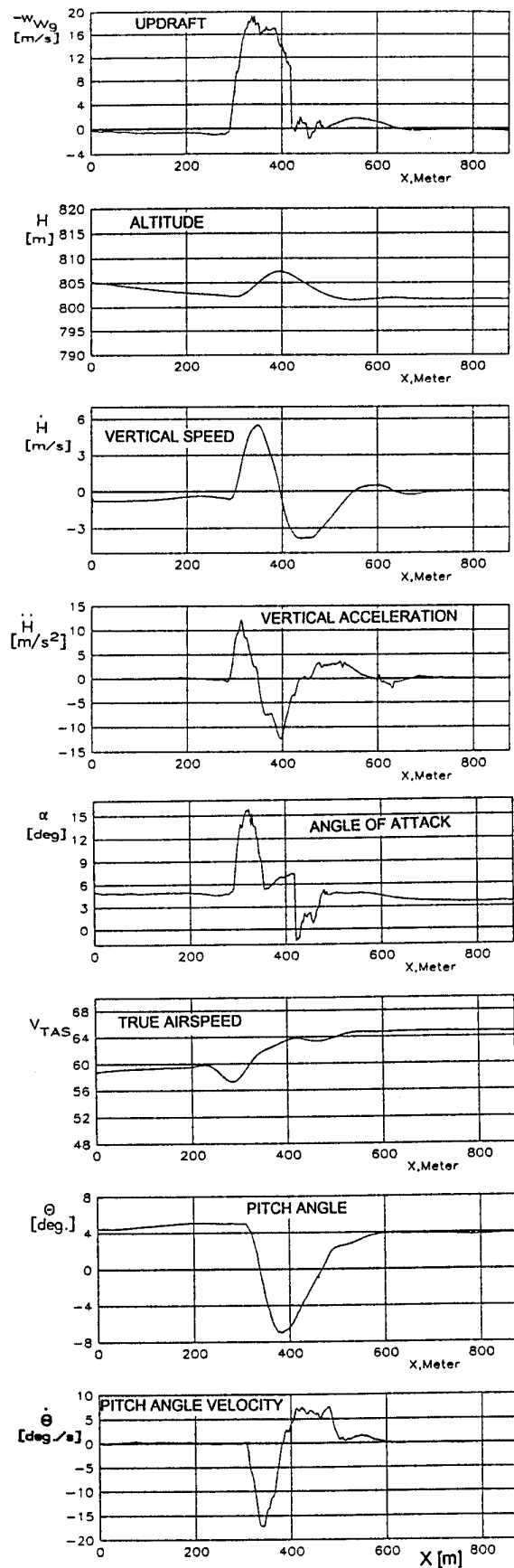


Fig.4.2 Test results from flights across cooling tower updraft

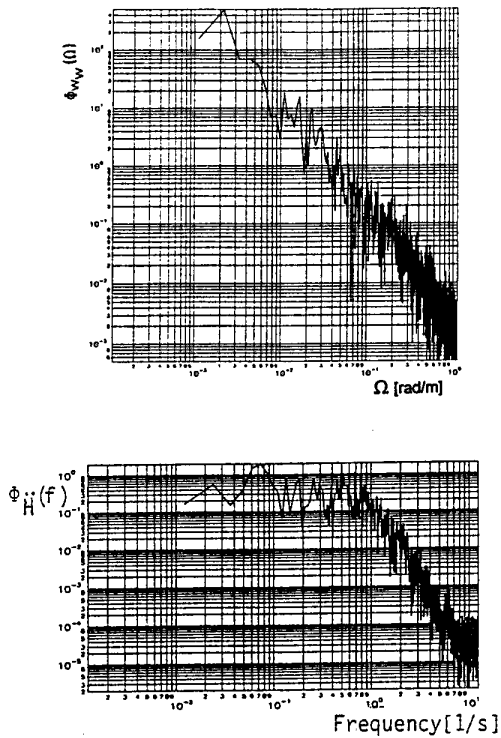


Fig.4.1 (Continuation) Sample of flight test results during flight in turbulence: PDS of the vertical turbulence component and of the vertical aircraft acceleration

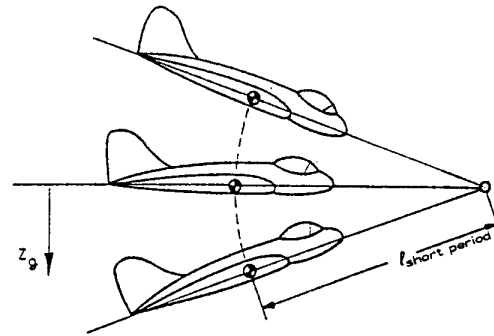


Fig.4.3 Typical kind of aircraft motion in a discrete vertical gust

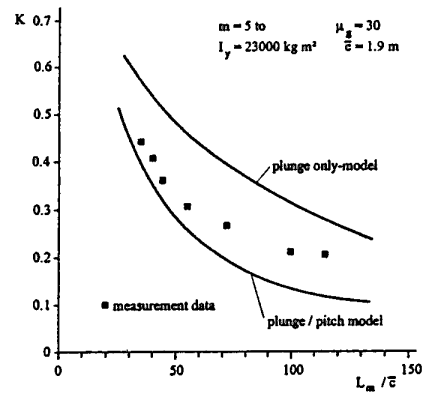


Fig.4.4 Comparison of gust response factors from flight tests, plunge only- and plunge-pitch-models

REPORT DOCUMENTATION PAGE

1. Recipient's Reference	2. Originator's Reference AGARD-LS-197	3. Further Reference ISBN 92-836-1006-7	4. Security Classification of Document UNCLASSIFIED														
5. Originator Advisory Group for Aerospace Research and Development North Atlantic Treaty Organization 7 rue Ancelle, 92200 Neuilly-sur-Seine, France																	
6. Title Flight in an Adverse Environment																	
7. Presented on 7-8 November 1994 in Braunschweig, Germany, 10-11 November 1994 in Lisbon, Portugal, and 15-16 November 1994 in Atlantic City, USA.																	
8. Author(s)/Editor(s) Multiple			9. Date November 1994														
10. Author's/Editor's Address Multiple			11. Pages 168														
12. Distribution Statement There are no restrictions on the distribution of this document. Information about the availability of this and other AGARD unclassified publications is given on the back cover.																	
13. Keywords/Descriptors <table style="width: 100%; margin-top: 10px;"> <tr> <td style="width: 50%;">Aviation safety</td> <td style="width: 50%;">Gusts</td> </tr> <tr> <td>Aircraft</td> <td>Storms</td> </tr> <tr> <td>Flight</td> <td>Rain</td> </tr> <tr> <td>Flight tests</td> <td>Icing</td> </tr> <tr> <td>Turbulence</td> <td>Lightning</td> </tr> <tr> <td>Wakes</td> <td>Electromagnetic environments</td> </tr> <tr> <td>Wind shear</td> <td>Adverse conditions</td> </tr> </table>				Aviation safety	Gusts	Aircraft	Storms	Flight	Rain	Flight tests	Icing	Turbulence	Lightning	Wakes	Electromagnetic environments	Wind shear	Adverse conditions
Aviation safety	Gusts																
Aircraft	Storms																
Flight	Rain																
Flight tests	Icing																
Turbulence	Lightning																
Wakes	Electromagnetic environments																
Wind shear	Adverse conditions																
14. Abstract <p>The environment in which an airplane must operate is a major cause of aircraft accidents. This lecture series focuses on specific aspects of the environment, both natural and man-made, which are the major contributors to these accidents as follows:</p> <ul style="list-style-type: none"> — wake turbulence and the generation of trailing vortex systems; — the results of an extensive flight test program concerning winter storms off the east coast of Canada including effect on aircraft operations. The Canadian Atlantic Storms Program (CASP) includes effects of airframe icing, strong winds, turbulence, wind shear, precipitation, reduced visibility, reduced ceilings and electrification; — electromagnetic effects including electrical discharge properties, in-flight test programs, in-flight lightning models and lightning simulation techniques; — response of an aircraft to wind shear and methods of detection and quantifying this natural hazard; — heavy rain effects on aircraft systems performances in the light of full-scale and model tests with analysis of the results on aerodynamic performance and operations; — measurements of atmospheric turbulence, treatment of aircraft response to random turbulence and discrete gusts. <p>This Lecture Series, sponsored by the Flight Vehicle Integration Panel of AGARD, has been implemented by the Consultant and Exchange Programme.</p>																	

Aucun stock de publications n'a existé à AGARD. A partir de 1993, AGARD détiendra un stock limité des publications associées aux cycles de conférences et cours spéciaux ainsi que les AGARDographies et les rapports des groupes de travail, organisés et publiés à partir de 1993 inclus. Les demandes de renseignements doivent être adressées à AGARD par lettre ou par fax à l'adresse indiquée ci-dessus. *Veuillez ne pas téléphoner.* La diffusion initiale de toutes les publications de l'AGARD est effectuée auprès des pays membres de l'OTAN par l'intermédiaire des centres de distribution nationaux indiqués ci-dessous. Des exemplaires supplémentaires peuvent parfois être obtenus auprès de ces centres (à l'exception des Etats-Unis). Si vous souhaitez recevoir toutes les publications de l'AGARD, ou simplement celles qui concernent certains Panels, vous pouvez demander à être inclu sur la liste d'envoi de l'un de ces centres. Les publications de l'AGARD sont en vente auprès des agences indiquées ci-dessous, sous forme de photocopie ou de microfiche.

CENTRES DE DIFFUSION NATIONAUX

ALLEMAGNE

Fachinformationszentrum,
Karlsruhe
D-76344 Eggenstein-Leopoldshafen 2

BELGIQUE

Coordonnateur AGARD-VSL
Etat-major de la Force aérienne
Quartier Reine Elisabeth
Rue d'Evere, 1140 Bruxelles

CANADA

Directeur, Services d'information scientifique
Ministère de la Défense nationale
Ottawa, Ontario K1A 0K2

DANEMARK

Danish Defence Research Establishment
Ryvangs Allé 1
P.O. Box 2715
DK-2100 Copenhagen Ø

ESPAGNE

INTA (AGARD Publications)
Pintor Rosales 34
28008 Madrid

ETATS-UNIS

NASA Headquarters
Code JOB-1
Washington, D.C. 20546

FRANCE

O.N.E.R.A. (Direction)
29, Avenue de la Division Leclerc
92322 Châtillon Cedex

GRECE

Hellenic Air Force
Air War College
Scientific and Technical Library
Dekelia Air Force Base
Dekelia, Athens TGA 1010

ISLANDE

Director of Aviation
c/o Flugrad
Reykjavik

ITALIE

Aeronautica Militare
Ufficio del Delegato Nazionale all'AGARD
Aeroporto Pratica di Mare
00040 Pomezia (Roma)

LUXEMBOURG

Voir Belgique

NORVEGE

Norwegian Defence Research Establishment
Attn: Biblioteket
P.O. Box 25
N-2007 Kjeller

PAYS-BAS

Netherlands Delegation to AGARD
National Aerospace Laboratory NLR
P.O. Box 90502
1006 BM Amsterdam

PORTUGAL

Força Aérea Portuguesa
Centro de Documentação e Informação
Alfragide
2700 Amadora

ROYAUME-UNI

Defence Research Information Centre
Kentigern House
65 Brown Street
Glasgow G2 8EX

TURQUIE

Millî Savunma Başkanlığı (MSB)
ARGE Dairesi Başkanlığı (MSB)
06650 Bakanlıklar-Ankara

Le centre de distribution national des Etats-Unis ne détient PAS de stocks des publications de l'AGARD.

D'éventuelles demandes de photocopies doivent être formulées directement auprès du NASA Center for AeroSpace Information (CASI) à l'adresse ci-dessous. Toute notification de changement d'adresse doit être fait également auprès de CASI.

AGENCES DE VENTE

NASA Center for
AeroSpace Information (CASI)
800 Elkridge Landing Road
Linthicum Heights, MD 21090-2934
Etats-Unis

ESA/Information Retrieval Service
European Space Agency
10, rue Mario Nikis
75015 Paris
France

The British Library
Document Supply Division
Boston Spa, Wetherby
West Yorkshire LS23 7BQ
Royaume-Uni

Les demandes de microfiches ou de photocopies de documents AGARD (y compris les demandes faites auprès du CASI) doivent comporter la dénomination AGARD, ainsi que le numéro de série d'AGARD (par exemple AGARD-AG-315). Des informations analogues, telles que le titre et la date de publication sont souhaitables. Veuillez noter qu'il y a lieu de spécifier AGARD-R-nnn et AGARD-AR-nnn lors de la commande des rapports AGARD et des rapports consultatifs AGARD respectivement. Des références bibliographiques complètes ainsi que des résumés des publications AGARD figurent dans les journaux suivants:

Scientific and Technical Aerospace Reports (STAR)
publié par la NASA Scientific and Technical
Information Division
NASA Headquarters (JTT)
Washington D.C. 20546
Etats-Unis

Government Reports Announcements and Index (GRA&I)
publié par le National Technical Information Service
Springfield
Virginia 22161
Etats-Unis
(accessible également en mode interactif dans la base de
données bibliographiques en ligne du NTIS, et sur CD-ROM)



AGARD holds limited quantities of the publications that accompanied Lecture Series and Special Courses held in 1993 or later, and of AGARDographs and Working Group reports published from 1993 onward. For details, write or send a telefax to the address given above. *Please do not telephone.*

AGARD does not hold stocks of publications that accompanied earlier Lecture Series or Courses or of any other publications. Initial distribution of all AGARD publications is made to NATO nations through the National Distribution Centres listed below. Further copies are sometimes available from these centres (except in the United States). If you have a need to receive all AGARD publications, or just those relating to one or more specific AGARD Panels, they may be willing to include you (or your organisation) on their distribution list. AGARD publications may be purchased from the Sales Agencies listed below, in photocopy or microfiche form.

NATIONAL DISTRIBUTION CENTRES

BELGIUM

Coordonnateur AGARD — VSL
Etat-major de la Force aérienne
Quartier Reine Elisabeth
Rue d'Evere, 1140 Bruxelles

CANADA

Director Scientific Information Services
Dept of National Defence
Ottawa, Ontario K1A 0K2

DENMARK

Danish Defence Research Establishment
Ryvangs Allé 1
P.O. Box 2715
DK-2100 Copenhagen Ø

FRANCE

O.N.E.R.A. (Direction)
29 Avenue de la Division Leclerc
92322 Châtillon Cedex

GERMANY

Fachinformationszentrum
Karlsruhe
D-76344 Eggenstein-Leopoldshafen 2

GREECE

Hellenic Air Force
Air War College
Scientific and Technical Library
Dekelia Air Force Base
Dekelia, Athens TGA 1010

ICELAND

Director of Aviation
c/o Flugrad
Reykjavik

ITALY

Aeronautica Militare
Ufficio del Delegato Nazionale all'AGARD
Aeroporto Pratica di Mare
00040 Pomezia (Roma)

LUXEMBOURG

See Belgium

NETHERLANDS

Netherlands Delegation to AGARD
National Aerospace Laboratory, NLR
P.O. Box 90502
1006 BX Amsterdam

NORWAY

Norwegian Defence Research Establishment
Attn: Biblioteket
P.O. Box 25
N-2007 Kjeller

PORTUGAL

Força Aérea Portuguesa
Centro de Documentação e Informação
Alfragide
2700 Amadora

SPAIN

INTA (AGARD Publications)
Pintor Rosales 34
28008 Madrid

TURKEY

Millî Savunma Başkanlığı (MSB)
ARGE Dairesi Başkanlığı (MSB)
06650 Bakanlıklar-Ankara

UNITED KINGDOM

Defence Research Information Centre
Kentigern House
65 Brown Street
Glasgow G2 8EX

UNITED STATES

NASA Headquarters
Code JOB-1
Washington, D.C. 20546

The United States National Distribution Centre does NOT hold stocks of AGARD publications.

Applications for copies should be made direct to the NASA Center for AeroSpace Information (CASI) at the address below.

Change of address requests should also go to CASI.

SALES AGENCIES

NASA Center for

AeroSpace Information (CASI)
800 Elkridge Landing Road
Linthicum Heights, MD 21090-2934
United States

ESA/Information Retrieval Service

European Space Agency
10, rue Mario Nikis
75015 Paris
France

The British Library

Document Supply Centre
Boston Spa, Wetherby
West Yorkshire LS23 7BQ
United Kingdom

Requests for microfiches or photocopies of AGARD documents (including requests to CASI) should include the word 'AGARD' and the AGARD serial number (for example AGARD-AG-315). Collateral information such as title and publication date is desirable. Note that AGARD Reports and Advisory Reports should be specified as AGARD-R-nnn and AGARD-AR-nnn, respectively. Full bibliographical references and abstracts of AGARD publications are given in the following journals:

Scientific and Technical Aerospace Reports (STAR)
published by NASA Scientific and Technical
Information Division
NASA Headquarters (JTT)
Washington D.C. 20546
United States

Government Reports Announcements and Index (GRA&I)
published by the National Technical Information Service
Springfield
Virginia 22161
United States
(also available online in the NTIS Bibliographic
Database or on CD-ROM)

